TECHNISCHE UNIVERSITÄT BERLIN

Atmospheric Remote Sensing with Airborne and Spaceborne GNSS Reflectometry: from Tropospheric to Ionospheric Applications

vorgelegt von
Mario Andrés Moreno Bulla, M. Sc.
ORCID: 0009-0009-9124-8063

an der Fakultät VI – Planen Bauen Umwelt
der Technischen Universität Berlin
zur Erlangung des akademischen Grades

Doktor der Ingenieurwissenchaften
- Dr.-Ing. -

genehmigte Dissertation

Promotionsausschuss:

Vorsitzender:	Prof. Dr. Frank Flechtner
Gutachter:	Prof. Dr. Jens Wickert
Gutachterin:	Prof. Dr. Yu Jade Morton
Gutachter:	Prof. Dr. Felipe Geremia-Nievinski
Gutachter:	Dr. Maximilian Semmling

Tag der wissenschaftlichen Aussprache: 17. Oktober 2025

Berlin 2025

Para mi esposa, mis padres, mis hermanos y sobrinos.

La constancia en algún punto superará al talento… ¿vamos?

I hereby declare that I have prepared the present work independently and with my own hands, and without unauthorized outside help, and exclusively using the sources and resources listed.

During the preparation of this document, AI-powered tools were used for translation (Spanish < > English < > German), grammar checking, and language refinement assistance. The AI-generated suggestions were carefully reviewed.

Berlin, 21.07.2025

……
Mario Andrés Moreno Bulla

Hiermit erkläre ich, dass ich die vorliegende Arbeit selbstständig und eigenhändig sowie ohne unzulässige fremde Hilfe angefertigt und ausschließlich die in der Arbeit angegebenen Quellen und Hilfsmittel verwendet habe.

Während der Erstellung dieses Dokuments wurden KI-gestützte Werkzeuge für Übersetzungen (Spanisch < > Englisch < > Deutsch), Grammatikprüfungen und sprachliche Überarbeitungen eingesetzt. Die von der KI generierten Vorschläge wurden von mir sorgfältig geprüft und überarbeitet.

Berlin, 21.07.2025

……
Mario Andrés Moreno Bulla

Abstract

Since its introduction in the 1990s, GNSS Reflectometry (GNSS-R) has emerged as a revolutionary remote sensing technique, demonstrating vast potential for characterizing surface properties across various applications and environments. Today, GNSS-R continues to evolve, supported by increasing operational spaceborne missions such as PRETTY, CYGNSS, SMAP GNSS-R, and TRITON, alongside upcoming missions like HydroGNSS. These missions aim to advance scientific knowledge and generate commercial products such as the LEMUR constellation operated by Spire Global Inc.

In addition to its surface-related applications, GNSS-R offers significant potential for atmospheric monitoring by exploiting the differences between the direct signals (providing information above the receiver) and reflected signals (capturing information below the receiver). However, compared to its extensive application in surface studies, the use of GNSS-R for atmospheric research remains relatively underdeveloped, presenting an opportunity for further exploration to enhance its capabilities in ionospheric and tropospheric studies.

This dissertation addresses this opportunity initially through airborne experiments, which serve as an effective tool for testing concepts and refining methodologies. Airborne GNSS-R data is utilized to demonstrate the feasibility of tropospheric parameter retrieval, specifically Zenith Total Delay (ZTD), over coastal waters. The proposed method yielded promising results, with relative deviations between 5% and 24% compared to the typical ZTD value of 2.3 m at sea level, highlighting the potential for tropospheric monitoring using coherent phase observations.

For ionospheric studies, this thesis begins by conducting a simulation to characterize ionospheric effects on GNSS-R signals at grazing angles, leveraging orbital data from low Earth orbit CubeSats and climatological 3D electron density models. These efforts provided significant insights into model-based ionospheric delays, Doppler shifts, and variations in electron density peak height across diverse scenarios, including elevation ranges from 5° to 30°, established geographic regions, local times, and solar activity levels for spaceborne applications. The analysis further compares the findings from these simulations with GNSS-R code delay observations from the PRETTY mission. Results demonstrated deviation of the estimations between 1.28 m and 4.96 m when compared with state-of-the-art climatological ionospheric models. Additionally, by applying a fitting of the F-layer Chapman model, the observations provide valuable insights into the vertical structure of the ionosphere, showing a difference in peak electron density height of ±15 km compared to values obtained from ionosondes and EISCAT ground stations.

This thesis contributes to advancing GNSS-R as a potential tool for atmospheric and ionospheric monitoring, demonstrating its capability in retrieving tropospheric parameters and characterizing ionospheric effects, while also highlighting the opportunities and challenges for future research.

Keywords: GNSS Reflectometry; grazing angles; atmospheric monitoring; ionospheric delay; tropospheric delay; zenith total delay; slant total electron content; NEDM2020 model; PRETTY mission; code delay; carrier phase delay.

Zusammenfassung

Seit ihrer Einführung in den 1990er Jahren hat sich die GNSS-Reflektometrie (GNSS-R) als eine bahnbrechende Fernerkundungstechnik etabliert, die ein enormes Potenzial zur Charakterisierung von Oberflächeneigenschaften in verschiedenen Anwendungen und Umgebungen aufweist. Heute entwickelt sich GNSS-R kontinuierlich weiter, unterstützt durch eine wachsende Anzahl operationeller Missionen wie PRETTY, CYGNSS, SMAP GNSS-R und TRITON, sowie zukünftige Missionen wie HydroGNSS. Diese Missionen zielen darauf ab, das wissenschaftliche Verständnis zu erweitern und kommerzielle Produkte wie die der LEMUR-Konstellation von Spire Global Inc. zu generieren.

Neben seinen oberflächenbezogenen Anwendungen bietet GNSS-R erhebliches Potenzial für die atmosphärische Sondierung, indem es die Unterschiede zwischen direkten Signalen (die Informationen oberhalb des Empfängers liefern) und reflektierten Signalen (die Informationen unterhalb des Empfängers erfassen) nutzt. Im Vergleich zu seiner umfassenden Anwendung in der Oberflächenforschung ist die Nutzung von GNSS-R für atmosphärische Studien jedoch noch relativ wenig erforscht, was die Möglichkeit bietet, die Methode weiterzuentwickeln und ihre Anwendung für ionosphärische und troposphärische Untersuchungen zu verbessern.

Diese Dissertation nutzt diese Gelegenheit durch luftgestützte Experimente, die als effektives Instrument zur Überprüfung von Konzepten und zur Optimierung von Methoden dienen. Die Analyse von luftgestützten GNSS-R-Daten zeigt die Machbarkeit der troposphärischen Parameterschätzung, insbesondere der Zenith Total Delay (ZTD), über Küstengewässern. Die vorgeschlagene Methode lieferte vielversprechende Ergebnisse, mit relativen Abweichungen von 5 % und 24 % im Vergleich zu theoretischen Werten auf Meereshöhe, was das Potenzial kohärenter Phasenbeobachtungen für die troposphärische Sondierung unterstreicht.

Für die ionosphärische Sondierung beginnt diese Arbeit mit der Simulation ionosphärischer Effekte auf GNSS-R-Signale bei sehr niedrigen Elevationswinkeln, basierend auf Orbitaldaten von Spire Global Inc. sowie klimatologischen 3D-Elektronendichtemodellen. Diese Simulation liefern wertvolle Einblicke in die ionosphärischen Verzögerungen, Doppler-Verschiebungen und Variationen der Höhe der Elektronendichtemaximum unter verschie-

denen Bedingungen, darunter Elevationsbereiche von 5° bis 30°, geografische Regionen, lokale Tageszeiten und solare Aktivitätsniveaus für weltraumgestützte Anwendungen. Die Analyse verbindet diese Simulationsergebnisse mit GNSS-R-Codeverzögerungsbeobachtungen der PRETTY-Mission. Die Ergebnisse zeigen, dass die Schätzungen der relativen ionosphärischen Verzögerung um 0,5 % bis 18 % von etablierten ionosphärischen Modellen abweichen. Darüber hinaus liefern diese Beobachtungen wertvolle Erkenntnisse über die vertikale Struktur der Ionosphäre, einschließlich der Korrelation zwischen Variationen der F-Schicht-dichtmaximum und den beobachteten Aufhebungspunkten ionosphärischer Verzögerungen.

Diese Arbeit trägt zur Weiterentwicklung von GNSS-R als potenzielles Werkzeug für die atmosphärische und ionosphärische Überwachung bei. Sie demonstriert die Fähigkeit, troposphärische Parameter zu erfassen und ionosphärische Effekte zu charakterisieren, und hebt zugleich die Chancen und Herausforderungen für zukünftige Forschungsarbeiten hervor

Schlüsselwörter: *GNSS-Reflektometrie; Streifender Geometrie; atmosphärische Sondierung; ionosphärische Verzögerung; troposphärische Verzögerung; zenitale Gesamtverzögerung; schräge Gesamtelektronendichte; NEDM2020-Modell; PRETTY-Mission; Code-Verzögerung; Trägerphasenverzögerung.*

Acknowledgments

This dissertation marks the culmination of a new chapter in my academic journey, one I chose to pursue after several years away from university life. It would not have been possible without the support, guidance, and encouragement of the exceptional people around me.

First and foremost, I would like to express my sincere gratitude to Prof. Dr. Jens Wickert, who has supported me since my master's studies and encouraged me continuously throughout the early stages of my scientific career and during this doctoral process.

I am deeply thankful to Dr. Maximilian Semmling, who has not only been a key advisor in my research but also a mentor in both professional and personal aspects. His constant support and guidance have been fundamental in enriching this work and shaping my development as a researcher.

My sincere thanks also go to Dr. Mainul Hoque, whose valuable feedback, technical advice, leadership, and patience greatly contributed to making my doctoral experience at the German Aerospace Center (DLR) both fulfilling and successful.

To my colleagues at GFZ and DLR, I extend my heartfelt thanks for their collaborative spirit and constructive discussions, which made the working environment both productive and enjoyable.

A special acknowledgment goes to Ing. Jairo Lozano, my first mentor in my professional career, from whom I learned not only countless technical skills but, more importantly, the principles, values, and professional ethics upon which I have built my career, and now my path as a researcher.

To my family: my wife Mafe, who has been my partner in countless adventures for more than half my life, including this doctoral journey, always there with her smile and unconditional support. To my parents, Doris and Guillermo, to whom I owe much of who I am today. Their love, patience, and unwavering belief in me have been the foundation of my resilience and determination. To my brother, sisters, nephew, and nieces, you have been a constant source of motivation and encouragement, especially during moments when my energy felt depleted. To all of you, thank you!

This work is dedicated to all those who inspire perseverance and remind us that "constancy, at some point, surpasses talent".

List of Publications

This thesis is based on the research presented in the following appended papers:

- **Paper 1:**
  Moreno, M., Semmling, M., Stienne, G., Dalil, W., Hoque, M., Wickert, J., & Reboul, S. (2022). "Airborne Coherent GNSS Reflectometry and Zenith Total Delay Estimation over Coastal Waters". *Remote Sensing, 14(18), Article 18.* DOI: 10.3390/rs14184628.

- **Paper 2:**
  Moreno, M., Semmling, M., Stienne, G., Hoque, M., & Wickert, J. (2023). "Characterizing Ionospheric Effects on GNSS Reflectometry at Grazing Angles from Space". *Remote Sensing, 15(20), Article 20*. DOI: 10.3390/rs15205049

- **Paper 3:**

  Moreno, M., Semmling, M., Zus, F., Stienne, G., Dielacher, A., Hoque, M., Wickert, J., & Nahavandchi, H. (2025). Grazing-angle ionospheric delays observed during the GNSS-R PRETTY mission. Journal of Geodesy, 99(11), 89. DOI: https://doi.org/10.1007/s00190-025-02010-z

Publications Contribution

Author	**Mario Moreno**	**MM**
Co-authors	Maximilian Semmling	MS
	Georges Stienne	GS
	Wafa Dalil	WD
	Mainul Hoque	MH
	Jens Wickert	JW
	Serge Reboul	SR
	Florian Zus	FZ
	Andreas Dielacher	AD
	Hossein Nahavandchi	HN

Item	**Paper 1**	**Paper 2**	**Paper 3**
Conceptualization	MM (70%), MS (15%), GS (15%)	MM (80%), MS (10%), GS (10%)	MM (80%), MS (10%), GS (5%), FZ (5%)
Methodology	MM (80%), MS (10%), GS (10%)	MM (80%), MS (10%), GS (10%)	MM (80%), MS (10%), FZ (10%)
Software	MM (60%), MS (10%), GS (30%)	MM (80%), MS (20%)	MM (80%), MS (10%), AD (10%)
Data resources	MM (70%), MS (10%), GS (10%), WD (10%)	MM (80%), MS (20%)	MM (70%), MS (10%), FZ (10%), AD(10%)
Writing—original draft preparation	MM (100%)	MM (100%)	MM (100%)
Writing—review and editing	MM (10%) MS (15%), GS (15%), WD (15%), MH (15%), JW (15%), SR (15%)	MM (8%), MS (23%), GS (23%), MH (23%), JW (23%)	MM (9%), MS (13%), FZ (13%), GS (13%), AD(13%), MH (13%), JW (13%), HN (13%)
Visualization	MM (100%)	MM (100%)	MM (100%)
Supervision	MS (40%), JW (40%), MH(20%)	MS (40%), JW (40%), MH(20%)	MS (40%), JW (40%), MH(20%)

Contents

List of Figures

List of Tables

List of Abbreviations

BDGIM	BeiDou Global Ionospheric Delay Correction Model
BDS	Chinese Beidou System
BRCS	Bistatic Radar Cross Section
CHAMP	CHAllenging Minisatellite Payload
CYGNSS	Cyclone Global Navigation Satellite System
DLR	Deutsches Zentrum für Luft- und Raumfahrt
DDM	Delay Doppler Map
DM	Delay Map
DTU18	Danmarks Tekniske Universitet - 18 Model
ECMWF	European Centre for Medium-Range Weather Forecasts
EMW	Electromagnetic Wave
EPB	Equatorial Plasma Bubbles
ESA	European Space Agency
EUV	Extreme Ultraviolet
GEO	Geostationary Earth Orbits
GFZ	Deutsche GeoForschungsZentrum
GGOS	Global Geodetic Observing System
GIM	Global Ionospheric Map
GLONASS	GLObal NAvigation Satellite System
GNSS	Global Navigation Satellite System
GNSS-R	Global Navigation Satellite System Reflectometry
GPS	Global Positioning System
GRACE	Gravity Recovery and Climate Experiment mission
HSA	High Solar Activity
IGS	International GNSS Service
IPP	Ionospheric Piercing Point
IRI	International Reference Ionosphere
IRNSS	Indian Regional Navigation Satellite System
LEO	Low Earth Orbit
LHCP	Left Hand Circularly Polarized
LOS	Line of Sight
LSA	Low Solar Activity
MAD	Mean Absolute Deviation
MEO	Medium Earth Orbit
MSS	Mean Sea Surface

NASA	National Aeronautics and Space Administration
NEDM2020	Neustrelitz Electron Density Model 2020
NTCM	Neustrelitz TEC Model
PARIS	Passive Reflectometry and Interferometry System
PNT	Position, Navigation, and Time
PRETTY	Passive REflecTomeTry and dosimetry
PRN	Pseudorandom Noise code
PSD	Power Spectral Density
PWV	Precipitable Water Vapor
QZSS	Japanese Quasi-Zenith Satellite System
RHCP	Right Hand Circularly Polarized
RMSE	Root Mean Squared Error
RO	Radio Occultation
SNR	Signal-to-Noise Ratio
SVN	Space Vehicle Number
SWH	Significant Wave Height
TCWV	Total Column Water Vapor
TDS-1	Technology Demonstration Satellite-1
TEC	Total Electron Content
TECU	Total Electron Content Units
UK-DMC	United Kingdom Disaster Monitoring Constellation
UT	Universal Time
VLBI	Very Long Baseline Interferometry
VMF	Vienna Mapping Function
WGS84	World Geodetic System 1984
ZHD	Zenith Hydrostatic Delay
ZTD	Zenith Total Delay
ZWD	Zenith Wet Delay

Chapter 1.

Introduction

Our planet is an extremely complex system composed of multiple coupled subsystems, including the biosphere, hydrosphere, lithosphere, atmosphere, and social systems. One of the primary challenges of the 21st century, climate change, influenced also by anthropogenic activities, has significantly affected these subsystems and their interactions, leading to natural disasters, severe weather conditions, and substantial impacts on human activities. Therefore, it is essential to employ various technical tools and technologies to ensure continuous and precise monitoring and research of these phenomena, in order to provide accurate and timely information to support decision-making to mitigate climate change impacts.

Global Navigation Satellite Systems (GNSS) developed for Positioning, Navigation, and Timing (PNT), are undoubtedly among the technologies that have contributed most to Earth observation, remote or in situ. The GNSS capabilities allow us to measure continuously with high precision a wide range of geophysical phenomena, including the movement of tectonic plates, changes in ocean level, volcanic behavior, landslides, and local deformations, etc. Moreover, as a continuous operating technology capable of transmitting real-time signals in all-weather conditions, GNSS applications extend beyond PNT-based uses. As GNSS signals travel from the transmitter to the receiver, they experience refraction effects induced by the atmospheric layers, influencing their path and speed. This characteristic has enabled the development of *Remote Sensing* (RS) methods based on GNSS signals for atmospheric monitoring. Notable examples include GNSS Radio Occultation (GNSS-RO) (Mannucci et al., 2020) and GNSS Meteorology (Brenot, 2020), which have been extensively employed over the past decades to retrieve key tropospheric and ionospheric parameters (Jin et al., 2014).

The troposphere is the lowest layer of the Earth's atmosphere that induces delays in GNSS signals depending on variations in temperature, pressure, water vapor, and the relative positions of the transmitter and receiver. As a result, it is possible to determine signal delay parameters like the precipitable water vapor (PWV) from Zenith Total Delays (ZTD). Global and local GNSS ground-based networks have been widely employed in providing meteorological observations to monitor the PWV, enhancing the understanding of water vapor distribution by offering high spatiotemporal variability, and capturing long-term trends in atmospheric water vapor (Brenot, 2020).

The ionosphere is a layer of the Earth's upper atmosphere that induces delays in GNSS signals depending on variations in the total number of electrons between the GNSS satellite and the receiver, referred to as Total Electron Content (TEC). Networks such as the International GNSS Service (IGS) network have made it possible to generate reliable global TEC maps. These maps have significantly contributed to understanding ionospheric gradients and anomalies, advancing space weather research, and improving models of ionospheric behavior (Morton et al., 2020). However, ground-based networks have certain drawbacks, including limited spatial coverage, particularly over oceans and remote areas, and susceptibility to data gaps due to environmental factors or maintenance issues. Addressing these limitations requires complementing ground-based data with satellite-based GNSS observations, which provide more comprehensive and continuous global coverage.

GNSS Radio Occultation is a spaceborne GNSS remote sensing technique capable of providing valuable datasets in atmospheric investigations. GNSS-RO relies on GNSS signals tracked by a Low Earth Orbit (LEO) satellite in a limb-crossing geometry to infer atmospheric properties. Observations from GNSS-RO have contributed to retrieving accurate tropospheric parameters, such as refractive index, pressure, and density profiles. Additionally, due to its sensitivity to the ionosphere vertical plasma density structure, GNSS-RO observations provide ionospheric electron density profiles and information on TEC variability. Satellite missions like CHAMP (Reigber et al., 2002), GRACE (Tapley et al., 2004), and COSMIC/FORMOSAT-3 (Anthes et al., 2008) have provided long-term stable data for atmospheric climate monitoring, climate change studies, and space weather research (Wickert et al., 2009). Although GNSS-RO is a valuable source of atmospheric data, it has certain limitations. These include relatively coarse horizontal resolution and limited coverage in some regions. The latter is primarily due to the relative position of the GNSS and low orbit inclination of LEO satellites, particularly in polar areas.

A relatively new technique has emerged in GNSS remote sensing: GNSS Reflectometry (GNSS-R). GNSS-R leverages signals transmitted by GNSS satellites and reflected off Earth's surface to derive information about surface characteristics. This technique has found numerous applications by deploying GNSS-R receivers in a variety of ground-based scenarios and on moving platforms, including ships (Ichikawa et al., 2024), unmanned aerial vehicles (Regmi et al., 2021), aircrafts , and spacecrafts (Foti et al., 2015) . GNSS-R capabilities include retrieving sea surface altimetry and sea state (Semmling et al., 2012; Wang et al., 2018) , detecting sea ice (Yan & Huang, 2019), estimating snow thickness (Munoz-Martin et al., 2020), measuring ocean wind speed (Komjathy et al., 2004), monitoring soil moisture content (Larson et al., 2008), assessing vegetation changes (Asgarimehr et al., 2024), detecting ocean microplastics (Hoseini et al., 2021), identifying sea surface targets (Di Simone et al., 2018) , and monitoring rainfall, hurricanes, and typhoons (Foti et al., 2017), among others.

Although the primary applications of GNSS-R have been related to surface properties retrieval, its potential in atmospheric monitoring has also been explored. In 1996, Katzberg & Garrison proposed using the U.S. Global Positioning System (GPS) to determine ionospheric delay over the ocean. Since then, multiple studies have been conducted to demonstrate the capabilities of GNSS-R to monitor tropospheric (Wang, 2023) and ionospheric conditions (Liu

et al., 2022), as well as investigate other atmospheric properties. This makes GNSS-R a complementary technique that can help fill the gaps left by other remote sensing methods.

This dissertation aims to enhance our understanding of GNSS Reflectometry as a valuable tool for atmospheric studies. The research presented in this thesis is based on three scientific publications (refer to the List of Publications) that utilize both airborne and spaceborne GNSS-R data to derive and analyze tropospheric and ionospheric parameters. The research objectives and thesis structure are described in the following sections.

1.1 Objectives and Research Questions

Although GNSS was originally designed for PNT applications, its L-band signals have proven highly valuable for remote sensing. GNSS-R leverages these existing signals, making it a cost-effective technique that utilizes the already established GNSS infrastructure. This makes GNSS-R adaptable for deployment on airborne platforms, enabling large-scale studies of geophysical properties and atmospheric parameters over diverse environments. Additionally, spaceborne configurations, particularly with the emergence of CubeSats and small satellite constellations, offer a unique opportunity for global-scale reflectometry observations.

The progressive development highlights the need for further research and methodological advancement in GNSS-R for atmospheric applications. This approach has the potential to deliver stable and high spatiotemporal resolution datasets for: 1) the troposphere, by monitoring water vapor distribution and enhancing our understanding of the hydrological cycle; and 2) The ionosphere, by offering valuable insights into TEC variability, which is essential for space weather research. Therefore, this dissertation focuses on exploring these GNSS-R scenarios, providing insights into evaluating current measurement capabilities and developing new applications for tropospheric parameter retrieval and ionospheric studies. The objectives of this thesis can be summarized as follows:

- **Objective 1: To contribute to advancing airborne GNSS reflectometry techniques for tropospheric parameter retrieval over the sea and analyze the impact of sea state on GNSS-R observables.**

The following Research Questions (RQ) are formulated to develop this objective:

  - *RQ 1.1: How effectively can phase observations from airborne GNSS-R data be utilized to retrieve atmospheric parameters, such as ZTD, over coastal waters?*
  - *RQ 1.2: What is the influence of surface roughness (sea state) on airborne GNSS-R measurements, and how does this affect the Doppler spread and phase coherence?*

To address these research questions, a four-day GNSS-R flight campaign, organized by the GFZ, was conducted in 2019 over the coastal waters near Calais, France. This campaign utilized an innovative data collection platform configuration, deploying a low-cost ultralight aircraft equipped with a GNSS antenna and receiver to capture signals reflected from the sea

surface. These observations provide a valuable dataset for assessing the potential of tropospheric retrievals using airborne GNSS-R, under varying sea state conditions. The results evaluate the accuracy and reliability of atmospheric parameters obtained from airborne GNSS-R and provide insights into how environmental factors (sea state) influence the Doppler spreading and the phase coherence of the observations.

Objective 2: To contribute to enhancing the understanding of ionospheric effects on spaceborne GNSS-R through model-based simulations across polar and tropical latitudes, aiming to improve the accuracy of remote sensing applications at grazing angles.

The following research questions can articulate this objective:

- *RQ 2.1: How do varying ionospheric conditions, including slant TEC and F-layer peak height variations, affect spaceborne GNSS-R signal delays and Doppler shifts at grazing angles?*
- *RQ 2.2: To what extent can ionospheric delay be characterized and modeled to improve the accuracy of GNSS-R applications at grazing angles?*

To investigate these research questions, over 1200 satellite orbit tracking arcs from specialized GNSS-R CubeSats from SPIRE Global Inc. were analyzed to comprehensively assess ionospheric effects on spaceborne GNSS-R at grazing angles ranging from 5° to 30°. The TEC is computed using the Neustrelitz Electron Density Model (NEDM2020) (Hoque et al., 2022). The NEDM2020 is an empirical ionospheric model that delivers three-dimensional electron density distributions for both the ionosphere and plasmasphere integrating distinct models for the F and E layers[1]. The derived TEC is the basis for estimating the ionospheric delays and Doppler shifts. The results provide insights into ionospheric effects depending on latitude regions, diurnal variations, and changes in solar activity. These findings contribute to future GNSS-R missions by quantifying the modeled ionospheric impact on signal delay and frequency shifts, based on observation time and location.

- **Objective 3: To enhance the understanding of ionospheric delays in the Arctic region using spaceborne single-frequency GNSS-R observations and to assess model-based corrections for improving atmospheric delay estimations.**

The following research questions cover this objective:

- *RQ 3.1: How accurately can spaceborne single-frequency GNSS-R data be used to estimate ionospheric delays at grazing angles?*
- *RQ 3.2: What insights can be gained into the ionospheric structure from analyzing spaceborne GNSS-R observations at grazing angles?*

These research questions are addressed by analyzing spaceborne reflectometry data from the CubeSat Passive Reflectometry and Dosimetry (PRETTY) mission, launched by the European Space Agency (ESA) in October 2023. PRETTY is a pioneering mission in reflectometry, utilizing E5/L5 signal bands from the GNSS European Galileo and U.S. Global Positioning System (GPS) satellites. The dataset consists of Delay Maps (DM) GNSS-R observations over the Artic region at grazing elevations angles ranging from 15° to 0.01°. The investigations aim to

[1] https://www.dlr.de/en/so/research-transfer/research-infrastructure/models/nedm

utilize and exploit PRETTY data for ionospheric delay estimation and analysis, making this research one of the first significant contributions produced from the mission's data since its launch.

1.2 Thesis Structure

This thesis comprises five chapters. The first chapter introduces the topic, providing an overview of the significance of GNSS Reflectometry in atmospheric studies and articulating the motivation behind this research. It also presents the research questions and objectives that guide the subsequent investigations.

The second chapter presents the basics of the research, covering key concepts related to GNSS Reflectometry, atmospheric monitoring, and the interaction of GNSS signals with atmospheric layers. It also discusses the relevant methodologies and models used in GNSS-R studies, providing a theoretical foundation for the work presented in this thesis.

This dissertation is based on three appended papers. Chapter 3 discusses the key findings from these papers, highlighting the results of airborne and spaceborne GNSS Reflectometry for atmospheric parameter retrievals. The chapter provides an in-depth analysis of the methodologies used and the implications of the results in the context of tropospheric and ionospheric studies.

Chapter 4 presents the conclusions of this research, summarizing the key findings and their significance. It also outlines potential future work, suggesting possibilities for further research to build upon the advancements made in this dissertation.

Finally, Chapter 5 presents the appended publications, providing the complete versions of the three scientific papers that form the foundation of this dissertation.

Chapter 2.

Fundamentals

2.1 Overview of the Global Navigation Satellite Systems

A constellation of satellites offering worldwide Positioning, Navigation, and Timing services is called a Global Navigation Satellite System (GNSS). The system may consist of a constellation of satellites in Medium Earth Orbit (MEO), along with satellites in Inclined Geosynchronous Orbits (IGSO) or Geostationary Orbits (GEO) for regional applications, or a combination of these configurations. Together, these satellites form the space segment, which is complemented by the control segment and the user segment. The control segment includes a global network of ground stations responsible for monitoring and data uploading. The user segment comprises devices ranging from smartphones to specialized high-end receivers that process the continuously transmitted signals from GNSS satellites to derive precise location and timing information. Today, GNSS plays a crucial role in everyday societal activities, supporting a wide range of applications. Readers can refer to sources such as Hofmann-Wellenhof et al. (2008), Teunissen & Montenbruck (2017), and Morton et al. (2020) for a comprehensive description of GNSS and its applications.

Satellite-based positioning is based on the traditional resection method used in classical geodesy, where an unknown position is determined by measuring distances to various objects with known positions. In satellite-based positioning, electromagnetic waves or GNSS signals are used to estimate these distances. The transmitted frequencies fall within the L-band spectrum, which spans approximately 1.2 to 1.6 GHz, corresponding to wavelengths of roughly 25 cm to 19 cm, respectively. This designated frequency range is optimal for signal propagation through the atmosphere due to its low susceptibility to ionospheric absorption and scattering effects, as well as minimal attenuation by atmospheric gases and precipitation. This ensures reliable signal reception under a wide range of atmospheric and space weather conditions, making the L-band an ideal choice for satellite-based navigation and remote sensing applications.

At present, multiple countries operate or plan to develop their own GNSS systems, each featuring independent satellite constellations. These include the U.S. Global Positioning System (GPS), the Russian GLObal NAvigation Satellite System (GLONASS), the European Galileo, the Chinese Beidou (BDS), the Japanese Quasi-Zenith Satellite System (QZSS), and the Indian

Regional Navigation Satellite System (IRNSS). The availability of these multiple constellations significantly increases the number of observations, providing stable simultaneous data for various GNSS applications, including reflectometry. Table 2.1 presents an overview of the operational GNSS, detailing their satellite orbit types, number of satellites, origin, and utilized frequencies (Teunissen & Montenbruck, 2017).

Table 2.1 Description of Operational GNSS system constellations.

System	GPS	GLONASS	Galileo	BeiDou	QZSS	IRNSS/ NavIC
Orbit	MEO	MEO	MEO	MEO, IGSO, GEO	GEO, IGSO	GEO, IGSO
Nominal satellites	24	24	30	27, 3, 5	1, 3	3, 4
Orbit inclination	56°	64.8°	56°	55°	43°	29°
Initial service	1993	1993	2016	2012	2018	2018
Origin	USA	Russia	Europe	China	Japan	India
Frequency (MHz)	L1 1575.42 L2 1227.60 L5 1176.45	L1 1602.00 L2 1246.00 L3 1202.025	E1 1575.42 E5a 1176.45 E5b 1207.14 E6 1278.75	B1 1561.098 B2 1207.14 B3 1268.52	L1 1575.42 L2 1227.60 L5 1176.45 LEX 1278.75	L5 1176.45 S 2492.028

2.1.1 GNSS Signals Characteristics

GNSS relies on electromagnetic (EM) waves due to their advantageous propagation characteristics. The EM waves consist of synchronized oscillations of the electric field $\boldsymbol{E}$ and the magnetic field $\boldsymbol{B}$. EM characteristics are described by Maxwell's equations, which specify that a spatially varying electric field is associated with a time-varying magnetic field. The harmonic representation of the electric and magnetic fields, as a function of time and space is given by:

$$\boldsymbol{E}(x,t) = E_0 \cos\left(\frac{2\pi t}{T} - \frac{2\pi x}{\lambda} + \phi\right)\hat{\boldsymbol{e}}. \tag{2.1}$$

$$\boldsymbol{B}(x,t) = B_0 \cos\left(\frac{2\pi t}{T} - \frac{2\pi x}{\lambda} + \phi\right)\hat{\boldsymbol{b}}. \tag{2.2}$$

Here, E_0 and B_0 represent the amplitudes of electric and magnetic fields, respectively. The period T is the time it takes for one complete oscillation or cycle of the wave. The wavelength λ is defined as the distance between identical points, such as consecutive crests, in adjacent cycles of the EM wave as it propagates through space. The phase ϕ specifies the position in the oscillation cycle of the wave at the reference point P, as presented in Figure 2.1. The $\hat{\boldsymbol{e}}$ and $\hat{\boldsymbol{b}}$ denote the direction of oscillation for the electric and magnetic fields, respectively.

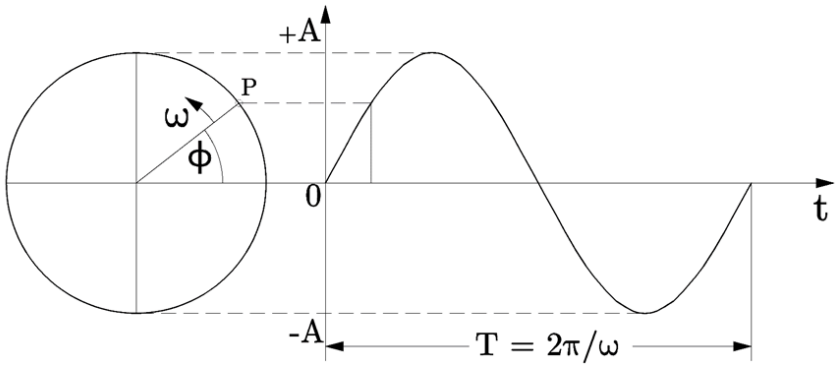

Figure 2.1 Wave representation. The angular velocity $\omega = 2\pi f$, with the linear frequency f given in Hertz (cycles per second)

The electric field of an EM wave oscillates perpendicular to the direction of propagation. It can be represented by the vector $\boldsymbol{E} = [E_x, E_y]$ which defines the polarization of the EM wave. When the direction of $\boldsymbol{E}$ is constant, the wave has linear polarization. If the ratio between the components of $\boldsymbol{E}$ varies, the wave exhibits circular or elliptical polarization. A clockwise rotation of the electric field vector indicates Right-Handed Circular Polarization (RHCP), while counterclockwise rotation indicates Left-Handed Circular Polarization (LHCP). An effect known as Faraday rotation occurs when a linearly polarized EM wave travels through ionized gases, causing a rotation in the plane of polarization. To counteract this effect, GNSS signals are transmitted as RHCP. When the GNSS signal reflects off Earth's surface, depending on the properties of the reflecting surface and the incident or elevation angle (E), and assuming specular reflection, the polarization may change from RHCP to LHCP (Hofmann-Wellenhof et al., 2008). This characteristic has been investigated by Hoseini et al. (2020) using GNSS reflectometry, who demonstrated that combining observations from RHCP and LHCP links significantly enhances the accuracy and sensitivity of sea surface roughness estimates, achieving an overall correlation of 0.82 with wind measurements.

Figure 2.2 illustrates the different types of polarization, including linear and circular polarization. Linear vertical polarization is represented in blue, linear horizontal polarization in green, and RHCP in red.

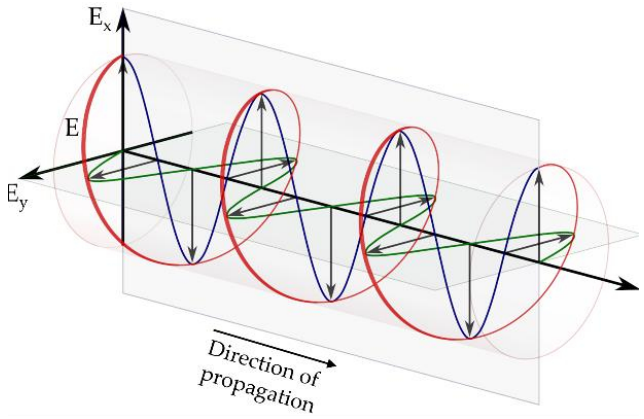

Figure 2.2 Linear (green and blue) and Circular (red) Polarization representation.

GNSS signals are transmitted using a modulated binary sequence called the Pseudo-Random Noise (PRN) code. The PRN code is typically transmitted at rates ranging from 1 to 10 MHz, with a repetition period that varies from milliseconds to seconds. Figure 2.3 illustrates the modulation scheme used in GPS satellites.

The PRN code acts as an identifier, allowing signals transmitted at the same frequency from different satellites to be distinguished. These modulated signals carry the transmission time, satellite ephemerides, and other essential information within the data message, which allows for calculating the range from the satellite to the receiver and determining the GNSS satellite's position.

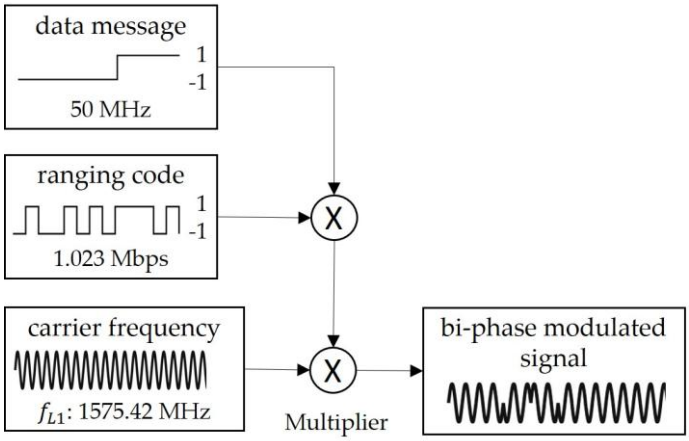

Figure 2.3 Representation of the range code layer and data message phase modulation on GPS carrier signals (L1). Based on Hofmann-Wellenhof et al. (2008).

The range is determined by estimating the time delay between the received signal and the original transmission time. This is accomplished by correlating the incoming signal with a locally generated replica of the satellite's PRN code, resulting in a waveform that exhibits a correlation peak when correctly aligned. Due to the relative movement between the satellite and the receiver, a frequency shift, known as the Doppler effect, is induced in the GNSS signal, which also influences the correlation process. Therefore, a search over both code delay

and Doppler frequency is necessary to accurately correlate the local replica with the incoming signals. To find the point of maximum correlation, the receiver generates a Delay Doppler Map (DDM), which represents variations in correlation values across different Doppler shifts and code delays. The representation of the DDM can be observed in Figure 2.4.

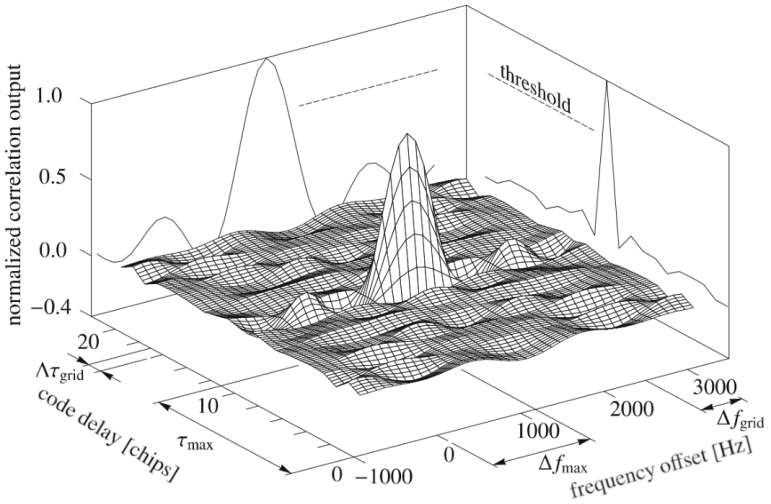

Figure 2.4 Delay Doppler Map: Correlation results as a function of code delay and frequency offset. Based on Hofmann-Wellenhof et al. (2008).

2.1.2 GNSS Observables

GNSS signals enable three fundamental types of measurements (Hofmann-Wellenhof et al., 2008):

Code Range (Pseudorange): This represents the time difference between the reception time (in the receiver's time frame) and the transmission time (in the satellite's time frame) of a specific satellite signal. This measurement represents the distance from the receiver's antenna to the satellite's antenna, incorporating receiver and satellite clock offsets, as well as other biases such as atmospheric delays. The pseudorange p can be modeled as the sum of the true geometric range between the satellite and receiver antenna p_{geo}, the receiver and transmitter clock biases dt_{Rx} and dT_{Tx} scaled by the speed of light c, the tropospheric and ionospheric delays p_{trop} and p_{iono}, instrumental delays p_{instr}, and unmodeled errors or noise n. This relationship is expressed mathematically as:

$$p = p_{geo} + c(dt_{Rx} - dT_{Tx}) + p_{trop} + p_{iono} + p_{inst} + n. \qquad (2.3)$$

Carrier Phase: Along with the local PRN code replica, the receiver generates a signal at a frequency close to that of the incoming carrier signal using a local oscillator. Any difference between the generated and incoming signals creates a beat frequency and a corresponding beat phase. By measuring the accumulated beat phase, the phase of the satellite signal can be

retrieved. Carrier phase measurements offer higher precision than the code range measurements. However, they are affected by an inherent ambiguity corresponding to an unknown integer number of wavelengths (λN). This ambiguity (N) resets arbitrarily every time the receiver loses lock on the signal, resulting in sudden jumps or discontinuities in the measured range. The carrier-phase measurements can be modeled as:

$$\Phi = p_{geo} + c(dt_{Rx} - dT_{Tx}) + p_{trop} - p_{iono} + \lambda N + p_{inst} + n. \qquad (2.4)$$

Here, in addition the terms in Equation (2.3), the carrier-phase measurements include the integer ambiguity N and the ionospheric terms appears with opposite sign since the ionosphere produces an advance of the carrier-phase measurement (see section 2.1.1)

Doppler Frequency: This is a measure of the frequency shift caused by the Doppler effect, which occurs when the observer (the GNSS receiver) moves relative to the signal source (the GNSS satellite). This shift provides information on the range rate, i.e., the time derivative of the carrier phase, corresponding to the line-of-sight velocity between the GNSS satellite and the receiver.

2.2 Atmospheric Effects on GNSS Signals

As GNSS signals travel from the satellite to the receiver, they traverse both the ionosphere and the neutral atmosphere (troposphere). Throughout this propagation path, the signals experience delays, attenuation, and refraction due to the refractive index (n) properties of these atmospheric layers (Hobiger & Jakowski, 2017). Based on Fermat's principle, the path length (L) is defined by integrating the refractive index (n) along the path of the signal as it travels from the transmitter to the receiver as follows:

$$L = \int_{Rx}^{Tx} n(s)\, ds. \qquad (2.5)$$

The refractive signal delay can be determined by comparing the path length with the geometric length between the satellite and the receiver. This delay is calculated using:

$$\Delta L = \int_{Rx}^{Tx} n(s)\, ds - \int_{Rx}^{Tx} ds. \qquad (2.6)$$

or simplified as:

$$\Delta L = \int_{Rx}^{Tx} (n-1)\, ds. \qquad (2.7)$$

In the context of GNSS signals, atmospheric delays are classified into contributions from the neutral atmosphere and the ionosphere. The delay caused by the neutral atmosphere is primarily referred to as the tropospheric delay, as the troposphere is the dominant source of such delays. The troposphere is a non-dispersive medium for signals the L-band, meaning that the delay it induces is independent of the signal frequency. In contrast, the ionosphere acts as a dispersive medium, leading to delays that depend on the signal frequency due to the levels of ionization within the ionospheric layers. Ionospheric and tropospheric delays are described in the sections below. A comprehensive representation of the Earth's atmospheric layers, along with an electron density profile and the depiction of satellite missions at various orbital heights, is provided by the Global Geodetic Observing System (GGOS) and illustrated in Figure 2.5.

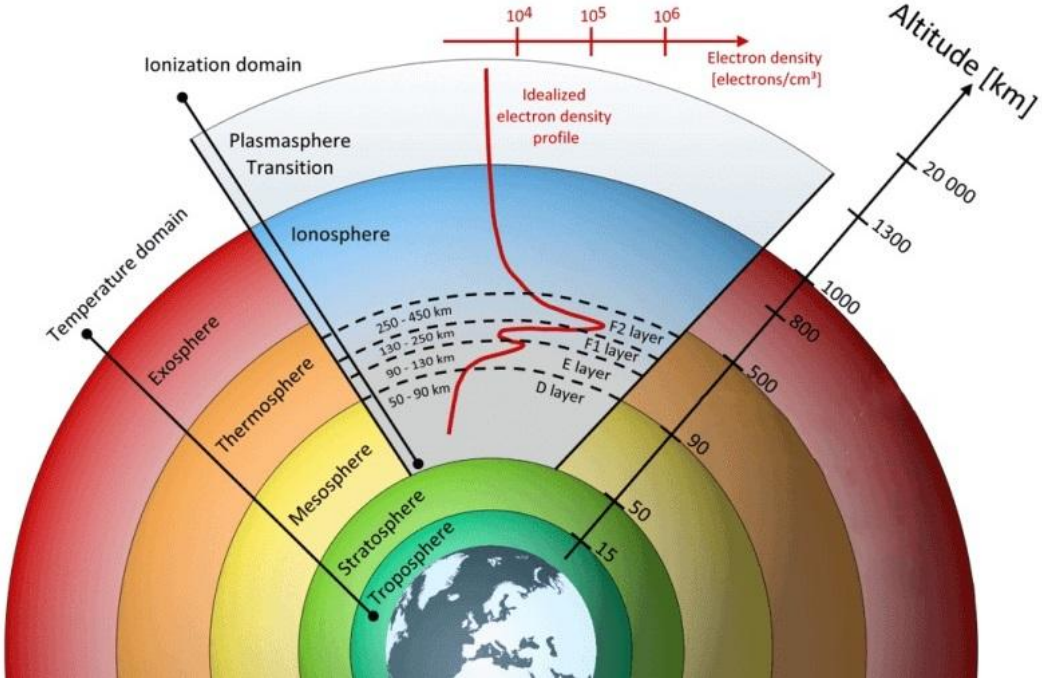

Figure 2.5 Representation of Earth's atmosphere, including the ionospheric layers and satellite missions at different orbital heights. Source: GGOS website.

2.2.1 Ionospheric Delay

The ionosphere is a region of the Earth's atmosphere that extends from approximately 50 kilometers to over 1,000 kilometers in altitude. In this layer, ionizing radiation from solar extreme ultraviolet (EUV) and X-ray emissions alters the electron density, which affects electromagnetic wave propagation. Electron density variations in the ionosphere are primarily influenced by two processes: During the day, solar radiation ionizes neutral atoms, producing free electrons and ions. At night, recombination becomes dominant, where free electrons recombine with ions to form neutral particles, reducing the electron density (Subirana et al., 2013).

As a dispersive medium for GNSS signals, the ionospheric refractive index is frequency-dependent, affecting pseudorange and carrier-phase observations differently. This results in two refractive indices: the group refractive index (n^{gr}) and the phase refractive index (n^{ph}). The corresponding ionospheric delay for pseudorange measurements leads to an increased range value, known as group delay, while the ionospheric phase advance for carrier-phase measurements results in a decreased range value. Besides the frequency of the signal, the refractive indices are also dependent on the electron density in the ionosphere. An approximation of n_{gr} and n_{ph} can be expressed as follows:

$$n^{gr} = 1 + \frac{40.3}{f^2} N_e , \qquad n^{ph} = 1 - \frac{40.3}{f^2} N_e . \tag{2.8}$$

where f represents the signal carrier frequency in Hertz (Hz) and N_e the electron density in units of electrons per cubic meter ($electrons/m^3$) .

By taking Equation (2.7) and substituting of n_{gr} and n_{ph} from (2.8), the ionospheric group and phase refraction can be approximated by:

$$p_{iono}^{gr} = + \frac{40.3}{f^2} \int N_e \, dl , \qquad p_{iono}^{ph} = - \frac{40.3}{f^2} \int N_e \, dl . \tag{2.9}$$

The integral of the electron density along the path of the signal is referred to as the slant Total Electron Content (sTEC), expressed in TEC units (TECU), where one TECU is equivalent to 10^{16} $electrons/m^2$. A good approximation of the ionospheric delay in meters is provided in Equation (2.10), with the sign differing depending on whether it is a group delay (positive) or a phase delay (negative). This effect is typically referred to as the *first-order* ionospheric effect.

$$p_{iono} = \frac{40.3}{f^2} TEC . \tag{2.10}$$

Figure 2.6 (left) illustrates the geographic distribution of the vertical Total Electron Content at 13:30 Universal Time (UT) on 23 February 2024. The equatorial anomalies are clearly visible along the geomagnetic equator. Variations in TEC are influenced by factors such as solar activity, geographic location, local time, season, and magnetic activity (Jakowski et al., 2001).

Solar flux is one of the key metrics used to measure solar activity. It quantifies the amount of radiation received from the Sun and serves as a primary indicator of solar activity levels. One well-established measure of solar activity is the solar radio flux at a wavelength of 10.7 cm, known as the F10.7 index. This index is particularly effective because of its strong correlation with ionizing solar radiation in the EUV band, which directly influences ionospheric conditions, such as TEC variability. The evolution of the F10.7 index since 1990 is shown in Figure 2.6 (right). Solar activity follows an approximately 11-year cycle, which can be observed by the variation in sunspot numbers. During each cycle, the Sun's magnetic field flips, switching its poles, leading to increased solar eruptions, including solar flares and coronal mass ejec-

tions (Hobiger & Jakowski, 2017). This augmented solar activity can affect radio communications and navigation systems, and extreme events have the potential to impact artificial satellites, which are integral to daily human activities, as well as surface infrastructure such as electrical grids. The Sun completed its 24th solar cycle in 2020 and has entered solar cycle 25th (at the writing of this thesis in 2024), with peak sunspot activity expected in 2025[2].

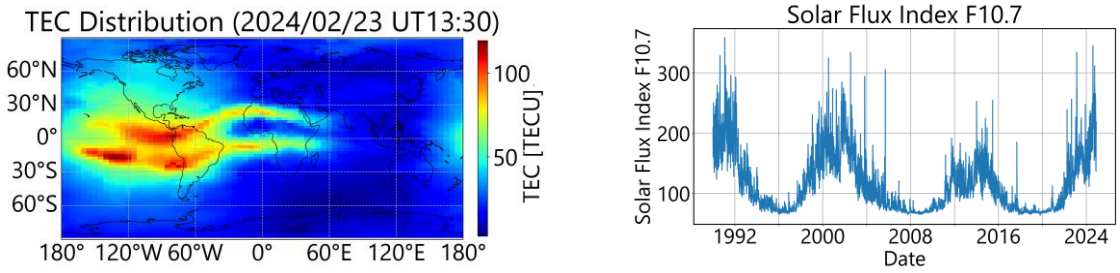

Figure 2.6 Left: Total Electron Content at 13:30 UT on 23 February 2024. Right: Solar flux index evolution based on dataset reported by the GFZ.

An additional contribution from the ionosphere is termed the *second-order* ionospheric effect ($I2$). This effect considers the magnetic field B on a certain height above the Earth within the refractive index. However, it accounts for only 0.1% of the total ionospheric effect, resulting in an impact of less than 1 mm in positioning applications (Hernández-Pajares et al., 2007). The second-order phase and code delays are described as follows:

$$p_{iono2}^{ph} = -\frac{7527c}{2f^3} \int_{Rx}^{Tx} N_e B \cos\theta \, dl \ . \tag{2.11}$$

$$p_{iono2}^{gr} = -2\, p_{iono2}^{ph}. \tag{2.12}$$

where c denotes the velocity of the light in vacuum, Ne represents the electron density along the propagation path of GNSS signal l between the transmitter (Tx) and the receiver (Rx), B is the magnetic field on a certain height above the Earth, and θ represents the angle between l and B.

As described above, the first-order ionospheric effect is inversely proportional to the square of the signal frequency. This property allows dual-frequency receivers to correct this effect by applying a linear combination of code or carrier measurements, known as the ionosphere-free combination. A detailed explanation of this method can be found in (Hofmann-Wellenhof et al., 2008). In contrast, single-frequency receivers depend on ionospheric models to compensate for ionospheric refraction error. These models are broadcast by each GNSS program, with their parameters transmitted within the navigation message (Morton et al., 2020). Table 2.2 presents the ionospheric model used by each GNSS constellation.

[2] National Oceanic and Atmospheric Administration (NOAA): https://www.weather.gov/news/201509-solar-cycle Accessed: 20.11.2023

Table 2.2 Ionospheric models for GNSS constellations.

GNSS	Ionospheric Model
GPS	Klobuchar model (Klobuchar, 1987)
GLONASS	None[3]
Galileo	NeQuick-G (Nava et al., 2008), NTCM-G (Hoque et al., 2018; Jakowski et al., 2011)
BDS	BeiDou Global Ionospheric Delay Correction Model (BDGIM) (Yuan et al., 2019)
QZSS	Klobuchar model with two sets of parameters
IRNSS	Grid-based model (Maheshwari & Nirmala, 2018)

While a summary of each model can be found in (Morton et al., 2020), a brief description of the models employed by the Galileo system is provided below, as these are the models used in the development of this thesis.

NeQuick 2 Model

The NeQuick 2 model (Nava et al., 2008), adapted for Galileo as the NeQuick-G model, was developed at the Aeronomy and Radiopropagation Laboratory of The Abdus Salam International Centre for Theoretical Physics (ICTP), Trieste, Italy, and at the Institute for Geophysics, Astrophysics, and Meteorology (IGAM) of the University of Graz, Austria. NeQuick 2 is a semi-empirical model consisting of vertical profiles formed by multiple Epstein layers to derive electron peak density and height through spatial and temporal interpolation using a set of global maps. The model's input parameters, which depend on solar activity, include the F10.7 index (or sunspot number), month, geographic latitude, longitude, height, and universal time. The output is the electron concentration at the specified location and time. The Total Electron Content along the ground-to-satellite ray path is then calculated through numerical integration.

Neustrelitz Electron Density Model (NEDM2020)

The NEDM2020 model (Hoque et al., 2022) incorporate the Neustrelitz Total Electron Content Model NTCM (Hoque et al., 2019) as integral component for deriving the total electron content. The NTCM has recently been accepted by the European GNSS Service Centre as a new ionospheric correction model for Galileo users, referred to as NTCM-G[4]. The NEDM2020 model was developed at the German Aerospace Center in the Institute for Solar–Terrestrial Physics (DLR-SO), Neustrelitz, Germany. This model is built upon approximately 100 model coefficients and a set of empirically fixed parameters. Similar to NeQuick, the input parameters include solar activity, geographic location, and local time, and the output is the electron density at the specified location and time. A notable advantage of NEDM2020 is its ability to compute electron density directly for any location and time, without requiring specialized

[3] Klobuchar, NeQuick or NTCM model can be used for any GNSS signal after setting the corresponding carrier frequency.

[4] https://www.gsc-europa.eu/news/good-performance-less-computation-a-new-ionospheric-model-for-the-galileo-open-service

temporal or spatial interpolation of parameters, resulting in higher computational efficiency compared to the NeQuick 2 model.

2.2.2 Tropospheric Delay

The troposphere is the lowest layer of the Earth's atmosphere, containing approximately 80% of the total atmospheric mass and 99% of its water vapor and aerosols. It is within the troposphere that most of the weather-related phenomena, such as precipitation, wind, and temperature variations, take place. Generally, the troposphere extends from the Earth's surface up to approximately 20 km above sea level, although this height can vary based on geographic location and season (Teunissen & Montenbruck, 2017)

The troposphere induces additional delays in GNSS signals that depend on parameters such as temperature, pressure, water vapor, and the relative positions of the transmitter and receiver. Based on Equation (2.7) the term 'refractivity', defined as $N = 10^6(n-1)$, is introduced, as the refractivity index n is very close to one, making it convenient to use refractivity to avoid dealing with values that differ only slightly from unity (Hobiger & Jakowski, 2017). Thus, the tropospheric delay can be mathematically represented as:

$$p_{trop} = \int (n-1)\, ds = 10^{-6} \int N\, ds. \tag{2.13}$$

The refractivity can be separated into two components: the *hydrostatic* or *dry* component N_h, which includes dry gases such as nitrogen and oxygen, and the *wet* component N_w, which accounts for water vapor (Hopfield, 1969). This distinction is represented as follows:

$$N = N_h + N_w. \tag{2.14}$$

Since the troposphere is a non-dispersive medium for EM waves up to 15 GHz, the effect on GNSS signals is independent of frequency. Consequently, both the phase and code observations are affected by the same delay. However, this implies that correcting for tropospheric refraction cannot be achieved using dual-frequency measurement combinations (Subirana et al., 2013). Instead, tropospheric effects must be corrected using model-based approaches or estimations derived from observational data.

Approximately 90% of the tropospheric refraction is caused by the dry component, which is more predictable due to its dependence on pressure and temperature. A delay of approximately 2.3 m is expected from this component in the zenith direction at sea-level conditions, representing the dry portion of the *Zenith Total Delay* (ZTD), commonly referred to as the *Zenith Hydrostatic Delay* (ZHD). The remaining 10% of the delay is caused by the wet component, known as the *Zenith Wet Delay* (ZWD), which is highly variable and depends on water vapor content. Although the delay from the wet component is relatively small, typically at the centimeter level, it exhibits rapid variations, making it more challenging to accurately model (Hofmann-Wellenhof et al., 2008).

Various nominal models have been proposed in the literature for correcting tropospheric effects in GNSS. Examples include the models developed by Hopfield, (1969) and Saastamoinen, (1973). These models establish separate approaches for estimating dry and wet tropospheric delays, each incorporating different assumptions based on vertical atmospheric profiles. Since the tropospheric delay also depends on the relative positions of the transmitter and receiver, the line-of-sight (LOS) must be considered. This requires the application of a mapping function, which projects the delays from the zenith direction to arbitrary zenith angles (90°- elevation angle E) along the transmitter-receiver path.

Introducing the mapping function, the tropospheric Slant Total Delay can be written as:

$$STD\ (E) = ZHD\ m_h(E) + ZWD\ m_w(E). \tag{2.15}$$

where $m_h(E)$ and $m_w(E)$ are the mapping functions for the dry and wet part respectively, as a function of the elevation E at the observation site.

According to Saastamoinen (1973), and revised by Davis et al. (1985), the ZHD can be determined using pressure measurements at the observation site by the following equation :

$$ZHD = \frac{0.0022768\ p}{1 - 0.00266\cos 2\varphi - 0.28 * 10^{-6} h_{ell}}. \tag{2.16}$$

where p represents the pressure and, φ and h_{ell} denote the latitude and the ellipsoidal height, respectively. Although the derivation of the ZWD results is more difficult, an approximation can be given by (Askne & Nordius, 1987):

$$ZWD = 10^{-6}\left(k_2' + \frac{k_3}{T_m}\right)\frac{R_d\ e}{g_m - (\lambda + 1)}. \tag{2.17}$$

where the required parameters are: water vapor pressure e, mean temperature weighted with water vapor pressure T_m and water vapor decrease factor λ. k_2' and k_3 denote refractivity constants empirically determined, R_d represents the specific gas constant for dry constituents and g_m is the mean gravity value. Additionally, ray-tracing techniques using numerical weather models (NWM) are capable of computing precise values for the total tropospheric delay (Hofmeister & Böhm, 2017).

Regarding the mapping functions $m(E)$ modern approaches, such as the Vienna Mapping Function 3 (VMF3) proposed by Landskron & Böhm (2018) rely on the model initially introduced in (Marini, 1972). The formulation of the mapping function as a function of the elevation angle is presented in Equation (2.18). The VMF3 is constructed using the coefficients a, b, and c which depend on integrals of refractivity along the atmosphere derived from models and ray-tracing data:

$$m(E) = \frac{1 + \dfrac{a}{1 + \dfrac{b}{1 + c}}}{\sin E + \dfrac{a}{\sin E + \dfrac{b}{\sin E + c}}}. \tag{2.18}$$

2.3 GNSS Reflectometry

2.3.1 Overview of GNSS Reflectometry

GNSS Reflectometry is based on the bistatic (multistatic) concept (Hall & Cordey, 1988), where the transmitter(s) and receiver(s) are separated by a distance comparable to the distance to the target. In 1993, Martín-Neira proposed using reflected GPS signals for ocean altimetry. This technique, called Passive Reflectometry and Interferometry System (PARIS), involves utilizing the delay between the direct and reflected signal to determine ocean surface height. This concept was experimentally tested by NASA in 1997 (Garrison & Katzberg, 1997) and by ESA in 2001 (Martín-Neira et al., 2001). Since then, GNSS-R has been continuously developed and has provided valuable data for numerous applications. A detailed description of the theory, applications using different receiver platforms, and prospects for GNSS-R can be found in Garrison et al. (2020), Yu (2021) or Jin et al. (2024).

GNSS-R is a versatile and cost-effective implementation technique that can be deployed across various platforms. Airborne-based reflectometry has played a significant role in advancing the technique. The first detection of GPS ocean-reflected signals during an airborne experiment was reported (Auber et al., 1994). Subsequently, multiple studies were conducted to establish the theoretical framework for specular and diffuse reflection of radio frequency radiation from rough surfaces (Garrison & Katzberg, 1997). These efforts included numerous airborne GNSS-R campaigns aimed at validating theoretical models by comparing experimental data with theoretical predictions and deriving surface geophysical characteristics such as sea surface roughness (Garrison et al., 1998), wind speed (Komjathy et al., 2000), wave height, salinity, and properties of inland waters (Komjathy et al., 2001). During that period, these studies also highlighted the potential use of GNSS-R for atmospheric monitoring, specifically for monitoring ionospheric TEC over ocean regions. Katzberg & Garrison (1996) proposed integrating a GPS receiver into satellite altimeters to estimate ionospheric delay, assessing the feasibility of using reflected signals for this purpose and the impact of surface roughness.

A schematic representation of the GNSS-R concept using a Low Earth Orbit (LEO) satellite as a receiver platform is presented in Figure 2.7. This figure illustrates the main components of GNSS-R, which are also utilized in this thesis. It denotes the direct signal path from the GNSS satellite transmitter (Tx) to the receiver (Rx). The incident signal path, from the GNSS satellite to the specular point (SP), is also depicted. The SP is the point where the specular reflection condition is met, where the elevation angle (E) of the incident ray equals the angle of the reflected ray that corresponds to the path from the SP to the receiver. This reflected signal is a composite, originating from numerous scatterers located at and near the specular point. The contribution area over which the signal reflects towards the receiver is referred to as the glistening zone.

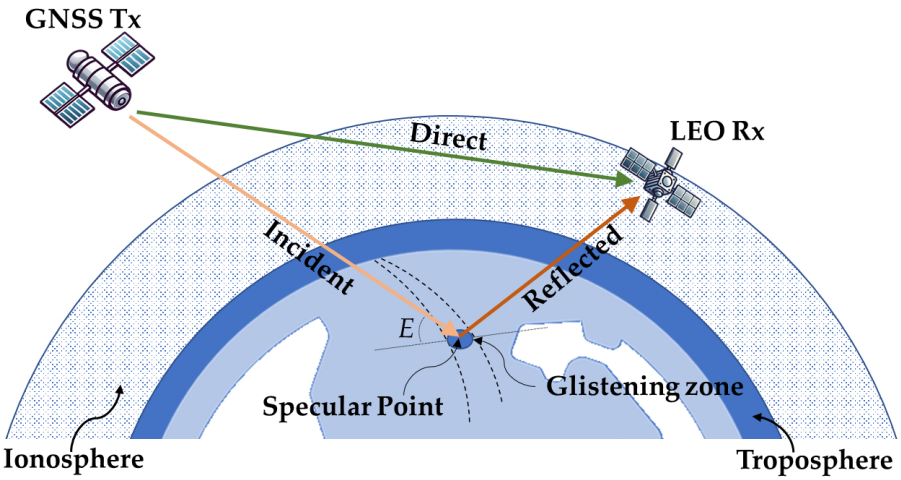

Figure 2.7 Representation of the LEO GNSS-R concept, illustrating its main components. In this context, the relative or interferometric delay is defined as the sum of the incident and reflected paths minus the direct signal path.

The excess path the reflected signal travels with respect to the direct signal, is referred to as the *relative* or *interferometric* path delay. It is defined as $\Delta p = p_r - p_d$, where p_r represents the combined path length of the incident and reflected rays, while p_d corresponds to the direct path length. This relative delay is influenced by various sources of delay affecting GNSS signals. Consequently, the extended form of Δp can be expressed as:

$$\Delta p = \Delta p_{geo} + \Delta p_{trop} + \Delta p_{iono} + \Delta p_{surf} + \Delta p_{instr} + n. \qquad (2.19)$$

where, Δp_{geo} is the relative geometrical delay, representing the purely geometric contribution to the path difference. Δp_{trop} and Δp_{iono} are the relative tropospheric and ionospheric delay, respectively. Surface height variations and roughness bias is introduced by the term Δp_{surf}. The instrumental delay is represented by Δp_{instr}, while unmodeled errors or noise are included in n.

Based on signal acquisition and processing techniques, GNSS-R can be categorized into two types: Conventional GNSS-R (cGNSS-R) and Interferometric GNSS-R (iGNSS-R). In the cGNSS-R approach, the reflected signal is correlated with a locally generated replica of the PRN code at the receiver, after compensating for time delays and Doppler frequency shifts. In contrast, iGNSS-R performs a correlation between the reflected signal and the direct signal received. Since direct signals contain more noise compared to idealized local clean replicas, this approach inherently increases noise levels unless highly directive antennas are used to precisely track both the reflection points and the transmitted signals (Cardellach et al., 2018).

In 2001, the first spaceborne GNSS-R mission was launched as part of the UK Disaster Monitoring Constellation (UK-DMC) program (see Table 2.3). This mission provided the capability to retrieve sea surface roughness and physical properties of the reflecting surface. Building on the success of this mission, the first dedicated GNSS-R Technology Demonstration Satel-

lite-1 (TDS-1) was launched in 2014. TDS-1 provided Delay Doppler Map (DDM) data products, setting a benchmark for the practical application of spaceborne GNSS reflectometry. Since then, numerous scientific, governmental, and commercial institutions have contributed to the design, development, and launch of various spaceborne GNSS-R missions. Among them, the GEROS-ISS project, proposed by Wickert et al. (2016) introduced an innovative remote sensing experiment aimed at performing radio occultation, reflectometry, and scatterometry observations onboard the International Space Station (ISS). GEROS-ISS served as a baseline mission concept, providing a detailed framework for future GNSS-R mission developments.

More recent advancements in spaceborne GNSS-R include the development of microsatellite constellations like the Cyclone Global Navigation Satellite System (CYGNSS) mission, operated by NASA in collaboration with the University of Michigan, as well as CubeSats such as the ESA PRETTY mission and the commercial constellation LEMUR by Spire Global Inc. Additionally, the experimental Nano-Satellte, 3CAT-2, developed by the Universitat Politècnica de Catalunya (UPC), has contributed to GNSS-R advancements. Table 2.3 provides an overview of these missions, including launching date, processing type, frequency band(s), and polarization as well as the GNSS constellation utilized.

Table 2.3 Overview of spaceborne GNSS-R missions.

Mission	Launch	Type	Band/Pol	GNSS
UK-DMC (Gleason et al., 2005)	2003	cGNSS-R	L1 / LHCP	GPS
UK-TDS-1 (Unwin et al., 2016)	2015	cGNSS-R	L1 / LHCP	GPS
CYGNSS (C. S. Ruf et al., 2016)	2016	cGNSS-R	L1 / LHCP	GPS
3Cat-2 (Carreno-Luengo et al., 2016)	2016	cGNSS-R, rGNSS-R, iGNSS-R	L1, L2 / LHCP, RHCP	GPS, GLONASS, Galileo, BDS
SMAP GNSS-R (Carreno-Luengo et al., 2017)	2017	cGNSS-R	L2 / H, V	GPS
BuFeng-1 A/B (Jing et al., 2019)	2019	cGNSS-R	L1 / LHCP	GPS, BDS
Spire series (Masters, 2019)	2019	cGNSS-R	L1 / LHCP	GPS, Galileo
Fengyun-3 series (Sun et al., 2023)	2021	cGNSS-R	L1 / LHCP	GPS, Galileo, BDS
3Cat-5 A/B (Camps et al., 2022)	2020	cGNSS-R	L1 / LHCP	GPS, Galileo
3Cat-4 (Munoz-Martin et al., 2018)	2021	cGNSS-R	L1, L2 / LHCP	GPS, Galileo
PRETTY (Dielacher et al., 2022)	2023	iGNSS-R, cGNSS-R	L5 / RHCP	GPS, Galileo
TRITON (Juang et al., 2016)	2023	cGNSS-R	L1 / LHCP	GPS
HydroGNSS (Unwin et al., 2021)	2025	cGNSS-R	L1 / LHCP + RHCP, L5 / LHCP + RHCP	GPS, Galileo

2.3.2 Specular Point Positioning

In GNSS Reflectometry, the determination of the specular point position relies on the following criteria: (i) the SP lies on the Earth's surface, (ii) the total propagation path, comprising the incident ray from the transmitter to the SP and the reflected ray from the SP to the receiver, is minimal among all possible paths, and (iii) the reflection law is satisfied, meaning the incidence angle at the SP equals the reflection angle (Juang, 2023).

For the computation of the SP position, the Earth's curvature must be considered. Early approaches assumed a spherical Earth model, where the SP location was computed by solving a quadratic polynomial equation, as proposed by Martín-Neira, (1993). However, since the Earth is more accurately represented as an ellipsoid, iterative methods are often employed to refine the SP solution. These methods leverage a spherical approximation to improve accuracy in an ellipsoidal Earth model, as described by Gleason, (2006) and Ruf et al. (2022).

During this research, the method used for computing the specular point (SP) position follows the approach described by Semmling et al. (2016). In this method, the WGS-84 (World Geodetic System 1984) ellipsoidal model serves as the reference surface, providing an Earth-centered, Earth-fixed (ECEF) coordinate system. Figure 2.8 illustrates the representation of the SP position using a spherical approximation, where the Earth's curvature is approximated by an osculating sphere near a reference specular point.

From this sphere, a 3D curvature centered system (3D-CCS) is defined with its origin at C. Positions in the ECEF frame (e.g., transmitter Tx and receiver Rx) can be transformed to the 3D-CCS through coordinate translation, and vice versa. The solution for the SP position is then expressed in the local reference system, defined by the base vectors $\hat{U}$ and $\hat{V}$ which are aligned with the reflection plane. Using trigonometric relationships, the triangles △Tx,C,SP and △Rx,C,SP are employed to establish an equation system that satisfies the specular point criteria. An iterative numerical method is then applied to refine the SP position until convergence.

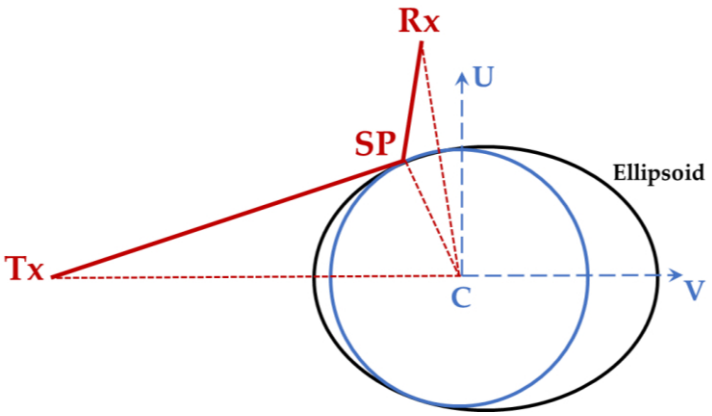

Figure 2.8 Representation of spherical surface approximation for SP positioning (not to scale).

Once the SP is defined, a *geoid undulation correction* is applied using the EIGEN-6C2 model (Foerste et al., 2013). The computed SP location enables the estimation of the excess path (delay) of the reflected signal relative to the direct signal, which is subsequently used in signal processing.

2.3.3 GNSS-R Observables

The primary observable in reflectometry is the Delay Doppler Map (DDM). When the Doppler frequency is either predetermined, modeled, or a central Doppler slice of the DDM is extracted, the cross-correlation is performed in the delay domain, resulting in the Delay Map (DM), also referred to as a "waveform" (Cardellach et al., 2018).

The next sections describe the derivation of the DDM in the GNSS-R process, following the interaction of the signal with the reflecting surface detailing, as well as the generation and characteristics of the DM.

Delay Doppler Map (DDM)

In the reflection process, the glistening zone contains numerous scatterers that contribute to the reflected signal received by the antenna. Given the coordinates of the transmitter (x_{Tx}, y_{Tx}, z_{Tx}), the receiver (x_{Rx}, y_{Rx}, z_{Rx}), and the position of the scatterer (x_s, y_s, z_s), the distance between the transmitter, the scatterer and the receiver is expressed as follows:

$$d_s(x_s, y_s, z_s) = \sqrt{(x_s - x_{Tx})^2 + (y_s - y_{Tx})^2 + (z_s - z_{Tx})^2} + \sqrt{(x_{Rx} - x_s)^2 + (y_{Rx} - y_s)^2 + (z_{Rx} - z_s)^2}. \quad (2.20)$$

The specular point (SP) is considered the scatterer where d_s is minimal. Signals arriving from other scatterers will have a delay compared to the arrival time of the signal from the SP. This delay is given by:

$$\delta\tau = d_s(x_s, y_s, z_s)/c + \tau_{SP}. \quad (2.21)$$

where $\tau_{SP} = d_s(x_{SP}, y_{SP}, z_{SP})/c$ and c is the speed of light. Given the transmitter and receiver positions, and the differential delay $\delta\tau$ the scatterers form an elliptical pattern, known as iso-delay lines, with the SP lying along the major axis of this ellipse. Consequently, for each specific delay, the signals reflected off points along this ellipse will reach the receiver simultaneously (Yu, 2021).

The Doppler frequency shift (f_d) due to the relative motion between the transmitter and receiver can be calculated using the following formula:

$$f_d = \frac{f}{c}\left((\vec{V}_{Rx} - \vec{V}_{Tx}) \cdot \hat{r}\right). \quad (2.22)$$

where f is the transmitted carrier frequency, $\vec{V}_{Rx}$ and $\vec{V}_{Tx}$ represent the velocity vector of the transmitter and the receiver, respectively. The unit vector pointing from the transmitter to the receiver is $\hat{r}$. A specific Doppler frequency in this equation corresponds to a hyperbolic path, called iso-Doppler lines, meaning that signals reflected from points along this hyperbola will exhibit the same Doppler frequency. The representation of the iso-Delay and Doppler lines are shown in Figure 2.9.

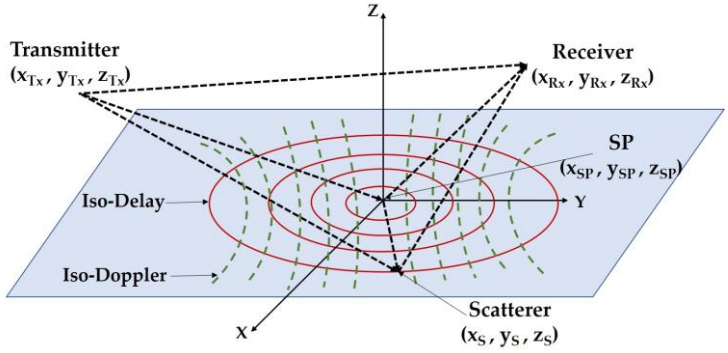

Figure 2.9 Representation of the scattering geometry, illustrating the Iso-Delay and Iso-Doppler lines, which indicate areas of equal signal delay and Doppler frequency shift.

The two-dimensional representation of the correlation power distribution as a function of time delay and Doppler frequency is the Delay Doppler Map (DDM), which is considered the fundamental observable in GNSS-R. The DDM combines the effects of signal propagation delay and the relative velocity between the satellite and the reflecting surface. This representation provides valuable insights into both the height of the reflecting surface and its roughness characteristics, offering a comprehensive analysis of the scattering properties and dynamics of the observed region.

A simulated spaceborne DDM (right) without noise and its corresponding representation in the specular point plane, illustrating the Iso-Delay and Iso-Doppler lines (left), is shown in Figure 2.10.

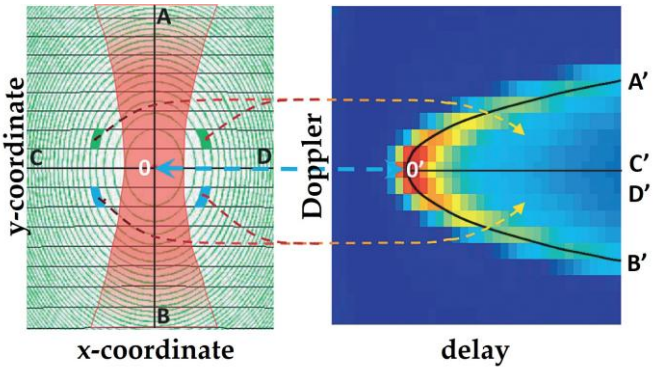

Figure 2.10 Left: Iso- Delay and Doppler lines at the specular point plane. Right: Corresponding Delay Doppler Map illustrating the equivalent cells derived from the SP plane positions (Zavorotny & Voronovich, 2000).

Delay Map (DM)

Considering a fixed frequency, including the Doppler shift at the specular point, (or integration over a range of frequencies), the delay is scanned in small increments within the expected range for the reflected signal (e.g., ±several chips around an initial geometric guess) (Garrison et al., 2020). For each incremental delay, the correlation power is computed. Plotting this power as a function of delay results in a one-dimensional correlation function**,** known as the Delay Map**.** The DM provides insights into the time delays of reflected signals relative to direct signals after interacting with the reflecting surface. Figure 2.11 (left) illustrates a code DM from the PRETTY mission on 11 March 2024, obtained from GPS PRN 11. This DM highlights how the reflected signals arrive at varying delays relative to the direct signals with the highest power response corresponding to a relative delay of approximately 60 meters. The resulting delay waveform after the correlation process can be visualized by slicing the DM at a specific epoch, as indicated by line A-A′. This waveform, depicted in Figure 2.11 (right), represents the correlation power, with the peak indicating the maximum response after the complex cross-correlation process.

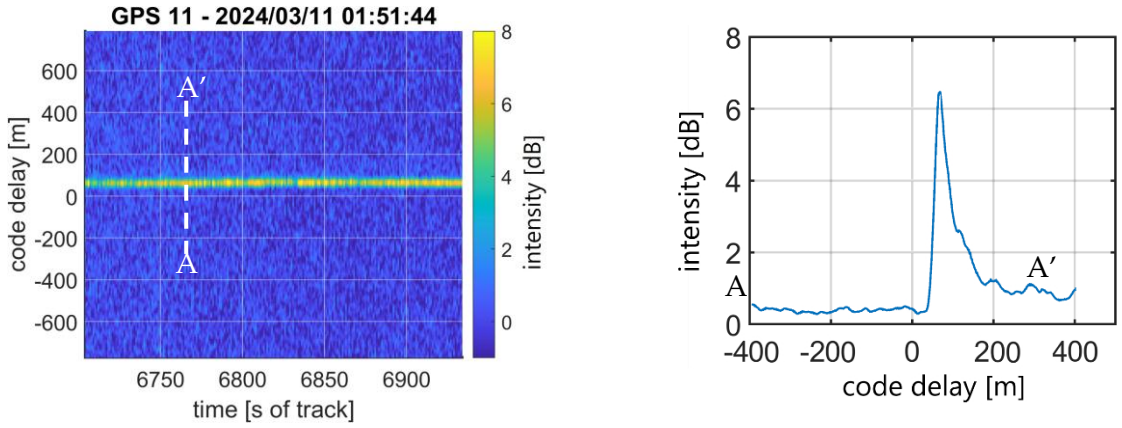

Figure 2.11 Left: Delay Map (DM) from the PRETTY mission on 11 March 2024 GPS PRN 11. Right: Corresponding delay waveform from line A-A′, where the peak intensity denotes the maximum correlation.

I/Q Components

The in-phase (I) and quadrature (Q) components of the reflected signal can be obtained as outputs after the correlation process. These components represent the amplitude and phase difference of the reflected signal relative to either the direct signal in iGNSS-R or the locally generated replica in the correlator in cGNSS-R**.**

The I and Q components form a complex signal, where I represents the real part and Q the imaginary part. From these components, the amplitude A, which determines the strength of of the received signal, can be computed as:

$$A = \sqrt{I^2 + Q^2}. \tag{2.23}$$

And the phase ϕ is given by:

$$\phi = atan2\,(Q, I). \tag{2.24}$$

The I/Q outputs are particularly valuable for applications requiring high sensitivity to phase variations and coherence, such as precise geophysical retrievals, where small phase shifts provide critical information about the reflecting surface and atmospheric conditions. Figure 2.12 present the representation of I/Q in cartesian coordinates, showing the amplitude and phase (left), along with the I/Q distribution over time of a reflected signal from an airborne coherent reflection event over calm sea waters in Calais, France (right).

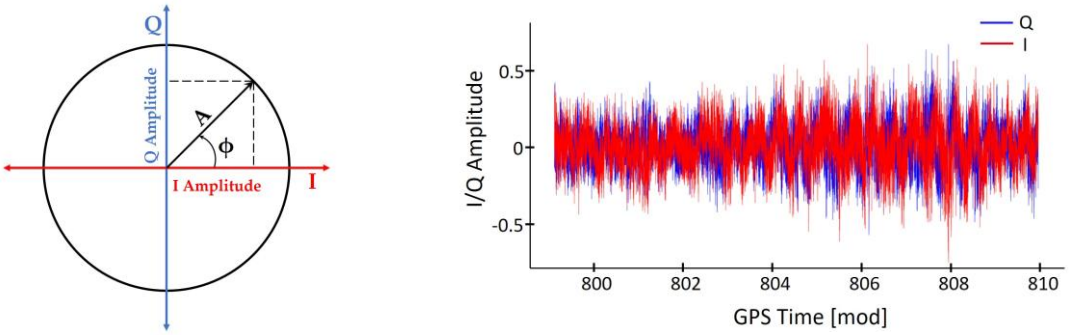

Figure 2.12 Left: I/Q components representation in cartesian coordinates. Right: I/Q distribution of the reflected signal from airborne coherent event over calm sea waters in July 2019.

2.3.4 Reflectometry and Atmospheric Retrievals

As previously described, delayed GNSS signals traveling through the atmosphere enable the derivation of critical atmospheric parameters, such as water vapor content in the troposphere or the Total Electron Content (TEC) in the ionosphere. Ground-based antennas, along with GNSS-RO satellite missions and airborne campaigns, are well-established techniques that utilize direct signals to retrieve these parameters. These methods have consistently provided observations suitable for short-term weather forecasting and have generated long-term time series essential for climate research and monitoring (Elgered & Wickert, 2017).

GNSS-R for atmospheric monitoring is an emerging application that extends the utility of GNSS signals beyond conventional "direct-signal" techniques. Recent advancements in GNSS-R technology, including dedicated missions and CubeSat constellations, have created new opportunities to investigate atmospheric processes with enhanced spatial and temporal resolution as described in the following sections. This progress contributes significantly to applications like meteorology, climatology, and space weather research.

One recent successful examples of GNSS-R reflectometry in atmospheric studies for meteorology applications is the CYGNSS Level 2 (L2) wind speed retrievals, which provide the average wind speed (m/s) and mean square slope (MSS) with a spatial resolution of 25x25 kilometers, derived from Delay Doppler Maps (*CYGNSS Level 2 Science Data Record Version 3.0*).

Wind speed, a fundamental atmospheric parameter driven by air movement between high and low-pressure systems and influenced by temperature gradients, is critical for understanding weather patterns and ocean dynamics. Recently, the Spire Global Data Assimilation team successfully integrated the CYGNSS wind speed product into NOAA's numerical weather model through the operational Gridpoint Statistical Interpolation (GSI) system[5]. This integration enhances weather forecasting accuracy and provides valuable data for meteorological and oceanographic applications, highlighting the potential of GNSS-R to complement and extend traditional atmospheric monitoring techniques.

GNSS-R and the Ionosphere

As in GNSS positioning applications, ionospheric delay is a significant source of error that affects the accuracy of GNSS-R retrievals, particularly in altimetry applications. To ensure high-quality height measurements, it is essential to accurately correct all biases introduced by atmospheric effects.

Ionospheric studies in GNSS-R cover two main objectives. The first focuses on correcting ionospheric delays to improve height retrieval accuracy, particularly in spaceborne platforms. The second aims to analyze ionospheric phenomena, such as plasma depletions, which introduce irregularities that can cause signal scintillation.

In both cases, the incident and reflected rays traversing the ionosphere provide valuable information about ionospheric conditions below the LEO satellite. Simultaneously, direct signals offer insights into ionospheric properties above the platform, as well as through the F-layer when propagating at very low elevation angles. These studies also involve a comprehensive analysis of the spaceborne GNSS-R geometry, as well as the theoretical and empirical frameworks needed to estimate Total Electron Content (TEC). TEC serves as a fundamental parameter for quantifying ionospheric delays and Doppler shifts, forming the basis for advanced ionospheric modeling and correction techniques.

- *Ionospheric Delay Characterization*

A comprehensive error budget analysis for GNSS-R surface height retrievals was conducted by Mashburn et al. (2018). This study analyzed a dataset of approximately 100,000 DDMs, covering global ocean surfaces within ±60° latitude, using TDS-1 satellite data at elevation angles around 60°.

The ionospheric delay was modeled using the International Reference Ionosphere 2012 (IRI-2012) model (Bilitza, 2015) to compute the vertical total electron content (vTEC) at ionospheric pierce points associated with the direct, incident, and reflected paths. The vTEC values were then mapped to slant total electron content (sTEC) using an appropriate mapping function. The results indicate that at elevation angles of 60°, ionospheric delays could reach approximately 15 m during daytime and 7 m at night under moderate solar activity.

[5]https://spire.com/blog/weather-climate/spires-data-assimilation-breakthrough-enhances-weather-forecast-accuracy-with-gnss-r/ Accessed: 08.12.2024

Similarly, the tropospheric delay modeled with the UNB3m model (Leandro et al., 2006), contributes significantly to the error budget, with delays in the order of 6 m at high elevation angles (60°). These findings highlight the critical need for accurate corrections of both ionospheric and tropospheric delays to improve the precision of GNSS-R altimetry.

Before the CYGNSS launch in 2016, Xing et al. (2015) developed a theoretical model to characterize ionospheric and tropospheric delays on DDM observables. The model accounts for geometric excess path delay, atmospheric refraction effects (neglecting signal bending), and noise from unmodeled biases. A global simulation was conducted to compute typical relative ionospheric delays across various scenarios, including variations in elevation angles, latitude, and local time.

The model introduces a "virtual ionospheric point," defined as the intersection of the incident ray with an extension of the receiver's position (similar to Figure 2.14). From this point, the relative ionospheric delay consists of contributions below the receiver-to-ionospheric point altitude and additional variations due to the horizontal offset of the ray path in this segment. Using the empirical International Reference Ionosphere model IRI-2007 (Bilitza & Reinisch, 2008) under moderate solar activity, the study conclude that ionospheric delays can reach up to 30 m at elevation angles of 30°.

- *Ionospheric Scintillation and Plasma Depletions*

Camps et al. (2016) conducted a study to assess the ionospheric impact on GNSS-R observations, focusing specifically on scintillation effects using TDS-1 data and determining the degradation of the SNR. Ionospheric scintillations are rapid temporal variations in the amplitude and phase of trans-ionospheric GNSS signals, caused by scattering due to ionospheric irregularities along the signal propagation path. These effects are most pronounced near the geomagnetic equator (within ±20°) and at auroral latitudes near the poles, with variability occurring day-to-day (Inside GNSS, 2014).

In that study, total electron content (TEC) and the scintillation index S_4 were computed along signal paths using the Global Ionospheric Scintillation Model (GISM) (Béniguel, 2002). A numerical model was developed to quantify the impact of S_4 on the SNR observable. Results indicated that scintillation primarily occurs along the incident signal path in regions below the LEO orbit height (~500 km). The study further highlighted that scintillation effects, which are associated with phase coherence, are more pronounced under calm water or smooth reflecting surface conditions. Additionally, higher standard deviations in SNR were observed in regions around ±20° from the geomagnetic equator, consistent with areas experiencing intense scintillation and characterized by smooth surface conditions. These findings were further investigated by Camps et al. (2018). The results show that fluctuations in the peak of the DDM are associated with ionospheric scintillation events. These fluctuations are also suspected to correlate with tropical storms and surface roughness, suggesting a potential coupling between atmospheric and surface conditions that influence GNSS-R observations.

Regarding the retrieval of ionospheric irregularities and parameters, one of the first studies was presented by Molina & Camps, (2020) who analyzed ionospheric plasma depletions using spaceborne GNSS-R data. The study focused on observing Equatorial Plasma Bubbles (EPBs) by leveraging data from the CYGNSS mission to monitor ionospheric activity. The signal intensity I is utilized as the primary measurement to compute the scintillation index S_4 index as follows:

$$S_4 = \sqrt{\frac{\langle I^2 \rangle - \langle I \rangle^2}{\langle I \rangle^2}}. \tag{2.25}$$

Here, the operator $\langle . \rangle$ represents the moving average, calculated using a 12-sample window along the track. As previously mentioned, scintillation events were identified in regions with smooth surfaces or calm water, conditions conducive to detecting ionospheric irregularities. Based on the results S_4 values between 0.2 and 0.5 were indicative of plasma bubbles, which were observed to extend over spatial scales of 25 km to 150 km and persist for durations of 5 to 30 seconds. The results were cross validated with geomagnetic and plasma density products from the SWARM satellite mission, showing consistent findings. These results showed the potential of GNSS-R for ionospheric studies, particularly in detecting and characterizing plasma depletions and irregularities.

- *Ionospheric Effects Correction and TEC estimation*

In recent approaches aimed at correcting ionospheric effects, Buendía et al. (2023) introduced an improved correction model utilizing dual-frequency carrier phase data from Spire Global Inc. GNSS-R observations at grazing elevation angles (5°-30°). This method was applied to remove the ionospheric delay and retrieve the relative surface height with enhanced accuracy. The study employed two methods, the first is the ionosphere-free combination. As ionospheric refraction is inversely proportional to the square of the signal frequency, the ionospheric effect can be effectively eliminated using a linear combination of code or carrier measurements in dual-frequency receivers (Jakowski, 2017). The first-order ionospheric delay is removed, and the ionosphere-free combination can be modeled as:

$$\Delta\phi_{iono-free}^{RD} = \frac{f_1^2\, \Delta\phi_1^{RD} - f_2^2\, \Delta\phi_2^{RD}}{f_1^2 - f_2^2}. \tag{2.26}$$

where f_1 and f_2 represent the center frequencies of the L1 and L2 bands, respectively, and $\Delta\Phi_{1,2}^{RD}$ are the total phase differences between the reflected (R) and direct (D) signals at L1 and L2.

The second method employed in the study is the frequency-specific ionospheric delay correction. This approach refines the dual-frequency correction by applying a smoothing technique using a local robust quadratic regression filter. The filter outputs a moving mean term over a fixed window, effectively reducing noise and ensuring a stable correction term. The correction model can be expressed as:

$$\Delta\phi^{RD}_{corr_{1,2}} = \Delta\phi^{RD}_{1,2} + \frac{f^2_{2,1}(\Delta\phi^{RD}_1 - \Delta\phi^{RD}_2)}{f_1^2 - f_2^2}. \quad (2.27)$$

The mean value of the corrected total phase differences for L1 and L2 is subsequently used to retrieve the relative surface height. This method demonstrated superior performance compared to the ionosphere-free combination approach, achieving a reduction in RMSE from 24.4 cm to 16.8 cm, a difference of 7.6 cm, when compared against the reference surface model (WGS84). Although both methods showed significant improvement in ionospheric delay correction, the frequency-specific approach offered a more precise retrieval of surface heights, underscoring its efficacy in mitigating ionospheric effects.

For TEC estimation, ionosonde measurements, incoherent scatter radars, and GNSS-based methods, such as dual-frequency ground-based GNSS stations, tomographic inversion techniques, and GNSS-RO, are well-established approaches (Jakowski, 2017). In the context of GNSS-R, ongoing investigations aim to refine its capability for providing reliable TEC information . Wang & Morton (2022) introduced a sophisticated methodology leveraging coherent dual-frequency GNSS-R data to estimate slant TEC using pseudorange and carrier phase observations from CubeSats constellation LEMUR-2 operated by Spire Global Inc. Their study focused on grazing elevation observations and demonstrated the potential of GNSS-R for sTEC estimation, particularly over polar regions, highlighting its applicability for monitoring ionospheric conditions in remote and challenging environments.

This approach involved TEC retrieval by considering the contributions of the incident ($sTEC_1$) and reflected rays ($sTEC_2$). Additionally, the direct ray was utilized to estimate the TEC above the receiver ($sTEC_D$) and to determine the receiver's differential code bias (DCB), which is crucial for accurate TEC measurements, particularly when addressing ionospheric corrections using dual-frequency observations. Figure 2.13 illustrates the schematic representation of the proposed TEC retrieval model contribution from each ray. The ionospheric piercing point (IPP), typically assumed to be at an altitude between 250 and 450 km, represents the location where the ionosphere's electron density is expected to have the most significant contribution.

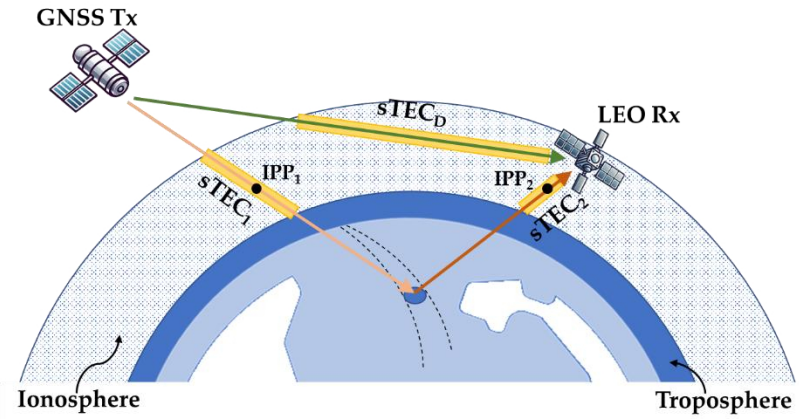

Figure 2.13 Schematic representation of sTEC contributions from the incident, reflected, and direct signals. Based on Y. Wang & Morton, (2022)

The processing workflow includes detailed steps for retrieving the SNR, pseudorange, and excess carrier phase by utilizing the in-phase (I) and quadrature (Q) channel correlator outputs generated by the Spire satellites. This is followed by carrier phase unwrapping, cycle slip correction, and noise filtering, which is performed using a technique called SCANF (Simultaneous Cycle Slip And Noise Filter) as detailed in Wang et al. (2021). The combined ionospheric delay term, $sTEC_R$, representing the contributions from both the incident ($sTEC_1$) and reflected rays ($sTEC_2$), from linear combination of f_1 and f_2 can then be modeled as:

$$sTEC_R = \frac{f_2^2 \cdot f_1^2}{40.3(f_2^2 - f_1^2)}\left(\phi_{R,2} - \phi_{R,1} + Z_R - DCB_{Rx} - DCB_{Tx}\right). \qquad (2.28)$$

where $DCB_{Rx,Tx}$ represents the difference in the receiver hardware bias for frequencies f_1 and f_2 accounting for instrumental delays at both the receiver and transmitter. Additionally, Z_R denotes the carrier phase bias introduced during processing, which includes unwrapping, cycle-slip correction, and noise filtering. The GNSS-R-based TEC retrieval demonstrated consistency in trends when compared to the Global Ionospheric Maps (GIM), while providing higher spatial and temporal resolution, revealing finer details of TEC variations related to ionospheric irregularities.

GIM products are global representations of vertical TEC generated by the International GNSS Service (IGS). These maps, available in final, rapid, real-time, and predicted versions, are based on a combination of ionospheric data from various processing centers[6]. To compare these products with GNSS-R-based sTEC, a mapping function is applied to convert vertical TEC at the ionospheric piercing point (IPP) into slant TEC.

A validation of the GNSS-R retrievals was also performed by comparing ocean surface height estimates against the DTU18 Mean Sea Surface (MSS) model (Andersen et al., 2018) supplemented by ocean tide models (Egbert & Erofeeva, 2002). The results showed that GNSS-R retrievals exhibited better agreement with the MSS model, demonstrating that accurate ionospheric corrections significantly improve height retrievals, achieving centimeter-level precision. However, challenges persist, particularly due to inconsistent differential code bias (DCB) estimations caused by antenna gain pattern variations and satellite hardware characteristics, which remain an area for further investigation.

Another approach for TEC estimation was proposed by Ren et al. (2022). This method is based on the well-established observation-vs-modeled framework, commonly applied in various disciplines. The approach utilized the DDM data from the TDS-1 mission and the corresponding waveform extracted at the central Doppler slice, focusing on elevation angles greater than 70°. The observed waveform inherently includes all delay biases, such as atmospheric effects from the ionosphere and troposphere, surface roughness contributions, and instrumental effects.

The atmospheric delay component, accounting for both ionospheric and tropospheric contributions is included within the DDM. This delay is estimated by fitting a modeled DDM based

[6] https://igs.org/wg/ionosphere/ Accessed: 10.12.2024

on the Z-V model to observed waveforms using an iterative least-squares approach. To isolate the ionospheric delay, the tropospheric contribution is corrected using the GPT2w model (Böhm et al., 2015). The resulting TEC estimates (20-second resolution) are then compared with GIM (CODE), empirical models such as NeQuick and IRI**,** and ground-based GNSS-derived TEC values. The results demonstrated a notable improvement in mean absolute deviation (MAD) when comparing GNSS-R TEC retrievals with ground-based TEC observations. During periods of low solar activity, the MAD for NeQuick was 11.8 TECU, compared to 13.5 TECU for GIM, 15.1 TECU for IRI. Under high solar activity, GNSS-R showed further improvement, with MADs of 9.2 TECU compared to 12.3 TECU for GIM and 12.7 TECU for IRI. However, significant deviations were observed in coastal regions, attributed to poor-quality GNSS-R products in these areas. This highlights the need for continued research and refinement of GNSS-R-based TEC retrieval methods.

GNSS-R and the Troposphere

The tropospheric delay is also a major source of error in GNSS-R retrievals, particularly in low-elevation angle applications such as grazing angle altimetry. Early investigations aimed to assess the error factors that could impact surface height retrievals, with tropospheric effects being a key focus. Treuhaft et al. (2001) conducted the first ground-based altimetric demonstration using GPS-reflected signals from the surface of a Crater Lake, focusing on identifying and quantifying fundamental experimental errors. Their analysis of the time series revealed that tropospheric effects, along with noise from temperature fluctuations, were the major contributors to the altimetric error budget.

- *Tropospheric delay modelling and characterization*

Several GNSS-R ground-based experiments did not account for the tropospheric delay, as the antenna's height relative to the reflecting surface was relatively small (<10 m), and no significant tropospheric effects were detected in the data (Williams & Nievinski, 2017). However, in higher-altitude experimental configurations, tropospheric effects emerged as a critical issue, becoming one of the largest biases in height retrievals. Consequently, various approaches have been developed to mitigate the impact of tropospheric refraction.

For instance, Treuhaft et al. (2001) estimated the ZTD using a mapping function to adjust the reflecting surface height. Semmling et al. (2012) employed a ray-tracing tool to account for tropospheric refraction over a spherical Earth model. Fabra et al. (2012) incorporated Niell's mapping function, an exponential vertical decay model for tropospheric scale height, and zenith delay estimates from GNSS positioning data. Santamaría-Gómez & Watson (2017) introduced a tropospheric correction based on the bending angle, significantly improving results at low elevation angles.

In 2017, Williams & Nievinski conducted a detailed investigation into tropospheric delays in GNSS-R at elevations as low as 5°, using data from 20 IGS stations located near water bodies. Their study examined a relative tropospheric delay model introduced by Fabra et al. (2011), depicted in Figure 2.14. This model defines an equivalent point along the incident ray path,

effectively representing a theoretical adjustment to align the delay of the incident-reflected signal path with that of the direct path, thereby improving the accuracy of tropospheric delay estimations in GNSS-R.

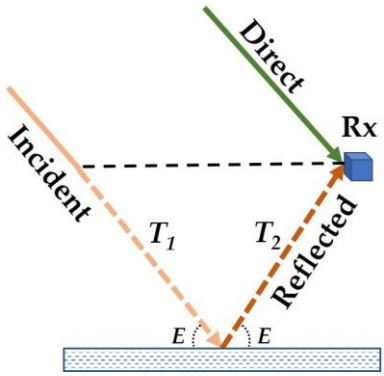

Figure 2.14 Representation of a theoretical model of the relative tropospheric delay in GNSS-R.

From this scheme, it follows that the relative tropospheric delay can be expressed as $T_1 + T_2 = 2T$. Using the definition of tropospheric delay as in Equation (2.15) the relative tropospheric delay is formulated as (Fabra et al., 2011):

$$\Delta p_{trop} = 2\left(ZHD\ m_h(E) + ZWD\ m_w(E)\right). \qquad (2.29)$$

In their study, the tropospheric delay was determined using the VMF/GPT2 models (Lagler et al., 2013), along with atmospheric ray tracing based on a basic climatology. The findings revealed that tropospheric delays introduce significant errors in height retrievals by acting as scaling factor inaccuracies. Correcting for these delays was shown to improve leveling results across all antenna heights. Recent approaches include a ray-tracing procedure for ground-based GNSS-R, defining the interferometric atmospheric delay and decomposing it into along-path and geometric components, while introducing new subcomponents to improve atmospheric altimetry corrections (Nikolaidou et al., 2020).

- *Tropospheric Effects Correction*

The application of various tropospheric correction approaches has been successfully demonstrated in multiple GNSS-R studies. Li et al. (2017) utilized carrier-phase observations from the TDS-1 satellite for sea ice altimetry. Tropospheric corrections were applied using the Hopfield model, leveraging meteorological parameters such as temperature, pressure, and integrated water vapor from the European Center for Medium-Range Weather Forecasts (ECMWF) reanalysis data. The retrievals demonstrated consistent results with agreement between the sea ice height from GNSS-R and the mean sea surface (MSS) model. This approach showed excellent performance with observations at elevation angles greater than 57°, validating the effectiveness of the applied tropospheric corrections.

In a similar application, Wang & Morton (2021) employed double frequency Spire Global Inc. GNSS-R data for sea ice height retrievals using carrier-phase measurements. Tropospheric delays were modeled using the VMF3/GPT-3 troposphere delay model, with the zen-

ith tropospheric delay adjusted by fitting to the MSS. The results demonstrated strong consistency with the ICESat-2 model but highlighted that tropospheric delay model errors are a significant source of uncertainty, contributing up to 30 cm of error in Sea Surface Height Anomalies (SSHA). Both studies confirmed the effectiveness of tropospheric corrections, with validation achieved by comparing height retrievals to external models. These findings therefore suggest the potential for directly extracting tropospheric parameters from GNSS-R observations, highlighting an opportunity for advancing atmospheric sensing techniques.

- *Tropospheric Parameters Estimations*

Investigating on GNSS-R potential, Jaberi Shafei & Mashhadi-Hossainali (2018) explored ground-based reflectometry observations for tropospheric tomography, a technique comprehensively described by Bender & Dick, 2021. This study focused on retrieving water vapor to enhance the accuracy of tomographic models, which are often constrained by rank deficiency, a condition where insufficient independent observations prevent the unique determination of all model parameters. The findings demonstrated that integrating GNSS-R data reduced rank deficiency by over 90%, particularly when optimizing spatial resolution. While challenges remain in precisely measuring tropospheric delays from reflected signals, this approach shows promise, especially in high-humidity environments.

Additionally, Wang (2023) utilized coherent carrier phase observations from Spire Global Inc. GNSS-R data at grazing angles below ~8° to estimate tropospheric zenith delay and Total Column Water Vapor (TCWV). These retrievals, validated with Sentinel-3 Ocean and Land Color Instrument (OLCI) and ERA5 model TCWV data over sea ice and calm water areas, achieved centimeter-level precision. Based on the definition of the relative tropospheric delay in Equation (2.29) , and assuming a well-modeled and stable ZHD, the estimation of the ZWD is expressed as:

$$\widehat{ZWD} = \frac{\frac{1}{2}\,\Delta p_{trop} - ZHD\; m_h - M\lambda}{m_w}. \tag{2.30}$$

where the term M represents the unknown integer associated with the phase ambiguity, and λ the wavelength of the carrier frequency. The TCWV can then be calculated using the following equation:

$$TCWV = \frac{10^6}{R_d\,(k_2' + \,k_3/T_m)} ZWD. \tag{2.31}$$

where R_d, k_2', and k_3 are the constants defined in Equation (2.17) and T_m is estimated using the relationship $T_m = 70.2 + 0.72T_s$ where T_s as the surface temperature obtained from ERA5 model. Figure 2.15 illustrates the agreement between GNSS-derived retrievals and ERA5 TCWV. The results demonstrated that low-elevation spaceborne GNSS-R observations can provide valuable information on water vapor, further expanding the application potential of GNSS-R for tropospheric monitoring studies.

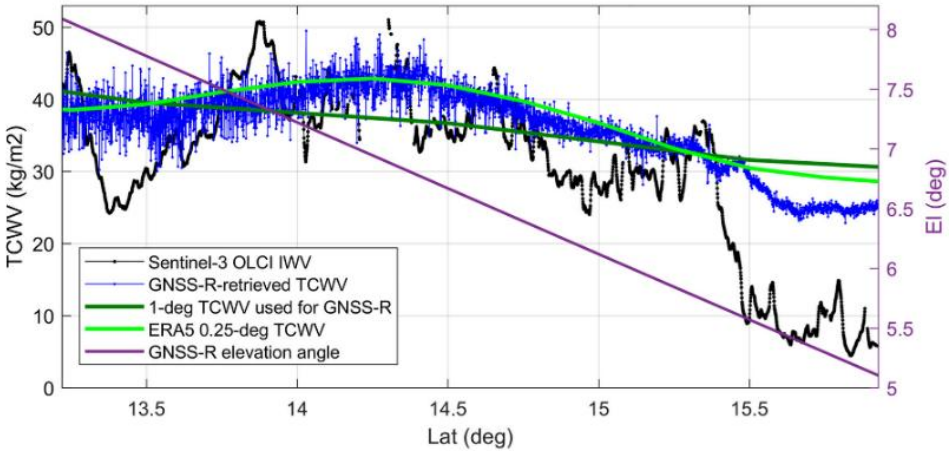

Figure 2.15 TCWV retrieval from GNSS-R compared against Sentinel-3 OLCI integrated water vapor measurement, ERA5 TCWV (0.25°x0.25° resolution) (Wang, 2023)

Chapter 3.

Research Contributions

This chapter presents the main results of the dissertation, which are organized according to the papers discussed in this thesis. As stated in Section 1.1, each paper addresses specific objectives and research questions outlined in this work.

Paper 1 introduces a novel experimental setup using a moving platform, specifically a gyrocopter equipped with a single antenna, to retrieve tropospheric parameters such as Zenith Total Delay (ZTD) from phase delay measurements over coastal waters (*RQ1.1*). Given the environmental conditions of coastal waters, the study also investigates the impact of surface roughness (sea state) on signal coherence. This is achieved by analyzing the Doppler spread caused by varying sea states, providing insights into how roughness affects GNSS-R measurements (*RQ1.2*).

Paper 2 focused on simulations conducted in the context of the new PRETTY mission, establishing a preparatory ionospheric study ahead of its launch in October 2023. The study extends the analysis of atmospheric impacts from airborne GNSS-R to spaceborne configurations, focusing specifically on the ionospheric effects at grazing angles (*RQ2.1*). PRETTY is a pioneering mission utilizing single-frequency E5/L5 observations with focus on altimetry at grazing angles. The mission relies on ionospheric corrections derived from empirical models. This paper investigates the implications of ionospheric model corrections on spaceborne GNSS-R for altimetry retrievals (*RQ2.2*), contributing to a deeper understanding of their role in enhancing retrieval accuracy.

Paper 3 represents the first results based on GNSS-R data observations collected from the PRETTY mission following its successful launch. The primary objective of this study is to estimate the relative ionospheric delays using code observations. By applying tropospheric corrections, the ionospheric contribution can be isolated and quantified. The resulting estimates are compared against established ionospheric models, including IRI, NEDM2020, and NeQuick, allowing for an evaluation of model performance under the specific conditions observed by PRETTY (*RQ3.1*). This analysis also builds on the simulations presented in Paper 2, bridging modeled ionospheric effects with in-orbit observations and estimations.

Furthermore, these estimates are utilized for fitting a Chapman layer function to infer the vertical structure of the ionosphere, providing insights into the F-layer peak height and its

variability (*RQ3.2*). This innovative application highlights the potential of PRETTY's single-frequency observations to enhance ionospheric characterization and model validation.

3.1 Airborne GNSS-R and Zenith Total Delay Estimation

Tropospheric effects in GNSS-R have been extensively investigated, with most efforts focused on correcting these effects to enhance the accuracy of surface height retrievals. Despite the growing interest in this field, relatively few studies have explored the potential of GNSS-R for directly estimating tropospheric parameters. This study addresses this gap by proposing an innovative approach to assess the feasibility of estimating Zenith Total Delay (ZTD) from airborne GNSS-R observations over coastal waters at low elevation angles. It builds upon previously established methodologies for tropospheric corrections in GNSS-R, adapting them to enable ZTD retrievals at sea surface levels.

The ZTD estimations in this study relied on coherent carrier phase observations, where coherence is closely associated with elevation angles and surface roughness. To complement this, the study also examines the influence of sea state on coherent observations, utilizing Doppler spreading as a metric to quantify the relationship between surface roughness and observation coherence from airborne data collected under distinct coastal water conditions.

The proposed methodology and analysis are applied to GPS L1 tracks collected on different days along the coast of Calais, France. This study provides insights into the accuracy of ZTD retrievals and the impact of sea state on coherence, contributing to the broader understanding of airborne GNSS-R applications in atmospheric remote sensing.

3.1.1 Experiment and Methodology

While GNSS-R dual-antenna configurations are commonly used in airborne missions, this study implement a novel experimental setup featuring a single right-hand circularly polarized (RHCP) antenna mounted on the front of a gyrocopter. The gyrocopter is an ultralight and stable aircraft traveling at an approximate speed of ~90 km/h (0.025 km/s). The antenna is tilted ~43° relative to the zenith direction to optimize signal reception and is connected to two receivers: one dedicated to recording GPS L1 signals for reflectometry and another for trajectory solution calculations. The measurement campaign is conducted along the North Sea coast, between Calais and Boulogne-sur-Mer, covering trajectories at distances of 700 m and 2,000 m from the shoreline. To ensure reflections are solely from the ocean surface, land masking was applied. Data collection was performed over four days allowing for observations under varying sea state conditions as detailed in Table 3.1.

Table 3.1 Overview of observation experimental campaign in Calais, France.

PRNs:	GPS: 1, 7, 8, 10, 11, 16, 18,30

Elevation Range:	4° to 70° at specular point			
Dates:	2019/07/12	2019/07/15	2019/07/17	2019/07/19
Wind Speed [m/s]:	5.49	4.29	2.92	6.50
SWH [m]:	0.30	0.58	0.26	0.55

The proposed methodology is outlined in the flowchart shown in Figure 3.1. It consists of three main components: signal processing using a software receiver, Doppler spread analysis, and Zenith Total Delay estimation.

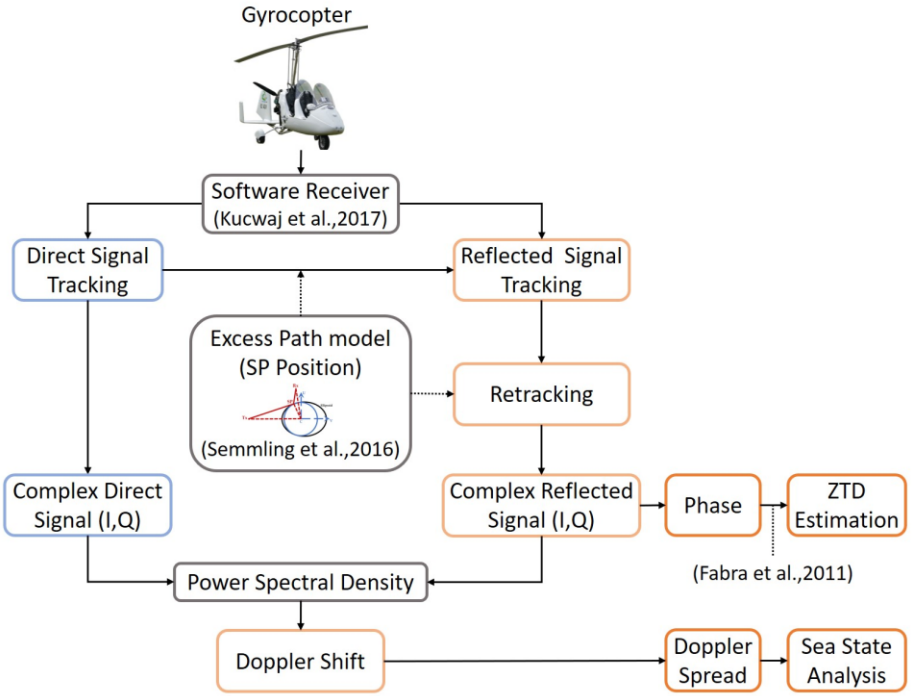

Figure 3.1 Flowchart illustrating the proposed methodology for ZTD estimation and Sea state analysis from airborne GNSS-R observations.

Signal Processing

Signal processing is performed using a model-aided software receiver, which is supported by the geometrical excess path model. The model incorporates the transmitter and receiver positions, and specular point positioning as described in Section 2.3.2. It predicts the expected delay and Doppler shift of the reflected signal relative to the direct signal, enabling accurate signal tracking. The processing output consist of complex reflected signals, represented by their in-phase (I) and quadrature (Q) components. A retracking module is integrated to refine Doppler and delay corrections to compensate variations arising from the relative motion of the transmitter, specular point, and receiver.

Doppler Spread Analysis

To evaluate sea state conditions, the power spectral density (PSD) of the reflected signal is analyzed. The PSD characterizes the distribution of power across frequencies, and the standard deviation of the five highest peaks is computed to quantify the Doppler spread. This Doppler spread is correlated with sea state conditions, including wind speed (WS) and significant wave height (SWH), using ERA5 reanalysis data (Hersbach et al., 2020). Additionally, the analysis identifies events where coherent observations are obtained, establishing a link between Doppler spread, surface roughness, and sea state conditions.

Zenith Total Delay Estimation

The relative tropospheric delay model used in this study followed the formulation in the Section 2.3.4, Equation (2.29). Since the dry component accounts for approximately 90% of the total tropospheric delay, the wet component was neglected. A decay function is applied to scale the delay from the receiver to sea surface level, while the Vienna Mapping Function 3 (VMF3) (Landskron & Böhm, 2018) is used to compute the hydrostatic mapping factor. The retracked and unwrapped carrier-phase observations are linked to the mapping factor, decay factor, and phase ambiguity through a linear regression model, enabling the inversion of the ZTD over coastal waters.

3.1.2 Results and Discussion

Different sea states conditions were observed during the experiment, with the calmest conditions observed on 2019/07/17 and the roughest on 2019/07/19 (see Table 3.1). The analysis reveals a direct correlation between the Doppler spread estimates and sea state conditions, showing that both the mean value and dispersion of the Doppler spread increased with rougher sea states.

Figure 3.2 illustrates the distribution of Doppler spread values across the four campaign dates, highlighting its sensitivity to sea state conditions. For instance, on 2019/07/17, the distribution is concentrated below 1 Hz, with a mean value of 0.5 Hz. This value is empirically identified as a threshold, indicating conditions favorable for coherent observations, as further discussed in Figure 3.3 (first row).

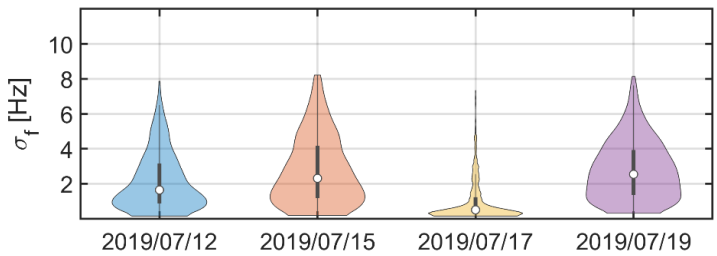

Figure 3.2 Doppler spread distribution. The mean value of the highest sea-state day is 2.5 Hz, while the lowest sea state represents a mean value of 0.5 Hz.

Under the conditions of the airborne GNSS-R observations over coastal waters, the loss of coherence in phase observations is consistently associated with a Doppler spread exceeding 0.5 Hz. The 0.5 Hz threshold corresponds to sea state parameters of SWH around 0.3 m and wind speeds WS of approximately 3 m/s, particularly when elevation angles fall below 10°. Figure 3.3 shows an example of four selected events with varying elevation ranges observed on 2019/07/17, providing further insight into the relationship between coherence and sea state conditions.

In the first row of Figure 3.3 presents, the Doppler spread remains below 0.5 Hz at low elevation angles, exhibiting reduced variations and aligning with stable, coherent scattering conditions. However, as the elevation angle increases, greater variability is observed, and the Doppler spread surpasses the threshold, indicating a transition to less coherent scattering.

Two factors may contribute to reduced sensitivity at mid and high elevation angles in the experiment: (1) at higher elevation angles, signals arrive closer to nadir, deviating from the antenna's upward-tilted boresight, resulting in a decrease in antenna gain. (2) high-elevation reflection events occur near or directly over the coastline, where the impact of sea state variations is minimal, reducing the sensitivity to surface roughness effects.

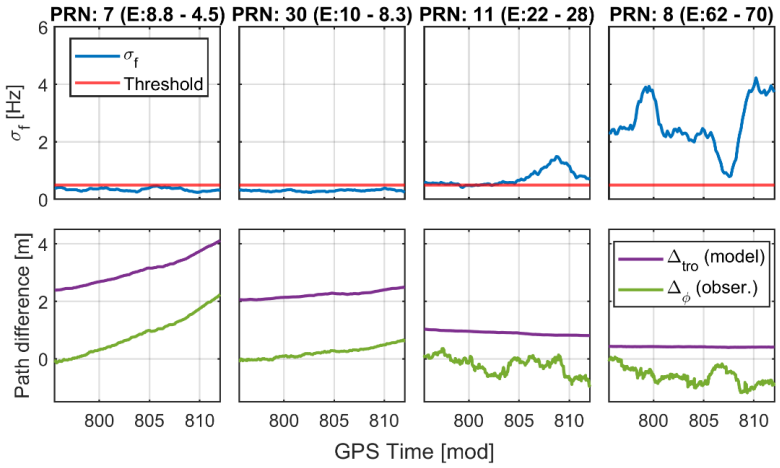

Figure 3.3 First row: Doppler spread σ_f. Second row: Relative tropospheric model compared with observed carrier phase delay in meters on 2019/07/17.

The second row of Figure 3.2 presents the relative unwrapped carrier phase delay in meters (green), showing a continuous trend at grazing angles, indicative of coherent observations. The relative carrier phase delay is compared with the established modeled relative tropospheric delay (purple), demonstrating consistent agreement between the two, with a residual offset due to the unresolved phase ambiguity. Utilizing the modeled tropospheric delay and the observed phase delay, the Zenith Total Delay is computed through linear regression.

The regression results reveal that under smooth sea surface conditions (on 2019/07/17) at low elevation angles (below 10°), the estimated ZTD for PRNs 7 and 30 is 2.437 m and 2.853 m,

respectively, with an uncertainty of 0.02 m in both cases. These values correspond to differences of 5% and 24%, respectively, when compared to the expected tropospheric delay value of 2.3 m for sea-level locations.

These findings validate the feasibility of estimating ZTD from coherent GNSS-R observations using the proposed methodology and highlight its potential application for atmospheric retrievals, such as the estimation of water vapor content.

3.2 Ionospheric Effects on GNSS-R at Grazing Angles from Space

The grazing angle geometry and smooth reflecting surfaces provide an optimal scenario for coherent observations in GNSS reflectometry. GNSS-R satellites missions, such as ESA's PRETTY and the commercial LEMUR-2 constellation operated by Spire Global, have ventured into this spectrum of observation through cost-effective CubeSat platforms. However, at such extreme geometric configurations, GNSS signals must traverse longer paths through the atmosphere, resulting in more pronounced ionospheric and tropospheric effects. While most of previous spaceborne studies have primarily analyzed ionospheric effects on GNSS-R observations at higher elevation angles, this study aims to extends the understanding of first-order ionospheric effects on single-frequency spaceborne GNSS-R observations at very low elevation angles (5°–30°).

The ionosphere exhibits highly dynamic conditions, with electron density varying significantly based on geographic location, time, and solar and geomagnetic activity. This study provides a comprehensive characterization of ionospheric effects under varying conditions, considering parameters such as elevation ranges, latitude-dependent regions, local time variations, and solar activity: low (LSA) and high solar activity (HSA). The analysis is grounded in the theoretical foundations on GNSS ionospheric delay (Section 2.2.1) and employs a 3D electron density model-based simulation to quantify the effects.

The proposed methodology is developed within the framework of the ESA PRETTY mission, serving as a preparatory study prior to its successful launch in October 2023. To simulate a real PRETTY-like grazing angle scenario, orbital data from the Spire Global Inc. CubeSat constellation was utilized. Contrary to some prior studies that disregarded the contribution of the direct signal in GNSS-R observations due to geometric configuration, this signal plays a critical role in estimating relative ionospheric delays at very low elevation angles. Its impact is particularly pronounced in Doppler shift and code-delay-based altimetry products, highlighting its importance for accurate retrievals in GNSS-R applications at extreme grazing angles.

3.2.1 Data and Methodology

To conduct this study, approximately 1,200 tracks from Spire Global Inc.'s LEMUR-2 CubeSat constellation on 1 March 2021 are analyzed. The LEMUR-2 constellation comprises over 80

CubeSats primarily designed for radio occultation, with around 30 configured to collect GNSS-R measurements. These observations resulted in a dataset of approximately 29,000 reflection events (specular points sampled at 10-second intervals along the satellite tracks). The observations are globally distributed and categorized into three geographic regions: North Region (latitudes above 40°N), Tropic Region (latitudes between 40°N and 40°S), and South Region (latitudes below 40°S). A high concentration of observations is present in the polar regions, primarily due to the constellation's design, which emphasizes sea ice monitoring. Additional areas with high data density included tropical regions with calmer ocean waters, such as the Gulf of Mexico and Southeast Asia, making them valuable for GNSS-R investigations.

Each CubeSat in the LEMUR-2 constellation is identified by a unique Space Vehicle Number (SVN). For this study, data from 21 CubeSats configured for GNSS-R observations are utilized, allowing for coverage across different local times. This ensured sufficient spatial and temporal representation across the defined regions, enabling a comprehensive analysis of ionospheric effects on GNSS-R observations under varying conditions.

The proposed methodology is outlined in the flowchart shown in Figure 3.4. It consists of three main retrievals from the modeled electron density: Ionospheric delay, Doppler shift, and electron density peak height.

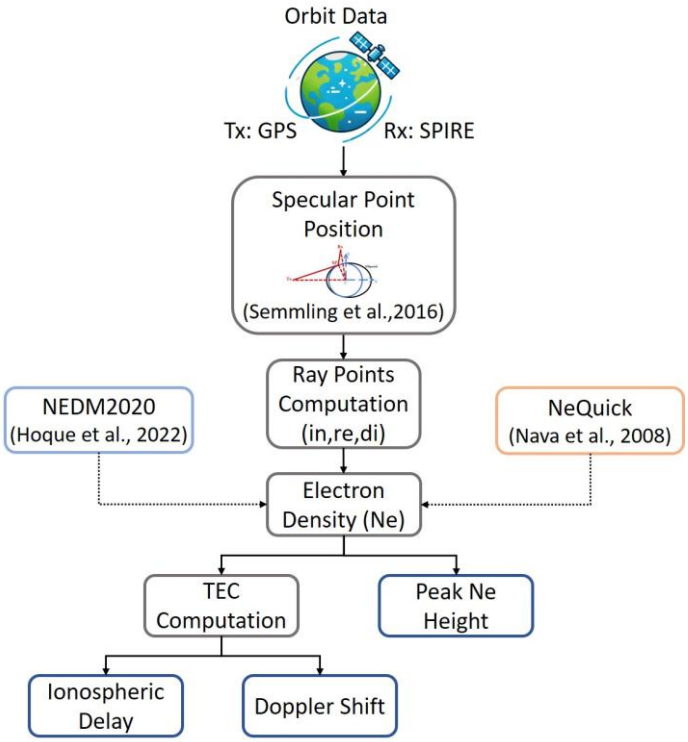

Figure 3.4 Flowchart illustrating the proposed methodology for ionospheric delay, Doppler shift and peak electron density height retrievals based on NEDM2020 and NeQuick models.

Electron Density Retrievals

The electron density for ionospheric estimations are obtained from two 3D electron density models: the NEDM2020 model and the NeQuick model. Both models require inputs such as solar activity indices, geographic location, and local time and provide the electron density at specified points along the ray path.

For this analysis, ray points along the incident, reflected, and direct signal paths are computed at intervals of 10 km. This computation relies on the determination of specular point positioning (Section 2.3.2). The specular points are sampled every 10 seconds over the approximately 4-minute duration of each event.

Figure 3.5 illustrates the electron density values derived from the NEDM2020 model for each ray point along the signal path during a low elevation event. The zoomed-in areas highlight the separation between computed ray points (red dots), and the interval of specular point samples (blue stars), providing insight into the spatial distribution along the reflection geometry.

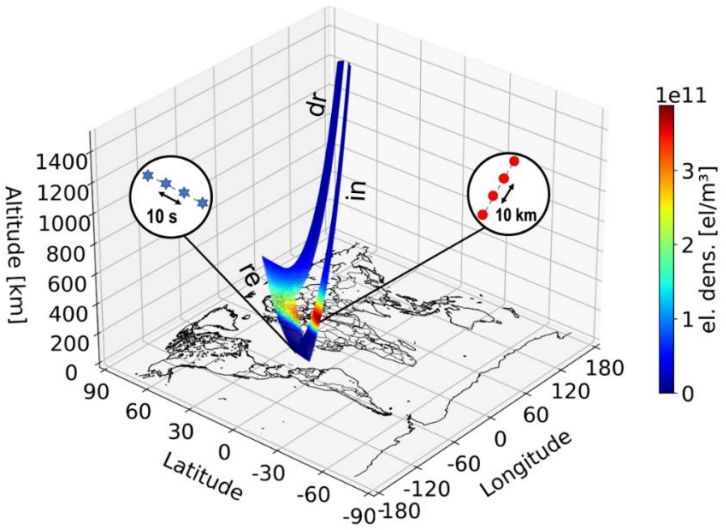

Figure 3.5 Electron density derived from NEDM2020 model for each ray point along the signal path. Red points show the distance between ray points, and blue stars show the interval between specular points.

sTEC, Ionospheric Delay and Doppler Shift

The slant total electron content (sTEC) for each ray path is computed as described in Equation (2.9), using numerical integration of the electron density along the path. The relative TEC, $\Delta sTEC$, is calculated as the sum of the slant TEC contributions from the incident ($sTEC_{in}$) and the reflected ($sTEC_{re}$) rays, minus the slant TEC of the direct ray ($sTEC_{di}$). This $\Delta sTEC$ was used to compute the relative ionospheric delay by applying the factor $40.3/f^2$, where f is the carrier frequency in Hz.

Variations in the ionosphere's electron density and its redistribution induce carrier phase delays, leading to Doppler shifts. These shifts can be computed as the time derivative of the signal's phase delay. Based on Equation (2.10) the phase delay is first expressed in cycle units by dividing by the signal's wavelength. The time derivative of the phase is then taken to determine the Doppler shift, offering insights into the ionospheric dynamics affecting the GNSS-R observations.

F-Layer Electron Density Peak Height Changes

The ionosphere exhibits significant variability in both temporal and spatial dimensions, influenced by factors such as time of day, geographic location, and solar activity. This variability affects the height at which the maximum electron density occurs, denoted as H_m occurs.

In this study, H_m is determined for both the incident and reflected rays corresponding to the point of the electron density peak in the density profile obtained from the NEDM2020 model. This approach provides a detailed investigation into the vertical dynamics of the ionosphere, particularly at grazing angles, where GNSS-R observations provide enhanced sensitivity to electron density fluctuations.

3.2.2 Results and Discussion

The analysis is structured based on grazing elevation ranges categorized into the three groups: 5°–10° (very-low), 10°–20° (low), and 20°–30° (mid-low). It incorporates the three latitude-defined regions (North, Tropics, and South), while including for local daytime (DT) and nighttime (NT) classification and variations in solar activity levels, defined as low (F10.7 = 75) and high (F10.7 = 180).

Figure 3.6 presents the mean sTEC distribution as a function of local time (hourly intervals) for the incident, reflected, and direct rays under low solar activity (LSA) using the NEDM2020 model. This visualization provides insights into the diurnal variation of sTEC, highlighting its dependence on elevation angles, geographic regions, and external space weather influences, such as solar cycles and ionospheric dynamics. Additionally, it serves as a reference for interpreting subsequent figures, which analyze variations in ionospheric delays, Doppler shifts, and peak electron density heights, offering a comprehensive assessment of the ionospheric effects influencing GNSS-R observations.

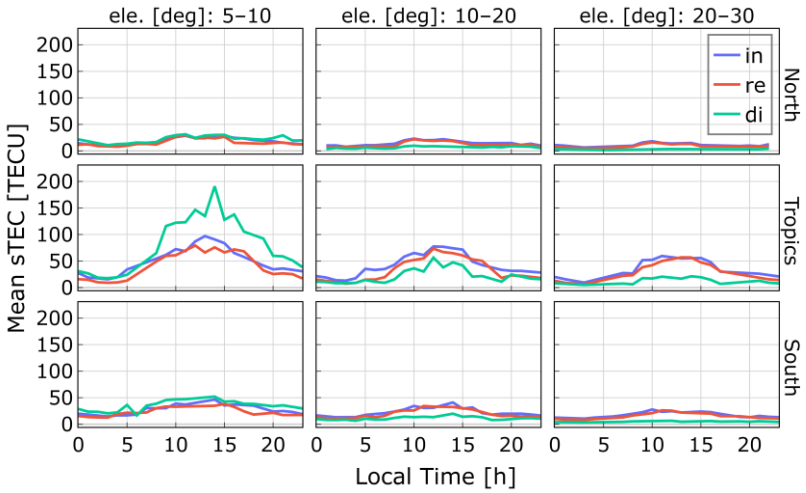

Figure 3.6 Mean sTEC values every hour obtained from NEDM2022 Model. Color-coded according to the direct (di), incident (in), and reflected (re) rays.

The results indicate that sTEC peaks occur around midday (12–14 hours local time), with the most significant increase observed in the tropics. This pattern highlights two key factors: (i) diurnal ionospheric variations, driven by intensified ionization at midday, and (ii) the stronger solar radiation in equatorial regions, leading to higher mean sTEC values (~32 TECU) compared to the North (~15 TECU) and South (~18 TECU) regions.

The incident and reflected rays exhibit similar trends across all scenarios, maintaining stable and comparable values. However, around midday, a small difference emerges, where the incident ray shows slightly larger values. This discrepancy reflects the geometric influence since the incident ray traverses a longer ionospheric path, traveling from the transmitter to the specular point.

In the very-low elevation range (below 10°), geometric effects become increasingly significant. At such low elevation angles, the direct signal travels a longer path through the densest layers of the ionosphere. This results in a more pronounced ionospheric effect, leading to higher sTEC values across all three regions. However, in the tropics, the direct signal also exhibits the highest variability, further emphasizing the strong influence of equatorial ionospheric dynamics. These geometric effects play a crucial role in computing the relative ionospheric delay ($in + re - di$) and Doppler shift, as they influence the path length differences between the various signal components.

Figure 3.7 illustrates the median relative ionospheric delay and the standard deviation as a function of elevation angle (columns) and geographic region (rows). The plot differentiates between daytime - DT (blue) and nighttime - NT (red), while solar activity levels are represented by circle for low solar activity and diamond for high solar activity

Consistent with the sTEC values, the relative ionospheric delay exhibits higher values during daytime across all scenarios, as solar radiation drives ionization, while at night, electron recombination reduces electron density. The tropics show larger delays and higher variability,

influenced by equatorial ionospheric dynamics. Under HSA, the mean delay values increase significantly, by approximately 2–4 times compared to LSA, nevertheless the path geometry introduces non-linear effects.

At very low elevations (<10°) during HSA, negative mean delay values (~-24.5 m) suggest a dominant direct ray contribution, leading to higher variability (standard deviation ~24.43 m) and making this the most sensitive region and elevation range. On the contrary, in the low-elevation range (10°–20°), the combined contributions of the incident and reflected rays is higher than the direct ray leading to an increase in relative ionospheric delay of up to ~28.45 m. This suggests that geometry-dependent cancellation effects may become dominant under specific solar and geographic conditions.

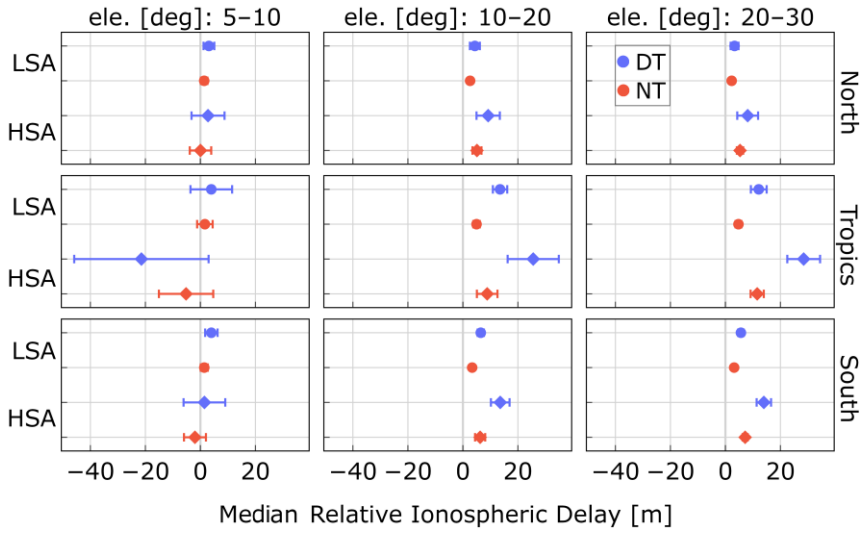

Figure 3.7 Median relative ionospheric delay values and their standard deviations, as a function of region, elevation range, daytime (DT/NT) and solar activity levels (LSA/HSA).

Doppler shifts driven by ionosphere-induced phase rate changes are also analyzed. Figure 3.8 presents the median Doppler shift values following the same plotting structure as the delay analysis. Similar to the relative ionospheric delay, the HSA period, during DT, in the tropical region, and very-low elevation angles (<10°) exhibit the highest Doppler shift values and the largest variability.

Under HSA, the Doppler shift increases by a factor of 3–10, with its standard deviation increasing by 2–5 times. The peak mean Doppler shift occurs in the tropics during daytime under HSA, reaching 2.33 Hz, which significantly exceeds the values observed in polar regions. Notably, even during LSA and nighttime, the tropical Doppler shifts surpass those recorded in polar regions during daytime.

The elevation group analysis confirms that Doppler shift decreases as elevation increases. This trend aligns with the fact that at higher elevations, the signal path through the ionosphere is shorter, reducing the ionospheric impact. On the other hand, at lower elevations, signal paths extend through denser ionospheric layers, amplifying phase rate gradients and

leading to higher Doppler shifts. This underscores the challenges in correcting ionospheric effects for altimetric applications, as uncertainties increase significantly at lower elevation angles.

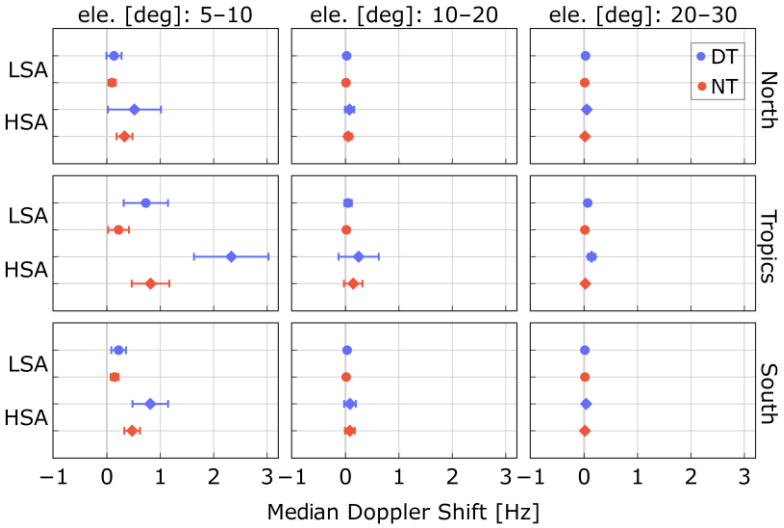

Figure 3.8 Median Doppler Shift magnitude and their standard deviations, as a function of region, elevation range, daytime (DT/NT) and solar activity levels (LSA/HSA).

Regarding the peak electron density height (H_m), Figure 3.9 illustrates its variation across regions and elevation ranges, highlighting its dependence on solar activity and diurnal ionosphere variations. During HSA, H_m increases by approximately 50–60 km across all regions. This is attributed to higher ionization rates, which enhance vertical plasma transport, leading to the uplift of the F2-layer peak. Additionally, the ionospheric diurnal cycle plays a significant role, creating a distinct contrast between daytime and nighttime values.

At nighttime, H_m is 20–50 km higher than during the daytime, with the most pronounced differences observed in the tropical region. This effect is explained by post-sunset recombination, which depletes the lower ionosphere (E and F1 layers), while the F2-layer persists longer due to its slower recombination rates (Jakowski, 2017).

The variation in H_m is also crucial for GNSS applications, as a higher F2-layer peak means that signals traverse a larger portion of the ionosphere, potentially leading to increased delays and Doppler shifts. These findings provide valuable insights into the vertical structure of the ionosphere, demonstrating the capability of GNSS-R grazing-angle observations to characterize ionospheric dynamics effectively.

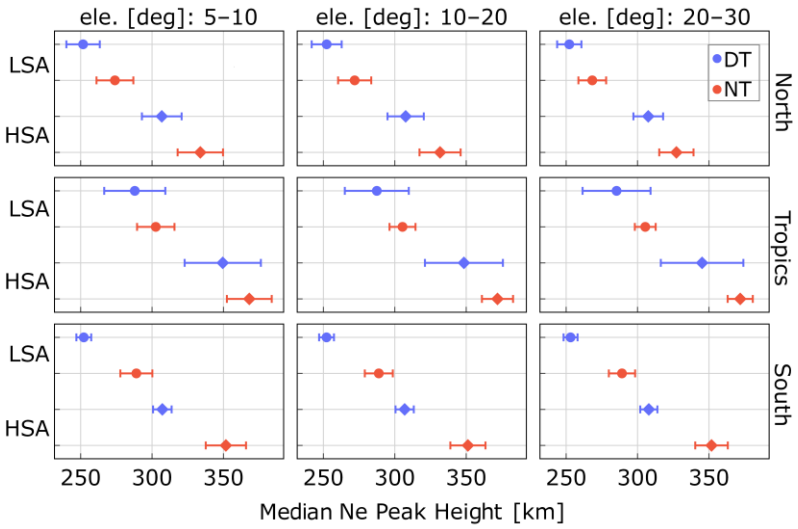

Figure 3.9 Median electron density peak height values and their standard deviations, as a function of region, elevation range, daytime (DT/NT) and solar activity levels (LSA/HSA).

3.3 Grazing-angle Ionospheric Delays Observed from PRETTY

Since the beginning of GNSS-R, one of the earliest proposed applications, alongside altimetry, was ionospheric monitoring, emphasizing its potential to provide valuable insights into the ionosphere over oceans. Double-frequency GNSS-R missions facilitate ionospheric studies by leveraging the differential response of signals at distinct frequencies. However, the PRETTY mission introduces an innovative approach by utilizing single-frequency GNSS-R data, demonstrating its capability to estimate ionospheric effects with a unique configuration.

This paper focuses on estimating relative ionospheric delays using code delay data collected from the PRETTY CubeSat in the Artic region. An onboard software module configures the code generator to account for instrumental biases and model the relative geometric delay, enabling precise corrections. Since tropospheric effects are significant at low elevation angles, corrections are applied using ray tracing techniques incorporating pressure, temperature, and humidity data from the ERA5 reanalysis model. The estimated relative ionospheric delays are then compared against three established models validating the methodology and highlights its potential for ionospheric delay estimations in GNSS-R applications.

The relative ionospheric delay estimates are subsequently used to fit the Chapman layer model, enabling the retrieval of key ionospheric parameters such as the F-layer peak electron density (N_0) and peak height (h_m). Comparisons with independent datasets, including ionosonde and EISCAT ground-based observations, show consistent results, with differences in the F-layer peak height within ±15 km. This demonstrates the feasibility of using GNSS-R code delay observations at grazing angles for characterizing the vertical structure of the ionosphere, offering a novel perspective on ionospheric monitoring in regions where conventional techniques are limited.

3.3.1 Data and Methodology

As of the writing of this thesis, the PRETTY mission has collected approximately 150 observation tracks across various regions, with a primary focus on the polar regions. These observations are recorded in both cGNSS-R and iGNSS-R modes.

For this study, six cGNSS-R events over the Artic region are selected due to their higher SNR responses, which are attributable to smooth surface conditions favorable for coherent signal reflection. The selected events are recorded in July 2024 with each event lasting on average six minutes. Table 3.2 provides an overview of the sample dataset, including the GNSS constellation, elevation range, UTC, local time and solar activity variations, represented by the solar flux index F10.7 on each observation day.

Table 3.2 PRETTY observation overview including the solar flux index.

Date	GNSS – PRN	Ele. Range	UTC	Local Time		F10.7
				Date	Time	
2024/07/06	GAL – 7	7 – 1	01:35:48	2024/07/05	23:57:32	169.9
2024/07/16	GAL – 7	10 – 1	00:55:51	2024/07/15	21:11:14	242.4
2024/07/25	GPS – 4	9 – 0.01	05:05:53	2024/07/24	21:04:56	172.0
2024/07/27	GPS – 8	11 – 0.01	04:55:51	2024/07/26	21:59:57	186.7
2024/07/28	GPS – 8	13 – 0.01	04:50:52	2024/07/27	21:54:43	216.6
2024/07/29	GPS – 8	15 – 0.01	04:45:50	2024/07/28	21:51:20	224.2

The proposed methodology is outlined in the flowchart shown in Figure 3.10. It consists of three main components:

Delay Maps Processing – Used for ionospheric delay estimations from PRETTY GNSS-R observations.

Modeled Tropospheric Delay – Applied for corrections to account for atmospheric effects at low elevation angles.

Modeled Ionospheric Delay – Used for comparison with the estimated ionospheric delays, ensuring validation against state-of-the-art ionospheric models

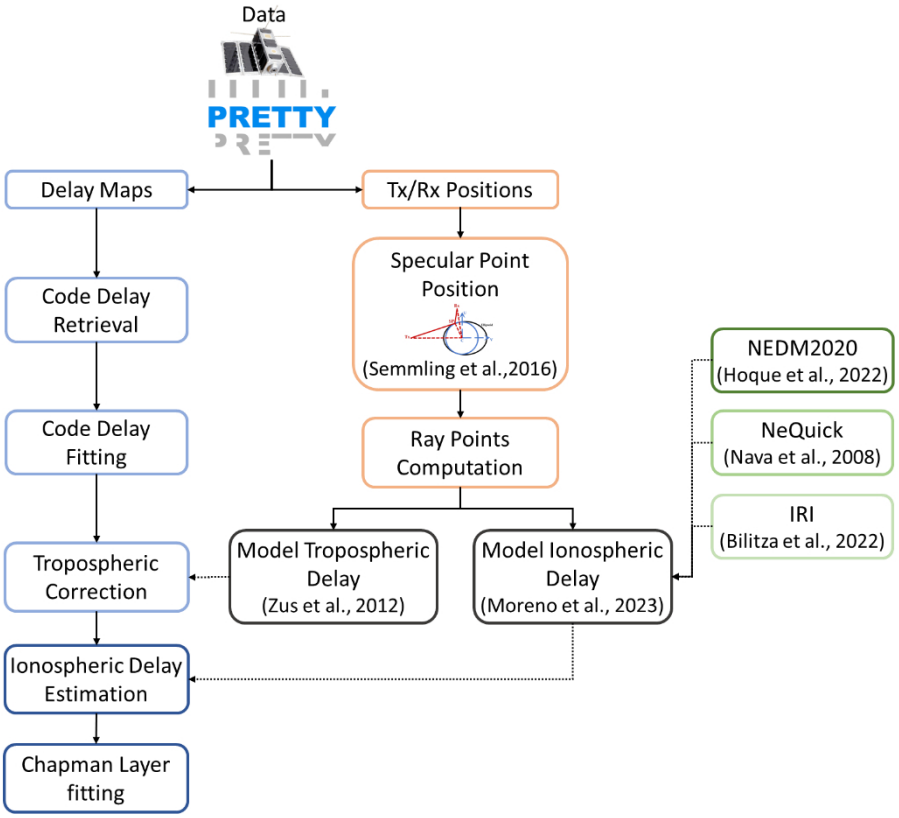

Figure 3.10 Flowchart illustrating the proposed methodology for relative ionospheric delay estimations from PRETTY GNSS-R observations, incorporating tropospheric corrections and state-of-the-art ionospheric models for comparison.

Delay Maps Processing

The PRETTY observations utilized Delay Maps created in post-processing, which are incoherently integrated every second. The delay domain is divided into 200 discrete bins, providing a resolution of 7.8071 meters. For each waveform within the DM, the peak value is selected to represent the relative delay of the reflected signal with respect to the direct signal. This delay inherently includes onboard instrumental bias corrections. The resulting dataset comprises a series of delay along the event track. To effectively capture the trend of the discrete code delay data, an exponential fitting approach is applied. This method smooths the data while accounting for model uncertainties associated with the fitting process, ensuring an accurate representation of delay trends across the observed tracks.

Modeled Ionospheric Delay

The methodology for computing the modeled ionospheric delay follows the framework established in Paper 2. For each event, the specular point position is determined as described in Section 2.3.2. Subsequently, a series of ray points is calculated at one-second intervals along the signals path. Using the NEDM2020 and NeQuick models, the electron density is obtained

for each ray point. The sTEC is computed by integrating the electron density along the signals path.

Additionally, model-based ionospheric delay is computed using the IRI model to provide comparative analysis. The computation of sTEC is complemented by tropospheric corrections applied via a ray tracing based on (Zus et al., 2012), ensuring accurate separation of ionospheric and tropospheric effects. Further details on the tropospheric correction methodology are discussed in the subsequent section, which ensures consistency across all atmospheric corrections.

Modeled Tropospheric Delay

The calculation of the relative tropospheric delay relies on a ray tracing employing a point-to-point algorithm. The process begins by determining the ray path between the transmitter, specular point and receiver and calculating the optical path length through numerical integration of the refractive index along the ray path. Initially, the algorithm assumes a specular point position (based on Paper 1 and 2 methodology) and computes the relative geometric excess path P without incorporating atmospheric effects.

To account for the tropospheric delay, the specular point position is iteratively adjusted. This iterative process ensures that the reflection law is satisfied, where the incident angle equals the reflected angle. By including the tropospheric effects, the algorithm refines the specular point position and recalculates the total relative path length. This corrected path length now integrates the tropospheric contribution alongside the geometric excess path, referenced as P_t.

Following the determination of the corrected specular point from previous step, the ionospheric delay is recalculated using the updated reflection geometry denoted as P_i. The final step involves isolating the contributions of the tropospheric and ionospheric delays from the total relative path delay, which is expressed as:

$$P_i = P + (P_t - P) + (P_i - P_t). \tag{3.1}$$

This separation is achieved by comparing the computed relative path length to the geometric excess path P, allowing for precise estimation of both tropospheric $(P_t - P)$ and ionospheric $(P_i - P_t)$ delay components.

3.3.2 Results and Discussion

The computation process for the corresponding tropospheric or ionospheric delay from the models serves two primary purposes. First, calculating the delay for each ray provides valuable insights into the individual contributions of the incident, reflected, and direct rays, allowing for a detailed understanding of their influence on the total delay. Second, these modeled delays are used as a reference for comparing observations to theoretical expectations.

While the observed delay represents the accumulated relative delay, which inherently includes contributions from all rays (direct, incident and reflected), ist is challenging to separate the individual contributions from each ray directly through observations alone. This is due to the integrated nature of the observed delay, which encapsulates all path-dependent atmospheric effects as a single measurable quantity. Therefore, the modeled delays play a critical role in separating and understanding the contributions of individual atmospheric components. Figure 3.11 presents a two events example of the modeled ionospheric and tropospheric delay for each ray path for two different days under varying solar activity conditions.

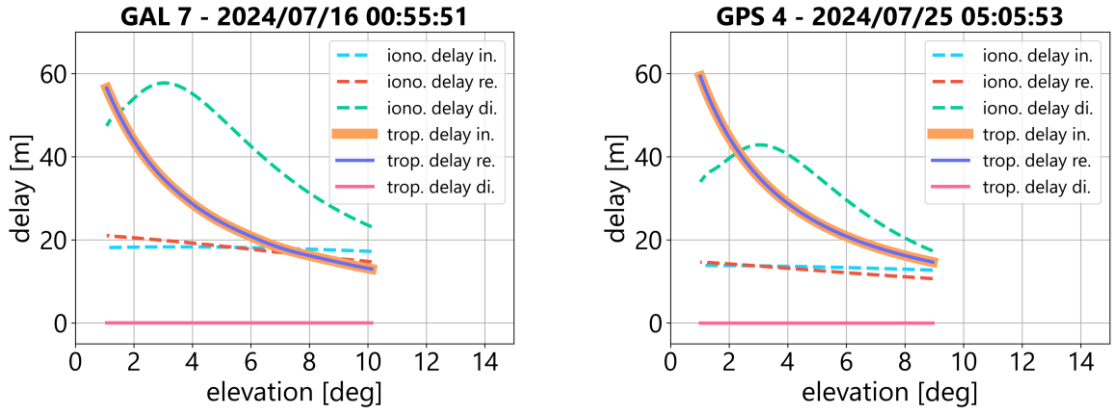

Figure 3.11 Modeled ionospheric and tropospheric delays for incident (in), reflected (re), and direct (di) rays for two different events observed on separate days with varying solar flux index values, left: 242.4 and right: 172.0.

Based on the tropospheric model presented in Section 2.3.4 (Figure 2.14), the incident and reflected rays exhibit similar contributions. For the analyzed events, both rays showing an exponential increase as the elevation angle decreases, reaching approximately 60 m at 1° elevation. The contribution from the direct ray, however, is negligible until the elevation angle drops below 1°. Below this range, the direct ray tropospheric delay contribution becomes significant, averaging around 100 m.

In contrast, for the ionospheric delay, the contributions of the incident and reflected rays are slightly different but remain relatively stable across the elevation angle range. The direct ray, however, exhibits significant change, with an exponential increase in delay, peaking at approximately 3° elevation. Beyond this point, the delay contribution begins to decrease gradually as the elevation angle approaches 1°. Solar activity also plays a critical role in these dynamics, as higher solar activity as presented in Paper 2. High solar activity correlates with increased TEC, resulting in larger ionospheric delays. This trend is particularly evident on 16/07/2024, a day characterized by elevated solar activity with an F10.7 index of 242.4, corresponding to the highest observed delays during the study.

When combining the modeled tropospheric and ionospheric delays and comparing them with the exponential-fitted observed code delay, a strong agreement is observed. Minor discrepancies remain, attributed to unmodeled or mis-modeled errors and noise. This alignment

demonstrates the ability of the models to effectively capture atmospheric effects on GNSS-R signals. The agreement also enables the removal of the tropospheric delay from the observations, isolating the ionospheric contribution to estimate the relative ionospheric delay. Figure 3.12 presents the comparison of the ionospheric delay estimates with the NEDM2020, NeQuick, and IRI models for the four analyzed events, highlighting the performance of the models under varying atmospheric and geometric conditions. Light red area represents the uncertainty of the fitting process and the tropospheric model correction.

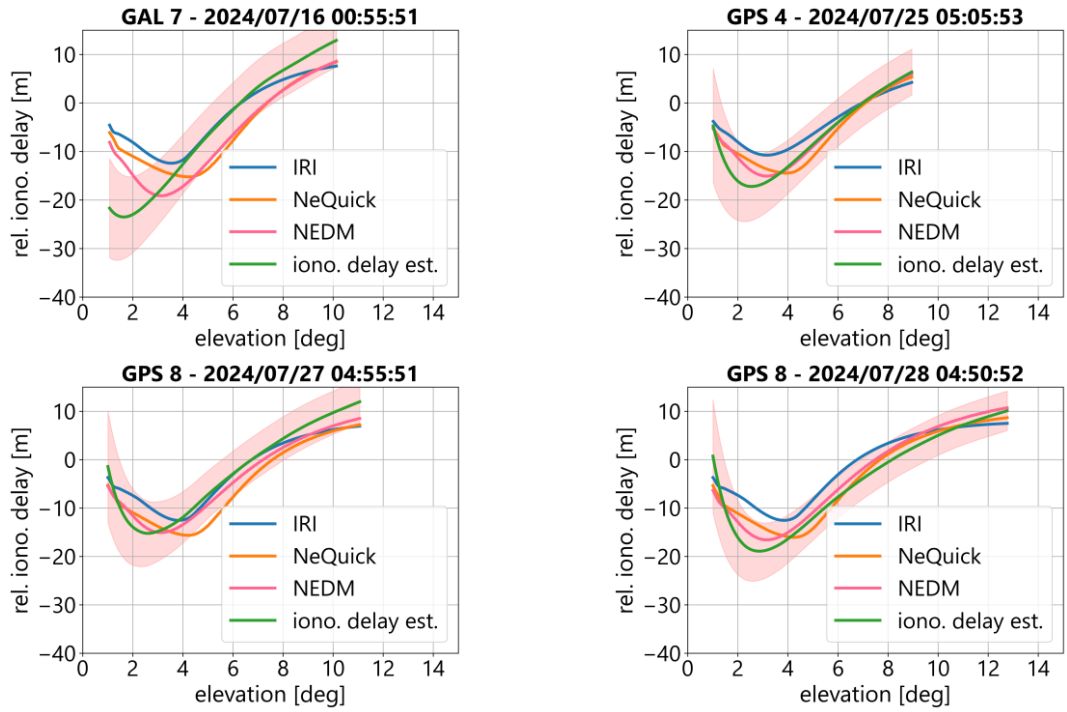

Figure 3.12 Relative ionospheric delay computed using the IRI, NeQuick, and NEDM2020 models, compared with the estimated relative ionospheric delay derived from observations. The associated uncertainties from model fitting and tropospheric corrections are also included in the light red area.

As the relative ionospheric delay estimates effectively capture first-order ionospheric effects, the next step involves inverting Chapman layer parameters to infer the ionosphere's vertical structure. The Chapman layer function (Chapman, 1931) models the electron density N_e as a function of altitude h providing a representation of the ionospheric F-layer as follows:

$$N_e(h) = N_0 \cdot \exp\left(\frac{1}{2} * \left(1 - \left(\frac{h - h_m}{H}\right) - \exp\left(-\frac{h - h_m}{H}\right)\right)\right). \qquad (3.2)$$

Where N_0 represents the peak electron density of the F-Layer, h_m is the height of the F-Layer peak, and H represents the scale height.

This process aims to determine the set of Chapman parameters, h_m and N_0 , that best reproduce the observed GNSS-R relative ionospheric delays. The results show strong agreement

between the GNSS-R observations, and the Chapman model estimates across all events. The fits capture both the overall shape and magnitude of the relative ionospheric delay, including the local minima typically observed between 2° and 4° elevation as presented in Figure 3.13. These findings highlight the capability of GNSS-R code delay observations at grazing angles to retrieve ionospheric vertical profile characteristics in line with the classical Chapman layer representation.

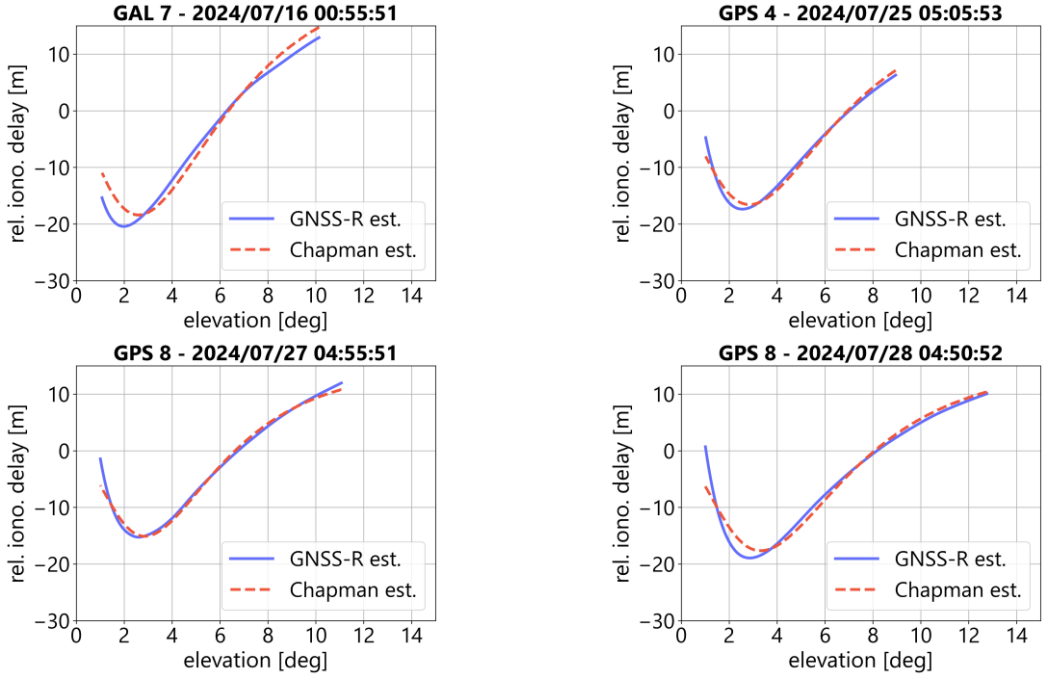

Figure 3.13 Comparison between GNSS-R ionospheric delay estimate and the ionospheric F-layer Chapman layer fitting.

Table 3.3 present the chapman parameters estimations along with the RMSE of the estimates. The RMSE values of the fits remain below 1.7 meters for all cases, indicating good consistency between the GNSS-R-derived ionospheric delay and the Chapman model reconstructions.

Table 3.3 Estimated h_m and N_0 from Chapman layer fitting process

Date	GNSS – PRN	h_m [km]	N_0 [el/m^3]	RMSE [m]
2024/07/06	GAL – 7	315.71	5.35e11	1.47
2024/07/16	GAL – 7	307.35	6.34e11	1.66
2024/07/25	GPS – 4	323.26	4.33e11	0.83
2024/07/27	GPS – 8	310.34	3.64e11	0.74
2024/07/28	GPS – 8	361.29	4.09e11	1.31
2024/07/29	GPS – 8	337.49	3.80e11	1.25

To compare the peak electron density heights estimations with ionosonde and EISCAT measurements, three stations near the analyzed GNSS-R events were selected: TROMSØ (URSI code TR169) and EISCAT TROMSØ (TR170) in northern Scandinavia, and THULE (THJ76)

in Greenland. For most events, the differences between the GNSS-R-derived estimates and the reference values remained within ±15 km, which is consistent with expected spatial and temporal ionospheric variations. These results highlight the capability of GNSS-R code delay observations at grazing angles to provide meaningful insights into the vertical ionospheric structure.

Table 3.4 presents a comparison between the GNSS-R-derived h_m estimates (in kilometers) and those obtained from ground-based ionosonde and EISCAT stations

Table 3.4 F-layer peak height h_m (in km) retrieved from GNSS-R in comparison with ionosonde and EISCAT stations

Date	GNSS – PRN	GNSS-R	TR170	TR169	THJ76
2024/07/06	GAL – 7	315.71	313.30	309.90	307.60
2024/07/16	GAL – 7	307.35	ND	315.30	299.30
2024/07/25	GPS – 4	323.26	318.50	307.50	294.10
2024/07/27	GPS – 8	310.34	307.20	294.00	300.20
2024/07/28	GPS – 8	361.29	350.60	327.50	306.30
2024/07/29	GPS – 8	337.49	339.60	297.40	327.30

Chapter 4.

Conclusions and Future Research

The conclusions provided in this chapter are based on the research conducted throughout this dissertation. They are guided by the research questions established in the introductory section, offering a synthesis of the findings and their implications. Additionally, this chapter includes insights into potential future research, aimed at advancing the field of GNSS-R and its applications.

4.1 Conclusions

RQ 1.1: How effectively can phase observations from airborne GNSS-R data be utilized to retrieve atmospheric parameters, such as ZTD, over coastal waters?

Coherent phase observations have proven to be a precise and reliable observable for GNSS-R altimetry applications, as demonstrated in both airborne (Semmling et al., 2014) and spaceborne studies (Cardellach et al., 2020). In this dissertation, a novel method was developed to effectively estimate Zenith Total Delay from airborne GNSS-R data over coastal waters, showing the potential of using coherent phase observations for atmospheric parameter retrieval, under specific conditions, particularly in low sea state scenarios and favorable geometric configurations.

The ZTD estimation results showed agreement with theoretical values expected at sea level of approximately 2.3 m. The events with best performance, which occurred at elevation angles below 10° and under calm sea state conditions, present ZTD estimates of 2.437 m and 2.853 m, corresponding to differences of 5% and 24%, respectively. These results highlight the capability of coherent phase observations to retrieve atmospheric parameters with notable accuracy over coastal waters.

These results are achieved under the following considerations: (1) ZTD is approximated by focusing on the dry component, which accounts for approximately 90% of the tropospheric delay; (2) precise specular point positioning and platform trajectory data are critical to compute reliable geometric excess path model; (3) the modeled tropospheric delay, calculated using the Vienna Mapping Function (VMF3), exhibited a linear relationship with the coherent

unwrapped phase observation, enabling least-squares linear regression with associated uncertainties of 0.02 m; and (4) while unresolved phase ambiguities persist, they do not influence the inversion of ZTD solutions. These solutions may include potential hardware delays from both the satellite and receiver, as well as clock and other systematic biases. These considerations highlight the robustness of the methodology while leaving room for further refinement to enhance its accuracy and applicability.

In addition, the proposed methodology employs a cost-effective experimental configuration, using a single RHCP antenna mounted on a gyrocopter. This setup is not only innovative but also reproducible and accessible for researchers aiming to adapt it for various applications. For example, it could be expanded by incorporating an additional LHCP antenna to enable complementary observations, such as those used in water body detection (Issa et al., 2021).

RQ 1.2: What is the influence of surface roughness (sea state) on airborne GNSS-R measurements, and how does this affect the Doppler spread and phase coherence?

Surface roughness, as influenced by sea state, plays an important role in determining the behavior of GNSS-R signals, particularly considering Doppler spread and coherent phase retrievals. Based on the Rayleigh criterion, the transition from specular reflection to diffuse scattering depends on factors such as signal wavelength, surface roughness, and elevation angle. These factors also impact whether phase observations remain coherent or become incoherent. The phase observable is fundamentally tied to the Doppler shift, which represents the rate of change in phase over time and serves as a key metric in this analysis. This dissertation demonstrated that Doppler spread from the reflected signal, closely associated with the randomness of ocean wave facets causing diffuse scattering (Elfouhaily et al., 2002), provides not only information about sea state conditions but also acts as an indicator of phase coherence from which the inversion of the ZTD was possible. When Doppler spread exceeds a certain threshold, it reflects a transition from coherent to incoherent phase observations. However, it is not only the sea state that influences Doppler spread changes. Residual effects, such as those coming from trajectory variations of the airborne receiver after geometric path corrections, can also have a significant impact.

In the context of airborne GNSS-R over coastal waters, this study showed that under wind speeds of approximately 3 m/s and significant wave heights of ~0.3 m, Doppler spread values exceeding 0.5 Hz corresponded to segments of phase observations where coherence was lost. These findings denote the relationship between surface roughness, signal scattering behavior, and phase coherence, emphasizing the importance of understanding and mitigating these factors to enhance the reliability of airborne GNSS-R observations.

RQ 2.1: How do varying ionospheric conditions, including slant TEC and F-layer peak height variations, affect spaceborne GNSS-R signal delays and Doppler shifts at grazing angles?

Regions experiencing higher solar radiation and periods of increased solar activity exhibit greater variations in ionospheric conditions, particularly in slant Total Electron Content and

electron density distribution. These variations are influenced by geographic location and diurnal cycles, leading to pronounced effects on electromagnetic wave propagation. Such impacts are evident not only in other GNSS-based applications but also in GNSS reflectometry, where the interaction between ionospheric irregularities and signal propagation is critical.

In GNSS reflectometry, the observation geometry plays a crucial role. This study addresses a notable knowledge gap in understanding ionospheric impacts at grazing angles observations.

Each observation involves three primary ray paths: incident, reflected, and direct. Since GNSS-R signals are inherently relative (the reflected signal relative to the direct signal), the contribution of each ray path significantly influences the overall retrieval. This study addresses the knowledge gap in ionospheric impacts at grazing angles. At very low elevation angles during daytime, the direct signal traverses a longer path through the ionosphere, particularly through regions with high electron density concentrations, including the F1 and F2 layers that predominantly form during daytime. This geometry results in a more considerable delay for the direct signal compared to the combined contributions of the incident and reflected rays, showing the complex interaction between ionospheric structure and observation geometry.

In the very-low elevation range (below 10°), geometric effects become increasingly significant, amplifying the ionospheric impact across all analyzed regions. This leads to higher sTEC values, particularly in the tropics, where the direct signal exhibits the highest variability, emphasizing the strong influence of equatorial ionospheric dynamics. As a result, these regions experience larger relative ionospheric delays, extending from approximately ~22 m under LSA up to ~75 m under HSA for L1 signals. Similarly, Doppler shifts range from ±2 Hz in LSA to ±4 Hz in HSA, reflecting the stronger ionospheric influence depending also on seasonal variations. In contrast, polar regions, which are exposed to less direct solar radiation, exhibit reduced first-order ionospheric effects on GNSS-R signals. This results in smaller ionospheric delays and less pronounced Doppler effects, highlighting the spatial variability of ionospheric influence across different latitudes.

These results show the spatial and temporal variability of ionospheric conditions, highlighting the challenges and opportunities for GNSS-R observations at grazing angles across different latitudinal regions. The described dynamics provide insights into how ionospheric variations impact signal delays (Figure 3.7) and Doppler shifts (Figure 3.8), underscoring the importance of considering regional ionospheric behaviors for accurate GNSS-R retrievals and atmospheric studies from grazing angle observations.

RQ 2.2: To what extent can ionospheric delay be characterized and modeled to improve the accuracy of GNSS-R applications at grazing angles?

This dissertation conducted a comprehensive characterization of ionospheric effects on spaceborne GNSS-R observations at grazing angles, leveraging empirical 3D ionospheric models for single-frequency applications correction. This foundation was further validated using PRETTY mission observations, showing consistent agreement between the modeled

ionospheric delays and the observed data, even under challenging geometric configurations. The analysis successfully demonstrated that these models, including NEDM2020 and NeQuick could effectively provide valuable tools for mitigating first-order ionospheric effects on GNSS-R products, provided the associated uncertainties are properly considered.

The study characterized ionospheric effects based on parameters such as geographical regions, grazing elevation ranges, solar activity levels, diurnal variations, and rising or setting events. These results provide two significant insights:

Extent of Ionospheric Correction Feasibility: The findings demonstrated that first-order ionospheric delays can be effectively corrected using empirical models, but with inherent uncertainties of approximately 30% (Subirana et al., 2013). Under adverse conditions and extreme geometries, these uncertainties can lead to altimetric errors at the meter level. However, these errors can be reduced to decimeter levels as the elevation angle increases. This underscores the importance of understanding the limitations of ionospheric corrections and their impact on GNSS-R applications, such as surface height retrievals.

Strategic Data Collection for Future Missions: The results provide critical insights for planning future GNSS-R missions. For instance, they help identify optimal regions, solar activity periods, and daytime intervals where ionospheric impacts are minimized, depending on the mission's objectives. This is particularly relevant for missions like PRETTY, which focus on ocean and sea-ice height retrievals and are limited to recording data for only 30 minutes per day. Strategic planning of data collection is essential to maximize the quality of observations while minimizing the influence of ionospheric effects to enhance the reliability and accuracy of GNSS-R products.

RQ 3.1: How accurately can spaceborne single-frequency GNSS-R data be used to estimate ionospheric delays at grazing angles?

Code delay estimations provide a robust approach for retrieving absolute pseudorange information. This advantage is particularly favorable when using wideband signals such as the L5/E5 GNSS signals, which allow for the accurate estimation of relative ionospheric delays. In this study, relative deviations between grazing angles observations and 3D electron density models ranged from 0.5% to 18%, depending on solar activity conditions, demonstrating the reliability of this method.

As expressed in the model of Equation (2.19) the relative delay, expressed in this case as the observed code delay, comprises contributions from the geometric range, tropospheric delay, instrumental biases, and unmodeled or mis-modeled errors, as well as noise. Accurate estimation of ionospheric delays requires effective correction for these contributions. This study demonstrated proper agreement between observations and models, confirming the successful application of atmospheric delay correction methodologies.

Table 4.1 provides an overview of the mean and standard deviation values for the estimated relative ionospheric delay, the tropospheric delay correction, and the observation error estimation based on the residuals from the fitting process, all expressed in meters. The PRETTY

observations in the Arctic region enable the collection of data within the sensitive elevation range of 1°–5°, further emphasizing the importance of grazing-angle observations for characterizing ionospheric and tropospheric effects in GNSS-R.

Table 4.1 Statistics of estimated relative ionospheric delay, tropospheric delay correction and observation precision by elevation range.

		Elevation								
		1°–5°			5°–10°			10°–15°		
		Trop.	Iono.	Obs.	Trop.	Iono.	Obs.	Trop.	Iono.	Obs.
F10.7	mean	73.26	-14.02	-	37.16	0.21	-	24.44	10.82	-
< 190	std	18.10	4.07	3.45	6.19	4.07	2.92	0.59	0.67	6.27
F10.7	mean	73.20	-15.51	-	36.13	0.13	-	22.38	10.01	-
> 190	std	18.51	5.34	3.89	6.12	5.34	1.59	1.75	2.62	0.65

Corrections for geometric delays using an internal digital elevation model to were needed to accurately locate the specular point. Additional surface corrections accounted for Earth's curvature and geoid undulations, ensuring precise geometric modeling. Tropospheric corrections are implemented using a ray tracing approach validated for low uncertainty, effectively isolating the relative ionospheric delay component. Although, the ionospheric delay estimations still contain some unmodeled errors and noise, they exhibit alignment with values derived from 3 different electron density models, confirming the reliability of the approach.

These findings confirm that single-frequency GNSS-R observations at grazing angles can provide reliable atmospheric delay estimations, even under extreme geometric configurations. This capability supports the potential of getting accurate slant TEC estimations, contributing significantly to ionospheric studies and enhancing GNSS-R applications such as altimetry and atmospheric monitoring.

RQ 3.2: What insights can be gained into the ionospheric structure from analyzing spaceborne GNSS-R observations at grazing angles?

The initial simulation study in Paper 2, provided a foundational understanding of the expected ionospheric effects and vertical structure variations at grazing angles ranging from 5° to 30°, coming from the diurnal variations of the ionosphere. Observations from the PRETTY mission extended this range, offering data at elevation angles as low as 0.01°. This unprecedented capability revealed key aspects of both tropospheric and ionospheric effects on GNSS-R signals.

From a tropospheric perspective, the direct signal's contribution to the delay was negligible above 1° of elevation. Below this threshold, however, its influence became significant, with the direct ray tropospheric delay reaching values of approximately 100 m. On the ionospheric side, observations revealed a distinct pattern: the direct ray's delay increased with decreasing elevation angle until reaching its maximum at an elevation of 3°. Beyond this point, its contribution began to decrease, while the relative ionospheric delay, dominated by the direct signal, reaches its maximum (negative value) at the same elevation. At this critical elevation,

the direct signal accounted for approximately 60% of the total ionospheric delay, highlighting the significance of its role at very low elevation angles.

Furthermore, by applying Chapman layer fitting to GNSS-R-derived relative ionospheric delays, it is possible to retrieve key parameters of the ionospheric F-layer, including the peak electron density and peak height, which ranged from 307 to 367 km. These values agree with expected conditions for high-latitude regions under high solar activity levels (F10.7 = 150–250). This analysis provides valuable initial insights into the potential of GNSS-R code delay observations for characterizing ionospheric parameters, as the retrieved peak heights show strong consistency with ground-based measurements from ionosondes and EISCAT stations.

Finally, as shown in Figure 3.12, a cancellation point is observed in the relative ionospheric delay, defined as the elevation angle where the contributions from the direct and combined incident-reflected signal paths cancel each other out. Simulations employing a Chapman layer model for the F-layer revealed a strong correlation between the elevation angle of the cancellation point and the height of the F-layer peak. Specifically, higher F-layer peak heights are associated with higher elevation angles at which the cancellation point occurs. This finding opens new perspectives for utilizing GNSS-R observations at grazing angles to infer the vertical structure of the ionosphere. Moreover, it suggests that the cancellation point could serve as a proxy for estimating the F-layer peak height

4.2 Future Research

Airborne experiments remain a crucial and cost-effective tool in GNSS-R research. They enable the testing of concepts and the refinement of theories or models on moving platforms, which can then be extended to satellite-based applications. The airborne configuration implemented in this study demonstrated good performance; however, it was performed over coastal water, limiting its applicability to certain scenarios. To broaden the scope, complementary and diverse airborne configurations could be implemented to focus specifically on tropospheric studies. Future research could explore diverse airborne configurations focusing on tropospheric studies, extending the ZTD estimation methodology to inland water bodies, rougher seas, or sea ice regions to assess robustness and adaptability

While the ZTD estimations derived during this study accounted for approximately 90% of the tropospheric delay by considering only the dry component, future efforts could focus on integrating and validating models for the wet component of the tropospheric delay. This would allow for a more comprehensive estimation, especially under varying meteorological conditions, such as high humidity or extreme weather events.

For ionospheric studies, the empirical models used in this dissertation are climatological, describing the average behavior of the ionosphere under quiet geomagnetic conditions. To extend the understanding of ionospheric effects in GNSS-R and establish the technique as a reliable tool for atmospheric monitoring, future research could explore geomagnetic influences and scintillation at low elevation angles. Spaceborne GNSS-R observations, with their

rapid movement and broader coverage, offer a unique opportunity to investigate irregular electron density structures, such as traveling ionospheric disturbances.

The temporal and spatial evolution of the ionosphere could also be studied using longer-term data from GNSS-R constellations like CYGNSS or Spire. This would enable the analysis of seasonal effects and events under high space weather conditions. Additionally, PRETTY's data could be refined further by incorporating precise orbit solutions for GNSS and low-Earth orbit (LEO) satellites, GNSS satellite clock corrections, and high-resolution ocean and sea ice surface height models. Complementary validation against ground-based observations, such as GNSS-TEC measurements or ionospheric data from ground stations in another geographic location, would strengthen the reliability of the derived ionospheric delays. PRETTY's programmable observation capability allows for collocation with ground-based observations or other spaceborne GNSS-R missions, offering opportunities for comparison and validation.

The ionospheric parameters derived from the Chapman layer fitting approach and the observed cancellation point in the relative ionospheric delay were examined under specific conditions, such as similar local times in Arctic regions. Future studies could explore their broader applicability by considering factors such as diurnal and seasonal variations in the F-layer peak height (h_m), horizontal ionospheric gradients, and the sensitivity to GNSS-R geometry. These aspects are particularly relevant, as they can influence the accuracy of estimating the cancellation point and its potential as a proxy for retrieving the vertical structure of the ionosphere.

Further investigations into h_m could also contribute to its integration into ionospheric models through data assimilation techniques. Given the findings of this dissertation, which reveal, for instance, the sensitivity of relative ionospheric delays and cancellation points to variations in h_m, incorporating the GNSS-R-derived estimates into 3D electron density models could enhance their predictive capabilities. Future studies could focus on refining retrieval methods for estimates h_m from GNSS-R observations, particularly at grazing angles, and developing assimilation strategies to integrate these estimates into ionospheric models. Additionally, analyzing seasonal, latitudinal, and solar activity-dependent variations in h_m would help to assess its impact on GNSS signal propagation. Validation against independent datasets, such as ionosonde and radio occultation measurements. Integrating F-layer peak height variations into ionospheric models would improve ionospheric delay corrections for GNSS-based applications, including remote sensing, space weather monitoring, and precise positioning techniques.

Another promising avenue for research involves combining PRETTY single-frequency GNSS-R code and carrier phase observations to estimate TEC, which is currently under investigation. This approach could be compared or validated against dual-frequency data to assess accuracy and enhance reliability.

Finally, as demonstrated in this dissertation, both the ionosphere and troposphere exhibit complex interactions with GNSS signals. Although theoretical and physics-based foundations provide a solid basis, long-term datasets and advancements in machine learning (ML)

and deep learning (DL) could bring significant advantages. For example, physics-informed ML models could be employed to investigate residual biases in atmospheric estimations, and address unmodeled errors and noise. These innovative approaches may unlock new possibilities for enhancing GNSS-R applications in atmospheric and geophysical studies, as demonstrated in ocean wind speed retrievals (Asgarimehr et al., 2022) or soil moisture estimation (Roberts et al., 2022) using DL approaches. However, achieving these advancements requires the availability of large, stable, and consistent datasets to effectively train and validate data-driven models.

Bibliography

Andersen, O., Knudsen, P., & Stenseng, L. (2018). *A New DTU18 MSS Mean Sea Surface – Improvement from SAR Altimetry: 25 years of progress in radar altimetry symposium*. 172.

Anthes, R., Bernhardt, P., Cucurull, L., Dymond, K., Ector, D., Healy, S., Ho, shu-peng, Hunt, D., Kuo, Y., Manning, K., & McCormick, C. (2008). The COSMIC/Formosat-3 mission: Early results. *Bulletin of The American Meteorological Society - BULL AMER METEOROL SOC*, *89*, 313–333. https://doi.org/10.1175/BAMS-89-3-313

Asgarimehr, M., Arnold, C., Weigel, T., Ruf, C., & Wickert, J. (2022). GNSS reflectometry global ocean wind speed using deep learning: Development and assessment of CyGNSSnet. *Remote Sensing of Environment*, *269*, 112801. https://doi.org/10.1016/j.rse.2021.112801

Asgarimehr, M., Entekhabi, D., & Camps, A. (2024). Diurnal Vegetation Moisture Cycle in the Amazon and Response to Water Stress. *Geophysical Research Letters*, *51*(19), e2024GL111462. https://doi.org/10.1029/2024GL111462

Askne, J., & Nordius, H. (1987). Estimation of tropospheric delay for microwaves from surface weather data. *Radio Science*, *22*(3), 379–386. https://doi.org/10.1029/RS022i003p00379

Auber, J.-C., Bibaut, A., & Rigal, J. (1994, September 23). *Characterization of Multipath on Land and Sea at GPS Frequencies*. https://www.semanticscholar.org/paper/Characterization-of-Multipath-on-Land-and-Sea-at-Auber-Bibaut/77279bf24fd66ea386a3d9b7cfaf9c199b5c60fc

Bender, M., & Dick, G. (2021). GNSS Water Vapor Tomography. In T. Foken (Ed.), *Springer Handbook of Atmospheric Measurements* (pp. 1025–1049). Springer International Publishing. https://doi.org/10.1007/978-3-030-52171-4_36

Béniguel, Y. (2002). Global Ionospheric Propagation Model (GIM): A propagation model for scintillations of transmitted signals. *Radio Science*, *37*(3), 4-1-4–13. https://doi.org/10.1029/2000RS002393

Bilitza, D. (2015). The International Reference Ionosphere – Status 2013. *Advances in Space Research*, *55*(8), 1914–1927. https://doi.org/10.1016/j.asr.2014.07.032

Bilitza, D., & Reinisch, B. W. (2008). International Reference Ionosphere 2007: Improvements and new parameters. *Advances in Space Research*, *42*(4), 599–609. https://doi.org/10.1016/j.asr.2007.07.048

Böhm, J., Möller, G., Schindelegger, M., Pain, G., & Weber, R. (2015). Development of an improved empirical model for slant delays in the troposphere (GPT2w). *GPS Solutions*, *19*(3), 433–441. https://doi.org/10.1007/s10291-014-0403-7

Brenot, H. (2020). GNSS for Neutral Atmosphere and Severe Weather Monitoring. In *Position, Navigation, and Timing Technologies in the 21st Century* (pp. 849–878). John Wiley & Sons, Ltd. https://doi.org/10.1002/9781119458449.ch30

Buendía, R. N., Tabibi, S., & Talpe, M. (2023). An Improved Ionospheric Correction Model for Grazing Angle GNSS-R Altimetry. *IGARSS 2023 - 2023 IEEE International Geoscience and Remote Sensing Symposium*, 4332–4335. https://doi.org/10.1109/IGARSS52108.2023.10282507

Camps, A., Munoz-Martin, J. F., Ruiz-de-Azua, J. A., Fernandez, L., Perez-Portero, A., Llavería, D., Herbert, C., Pablos, M., Golkar, A., Gutiérrez, A., António, C., Bandeiras, J., Andrade, J., Cordeiro, D., Briatore, S., Garzaniti, N., Nichele, F., Mozzillo, R., Piumatti, A., … Reagan, A. (2022). FSSCat: The Federated Satellite Systems 3Cat Mission: Demonstrating the capabilities of CubeSats to monitor essential climate variables of the water cycle [Instruments and Missions]. *IEEE Geoscience and Remote Sensing Magazine*, *10*(4), 260–269. IEEE Geoscience and Remote Sensing Magazine. https://doi.org/10.1109/MGRS.2022.3219778

Camps, A., Park, H., Foti, G., & Gommenginger, C. (2016). Ionospheric Effects in GNSS-Reflectometry From Space. *IEEE Journal of Selected Topics in Applied Earth Observations and Remote Sensing*, *PP*, 1–11. https://doi.org/10.1109/JSTARS.2016.2612542

Camps, A., Park, H., Juan, J. M., Sanz, J., González-Casado, G., Barbosa, J., Fabbro, V., Lemorton, J., & Orús, R. (2018). Ionospheric Scintillation Monitoring Using GNSS-R? *IGARSS 2018 - 2018 IEEE International Geoscience and Remote Sensing Symposium*, 3339–3342. https://doi.org/10.1109/IGARSS.2018.8519088

Cardellach, E., Li, W., Rius, A., Semmling, M., Wickert, J., Zus, F., Ruf, C. S., & Buontempo, C. (2020). First Precise Spaceborne Sea Surface Altimetry With GNSS Reflected Signals. *IEEE Journal of Selected Topics in Applied Earth Observations and Remote Sensing*, *13*, 102–112. IEEE Journal of Selected Topics in Applied Earth Observations and Remote Sensing. https://doi.org/10.1109/JSTARS.2019.2952694

Cardellach, E., Wickert, J., Baggen, R., Benito, J., Camps, A., Catarino, N., Chapron, B., Dielacher, A., Fabra, F., Flato, G., Fragner, H., Gabarró, C., Gommenginger, C., Haas, C., Healy, S., Hernandez-Pajares, M., Høeg, P., JäGgi, A., Kainulainen, J., … Zuffada, C. (2018). GNSS Transpolar Earth Reflectometry exploriNg System (G-TERN): Mission Concept. *IEEE Access*, *6*, 13980–14018. IEEE Access. https://doi.org/10.1109/ACCESS.2018.2814072

Carreno-Luengo, H., Camps, A., Via, P., Munoz, J. F., Cortiella, A., Vidal, D., Jané, J., Catarino, N., Hagenfeldt, M., Palomo, P., & Cornara, S. (2016). 3Cat-2—An Experimental Nanosatellite for GNSS-R Earth Observation: Mission Concept and Analysis. *IEEE Journal of Selected Topics in Applied Earth Observations and Remote Sensing*, *9*(10), 4540–4551. IEEE Journal of Selected Topics in Applied Earth Observations and Remote Sensing. https://doi.org/10.1109/JSTARS.2016.2574717

Carreno-Luengo, H., Lowe, S. T., Zuffada, C., Esterhuizen, S., & Oveisgharan, S. (2017). Spaceborne GNSS-R from the SMAP mission: First assessment of polarimetric scatterometry. *2017 IEEE International Geoscience and Remote Sensing Symposium (IGARSS)*, 4095–4098. https://doi.org/10.1109/IGARSS.2017.8127900

Chapman, S. (1931). The absorption and dissociative or ionizing effect of monochromatic radiation in an atmosphere on a rotating earth part II. Grazing incidence. *Proceedings of the Physical Society*, *43*(5), 483. https://doi.org/10.1088/0959-5309/43/5/302

CYGNSS Level 2 Science Data Record Version 3.0. (n.d.). Physical Oceanography Distributed Active Archive Center (PO.DAAC). Retrieved December 8, 2024, from https://podaac.jpl.nasa.gov/dataset/CYGNSS_L2_V3.0

Davis, J. L., Herring, T. A., Shapiro, I. I., Rogers, A. E. E., & Elgered, G. (1985). Geodesy by radio interferometry: Effects of atmospheric modeling errors on estimates of baseline length. *Radio Science*, *20*(6), 1593–1607. https://doi.org/10.1029/RS020i006p01593

Di Simone, A., Braca, P., Millefiori, L. M., & Willett, P. (2018). Ship detection using GNSS-reflectometry in backscattering configuration. *2018 IEEE Radar Conference (RadarConf18)*, 1589–1593. https://doi.org/10.1109/RADAR.2018.8378804

Dielacher, A., Fragner, H., & Koudelka, O. (2022). PRETTY – passive GNSS-Reflectometry for CubeSats. *E & i Elektrotechnik Und Informationstechnik*, *139*(1), 25–32. https://doi.org/10.1007/s00502-022-00993-7

Egbert, G. D., & Erofeeva, S. Y. (2002). *Efficient Inverse Modeling of Barotropic Ocean Tides*. https://journals.ametsoc.org/view/journals/atot/19/2/1520-0426_2002_019_0183_eimobo_2_0_co_2.xml

Elgered, G., & Wickert, J. (2017). Monitoring of the Neutral Atmosphere. In P. J. G. Teunissen & O. Montenbruck (Eds.), *Springer Handbook of Global Navigation Satellite Systems* (pp. 1109–1138). Springer International Publishing. https://doi.org/10.1007/978-3-319-42928-1_38

Fabra, F., Cardellach, E., Rius, A., Ribo, S., Oliveras, S., Nogues-Correig, O., Belmonte Rivas, M., Semmling, M., & D'Addio, S. (2011). Phase Altimetry With Dual Polarization GNSS-R Over Sea Ice. *IEEE Transactions on Geoscience and Remote Sensing*, *50*(6), 2112–2121. IEEE Transactions on Geoscience and Remote Sensing. https://doi.org/10.1109/TGRS.2011.2172797

Foerste, C., Bruinsma, S., Flechtner, F., Marty, J.-C., Dahle, C., Abrykosov, O., Lemoine, J.-M., Neumayer, H., Barthelmes, F., Biancale, R., & König, R. (2013). EIGEN-6C2—A new combined global gravity field model including GOCE data up to degree and order 1949 of GFZ Potsdam and GRGS Toulouse. *Geophys. Res. Abstr. EGU Gen. Assembl.*, *15*, 4077.

Foti, G., Gommenginger, C., Jales, P., Unwin, M., Shaw, A., Robertson, C., & Roselló, J. (2015). Spaceborne GNSS reflectometry for ocean winds: First results from the UK TechDemoSat-1 mission. *Geophysical Research Letters*, *42*(13), 5435–5441. https://doi.org/10.1002/2015GL064204

Foti, G., Gommenginger, C., & Srokosz, M. (2017). First Spaceborne GNSS-Reflectometry Observations of Hurricanes From the UK TechDemoSat-1 Mission. *Geophysical Research Letters*, *44*(24), 12,358-12,366. https://doi.org/10.1002/2017GL076166

Garrison, J. L., & Katzberg, S. J. (1997). Detection of ocean reflected GPS signals: Theory and experiment. *Proceedings IEEE SOUTHEASTCON '97. "Engineering the New Century,"* 290–294. https://doi.org/10.1109/SECON.1997.598694

Garrison, J. L., Katzberg, S. J., & Hill, M. I. (1998). Effect of sea roughness on bistatically scattered range coded signals from the Global Positioning System. *Geophysical Research Letters*, *25*(13), 2257–2260. https://doi.org/10.1029/98GL51615

Garrison, J., Zavorotny, V. U., Egido, A., Larson, K. M., Nievinski, F., Mollfulleda, A., Ruffini, G., Martin, F., & Gommenginger, C. (2020). GNSS Reflectometry for Earth Remote Sensing. In *Position, Navigation, and Timing Technologies in the 21st Century* (pp. 1015–1114). John Wiley & Sons, Ltd. https://doi.org/10.1002/9781119458449.ch34

Gleason, S. (2006). *Remote Sensing of Ocean, Ice and Land Surfaces Using Bistatically Scattered GNSS Signals From Low Earth Orbit*. University of Surrey.

Gleason, S., Hodgart, S., Sun, Y., Gommenginger, C., Mackin, S., Adjrad, M., & Unwin, M. (2005). Detection and Processing of bistatically reflected GPS signals from low Earth orbit for the purpose of ocean remote sensing. *IEEE Transactions on Geoscience and Remote Sensing*, *43*(6), 1229–1241. IEEE Transactions on Geoscience and Remote Sensing. https://doi.org/10.1109/TGRS.2005.845643

Hall, C. D., & Cordey, R. A. (1988). Multistatic Scatterometry. *International Geoscience and Remote Sensing Symposium, "Remote Sensing: Moving Toward the 21st Century"*., 561–562. International Geoscience and Remote Sensing Symposium, "Remote Sensing: Moving Toward the 21st Century". https://doi.org/10.1109/IGARSS.1988.570200

Hernández-Pajares, M., Juan, J. M., Sanz, J., & Orús, R. (2007). Second-order ionospheric term in GPS: Implementation and impact on geodetic estimates. *Journal of Geophysical Research: Solid Earth*, *112*(B8). https://doi.org/10.1029/2006JB004707

Hobiger, T., & Jakowski, N. (2017). Atmospheric Signal Propagation. In P. J. G. Teunissen & O. Montenbruck (Eds.), *Springer Handbook of Global Navigation Satellite Systems* (pp. 165–193). Springer International Publishing. https://doi.org/10.1007/978-3-319-42928-1_6

Hofmann-Wellenhof, B., Lichtenegger, H., & Wasle, E. (2008). *GNSS - Global Navigation Satellite Systems, Original text: GPS, GLONASS, Galileo, and more*. Springer-Verlag. https://doi.org/10.1007/978-3-211-73017-1

Hofmeister, A., & Böhm, J. (2017). Application of ray-traced tropospheric slant delays to geodetic VLBI analysis. *Journal of Geodesy*, *91*(8), 945–964. https://doi.org/10.1007/s00190-017-1000-7

Hopfield, H. S. (1969). Two-quartic tropospheric refractivity profile for correcting satellite data. *Journal of Geophysical Research (1896-1977)*, *74*(18), 4487–4499. https://doi.org/10.1029/JC074i018p04487

Hoque, M. M., Jakowski, N., & Berdermann, J. (2018). Positioning performance of the NTCM model driven by GPS Klobuchar model parameters. *Journal of Space Weather and Space Climate*, *8*, A20. https://doi.org/10.1051/swsc/2018009

Hoque, M. M., Jakowski, N., Osechas, O., & Berdermann, J. (2019). *Fast and Improved Ionospheric Correction for Galileo Mass Market Receivers*. 3377–3389. https://doi.org/10.33012/2019.17106

Hoque, M. M., Jakowski, N., & Prol, F. S. (2022). A new climatological electron density model for supporting space weather services. *Journal of Space Weather and Space Climate*, *12*, 1. https://doi.org/10.1051/swsc/2021044

Hoseini, M., Semmling, M., Nahavandchi, H., Rennspiess, E., Ramatschi, M., Haas, R., Strandberg, J., & Wickert, J. (2020). On the Response of Polarimetric GNSS-Reflectometry to Sea Surface Roughness. *IEEE Transactions on Geoscience and Remote Sensing*, 1–12. IEEE Transactions on Geoscience and Remote Sensing. https://doi.org/10.1109/TGRS.2020.3031396

Hoseini, M., Strand, A., & Nahavandchi, H. (2021). *Monitoring the Distribution of Ocean Microplastics using GNSS-Reflectometry Technique*. *2021*, G35A-0288. AGU Fall Meeting Abstracts.

Ichikawa, K., Zhu, J. Q., Noda, J., Sakemi, R., Yufu, K., & Matsuura, K. (2024). Ship-borne wave gauge using GNSS interferometric reflectometry. *Coastal Engineering Journal*, *66*(2), 395–404. https://doi.org/10.1080/21664250.2024.2342596

Inside GNSS. (2014, January 19). Ionospheric Scintillation. *Inside GNSS - Global Navigation Satellite Systems Engineering, Policy, and Design*. https://insidegnss.com/ionospheric-scintillation/

Issa, H., Stienne, G., Reboul, S., Raad, M., & Faour, G. (2021). Airborne GNSS Reflectometry for Water Body Detection. *Remote Sensing*, *14*, 163. https://doi.org/10.3390/rs14010163

Jaberi Shafei, M., & Mashhadi-Hossainali, M. (2018). Application of the GNSS-R in tomographic sounding of the Earth atmosphere. *Advances in Space Research*, *62*(1), 71–83. https://doi.org/10.1016/j.asr.2018.04.003

Jakowski, N. (2017). Ionosphere Monitoring. In P. J. G. Teunissen & O. Montenbruck (Eds.), *Springer Handbook of Global Navigation Satellite Systems* (pp. 1139–1162). Springer International Publishing. https://doi.org/10.1007/978-3-319-42928-1_39

Jakowski, N., Heise, S., Wehrenpfennig, A., & Schlüter, S. (2001). TEC monitoring by GPS - a possible contribution to space weather monitoring. *Physics and Chemistry of the Earth, Part C: Solar, Terrestrial & Planetary Science*, *26*(8), 609–613. https://doi.org/10.1016/S1464-1917(01)00056-3

Jakowski, N., Hoque, M. M., & Mayer, C. (2011). A new global TEC model for estimating transionospheric radio wave propagation errors. *Journal of Geodesy*, *85*(12), 965–974. https://doi.org/10.1007/s00190-011-0455-1

Jin, S., Camps, A., Jia, Y., Wang, F., Martin-Neira, M., Huang, F., Yan, Q., Zhang, S., Li, Z., Edokossi, K., Yang, D., Xiao, Z., Ma, Z., & Bai, W. (2024). Remote sensing and its applications using GNSS reflected signals: Advances and prospects. *Satellite Navigation*, *5*(1), 19. https://doi.org/10.1186/s43020-024-00139-4

Jin, S., Cardellach, E., & Xie, F. (2014). *GNSS Remote Sensing: Theory, Methods and Applications*. Springer Netherlands. https://doi.org/10.1007/978-94-007-7482-7

Jing, C., Niu, X., Duan, C., Lu, F., Di, G., & Yang, X. (2019). Sea Surface Wind Speed Retrieval from the First Chinese GNSS-R Mission: Technique and Preliminary Results. *Remote Sensing*, *11*(24), Article 24. https://doi.org/10.3390/rs11243013

Juang, J.-C. (2023). Determination and Sensitivity Analysis of the Specular Reflection Point in GNSS Reflectometry. *IEEE Journal of Selected Topics in Applied Earth Observations and Remote Sensing*, *16*, 974–982. IEEE Journal of Selected Topics in Applied Earth Observations and Remote Sensing. https://doi.org/10.1109/JSTARS.2022.3233044

Juang, J.-C., Ma, S.-H., & Lin, C.-T. (2016). Study of GNSS-R Techniques for FORMOSAT Mission. *IEEE Journal of Selected Topics in Applied Earth Observations and Remote Sensing*, *9*(10), 4582–4592. IEEE Journal of Selected Topics in Applied Earth Observations and Remote Sensing. https://doi.org/10.1109/JSTARS.2016.2575069

Katzberg, S. J., & Garrison, J. L. (1996). *Utilizing GPS to Determine Ionospheric Delay over the Ocean* (No. NAS 1.15:4750). NASA Langley Research Center, Hampton, VA, USA.

Klobuchar, J. A. (1987). Ionospheric Time-Delay Algorithm for Single-Frequency GPS Users. *IEEE Transactions on Aerospace and Electronic Systems*, *AES-23*(3), 325–331. IEEE Transactions on Aerospace and Electronic Systems. https://doi.org/10.1109/TAES.1987.310829

Komjathy, A., Armatys, M., Masters, D., Axelrad, P., Zavorotny, V., & Katzberg, S. (2004). Retrieval of Ocean Surface Wind Speed and Wind Direction Using Reflected GPS Signals. *Journal of Atmospheric and Oceanic Technology*, *21*(3), 515–526. https://doi.org/10.1175/1520-0426(2004)021<0515:ROOSWS>2.0.CO;2

Komjathy, A., Garrison, J. L., & Zavorotny, V. (2001). GPS: A New Tool for Ocean Science. *GPS World Magazine*, *10*(4), 50–56.

Komjathy, A., Zavorotny, V. U., Axelrad, P., Born, G. H., & Garrison, J. L. (2000). GPS Signal Scattering from Sea Surface. *Remote Sensing of Environment*, *73*(2), 162–174. https://doi.org/10.1016/S0034-4257(00)00091-2

Lagler, K., Schindelegger, M., Böhm, J., Krásná, H., & Nilsson, T. (2013). GPT2: Empirical slant delay model for radio space geodetic techniques. *Geophysical Research Letters*, *40*(6), 1069–1073. https://doi.org/10.1002/grl.50288

Landskron, D., & Böhm, J. (2018). VMF3/GPT3: Refined discrete and empirical troposphere mapping functions. *Journal of Geodesy*, *92*(4), 349–360. https://doi.org/10.1007/s00190-017-1066-2

Larson, K. M., Small, E. E., Gutmann, E., Bilich, A., Axelrad, P., & Braun, J. (2008). Using GPS multipath to measure soil moisture fluctuations: Initial results. *GPS Solutions*, *12*(3), 173–177. https://doi.org/10.1007/s10291-007-0076-6

Leandro, R., Santos, M., & Langley, R. (2006). *UNB Neutral Atmosphere Models: Development and Performance*. *2*.

Li, W., Cardellach, E., Fabra, F., Rius, A., Ribó, S., & Martín-Neira, M. (2017). First spaceborne phase altimetry over sea ice using TechDemoSat-1 GNSS-R signals. *Geophysical Research Letters*, *44*(16), 8369–8376. https://doi.org/10.1002/2017GL074513

Liu, L., Morton, Y. J., Wang, Y., & Wu, K.-B. (2022). Arctic TEC Mapping Using Integrated LEO-Based GNSS-R and Ground-Based GNSS Observations: A Simulation Study. *IEEE Transactions on Geoscience and Remote Sensing*, *60*, 1–10. IEEE Transactions on Geoscience and Remote Sensing. https://doi.org/10.1109/TGRS.2021.3138692

Maheshwari, M., & Nirmala, S. (2018). IRNSS Ionosphere Modelling for Single Frequency Receiver using Data Ingestion Technique. *2018 4th International Conference for Convergence in Technology (I2CT)*, 1–5. https://doi.org/10.1109/I2CT42659.2018.9058028

Mannucci, A. J., Ao, C. O., & Williamson, W. (2020). GNSS Radio Occultation. In *Position, Navigation, and Timing Technologies in the 21st Century* (pp. 971–1013). John Wiley & Sons, Ltd. https://doi.org/10.1002/9781119458449.ch33

Marini, J. W. (1972). Correction of Satellite Tracking Data for an Arbitrary Tropospheric Profile. *Radio Science*, *7*(2), 223–231. https://doi.org/10.1029/RS007i002p00223

Martín-Neira, M. (1993). A Passive Reflectometry and Interferometry System (PARIS): Application to ocean altimetry. *ESA Journal*, *17*, 331–355.

Martín-Neira, M., Caparrini, M., Font-Rossello, J., Lannelongue, S., & Vallmitjana, C. S. (2001). The PARIS concept: An experimental demonstration of sea surface altimetry using GPS reflected signals. *IEEE Transactions on Geoscience and Remote Sensing*, *39*(1), 142–150. IEEE Transactions on Geoscience and Remote Sensing. https://doi.org/10.1109/36.898676

Mashburn, J., Axelrad, P., Lowe, S. T., & Larson, K. M. (2018). Global Ocean Altimetry With GNSS Reflections From TechDemoSat-1. *IEEE Transactions on Geoscience and Remote Sensing*, *56*(7), 4088–4097. IEEE Transactions on Geoscience and Remote Sensing. https://doi.org/10.1109/TGRS.2018.2823316

Masters, D. (2019). Design and planning for the first spire GNSS-R missions of 2019. *IEEE GRSS, Spec. Meeting Reflectometry Using GNSS Other Signals Opportunity*. IEEE GNSS+R, Benevento, Italy.

Molina, C., & Camps, A. (2020). First Evidences of Ionospheric Plasma Depletions Observations Using GNSS-R Data from CYGNSS. *Remote Sensing*, *12*(22), Article 22. https://doi.org/10.3390/rs12223782

Morton, Y. J., Yang, Z., Breitsch, B., Bourne, H., & Rino, C. (2020). Ionospheric Effects, Monitoring, and Mitigation Techniques. In *Position, Navigation, and Timing Technologies in the 21st Century* (pp. 879–937). John Wiley & Sons, Ltd. https://doi.org/10.1002/9781119458449.ch31

Morton, Y. T. J., van Diggelen, F., Spilker Jr., J. J., Parkinson, B. W., Lo, S., & Gao, G. (2020). *Position, Navigation, and Timing Technologies in the 21st Century* (1st ed.). John Wiley & Sons, Ltd. https://doi.org/10.1002/9781119458555

Munoz-Martin, J. F., Miguelez, N., Castella, R., Fernandez, L., Solanellas, A., Via, P., & Camps, A. (2018). 3Cat-4: Combined GNSS-R, L-Band Radiometer with RFI Mitigation, and AIS Receiver for a I-Unit Cubesat Based on Software Defined Radio. *IGARSS 2018 - 2018 IEEE International Geoscience and Remote Sensing Symposium*, 1063–1066. https://doi.org/10.1109/IGARSS.2018.8519037

Munoz-Martin, J. F., Perez, A., Camps, A., Ribó, S., Cardellach, E., Stroeve, J., Nandan, V., Itkin, P., Tonboe, R., Hendricks, S., Huntemann, M., Spreen, G., & Pastena, M. (2020). Snow and Ice Thickness Retrievals Using GNSS-R: Preliminary Results of the MOSAiC Experiment. *Remote Sensing*, *12*(24), Article 24. https://doi.org/10.3390/rs12244038

Nava, B., Coïsson, P., & Radicella, S. M. (2008). A new version of the NeQuick ionosphere electron density model. *Journal of Atmospheric and Solar-Terrestrial Physics*, *70*(15), 1856–1862. https://doi.org/10.1016/j.jastp.2008.01.015

Nikolaidou, T., Santos, M. C., Williams, S. D. P., & Geremia-Nievinski, F. (2020). Raytracing atmospheric delays in ground-based GNSS reflectometry. *Journal of Geodesy*, *94*(8), 68. https://doi.org/10.1007/s00190-020-01390-8

Regmi, A., Hänninen, T., Leinonen, M. E., Pärssinen, A., & Berg, M. (2021). Dynamic Dual Polarized GNSS Reflectometry Using UAV. *2021 15th European Conference on Antennas and Propagation (EuCAP)*, 1–5. https://doi.org/10.23919/EuCAP51087.2021.9411371

Reigber, Ch., Lühr, H., & Schwintzer, P. (2002). CHAMP mission status. *Advances in Space Research*, *30*(2), 129–134. https://doi.org/10.1016/S0273-1177(02)00276-4

Ren, X., Liu, H., Zhang, J., Mei, D., & Zhang, X. (2022). An Improved Method for Ionospheric TEC Estimation Using the Spaceborne GNSS-R Observations. *IEEE Transactions on Geoscience and Remote Sensing*, *60*, 1–12. IEEE Transactions on Geoscience and Remote Sensing. https://doi.org/10.1109/TGRS.2022.3192983

Roberts, T. M., Colwell, I., Chew, C., Lowe, S., & Shah, R. (2022). A Deep-Learning Approach to Soil Moisture Estimation with GNSS-R. *Remote Sensing*, *14*(14), Article 14. https://doi.org/10.3390/rs14143299

Ruf, C., McKague, D., Posselt, D., Gleason, S., Clarizia, M.-P., Zavorotny, V., & Butler, T. (2022). *CYGNSS Handbook*. Michigan Publishing Services. https://doi.org/10.3998/mpub.12741920

Ruf, C. S., Atlas, R., Chang, P. S., Clarizia, M. P., Garrison, J. L., Gleason, S., Katzberg, S. J., Jelenak, Z., Johnson, J. T., Majumdar, S. J., O'brien, A., Posselt, D. J., Ridley, A. J., Rose, R. J., & Zavorotny, V. U. (2016). *New Ocean Winds Satellite Mission to Probe Hurricanes and Tropical Convection*. https://doi.org/10.1175/BAMS-D-14-00218.1

Saastamoinen, J. (1973). Contributions to the theory of atmospheric refraction. *Bulletin Géodésique (1946-1975)*, *107*(1), 13–34. https://doi.org/10.1007/BF02522083

Santamaría-Gómez, A., & Watson, C. (2017). Remote leveling of tide gauges using GNSS reflectometry: Case study at Spring Bay, Australia. *GPS Solutions*, *21*(2), 451–459. https://doi.org/10.1007/s10291-016-0537-x

Semmling, A. M., Beckheinrich, J., Wickert, J., Beyerle, G., Schön, S., Fabra, F., Pflug, H., He, K., Schwabe, J., & Scheinert, M. (2014). Sea surface topography retrieved from GNSS reflectometry phase data of the GEOHALO flight mission. *Geophysical Research Letters*, *41*(3), 954–960. https://doi.org/10.1002/2013GL058725

Semmling, A. M., Leister, V., Saynisch, J., Zus, F., Heise, S., & Wickert, J. (2016). A Phase-Altimetric Simulator: Studying the Sensitivity of Earth-Reflected GNSS Signals to Ocean Topography. *IEEE Transactions on Geoscience and Remote Sensing*, *54*(11), 6791–6802. IEEE Transactions on Geoscience and Remote Sensing. https://doi.org/10.1109/TGRS.2016.2591065

Semmling, A. M., Schmidt, T., Wickert, J., Schön, S., Fabra, F., Cardellach, E., & Rius, A. (2012). On the retrieval of the specular reflection in GNSS carrier observations for ocean altimetry. *Radio Science*, *47*(6). https://doi.org/10.1029/2012RS005007

Subirana, J. S., Hernández-Pajares, M., & Zornoza, J. M. J. (2013). *GNSS Data Processing*. ESA Communications.

Sun, Y., Huang, F., Xia, J., Yin, C., Bai, W., Du, Q., Wang, X., Cai, Y., Li, W., Yang, G., Zhai, X., Xu, N., Hu, X., Liu, Y., Liu, C., Wang, D., Qiu, T., Tian, Y., Duan, L., … Song, D. (2023). GNOS-II on Fengyun-3 Satellite Series: Exploration of Multi-GNSS Reflection Signals for Operational Applications. *Remote Sensing*, *15*(24), Article 24. https://doi.org/10.3390/rs15245756

Tapley, B. D., Bettadpur, S., Watkins, M., & Reigber, C. (2004). The gravity recovery and climate experiment: Mission overview and early results. *Geophysical Research Letters*, *31*(9). https://doi.org/10.1029/2004GL019920

Teunissen, P. J. G., & Montenbruck, O. (Eds.). (2017). *Springer Handbook of Global Navigation Satellite Systems*. Springer International Publishing. https://doi.org/10.1007/978-3-319-42928-1

Treuhaft, R. N., Lowe, S. T., Zuffada, C., & Chao, Y. (2001). 2-cm GPS altimetry over Crater Lake. *Geophysical Research Letters*, *28*(23), 4343–4346. https://doi.org/10.1029/2001GL013815

Unwin, M. J., Pierdicca, N., Cardellach, E., Rautiainen, K., Foti, G., Blunt, P., Guerriero, L., Santi, E., & Tossaint, M. (2021). An Introduction to the HydroGNSS GNSS Reflectometry Remote Sensing Mission. *IEEE Journal of Selected Topics in Applied Earth Observations and Remote Sensing*, *14*, 6987–6999. IEEE Journal of Selected Topics in Applied Earth Observations and Remote Sensing. https://doi.org/10.1109/JSTARS.2021.3089550

Unwin, M., Jales, P., Tye, J., Gommenginger, C., Foti, G., & Rosello, J. (2016). Spaceborne GNSS-Reflectometry on TechDemoSat-1: Early Mission Operations and Exploitation. *IEEE Journal of Selected Topics in Applied Earth Observations and Remote Sensing*, *9*(10), 4525–4539. IEEE Journal of Selected Topics in Applied Earth Observations and Remote Sensing. https://doi.org/10.1109/JSTARS.2016.2603846

Wang, T., Zavorotny, V. U., Johnson, J., Ruf, C., & Yi, Y. (2018). Modeling of Sea State Conditions for Improvement of Cygnss L2 Wind Speed Retrievals. *IGARSS 2018 - 2018 IEEE International Geoscience and Remote Sensing Symposium*, 8288–8291. https://doi.org/10.1109/IGARSS.2018.8518686

Wang, Y. (2023). Troposphere Sensing Using Grazing-Angle GNSS-R Measurement From LEO Satellites. *Geophysical Research Letters*, *50*(24), e2023GL106249. https://doi.org/10.1029/2023GL106249

Wang, Y., Breitsch, B., & Morton, Y. T. J. (2021). A State-Based Method to Simultaneously Reduce Cycle Slips and Noise in Coherent GNSS-R Phase Measurements From Open-Loop Tracking. *IEEE Transactions on Geoscience and Remote Sensing*, *59*(10), 8873–8884. IEEE Transactions on Geoscience and Remote Sensing. https://doi.org/10.1109/TGRS.2020.3036031

Wang, Y., & Morton, Y. J. (2021). Evaluation of GNSS-R Retrieved Sea Ice Surface Height Using ICESat-2 Ice Freeboard Measurements. *2021 IEEE International Geoscience and Remote Sensing Symposium IGARSS*, 7803–7806. https://doi.org/10.1109/IGARSS47720.2021.9554623

Wang, Y., & Morton, Y. J. (2022). Ionospheric Total Electron Content and Disturbance Observations From Space-Borne Coherent GNSS-R Measurements. *IEEE Transactions on Geoscience and Remote Sensing*, *60*, 1–13. IEEE Transactions on Geoscience and Remote Sensing. https://doi.org/10.1109/TGRS.2021.3093328

Wickert, J., Cardellach, E., Martín-Neira, M., Bandeiras, J., Bertino, L., Andersen, O. B., Camps, A., Catarino, N., Chapron, B., Fabra, F., Floury, N., Foti, G., Gommenginger, C., Hatton, J., Høeg, P., Jäggi, A., Kern, M., Lee, T., Li, Z., … Zuffada, C. (2016).

GEROS-ISS: GNSS REflectometry, Radio Occultation, and Scatterometry Onboard the International Space Station. *IEEE Journal of Selected Topics in Applied Earth Observations and Remote Sensing*, *9*(10), 4552–4581. IEEE Journal of Selected Topics in Applied Earth Observations and Remote Sensing. https://doi.org/10.1109/JSTARS.2016.2614428

Wickert, J., Michalak, G., Schmidt, T., Beyerle, G., Cheng, C. Z., Healy, S. B., Heise, S., Huang, C. Y., Jakowski, N., Kohler, W., Mayer, C., Offiler, D., Ozawa, E., Pavelyev, A. G., Rothacher, M., Tapley, B., & Arras, C. (2009). GPS Radio Occultation: Results from CHAMP. GRACE and FORMOSAT-3/COSMIC. *Terrestrial, Atmospheric and Oceanic Sciences*, *20*(1), 35–50. https://doi.org/10.3319/TAO.2007.12.26.01(F3C)

Williams, S. D. P., & Nievinski, F. G. (2017). Tropospheric delays in ground-based GNSS multipath reflectometry—Experimental evidence from coastal sites. *Journal of Geophysical Research: Solid Earth*, *122*(3), 2310–2327. https://doi.org/10.1002/2016JB013612

Xing, J., Datta-Barua, S., Garrison, J., Ridley, A., & Pervan, B. (2015). Relative Ionospheric Ranging Delay in LEO GNSS Oceanic Reflections. *IEEE Geoscience and Remote Sensing Letters*, *12*(7), 1416–1420. IEEE Geoscience and Remote Sensing Letters. https://doi.org/10.1109/LGRS.2015.2404912

Yan, Q., & Huang, W. (2019). Sea Ice Remote Sensing Using GNSS-R: A Review. *Remote Sensing*, *11*(21), Article 21. https://doi.org/10.3390/rs11212565

Yu, K. (2021). *Theory and Practice of GNSS Reflectometry* (Vol. 9). Springer. https://doi.org/10.1007/978-981-16-0411-9

Yuan, Y., Wang, N., Li, Z., & Huo, X. (2019). The BeiDou global broadcast ionospheric delay correction model (BDGIM) and its preliminary performance evaluation results. *NAVIGATION*, *66*(1), 55–69. https://doi.org/10.1002/navi.292

Zavorotny, V. U., & Voronovich, A. G. (2000). Scattering of GPS signals from the ocean with wind remote sensing application. *IEEE Transactions on Geoscience and Remote Sensing*, *38*(2), 951–964. IEEE Transactions on Geoscience and Remote Sensing. https://doi.org/10.1109/36.841977

Zus, F., Bender, M., Deng, Z., Dick, G., Heise, S., Shang-Guan, M., & Wickert, J. (2012). A methodology to compute GPS slant total delays in a numerical weather model. *Radio Science*, *47*(2). https://doi.org/10.1029/2011RS004853

Appended Publications

remote sensing

MDPI

Article

Airborne Coherent GNSS Reflectometry and Zenith Total Delay Estimation over Coastal Waters

Mario Moreno [1,*], Maximilian Semmling [1], Georges Stienne [2], Wafa Dalil [2], Mainul Hoque [1], Jens Wickert [3,4] and Serge Reboul [2]

[1] German Aerospace Centre, Institute of Solar-Terrestrial Physics (DLR-SO), Kalkhorstweg 53, 17235 Neustrelitz, Germany
[2] Laboratoire d'Informatique, Signal et Image de la Côte d'Opale (LISIC), Université Littoral Côte d'Opale (ULCO), 50 rue Ferdinand Buisson, 62228 Calais, France
[3] German Research Centre for Geosciences (GFZ), Wissenschaftpark "Albert Einstein", Telegrafenberg, 14473 Potsdam, Germany
[4] Institute of Geodesy and Geoinformation Science, Department of GNSS Remote Sensing, Navigation and Positioning, Technical University of Berlin (TUB), Str. des 17. Juni 135, 10623 Berlin, Germany
* Correspondence: mario.moreno@dlr.de

Abstract: High-precision GNSS (global navigation satellite e system) measurements can be used for remote sensing and nowadays play a significant role in atmospheric sounding (station data, radio occultation observations) and sea surface altimetry based on reflectometry. A limiting factor of high-precision reflectometry is the loss of coherent phase information due to sea-state-induced surface roughness. This work studies airborne reflectometry observations recorded over coastal waters to examine the sea-state influence on Doppler distribution and the coherent residual phase retrieval. From coherent observations, the possibility of zenith total delay inversion is also investigated, considering the hydrostatic mapping factor from the Vienna mapping function and an exponential vertical decay factor depending on height receiver changes. The experiment consists of multiple flights performed along the coast between the cities of Calais and Boulogne-sur-Mer, France, in July 2019. Reflected signals acquired in a right-handed circular polarization are processed through a model-aided software receiver and passed through a retracking module to obtain the Doppler and phase-corrected signal. Results from grazing angle observations (elevation < 15°) show a high sensitivity of Doppler spread with respect to sea state with correlations of 0.75 and 0.88 with significant wave height and wind speed, respectively. An empirical Doppler spread threshold of 0.5 Hz is established for coherent reflections supported by the residual phase observations obtained. Phase coherence occurs in 15% of the observations; however, the estimated zenith total delay for the best event corresponds to 2.44 m, which differs from the typical zenith total delay (2.3 m) of 5%.

Keywords: GNSS reflectometry; sea state; Doppler spreading; zenith total delay; coastal zones

Citation: Moreno, M.; Semmling, M.; Stienne, G.; Dalil, W.; Hoque, M.; Wickert, J.; Reboul, S. Airborne Coherent GNSS Reflectometry and Zenith Total Delay Estimation over Coastal Waters. *Remote Sens.* **2022**, *14*, 4628. https://doi.org/10.3390/rs14184628

Academic Editors: Shuanggen Jin and Vladislav Demyanov

Received: 15 July 2022
Accepted: 14 September 2022
Published: 16 September 2022

1. Introduction

Climate change is one of the foremost topics of study within many fields in the scientific community. Different studies have been carried out in recent decades to determine the possible risks and hazards and their impact on humans and their environments. One of the most important parameters for climate change monitoring is the variability and changes in oceanic waters, particularly in coastal areas. There are two main parameters investigated in coastal sea surface variability. First, the sea-level change is primarily caused by global warming, which generates thermal expansion due to increasing seawater temperatures, the melting of sea ice and glaciers, and the loss of the terrestrial ice mass in Greenland and Antarctica [1]. Second, the sea state is the description of waves generated by the wind, including their height, direction, and period [2], where the wind–wave component can represent considerable changes in sea level along coasts [3,4].

Common techniques for sea-level and sea-state monitoring comprise tide gauges and buoys that generate precise in situ observations but sparse coverage and, therefore, limited spatial resolution. For global scale, satellite altimetric missions with temporal resolution between 6 and 12 days allow high-accuracy sea-level data in open water but reduced performance in coastal zones due to specific wind–wave influence on the sea surface and the combination of sea waters and land at shorelines [5]. In 1993, the European Space Agency (ESA) proposed a multistatic radar concept that relies on the use of global navigation satellite system (GNSS) signals with an interferometric approach, combining the direct signal with the signals reflected off the Earth's surface to retrieve sea surface height [6]. This technique is called nowadays GNSS reflectometry (GNSS-R). Figure 1 depicts a schematic representation of GNSS-R.

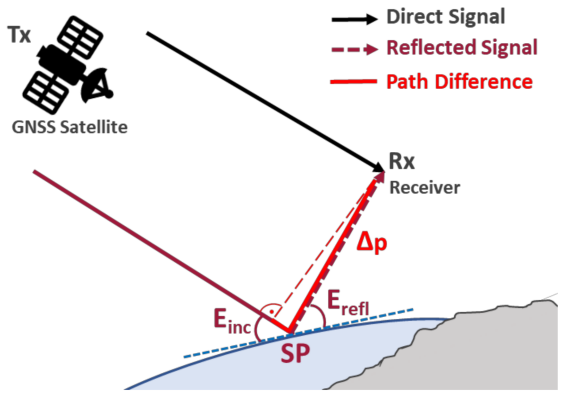

Figure 1. Scheme of GNSS-R configuration. T_x is the GNSS satellite transmitter. R_x is the receiver installed in a ground-based or moving platform. E_{inc} and E_{refl} are the satellite incident and reflected elevation angles. The reflection point where the incident and reflected angle are the same is called the specular point SP. Δ_p is the excess path that the reflected signal travels with respect to the direct signal.

Currently, GNSS-R has shown the capability of retrieving not only sea surface height [7–9], but also further applications, such as sea ice [10–12] and soil moisture detection [13–15]. For sea-state retrievals, represented by wind speed (WS) and significant wave height (SWH), different methods have been proposed in the literature. For example, in [16], the WS is retrieved by relating the waveforms (delay mapping) of the reflected signals to mean square slopes, which are comprised in a theoretical model from a bistatic radar equation (BRE). As the Doppler spreading effect impacts significantly the sea-state retrievals, for more accurate measurements, the paper also suggested the use of one of the main observables in GNSS-R, the delay–Doppler map (DDM), which represents the scattered power as a function of the time delay and Doppler frequency shift. Consequently, multiple studies have investigated the relation of the DDM and the sea surface roughness from ground-based experiments [17,18] or using satellite reflectometry data [19,20].

Water-surface-level monitoring is also a topic widely studied in GNSS-R. Mainly, determining the reflecting surface height requires modeling the interaction of the reflected signal with the water surface, modeling the signal propagation when passing through the atmosphere, and comparison between the observations and the modeled or ancillary data. The signal propagation modeling comprises a signal delay as electromagnetic waves pass through the atmosphere due to changes in medium density. The troposphere accounts for approximately 80% of the atmospheric delay, which is referred to as tropospheric delay. For coastal sea-level studies, from ground-based data, the tropospheric delay has been commonly disregarded apparently because of the lack or insignificant tropospheric effect seen in the data due to the small height of the reflecting surface. However, based on the results in [21], the correction of tropospheric delay is strongly advised regardless of the antenna height with respect to the sea surface, as it represents a scale error in the

measurements. The correction of tropospheric delays has been applied in GNSS-R altimetry retrievals in different studies. In [22], tropospheric correction was carried out by ray tracing using atmospheric refractivity profiles. A complementary approach was used in [23] for ray tracing the tropospheric refraction over a spherical Earth. In [24], a combination of zenith delay from GNSS positioning and Neill's mapping function was implemented for tropospheric delay corrections. From airborne data, an improvement of about 0.7 m was found in the sea surface height inversion in [25] after removing the tropospheric delay based on the model proposed in [26].

This study examines the occurrence of high-precision phase delay information for airborne reflectometry based on the Doppler spreading estimations under the condition of various sea states in coastal waters. In addition, the paper investigates the possibility of inversion of the zenith total delay at the reflecting surface level from coherent observations and using the Vienna mapping function. Multiple flights were conducted along Opal Coast between the cities of Calais and Boulogne-sur-Mer, France, in the North Sea. A software receiver based on [27] processes the direct and reflected signals. The reflected signals are retracked, aided by the signal path difference between the direct and reflected links retrieved from a specular reflection geometrical model [28]. The residual phase observable is computed from the I and Q components of the retracked signal, and the power spectral density (PSD) allows us to obtain the residual Doppler shift to estimate the Doppler spread, which is closely related to the randomness of ocean waves [29]. The inversion of the zenith total delay comprises the linear regression of the coherent residual phase on the hydrostatic mapping factor multiplied by an exponential vertical decay part depending on height receiver changes.

The paper is organized as follows: Section 2 describes the experiment conducted in July 2019. It includes the study area description and the used platform and antenna setup. Section 3 contains the data set collected, the methods implemented, and the processing steps. Section 4 presents the result analyzing the sea-state conditions and the Doppler spread limit considered for coherent observations. Finally, Section 5 discusses the findings, limitations, and possible further applications based on the presented methodology.

2. Experiment

An airborne GNSS-R measurement campaign was carried out in July 2019. Four flights following the same trajectory were performed on the 12th, 15th, 17th, and 19th along the Opal Coast in the North Sea between the cities of Calais and Boulogne-sur-Mer, France. The total length trajectory over the ocean was ~95 km with a duration of ~1 h each flight. To ensure a transmitter–surface–receiver geometry that includes most of the reflection measurements over the sea surface and near the coast, GPS signals coming from the westward direction (azimuths between 180° and 360°) were selected for the analysis. Besides, due to the loss of most of the GPS satellites in the tracking step along the west-to-east flight segment or insufficient reflection events over the sea surface, the north-to-south segment was analyzed in this study (highlighted in orange in Figure 2, right). In the north-to-south flight segment, it was possible to retrieve continuous reflection tracks from the chosen satellites G1, G7, G8, G10, G11, G16, G18, and G30.

The sea-state variations in the study area, given by the mean value of wind speed (WS), wind directions, and significant wave height (SWH), are presented in Table 1. These parameters are obtained from the ECMWF ERA5 model along the flight trajectory. The lowest sea state can be observed on 17 July 2019.

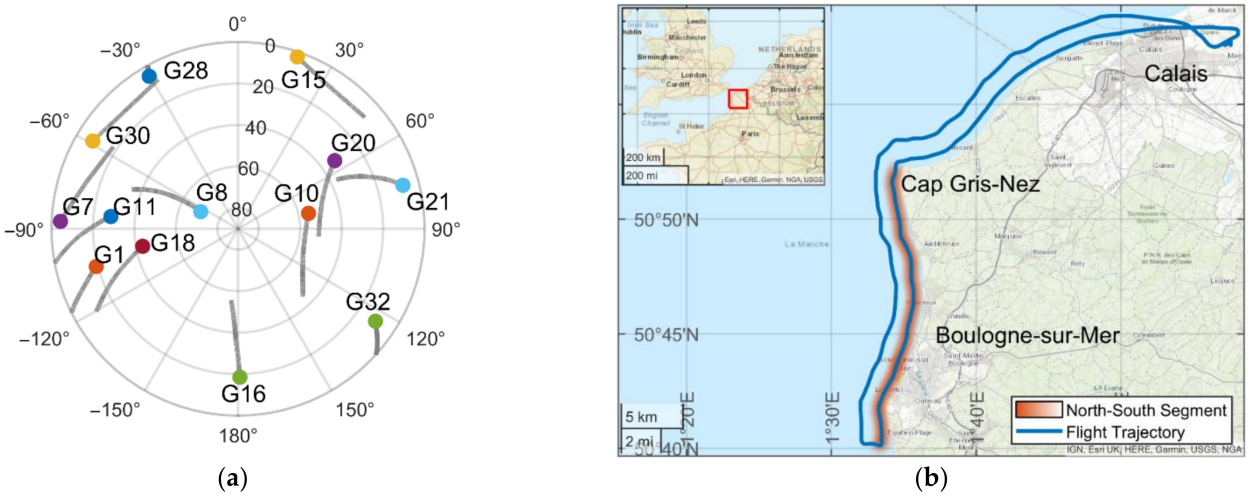

(**a**) (**b**)

Figure 2. (**a**) GPS satellites' sky plot at Cap Gris-Nez on 17 July 2019. (**b**) Experiment location and flight trajectory from Calais to Boulogne-sur-Mer. The flight trajectory consisted of two legs, one at 700 m from the coastline and the second at 2000 m.

Table 1. Sea-state parameters during the measurement campaign.

Date	Wind Speed (m/s)	Wind Direction (deg)	SWH (m)
12 July 2019	5.49	117	0.30
15 July 2019	4.29	67	0.58
17 July 2019	2.92	204	0.26
19 July 2019	6.50	240	0.55

The used platform was a gyrocopter, an ultralight and very stable aircraft. The flight altitude was ~780 m above sea level at a speed of ~90 km/h. The setup consisted of one antenna to acquire the direct and the reflected signal in a right-handed circular polarization (RHCP) similarly as presented in [30]. The antenna was linked to two receivers: a Syntony Echo-L receiver for the record of raw GPS L1 signals used for reflectometry and a Javad Delta GNSS receiver for the record of RINEX messages for precise trajectory solution in postprocessing. The antenna was mounted on the aircraft tilted ~43° with respect to the zenith direction, as it is shown in Figure 3.

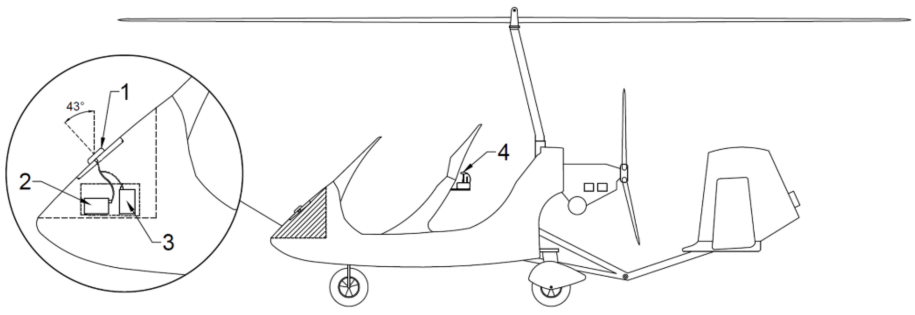

Figure 3. Antenna setup on board of the aircraft. (1) Right-hand circular polarized GNSS antenna, (2) receiver for reflectometry, (3) receiver for navigation, and (4) Extra GPS+INS Drone flight control.

3. GNSS-R Data and Methods

3.1. Data and Processing

The receiver Syntony Echo-L is capable of recording GPS L1 signals sampled at a frequency of 16.368 MHz. Four raw datasets were obtained for each day and classified

as data level 0. The duration of each set was ~18 min, which corresponded to the north-to-south segment of the trajectory to obtain reflection points on the sea surface from GPS satellites located in the west-side sky. Data level 1 included the complex direct and reflected signals, that is, the in-phase (I) and quadrature (Q) components after the tracking and retracking process at a rate of 50 Hz. Data level 2 comprised the power peak, and relative Doppler shift and Doppler spread $\left(\sigma_f\right)$ estimates of the residual reflected signal every 10 s from the power spectral density. The processing flowchart is shown in Figure 4.

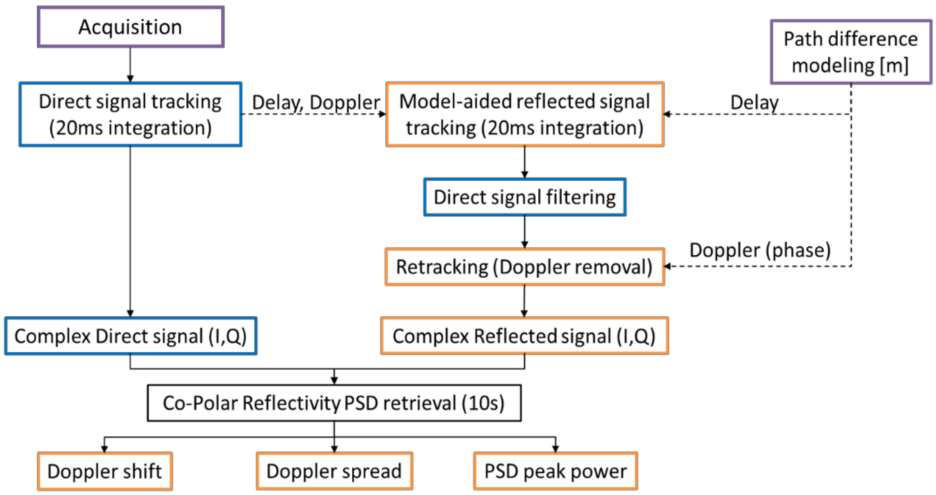

Figure 4. Signal processing flowchart.

3.1.1. Geometrical Path Difference Model

The specular point positions and the path difference between the direct and reflected signals are derived according to [23]. A geometrical model is implemented to characterize specular reflections considering surface curvature. This model requires the transmitter (T_x) and receiver (R_x) positions in an Earth-centered Earth-fixed (ECEF) frame. The T_x position is calculated from the broadcasted ephemeris. The R_x position is calculated by postprocessing using the nearby permanent GNSS antennas of the French National Institute of Geographic and Forest Information (IGN) network as reference stations. The Earth's curvature is modeled assuming a spherical surface. The latter is associated with the osculation sphere tangent to the ellipsoid World Geodetic System 1984 (WGS-84) in a reference specular point. From this point, an iterative process using different concentric sea levels (osculating spheres radii) is set until finding the sphere that best fits with the ellipsoid and satisfies that the incident angle equals the reflected angle (specular reflection). Once the final specular point (SP) is defined, a geoid undulation correction is applied using the EIGEN-6C2 model [31]. The link $T_x - SP - R_x$ is established as the reflected path L^R. The direct path is modeled from the $T_x - R_x$ link and is defined as L^D.

The path difference is given by the residual between the reflected and direct path, $\Delta_p(t) = L^R(t) - L^D(t)$, with changes over time mainly influenced by the passage of the GNSS satellite changing its elevation and the aircraft trajectory. Tropospheric and ionospheric delay corrections are disregarded for the geometrical path model. The optical path considering tropospheric delay using the International Standard Atmosphere parameters is implemented for the residual phase analysis in Section 4.2. Figure 5 shows the tracks of specular points retrieved from the geometrical difference path model on July 17 for the 8 satellites analyzed.

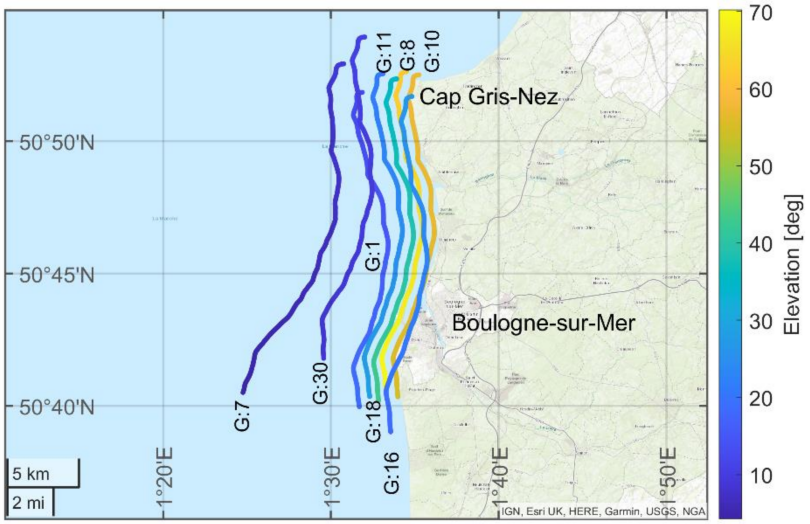

Figure 5. Specular point tracks for satellites 1, 7, 8, 10, 11, 16, 18, and 30 in the north-to-south segment from Cap Gris-Nez and Boulogne-sur-Mer on 17 July.

Considering a smooth reflecting surface, the spatial resolution of GNSS-R measurement can be linked to the first Fresnel zone [32]. The footprint associated with the first Fresnel zone is the active scattering region where most of the energy is reflected. The size of this ellipsoidal footprint is given by its major and minor axes, depending on the GPS L1 wavelength, satellite elevation, and receiver height [33]. In this experiment, the major and minor axes correspond to 950 and 55 m, respectively, for satellite elevation angles of 4°. For elevation angles of 70°, the axes correspond to 14 and 13 m, respectively.

3.1.2. Tracking and Retracking

The software receiver is constructed according to [27] to derive the in-phase and quadrature components of the reflected signal , I_0^R and Q_0^R, after the tracking stage (Equations (1)–(8) may be found in [27] with changes in notation). The direct and reflected signal, S^D and S^R, respectively, are defined by:

$$S^D = A^D CA\Big(t - \tau^D(t)\Big) \sin\Big(2\pi f^D t - \phi^D(t)\Big) + \eta^D(t) \tag{1}$$

$$S^R = A^R CA\Big(t - \tau^D(t) - \Delta_p(t)/c\Big) \sin\Big(2\pi f^D t - \phi^D(t) - \psi(t)\Big) + \eta^R(t) \tag{2}$$

where the amplitudes of the direct and reflected signal are given by A^D and A^R. CA is the code-division multiple access (CDMA) broadcasted by the GPS satellites. The code delay of the direct signal is represented by τ^D, and f^D and ϕ^D are the frequency and phase delay. η^D and η^R are zero-mean Gaussian noises. The path difference between the direct and reflected signal is represented by Δ_p, and c is the speed of light. The difference in the phase between the direct and reflected signal is denoted by ψ.

The tracking module processes the signals by means of delay, phase, and frequency locked tracking loops (DLL, PLL, and FLL) with an integration time of 20 ms. Refined estimates of τ^D, f^D, and ϕ^D are provided after the tracking of the direct signal. With the estimates, the local replica of the direct signal is constructed and expressed by the in-phase and quadrature components as follows:

$$p^{I,D}(t) = CA\Big(t - \tau^D(t)\Big) \sin\Big(2\pi f^D t - \phi^D(t)\Big) \tag{3}$$

$$p^{Q,D}(t) = CA\Big(t - \tau^D(t)\Big) \cos\Big(2\pi f^D t - \phi^D(t)\Big) \tag{4}$$

After the demodulation of the reflected signal with the local replica of the direct signal, its components, I_0^R and Q_0^R, can be obtained by:

$$I_0^R = \int_{k\ T_c}^{(k+1)T_c} S^R(t) p^{I,D}(t) dt \tag{5}$$

$$Q_0^R = \int_{k\ T_c}^{(k+1)T_c} S^R(t) p^{Q,D}(t) dt \tag{6}$$

where k is the measurement index, and T_c corresponds to the coherent integration time used in the direct signal tracking stage (20 ms). Making use of the geometrical path difference model, the I_0^R and Q_0^R components are finally given in Equations (7) and (8), where η_k^I and η_k^Q are two independent zero-mean Gaussian noises and $\Lambda(\ )$ models the normalized correlation function of the CDMA code.

$$I_0^R = \frac{A^R}{2} \Lambda\left(-\Delta_{p,k}/c\right) \cos(-\psi_k) + \eta_k^I \tag{7}$$

$$Q_0^R = \frac{A^R}{2} \Lambda\left(-\Delta_{p,k}/c\right) \sin(-\psi_k) + \eta_k^Q \tag{8}$$

The removal of the data bits on I_0^R and Q_0^R components is performed by using the sign function of the in-phase component of the direct signal [28] as follows:

$$D = \text{sign}\left(I_0^D\right), I_b^R = I_0^R D,\ Q_b^R = Q_0^R D \tag{9}$$

The complex representation of the resulting reflected signal is given by its phasor, $\gamma_b^R = I_b^R + iQ_b^R$. Subsequently, a moving mean filter is applied to extract the higher frequency component of the reflected signal and remove the low-frequencies contribution of the direct signal. The complex reflected filtered signal is given by $\gamma_a^R = I_a^R + iQ_a^R$. The phasor γ_a^R is passed through a retracking module based on [28] to correct the time variations of the transmitter and receiver trajectory, the elevation angle, and the reflecting surface height.

The signal retracking starts by modeling the phase difference ψ from the path difference model Δ_p. With λ as the wavelength of the GPS L1 signal (~0.1904 m), the phase difference is obtained by:

$$\psi_p = \text{mod}\left(\frac{2\pi\Delta_p}{\lambda}, 2\pi\right) \tag{10}$$

The phasor representation of the phase difference is built from:

$$\gamma_p = \exp(-i\psi_p) \tag{11}$$

Finally, the retracked reflected signal denoted as the residual phasor γ^R reads:

$$\gamma^R = \gamma_a^R\ \gamma_p^* \tag{12}$$

$$\Rightarrow\ \gamma^R = I^R + iQ^R$$

where * denotes the complex conjugate of the modeled phasor of the residual phase.

3.1.3. Spectral Retrievals

In addition to the signal as amplitude in the time domain, the PSD is used to reveal the power distribution of the residual retracked signal in the Doppler domain. We proceed as described in [34], and the PSD is defined by the Fourier amplitude as a function of the Doppler shift f of the reflected signal, $\Gamma(f)\ := \left|\mathfrak{F}\{\ \gamma^R\}(f)\right|$, where $\mathfrak{F}\{\}$ denotes the Fourier transformation.

The power spectral density is computed every 10 s for each satellite. Figure 6 shows the PSD of the reflected signal after the filtering (γ_a^R) and after retracking step (γ^R) for the GPS satellites PRN 30 ($E: \sim 9°$) and PRN 8 ($E: \sim 65°$) on two different days, 17 July 2019 and 19 July 2019, the lowest and highest sea state, respectively.

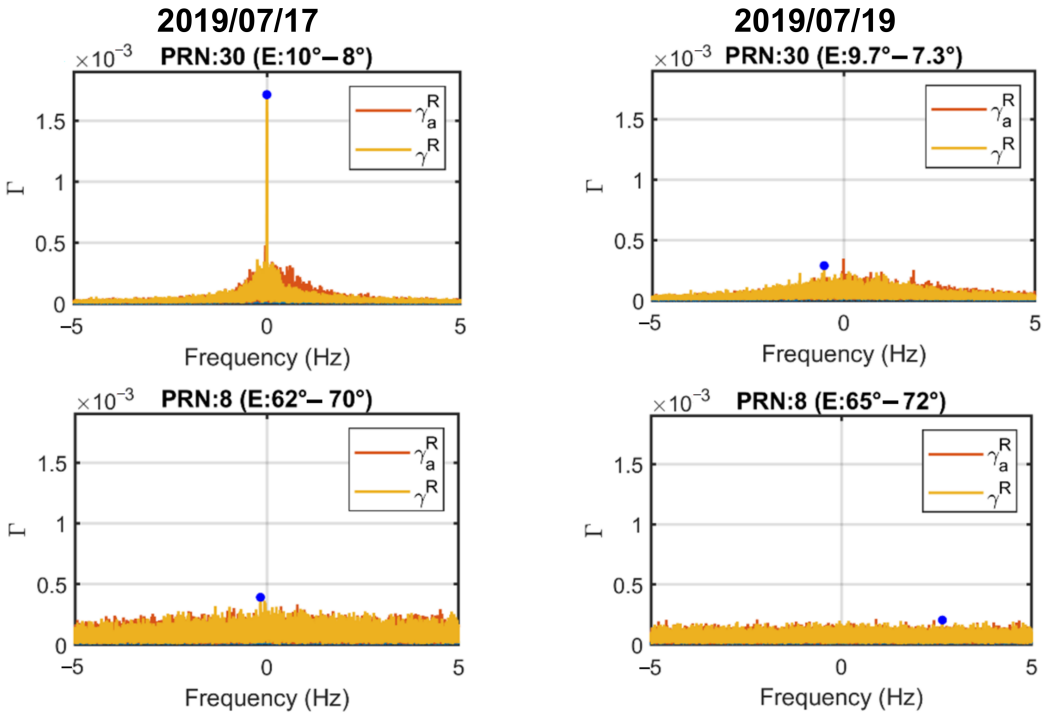

Figure 6. Power spectral density for low- and high-elevation satellites. The blue dot denotes the locations of the peak maxima. The wide distribution of the observed Doppler shift (red line) has been corrected in the retracking step (yellow line), yielding a narrower Doppler shift distribution.

In satellites with low elevations, a sharp spectrum with a noticeable peak is depicted. In contrast, high-elevation satellites show a spread spectrum with resulting peaks in the noise level. The effect of the sea state can be seen in PRN 30 on 19 July. In the presence of a higher sea state, the spectrum gets wider, losing its defined peak even when the elevation of this satellite is lower than on 17 July.

From each spectral retrieval integrated over 10 s, the five highest peaks of the spectrum $\hat{\Gamma}_j(f_j)$ are selected, and the respective Doppler frequencies f_j are retrieved from the x-axis location of the peaks in the spectrum. The Doppler spread σ_f is estimated by computing the standard deviation of the five frequencies obtained in the step before. Figure 7 shows the power and the residual Doppler frequencies of the retracked signal on a logarithmic scale, including the elevation of the 8 satellites for each day. Low-elevation satellites concentrate in the center of the spectrum toward the relative frequency much more prominently on days of the lower sea state. The opposite is the case with high-elevation measurements, which become more distant. In addition, there is a reduction of peak power on days when the sea state is higher.

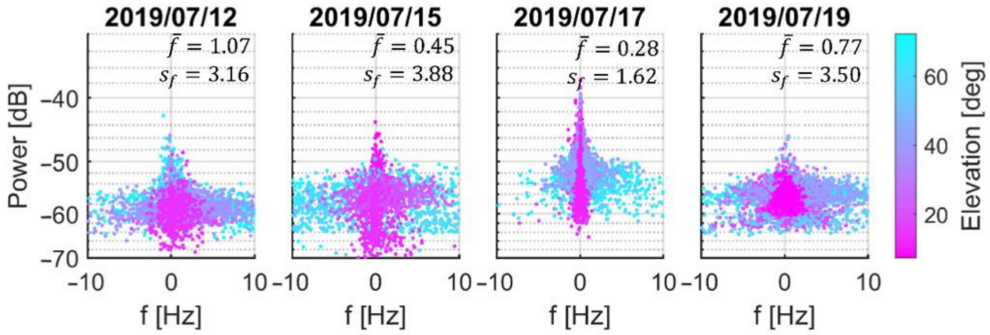

Figure 7. Doppler shift and power of the residual retracked signal. Elevations are represented by the color bar. The lower the elevation and the sea state, the lower the Doppler shift and the higher the power. The higher the elevation and the sea state, the higher the Doppler shift and the lower the signal power. The mean $\bar{f}$ and standard deviation s_f of the Doppler shift are shown in the upper-right corner for each day.

3.1.4. Residual Phase Retrieval and Tropospheric Residual Model

Based on the phasor γ^R in Equation (12), a residual phase path after retracking is obtained. The observed residual phase Δ_ϕ of the retracked reflected signal is computed as follows:

$$\Delta_\phi = \frac{\lambda}{2\pi}\left(\mathfrak{U}\left\{\arg\left\{\gamma^R\right\}\right\} + N\right) \tag{13}$$

where $\arg\{\}$ denotes the phase argument (defined between $-\pi$ and $+\pi$) and $\mathfrak{U}\{\}$ is the unwrapping operator to reconnect the phase argument by adding $\pm 2\pi$ when jumps greater than π occur. The ambiguity N remains unknown, and the factor $\frac{\lambda}{2\pi}$ is applied to obtain the residual phase in path difference representation. The phase residual has been corrected for geometric components of the differential path (reflected signal relative to a direct one). It can be expected that troposphere residuals remain in the phase after retracking. Especially, the rather long propagation paths in the troposphere at grazing elevation (<15°). The modeled tropospheric residual Δ_{tro} is obtained by the difference of the optical difference path, Δ_{opt}, using ray tracing as described in [23], assuming here the refractivity of a standard atmosphere [35] and the geometrical path difference Δ_p.

$$\Delta_{tro} = \Delta_{opt} - \Delta_p \tag{14}$$

3.1.5. Zenith Total Delay Inversion

Similarly, as in GNSS processing for positioning and navigation applications, tropospheric propagation delay is an error source in GNSS-R. As presented in [36], the difference path delay between the path length of the reflected and the direct signal includes the zenith tropospheric delay that, multiplied by a mapping function, gives the differential tropospheric delay. According to [24], the tropospheric delay at position P can be expressed as:

$$\rho_{tro}^P = m_{hz}{\cdot}ZHD + m_{wz}{\cdot}ZWD \simeq m_{hz}{\cdot}ZTD \tag{15}$$

where m_{hz} and m_{wz} are hydrostatic, and the wet mapping functions, ZHD and ZWD, are the zenith hydrostatic and wet delays. Therefore, ρ_{tro}^P can be approximated by the product of the hydrostatic mapping factor and the zenith total delay, ZTD, as the hydrostatic part accounts for 80–90% of the total delay. Assuming spherical symmetry in the atmosphere, the differential tropospheric delay $\rho_{\hat{tro}}$ is twice the delay experienced between the specular point and the receiver [24]. An estimation of the delay at the specular point level is needed since there is no receiver in that location. Therefore, it is assumed that receiver height variations imply variations in the ZTD, so a height-dependent factor with exponential

vertical decay, h_f, is included in the modeling. Finally, the approximation of the differential tropospheric delay is given by:

$$\hat{\rho_{tro}} = 2m_{hz}h_f ZTD - N = 2m_{hz}\left(1 - e^{-\frac{H}{h_{scale}}}\right)ZTD - N \quad (16)$$

where H is the height of the receiver, and h_{scale} is the scale height of the troposphere, assumed to be $h_{scale} = 7160$ m [24]. The hydrostatic mapping factor m_{hz} has been calculated from the Vienna mapping function (VFM3) [37,38], a discrete mapping function that employs the zenith distance $(90° - E)$, coordinates of the receiver, and day of the year.

As stated above, after the retracking step, troposphere residuals are expected in the residual phase from coherent observations. Thus, phase observations are used to inverse the ZTD by using the linear regression approach in the form $y = ax + b$. The dependent variable y corresponds to phase observations Δ_ϕ. From Equation (16), the term $2m_{\backslash hz}h_f$ represents the independent variable x; the ZTD is represented by a, which is the slope of the fitting line after the regression; and b is the intercept, which is linked to the unknown phase ambiguity N (see Equation (13)).

4. Results

4.1. Results on Residual Doppler Spread

The distribution of the Doppler spread on the four respective days is shown in Figure 8. For WS and SWH higher than 2.92 m/s and 0.26 m, respectively, the mean values of the Doppler spread are between 1.64 and 2.53 Hz with a dispersion that increases as the sea state increases. On the other hand, on 17 July, the mean Doppler spread value is 0.5 Hz, and the estimates are located close to this value, that is, a relatively low Doppler dispersion according to a calm sea for that date.

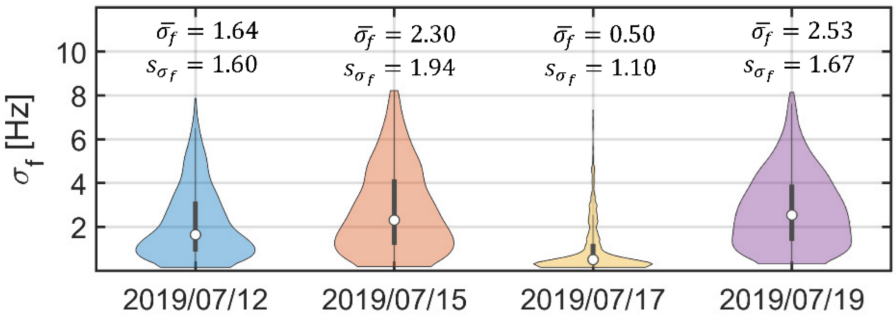

Figure 8. Doppler spread distribution for each flight day. Mean values of the Doppler spread $\overline{\sigma_f}$ and the standard deviation s_{σ_f} are shown above each violin plot for each day. The mean value of the highest sea-state day is 2.53 Hz, while the lowest sea state represents a mean value of 0.5 Hz.

As discussed in Figure 7, there is a dependence between the Doppler shift and sea state depending on satellite elevation. Similarly, as presented by [39], to reduce the satellite elevation effect and represent sea-state impact on the residual Doppler shift, f is multiplied by a mapping factor of $1/\sin(E)$ to obtain the mapped Doppler shift f_v. Figure 9 shows the mapped Doppler spread σ_{f_v} for each day of measurements in the study area. The results show agreement between σ_{f_v} and the sea state for each of the days. On 17 July, a blue response is shown for most of the satellite's tracks, which corresponds to relatively low σ_{f_v} levels $(0\ Hz < \sigma_{fc} \leq 2\ Hz)$. The mapped Doppler spread for the other days is higher, reaching values up to 10 Hz for some satellites.

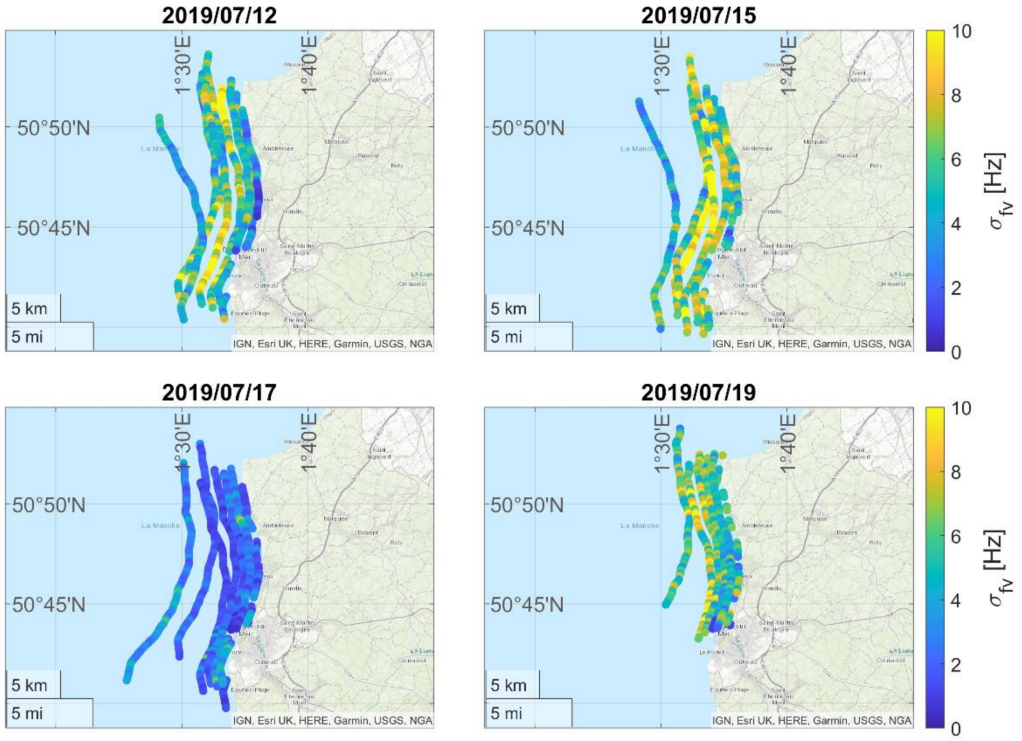

Figure 9. Mapped Doppler spread on the reflection point tracks of the eight GPS satellites analyzed along the coast for each day.

The mapped Doppler spread is the estimate to correlate with the ancillary data from the ERA5 model for determining the relationship between the sea state and the Doppler spreading. To compute the Pearson correlation coefficient between σ_{f_v} and the ancillary data, the mean value of σ_{f_v} over 120 s is considered. The corresponding values of the ERA5 model parameters WS and SWH are interpolated at the specular point location from the grid files downloaded from Copernicus Climate Change Service (C3S) [40] with a spatial resolution of 25 and 50 km, respectively.

The Pearson correlations are presented in Table 2. The events are classified depending on the elevation. Low events are satellites with $E \leq 10°$, mid events are satellites with $10 < E \leq 30°$, and high events are satellites with $E > 30°$.

Table 2. Pearson correlations between ERA5 parameters and mapped Doppler spread.

Parameter	Low	Mid	High
Wind Speed	0.88	0.66	0.58
SWH	0.75	0.58	0.56

Low-elevation satellites show a high correlation between σ_{fc} and sea-state parameters. Although for mid- and high-elevation events, the degree of correlation remains moderate, it is significantly reduced with increasing elevation. Two aspects of our experiment may reduce the sensitivity at mid and high elevations: 1. The antenna gain decreases towards higher-elevation events that arrive at the aircraft closer to the nadir far off the antenna's upward tilted boresight. 2. The high-elevation events lie close to or even on the beach where the sea-state effect is small.

4.2. Results on Carrier Phase Retrieval

In addition to the sea-state impact on Doppler spread, also a coherent carrier phase retrieval can be affected by sea state. As shown in [41], coherent GNSS-R observations tend

to have continuous carrier phase measurements. The first analysis consists of examining the observed residual phase angle of the retracked signal computed as $\Delta_{\phi a} = atan2(Q^R, I^R)$. Figure 10 depicts the $\Delta_{\phi a}$ of the satellites PRN 7, 30, 11, and 8 on two different days, including in the title the elevation angle range for each satellite. The first row shows the observations on 17 July, and the second row on 15 July. From initial inspection, PRN 7 and 30 show a continuous residual phase retrieval on 17 July. Continuous phase observations are lost when the elevation increases. At higher sea state (15 July), visual inspection suggests that no coherent observations are present except for the segment in the minute of the day from 760 to 763 for PRN 11, which corresponds to elevation angles between 5.9° and 7.5°.

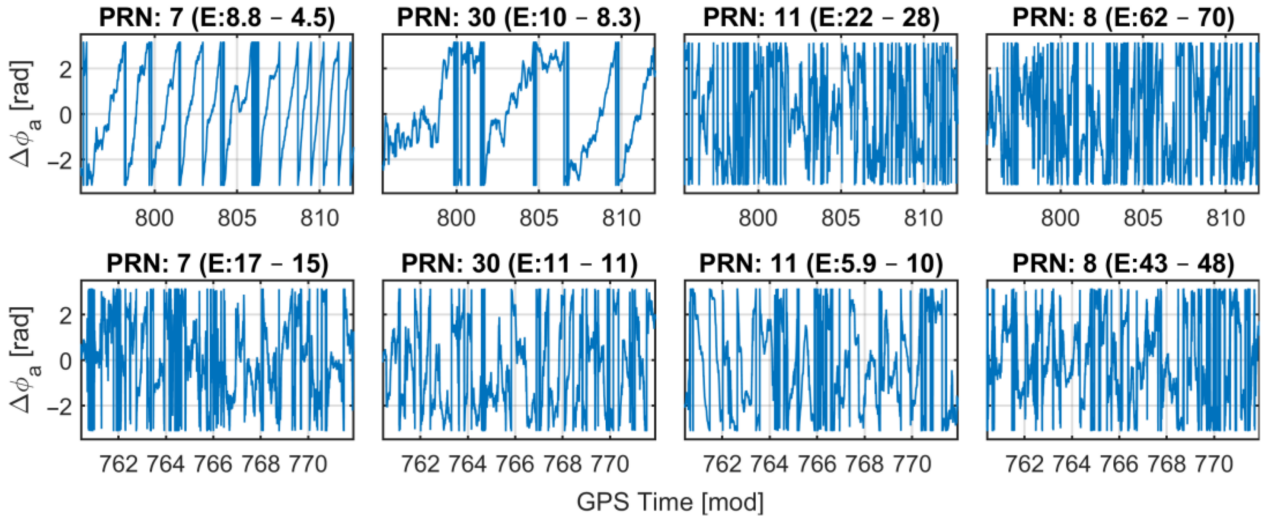

Figure 10. Observed residual phase angle of the retracked signal for PRN 7, 30, 11, and 8 on 2 different days. The first row is on 17 July 2019, and the second row is on 15 July 2019.

The relation between Doppler spread and residual phase retrievals is presented in Figures 11 and 12, on 17 and 15 July, respectively. As above, the same satellites with low, mid, and high elevations are analyzed on both days. The first row contains the Doppler spread over time σ_f in blue for PRN 7, 30, 11, and 8. The red line is an empirical threshold established as 0.5 Hz based on the σ_f mean value of the day with the lowest sea state. The second row contains the modeled and observed path differences. Δ_{tro} denotes the tropospheric residual model calculated in meters, and Δ_ϕ is the observed residual phase converted into a path as illustrated in Equations (14) and (13), respectively. The offset between the modeled and the observed path difference is due to the unknown ambiguity of the retrieved phase.

With a calm sea on 17th July, the low-elevation events $(E < 10°)$ have Doppler spread below 0.5 Hz (PRN 7 and 30). These events present a smooth Δ_ϕ that shows agreement with the tropospheric residual Δ_{tro} in the path model, indicating coherent reflections. For satellites with mid and high elevations (PRN 11 and 8), this behavior does not remain and Δ_ϕ is noisier, indicating a lack of coherent reflection.

On the other hand, with a rougher sea state on 15 July, the Doppler spread is significantly higher even for events below 10° elevation. Coherent phase retrieval fails except for a short period at the beginning of the event PRN 11 when the smooth phase appears at the lowest elevations $(\sim 6°)$.

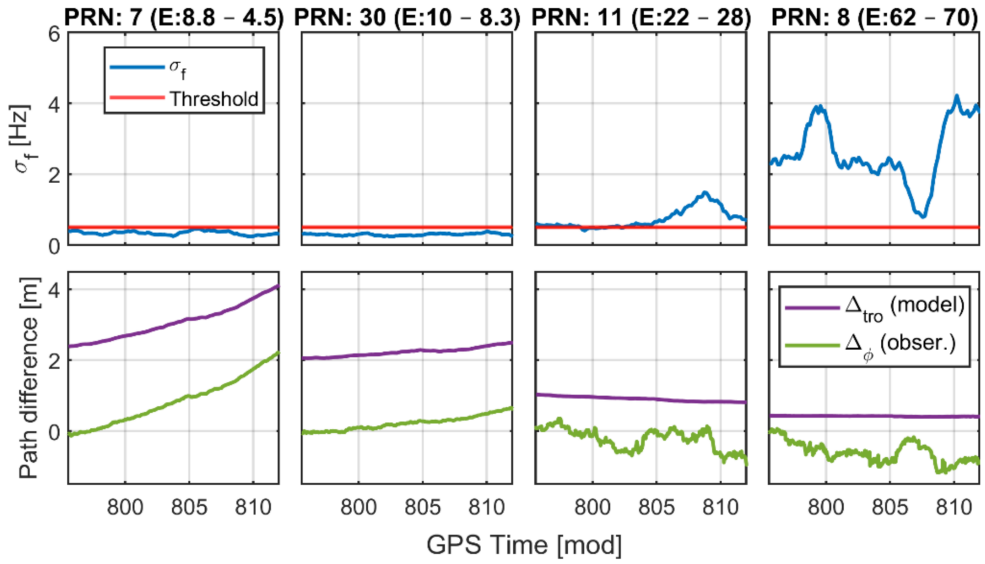

Figure 11. Doppler spread and tropospheric residual model compared with observed path difference from the residual phase on 17 July 2019. The satellite PRN number and the elevation angle range are indicated in the title of each column.

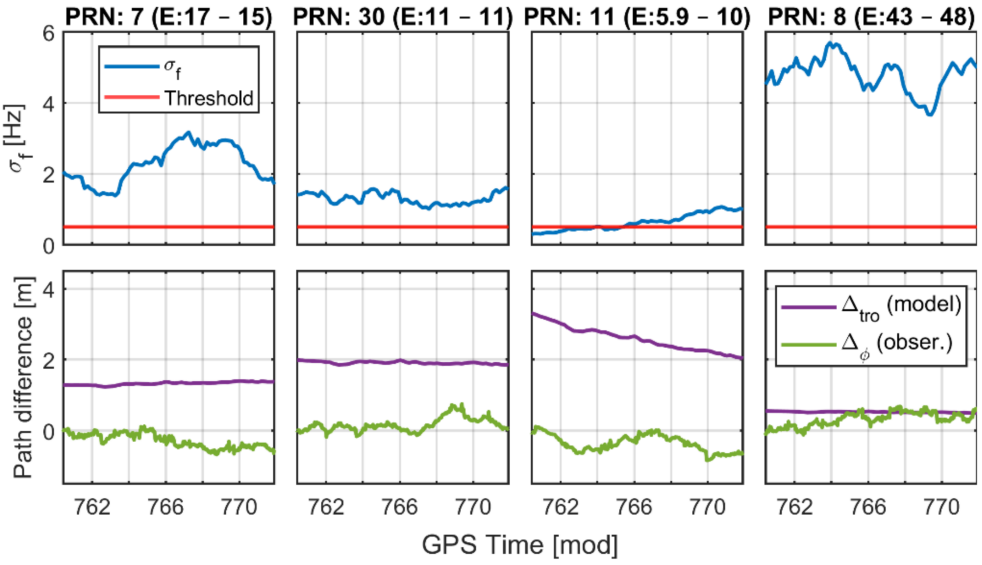

Figure 12. Doppler spread and tropospheric residual model compared with observed path difference from the residual phase on 15 July 2019. The satellite PRN number and the elevation angle range are indicated in the title of each column.

4.3. Results on Zenith Total Delay Inversion

From the coherent residual phase results, an agreement with the tropospheric residual model is found in the observations on 17 July 2019 at events with grazing elevation angles. Based on the observations and model correspondence, the ZTD is estimated from linear regression as explained above. Figure 13 shows the residual phase observation versus the independent variable (scale factor) computed by using VFM3 and the height variation factor on 17 July 2019 and on 15 July 2019. The figure includes the linear fitting equation after the regression and the model uncertainty, which is the standard deviation of the observed minus predicted values.

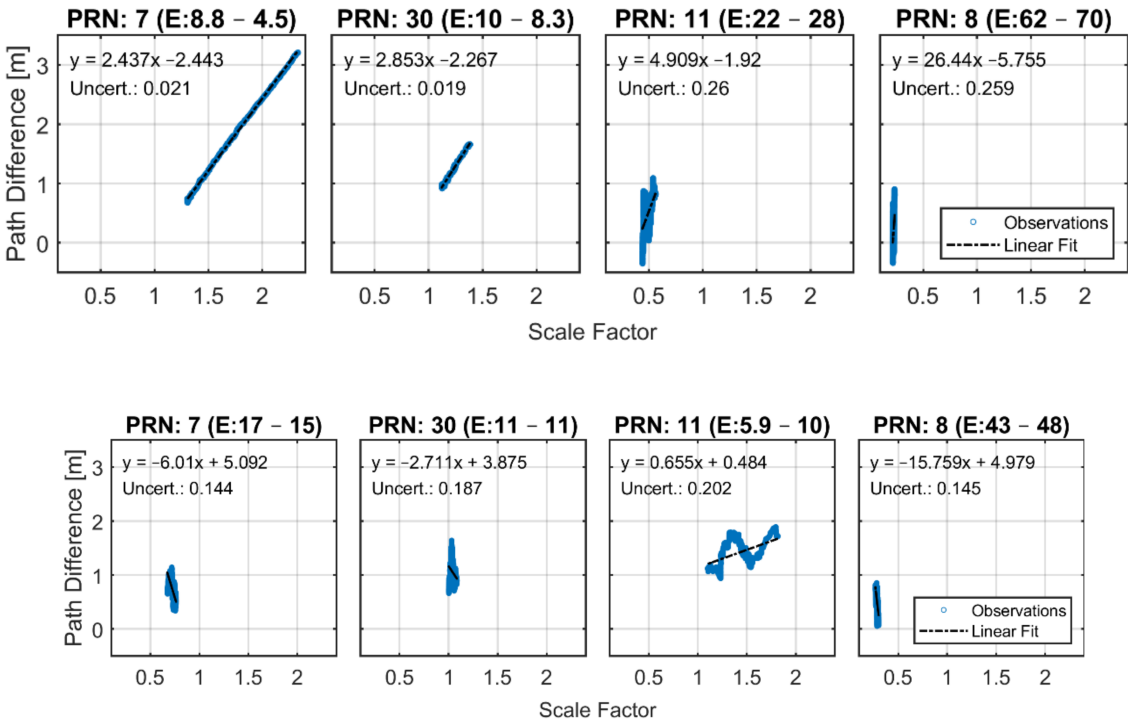

Figure 13. Residual phase (path difference representation) versus independent variable (scale factor) from the differential tropospheric delay approximation using the VFM3 and the height variation factor on 17 July 2019 (top row) and 15 July 2019 (bottom row). The linear regression equation and model uncertainty is presented in the top-left corner for each satellite.

The typical zenith total delay is about 2.3 m for a receiver located at mean sea level [42]. With smooth sea surface conditions (on 17 July 2019) at low-elevation angles, the estimated ZTD for PRN 7 and 30 is 2.437 and 2.853 m, respectively, with an uncertainty of 0.02 m in both cases. Those events correspond to phase-coherent observations from which the estimated ZTD only exceeds the expected value at 14 and 55 cm, respectively. Once the elevation angle increases and the phase coherence is lost, the ZTD is far from the regular value. On the other hand, for events on the rougher sea surface (on 15 July 2019), there is no signature of phase coherence for a complete satellite track, so the slope of the fitting line after regression differs completely from the typical ZTD value even for low-elevation observations (PRN 11).

5. Conclusions

The results show that loss of coherence in phase observations is accompanied by a Doppler spread of more than 0.5 Hz. The results also indicate a major influence of sea state in this respect depending on the elevation angle. As surface roughness and elevation angles increase, diffuse reflections dominate, and coherence in observation is lost. These findings apply to the here studied conditions of airborne observations over coastal waters. Similarly, as presented in [43] for reflectometry satellite measurements, it can be seen in this study that coherent observations respond to very calm waters and low-elevation angles. A Doppler spread σ_f beyond 0.5 Hz causes a loss of coherent observations. In the given setup, the 0.5 Hz threshold is reached for SWH of ~0.3 m, and wind speeds of about 3 m/s when elevation angles go beyond 10°.

However, even under coastal conditions, the coherent observations from airborne platform results are limited. For the 4-day measurement campaign, a total of 2646 Doppler spread estimations (every 120 s) are obtained. Out of these estimates, only 15% correspond to coherent observations below the σ_f threshold. These retrievals are distributed as 10%

and 5% for events at low and mid elevations, respectively, as shown in Table 3. None of the observations at high-elevation angles present coherence.

Table 3. Total of coherent reflections below the Doppler spread threshold at low, mid, and high elevation.

Threshold	Low	Mid	High
$\sigma_f \leq 0.5\ Hz$	10%	5%	0%

Nevertheless, it appears that even beyond the threshold, the Doppler spread carries information on sea state. By analyzing the Doppler spread of PRN 8 on 17 July, it is important to note the dependence on surface roughness even for high-elevation angles. Figure 14a shows σ_f plotted with a vertical time axis aligned to the specular point track on the map. The highlighted section in yellow, which corresponds to the minute of day 806 until 809, represents a part of the track that crosses over very calm water near the port of Boulogne-sur-Mer (b) created by the breakwater built at the port location (c). Even though the elevation angle is $\sim 70^\circ$ in this track section, the smoother surface produces a significant reduction in the Doppler spread, nearly reaching the threshold of 0.5 Hz for coherence, allowing us to identify sensitive changes in sea state.

Figure 14. (**a**) Doppler spread of PRN 8 on 17 July 2019 plotted with vertical time axis aligned with the track on the map. (**b**) Specular point track crossing the pond created by the structure on the Google Earth satellite image. (**c**) Breakwater structure in the Boulogne-sur-Mer port located at 50°43′53″N 01°34′19″E. How the sea state changes from rough water on the left side to calm water on the right side can be observed.

We found that the Doppler spread is an indicator for coherent observations, and it can furthermore carry sea-state information. However, it is not only the sea state that can affect the Doppler spread but also residuals that remain after correction with the geometric path model, in particular, variations of the receiver trajectory, which could have an effect. As discussed in the results sections, phase retrieval is possible under coherent reflection conditions below the 0.5 Hz threshold. Coherent phase observations over the sea surface are suitable for altimetric inversion. As described in [9,44], phase-coherent observations in GNSS-R allow altimetric retrievals from the carrier phase altimetry technique. Those studies have shown promising results in open ocean waters with high precision. This study may lead to potentially obtaining altimetric retrievals from airborne GNSS-R in coastal zones. However, when phase measurements are used, cycle slips caused by a low signal-to-noise ratio, ionospheric conditions, or aircraft dynamics need to be considered. Methods for cycle-slip correction are discussed in [24,39] by using airborne and satellite reflectometry data, respectively.

The standard GNSS antennas and receivers are capable of receiving RHCP signals only. At grazing angles, the reflected signal maintains its RHCP polarization. However, the

reflected signal will change its polarization to left-hand circular polarization (LHCP) when it is coming from close to the nadir. A different antenna(s) setup, such as uplooking RHCP and downlooking LHCP antennas, as configurated in [32], may help capture the direct and reflected signals as they have a better field of view that may improve the final results.

GNSS reflectometry coherent phase observations also have the potential for atmospheric and ionospheric sounding, for example, to retrieve total electron content [45]. In this study, the comparison of coherent phase residuals and excess path model (tropospheric contribution) shows agreement. However, an offset remains due to phase ambiguity. The ZTD estimations from linear regression and the expected zenith total delay value present differences at a centimetric level. Therefore, at low-elevation angles and smooth sea surface conditions, it is possible to retrieve zenith tropospheric delay from reflectometry airborne measurements. The literature suggests that the typical zenith total delay is approximately 2.3 m at mean-sea-level locations. On coastal calm waters (SWH: ~0.3 m, WS: 3 m/s), for elevation angles from 4.5° to 8.8°, the ZTD estimation exceeds only 5% of the expected value. Once the elevation increases, from 8.3° to 10°, the difference is up to 24%. Future studies may use the sensitivity of phase observations to tropospheric contribution to retrieve parameters, for example, atmospheric water vapor, based on coherent reflectometry observations.

Author Contributions: Conceptualization, M.M., M.S. and G.S.; methodology, M.M., M.S. and G.S.; software, G.S., M.S. and M.M.; data resources, M.M., M.S., G.S. and W.D.; writing—original draft preparation, M.M.; writing—review and editing, M.S., G.S., W.D., M.H., J.W. and S.R.; visualization, M.M.; supervision, M.S., J.W. and M.H. All authors have read and agreed to the published version of the manuscript.

Funding: This research was funded by the Deutsches GeoForschungsZentrum (GFZ).

Data Availability Statement: The GNSS data used for this experiment are available from GFZ. Data are available upon reasonable request from the corresponding author with permission of GFZ.

Acknowledgments: The authors would like to thank the project CPER MARCO 2015–2021 for their support. Acknowledgments to Cap Aviateur for the help provided with flights during the measurement campaign.

Conflicts of Interest: The authors declare no conflict of interest. The funders had no role in the design of the study; in the collection, analyses, or interpretation of data; in the writing of the manuscript; or in the decision to publish the results.

References

1. Cazenave, A.; Cozannet, G.L. Sea Level Rise and Its Coastal Impacts. *Earth's Future* **2014**, *2*, 15–34. [CrossRef]
2. ESA Climate Office. Sea State. Available online: https://climate.esa.int/en/projects/sea-state/ (accessed on 24 November 2021).
3. Bengtsson, L.; Hodges, K.I.; Roeckner, E. Storm Tracks and Climate Change. *J. Clim.* **2006**, *19*, 3518–3543. [CrossRef]
4. Melet, A.; Teatini, P.; Le Cozannet, G.; Jamet, C.; Conversi, A.; Benveniste, J.; Almar, R. Earth Observations for Monitoring Marine Coastal Hazards and Their Drivers. *Surv. Geophys.* **2020**, *41*, 1489–1534. [CrossRef]
5. Benveniste, J.; Cazenave, A.; Vignudelli, S.; Fenoglio-Marc, L.; Shah, R.; Almar, R.; Andersen, O.; Birol, F.; Bonnefond, P.; Bouffard, J.; et al. Requirements for a Coastal Hazards Observing System. *Front. Mar. Sci.* **2019**, *6*, 348. [CrossRef]
6. Martín-Neira, M. A Passive Reflectometry and Interferometry System (PARIS): Application to Ocean Altimetry. *ESA J.* **1993**, *17*, 331–355.
7. Semmling, M.; Beyerle, G.; Beckheinrich, J.; Ge, M.; Wickert, J. Airborne GNSS Reflectometry Using Crossover Reference Points for Carrier Phase Altimetry. In Proceedings of the 2014 IEEE Geoscience and Remote Sensing Symposium, Quebec City, QC, Canada, 13–18 July 2014; pp. 3786–3789.
8. Clarizia, M.P.; Ruf, C.; Cipollini, P.; Zuffada, C. First Spaceborne Observation of Sea Surface Height Using GPS-Reflectometry. *Geophys. Res. Lett.* **2016**, *43*, 767–774. [CrossRef]
9. Cardellach, E.; Li, W.; Rius, A.; Semmling, M.; Wickert, J.; Zus, F.; Ruf, C.S.; Buontempo, C. First Precise Spaceborne Sea Surface Altimetry with GNSS Reflected Signals. *IEEE J. Sel. Top. Appl. Earth Obs. Remote Sens.* **2020**, *13*, 102–112. [CrossRef]
10. Yan, Q.; Huang, W. Sea Ice Remote Sensing Using GNSS-R: A Review. *Remote Sens.* **2019**, *11*, 2565. [CrossRef]
11. Munoz-Martin, J.F.; Perez, A.; Camps, A.; Ribó, S.; Cardellach, E.; Stroeve, J.; Nandan, V.; Itkin, P.; Tonboe, R.; Hendricks, S.; et al. Snow and Ice Thickness Retrievals Using GNSS-R: Preliminary Results of the MOSAiC Experiment. *Remote Sens.* **2020**, *12*, 4038. [CrossRef]

12. Rodriguez-Alvarez, N.; Holt, B.; Jaruwatanadilok, S.; Podest, E.; Cavanaugh, K.C. An Arctic Sea Ice Multi-Step Classification Based on GNSS-R Data from the TDS-1 Mission. *Remote Sens. Environ.* **2019**, *230*, 111202. [CrossRef]
13. Larson, K.M.; Small, E.E.; Gutmann, E.; Bilich, A.; Axelrad, P.; Braun, J. Using GPS Multipath to Measure Soil Moisture Fluctuations: Initial Results. *GPS Solut.* **2008**, *12*, 173–177. [CrossRef]
14. Jia, Y.; Savi, P.; Pei, Y.; Notarpietro, R. GNSS Reflectometry for Remote Sensing of Soil Moisture. In Proceedings of the 2015 IEEE 1st International Forum on Research and Technologies for Society and Industry Leveraging a better tomorrow (RTSI), Torino, Italy, 16–18 September 2015; pp. 498–501.
15. Calabia, A.; Molina, I.; Jin, S. Soil Moisture Content from GNSS Reflectometry Using Dielectric Permittivity from Fresnel Reflection Coefficients. *Remote Sens.* **2020**, *12*, 122. [CrossRef]
16. Zavorotny, V.U.; Voronovich, A.G. Scattering of GPS Signals from the Ocean with Wind Remote Sensing Application. *IEEE Trans. Geosci. Remote Sens.* **2000**, *38*, 951–964. [CrossRef]
17. Marchan-Hernandez, J.F.; Valencia, E.; Rodriguez-Alvarez, N.; Ramos-Perez, I.; Bosch-Lluis, X.; Camps, A.; Eugenio, F.; Marcello, J. Sea-State Determination Using GNSS-R Data. *IEEE Geosci. Remote Sens. Lett.* **2010**, *7*, 621–625. [CrossRef]
18. Alonso-Arroyo, A.; Camps, A.; Park, H.; Pascual, D.; Onrubia, R.; Martin, F. Retrieval of Significant Wave Height and Mean Sea Surface Level Using the GNSS-R Interference Pattern Technique: Results from a Three-Month Field Campaign. *IEEE Trans. Geosci. Remote Sens.* **2015**, *53*, 3198–3209. [CrossRef]
19. Foti, G.; Gommenginger, C.; Jales, P.; Unwin, M.; Shaw, A.; Robertson, C.; Roselló, J. Spaceborne GNSS Reflectometry for Ocean Winds: First Results from the UK TechDemoSat-1 Mission. *Geophys. Res. Lett.* **2015**, *42*, 5435–5441. [CrossRef]
20. Jing, C.; Niu, X.; Duan, C.; Lu, F.; Di, G.; Yang, X. Sea Surface Wind Speed Retrieval from the First Chinese GNSS-R Mission: Technique and Preliminary Results. *Remote Sens.* **2019**, *11*, 3013. [CrossRef]
21. Williams, S.D.P.; Nievinski, F.G. Tropospheric Delays in Ground-Based GNSS Multipath Reflectometry—Experimental Evidence from Coastal Sites. *J. Geophys. Res. Solid Earth* **2017**, *122*, 2310–2327. [CrossRef]
22. Anderson, K.D. Determination of Water Level and Tides Using Interferometric Observations of GPS Signals. *J. Atmos. Ocean. Technol.* **2000**, *17*, 1118–1127. [CrossRef]
23. Semmling, A.M.; Schmidt, T.; Wickert, J.; Schön, S.; Fabra, F.; Cardellach, E.; Rius, A. On the Retrieval of the Specular Reflection in GNSS Carrier Observations for Ocean Altimetry. *Radio Sci.* **2012**, *47*, RS6007. [CrossRef]
24. Fabra, F.; Cardellach, E.; Rius, A.; Ribo, S.; Oliveras, S.; Nogues-Correig, O.; Belmonte Rivas, M.; Semmling, M.; D'Addio, S. Phase Altimetry with Dual Polarization GNSS-R Over Sea Ice. *IEEE Trans. Geosci. Remote Sens.* **2012**, *50*, 2112–2121. [CrossRef]
25. Yan, Z.; Zheng, W.; Wu, F.; Wang, C.; Zhu, H.; Xu, A. Correction of Atmospheric Delay Error of Airborne and Spaceborne GNSS-R Sea Surface Altimetry. *Front. Earth Sci.* **2022**, *10*, 730551. [CrossRef]
26. Nikolaidou, T.; Santos, M.; Williams, S.; Geremia-Nievinski, F. Development and Validation of Comprehensive Closed Formulas for Atmospheric Delay and Altimetry Correction in Ground-Based GNSS-R. *TechRxiv* **2022**, preprint.
27. Kucwaj, J.-C.; Reboul, S.; Stienne, G.; Choquel, J.-B.; Benjelloun, M. Circular Regression Applied to GNSS-R Phase Altimetry. *Remote Sens.* **2017**, *9*, 651. [CrossRef]
28. Semmling, M. Altimetric Monitoring of Disko Bay Using Interferometric GNSS Observations on L1 and L2. Ph.D. Thesis, Deutsches GeoForschungsZentrum GFZ, Potsdam, Germany, 2012; 136p.
29. Elfouhaily, T.; Thompson, D.R.; Linstrom, L. Delay-Doppler Analysis of Bistatically Reflected Signals from the Ocean Surface: Theory and Application. *IEEE Trans. Geosci. Remote Sens.* **2002**, *40*, 560–573. [CrossRef]
30. Semmling, A.M.; Beyerle, G.; Stosius, R.; Dick, G.; Wickert, J.; Fabra, F.; Cardellach, E.; Ribó, S.; Rius, A.; Helm, A.; et al. Detection of Arctic Ocean Tides Using Interferometric GNSS-R Signals. *Geophys. Res. Lett.* **2011**, *38*, L04103. [CrossRef]
31. Foerste, C.; Bruinsma, S.; Flechtner, F.; Marty, J.-C.; Dahle, C.; Abrykosov, O.; Lemoine, J.-M.; Neumayer, H.; Barthelmes, F.; Biancale, R.; et al. EIGEN-6C2—A New Combined Global Gravity Field Model Including GOCE Data up to Degree and Order 1949 of GFZ Potsdam and GRGS Toulouse. *Geophys. Res. Abstr. EGU Gen. Assem.* **2013**, *15*, 4077.
32. Issa, H.; Stienne, G.; Reboul, S.; Raad, M.; Faour, G. Airborne GNSS Reflectometry for Water Body Detection. *Remote Sens.* **2021**, *14*, 163. [CrossRef]
33. Zimmermann, F.; Schmitz, B.; Klingbeil, L.; Kuhlmann, H. GPS Multipath Analysis Using Fresnel Zones. *Sensors* **2018**, *19*, 25. [CrossRef]
34. Semmling, A.M.; Wickert, J.; Schön, S.; Stosius, R.; Markgraf, M.; Gerber, T.; Ge, M.; Beyerle, G. A Zeppelin Experiment to Study Airborne Altimetry Using Specular Global Navigation Satellite System Reflections. *Radio Sci.* **2013**, *48*, 427–440. [CrossRef]
35. *ISO 2533:1975*. International Organization for Standardization: Geneva, Switzerland, 1975.
36. Treuhaft, R.N.; Lowe, S.T.; Zuffada, C.; Chao, Y. 2-cm GPS Altimetry over Crater Lake. *Geophys. Res. Lett.* **2001**, *28*, 4343–4346. [CrossRef]
37. Landskron, D.; Böhm, J. VMF3/GPT3: Refined Discrete and Empirical Troposphere Mapping Functions. *J. Geod.* **2018**, *92*, 349–360. [CrossRef]
38. Böhm, J.; Boisits, J. *re3data.org: VMF Data Server*; Department of Geodesy and Geoinformation, TU Wien: Vienna, Austria, 2016. [CrossRef]
39. Wang, Y.; Breitsch, B.; Morton, Y.T.J. A State-Based Method to Simultaneously Reduce Cycle Slips and Noise in Coherent GNSS-R Phase Measurements From Open-Loop Tracking. *IEEE Trans. Geosci. Remote Sens.* **2021**, *59*, 8873–8884. [CrossRef]

40. Hersbach, H.; Bell, B.; Berrisford, P.; Biavati, G.; Horányi, A.; Muñoz Sabater, J.; Nicolas, J.; Peubey, C.; Radu, R.; Rozum, I.; et al. ERA5 Hourly Data on Single Levels from 1979 to Present. Available online: https://cds.climate.copernicus.eu/cdsapp#!/dataset/reanalysis-era5-single-levels?tab=overview (accessed on 11 December 2021).
41. Wang, Y.; Liu, Y.; Roesler, C.; Morton, Y.J. Detection of Coherent GNSS-R Measurements Using a Support Vector Machine. In Proceedings of the IGARSS 2020–2020 IEEE International Geoscience and Remote Sensing Symposium, Waikoloa, HI, USA, 26 September–2 October 2020; pp. 6210–6213.
42. Kačmařík, M. Retrieving of GNSS Tropospheric Delays from RTKLIB in Real-Time and Post-Processing Mode. In *Dynamics in GIscience, Proceedings of the GIS Ostrava, Ostrava, Czech Republic, 22–24 March 2017*; Ivan, I., Horák, J., Inspektor, T., Eds.; Springer International Publishing: Cham, Switzerland, 2018; pp. 181–194.
43. Li, W.; Cardellach, E.; Fabra, F.; Ribó, S.; Rius, A. Lake Level and Surface Topography Measured with Spaceborne GNSS-Reflectometry from CYGNSS Mission: Example for the Lake Qinghai. *Geophys. Res. Lett.* **2018**, *45*, 13332–13341. [CrossRef]
44. Semmling, A.M.; Beckheinrich, J.; Wickert, J.; Beyerle, G.; Schön, S.; Fabra, F.; Pflug, H.; He, K.; Schwabe, J.; Scheinert, M. Sea Surface Topography Retrieved from GNSS Reflectometry Phase Data of the GEOHALO Flight Mission. *Geophys. Res. Lett.* **2014**, *41*, 954–960. [CrossRef]
45. Wang, Y.; Morton, Y.J. Ionospheric Total Electron Content and Disturbance Observations from Space-Borne Coherent GNSS-R Measurements. *IEEE Trans. Geosci. Remote Sens.* **2022**, *60*, 5801013. [CrossRef]

remote sensing

MDPI

Article

Characterizing Ionospheric Effects on GNSS Reflectometry at Grazing Angles from Space

Mario Moreno [1,2,*], Maximilian Semmling [1], Georges Stienne [3], Mainul Hoque [1] and Jens Wickert [2,4]

[1] Deutsches Zentrum für Luft-und Raumfahrt, Institut für Solar-Terrestrische Physik (DLR-SO), Kalkhorstweg 53, 17235 Neustrelitz, Germany
[2] Institute of Geodesy and Geoinformation Science, Department of GNSS Remote Sensing, Navigation and Positioning, Technische Universität Berlin (TUB), Str. des 17. Juni 135, 10623 Berlin, Germany
[3] Laboratoire d'Informatique, Signal et Image de la Côte d'Opale (LISIC), Université Littoral Côte d'Opale (ULCO), 50 rue Ferdinand Buisson, 62228 Calais, France
[4] Deutsches GeoForschungsZentrum (GFZ), Wissenschaftpark "Albert Einstein", Telegrafenberg, 14473 Potsdam, Germany
* Correspondence: mario.moreno@dlr.de

Abstract: Coherent observations in GNSS reflectometry are prominent in regions with smooth reflecting surfaces and at grazing elevation angles. However, within these lower elevation ranges, GNSS signals traverse a more extensive atmospheric path, and increased ionospheric effects (e.g., delay biases) are expected. These biases can be mitigated by employing dual-frequency receivers or models tailored for single-frequency receivers. In preparation for the single-frequency GNSS-R ESA "PRETTY" mission, this study aims to characterize ionospheric effects under variable parameter conditions: elevation angles in the grazing range (5° to 30°), latitude-dependent regions (north, tropic, south) and diurnal changes (day and nighttime). The investigation employs simulations using orbit data from Spire Global Inc.'s Lemur-2 CubeSat constellation at the solar minimum (F10.7 index at 75) on March, 2021. Changes towards higher solar activity are accounted for with an additional scenario (F10.7 index at 180) on March, 2023. The electron density associated with each reflection event is determined using the Neustrelitz Electron Density Model (NEDM2020) and the NeQuick 2 model. The results from periods of low solar activity reveal fluctuations of up to approximately 300 TECUs in slant total electron content, 19 m in relative ionospheric delay for the GPS L1 frequency, 2 Hz in Doppler shifts, and variations in the peak electron density height ranging from 215 to 330 km. Sea surface height uncertainty associated with ionospheric model-based corrections in group delay altimetric inversion can reach a standard deviation at the meter level.

Keywords: GNSS reflectometry; grazing angles; ionospheric delay; ionospheric Doppler shift; NEDM2020 model; NeQuick model; PRETTY mission

Citation: Moreno, M.; Semmling, M.; Stienne, G.; Hoque, M.; Wickert, J. Characterizing Ionospheric Effects on GNSS Reflectometry at Grazing Angles from Space. *Remote Sens.* **2023**, *15*, 5049. https://doi.org/10.3390/rs15205049

Academic Editor: Mehrez Zribi

Received: 12 September 2023
Revised: 15 October 2023
Accepted: 17 October 2023
Published: 20 October 2023

1. Introduction

The ionosphere, situated between 60 and 2000 km above the Earth's surface, plays a vital role in electromagnetic wave propagation, influenced by solar-radiation-induced ionization [1]. The speed at which the transmitted electromagnetic signals from the GNSS (global navigation satellite system) satellites propagate through the ionosphere depends on the electron density along the line of sight between the satellite and the receiver. Upon traversing the ionosphere, GNSS signals may encounter two distinct forms of perturbations: Firstly, the introduction of an error in the estimated range due to the signal's delay that is proportional to the integrated electron density (slant total electron content—sTEC), and secondly, the occurrence of signal characteristic fluctuations resulting from irregularities in the ionosphere's electron density distribution [2].

The use of GNSS signals, renowned for their global availability and signal propagation characteristics, has been widely investigated and exploited as a powerful tool for

ionospheric studies across diverse spatial and temporal scales. Ground-based atmospheric-sounding techniques employing continuously operating reference station (CORS) networks and GNSS receivers, which operate on low Earth orbit (LEO) satellites for the analysis of refracted radio signals via GNSS radio occultation (GNSS-RO), provide key observations for improving global weather forecasts [3]. To further broaden the observations, GNSS reflectometry (GNSS-R) has emerged as a complementary technique that leverages signals reflected off the Earth's surface. This approach not only facilitates the retrieval of reflecting surface properties but also serves as an atmospheric-sounding tool.

In order to understand ionospheric ranging delays within space-borne GNSS-R, simulations are conducted as detailed in [4]. The simulation is based on the Cyclone GNSS (CYGNSS) [5] mission and encompasses different elevation angles, latitudes, and solar activities. The results reveal an inverse relationship between the satellite elevation angle and ionospheric delay, with a larger ionospheric influence at low latitudes. In [6], the impact of scintillation effects on reflectometry has been explored using data from UK TechDemoSat-1 [7]. These effects lead to a degradation of the signal-to-noise ratio that can be utilized for altimetry and scatterometry performance assessments. More recently, studies have been carried out to retrieve the total electron content (TEC) from coherent reflectometry observations. In the work presented in [8], a methodology was introduced for sTEC estimation along the paths of incident and reflected signal rays. This estimation is based on coherent dual-frequency GNSS-R measurements obtained from Spire Global low Earth orbit (LEO) CubeSats. The outcomes have demonstrated a favorable alignment between reflectometry sTEC estimations and the global ionospheric TEC maps (GIM). Furthermore, an algorithm outlined in [9] combines sTEC observation from space-borne reflectometry using CubeSats and data collected from ground-based GNSS stations to generate vertical TEC (vTEC) maps in the Arctic region. Simulations conducted within this study under diverse conditions, involving variations in temporal resolution, solar activity levels, and the number of reflection events, have demonstrated enhanced accuracy in vTEC estimations when coherent GNSS-R observations are incorporated.

In the domain of GNSS-R, it has been empirically established that coherent observations are more frequently observed in the presence of smooth reflecting surfaces, such as sea ice, regions with low sea states, or inland waters, and at low grazing angles [10–12]. Nonetheless, within this range of elevation angles, it is important to note that the trajectories of the LEO GNSS-R rays entail a longer path through the ionosphere. This extended path results in a more pronounced ionospheric impact on the signals themselves. The representation (not to scale) of the LEO GNSS-R configuration along the grazing angle rays' paths and its interaction with the ionosphere are illustrated in Figure 1.

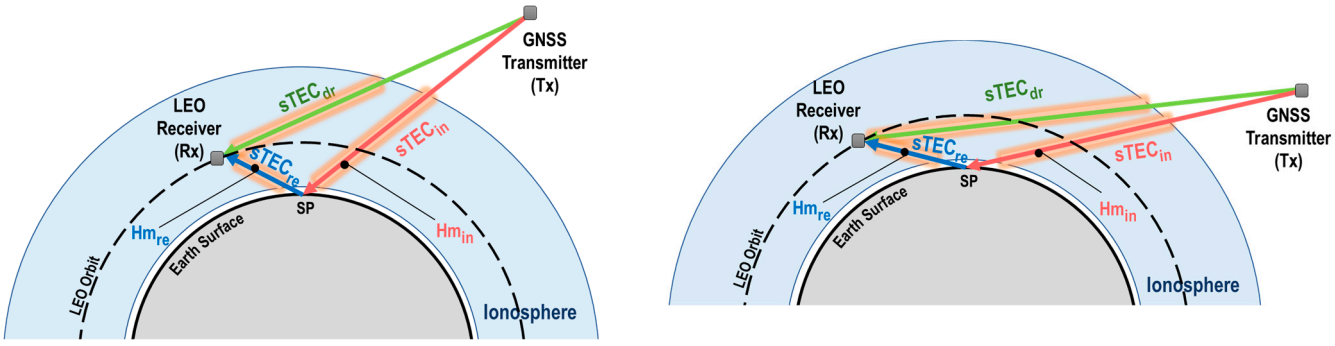

Figure 1. (**a**) LEO GNSS-R representation at 30° elevation angle at specular point. (**b**) LEO GNSS-R representation at 5° elevation angle. $sTEC_x$ denotes the slant total electron content. Subscripts dr, in, and re correspond to the direct ray (transmitter T_x to receiver R_x), incident ray (transmitter to specular point SP), and reflected ray (specular point to receiver), respectively. Hm_x represents the peak electron density height for the incident and reflected ray paths.

As described in [13], dual-frequency receivers possess the capability to mitigate these first-order ionospheric effects through the utilization of a linear combination (ionosphere-free) of either code or carrier measurements. Conversely, single-frequency receivers must rely on applying a model to correct for ionospheric refraction, which can introduce delays of several tens of meters. For the Galileo GNSS constellation, the European GNSS Open Service has adopted the Neustrelitz Total Electron Content Model NTCM [14] (NTCM-G) or NeQuick 2 [15] (NeQuick-G) models to provide real-time ionospheric corrections for single-frequency receivers [16].

This study is in preparation for the European Space Agency's GNSS-R CubeSat mission "PRETTY" (passive reflectometry and dosimetry) [17]. The mission's primary goal is to retrieve sea surface height using grazing angle observations. Since PRETTY operates at a single frequency (L5), it requires model-based ionospheric corrections. This study provides a comprehensive characterization of ionospheric effects, at the grazing angle range (5°–30°), considering satellite geometry, latitude-dependent regions, temporal variations, and solar activity. It analyzes variability in the ionospheric group delay, Doppler shift, and peak electron density height. Additionally, the uncertainty in model-based ionospheric corrections for GNSS-R group delay altimetry is assessed.

The analysis is based on utilizing the sTEC obtained from three-dimensional, time-dependent models. To assess model uncertainty, the sTEC values computed using the Neustrelitz Electron Density Model (NEDM2020) [18] are used as a reference and compared with the sTEC retrievals from NeQuick 2. Simulations are conducted to replicate conditions similar to those of the PRETTY mission, utilizing orbit data from the GNSS-R Spire Global Lemur-2 constellation. To provide a comprehensive analysis, the results are categorized into three elevation angle ranges: very-low (5°–10°), low (10°–20°), and mid-low (20°–30°). These categories are further grouped by latitude into three distinct regions: north, tropics, and south. Additionally, this study considers variations in local time and solar activity. Low solar activity (LSA) is represented by F10.7 = 75 in March 2021 and high solar activity (HSA) by F10.7 = 180 in March 2023.

The structure of this paper is outlined as follows: Section 2 presents the GNSS-R data descriptions, reflection events, and ray point settings for the simulations. Section 3 illustrates the methodologies utilized for the determination of parameters such as sTEC, relative ionospheric delay, Doppler shift, and ionospheric piercing points. Subsequently, Section 4 presents the results and analysis of the parameters explained in Section 3. Finally, in Section 5, a discussion of the findings is presented along with the conclusions in Section 6.

2. GNSS-R Data and Reflection Events

2.1. LEO Data

The LEO data used in this study consist of a total of 1188 reflection events on 1 March 2021, sourced from Spire Global Inc. Currently, the Spire Lemur-2 constellation comprises more than 80 GNSS radio occultation CubeSats, out of which about 30 have been adapted to acquire GNSS reflectometry measurements at grazing angles [19]. The Lemur-2 satellites follow a Sun-synchronous orbit, with altitudes ranging from 400 to 600 km and varying orbit inclinations. This orbital configuration enables them to conduct GNSS-R measurements, encompassing all latitudes of the Earth.

The Spire grazing angle GNSS-R products are collected with a focus on specific regions, including the polar areas, the Gulf of Mexico, and southeast Asia. These regions are selected due to their favorable characteristics, such as sea ice surfaces and calm ocean surfaces, which enable the best performance of coherent reflectometry measurements [10]. Figure 2 displays the track positions of the specular points distributed across both polar regions, as well as in the mid-latitude and tropical regions at different local times. Given the geographical distribution of the events, the dataset has been categorized into three distinct regions: north, covering latitudes between 40°N and 90°N; tropics, spanning latitudes between 40°N and 40°S; and south, covering latitudes between 40°S and 90°S.

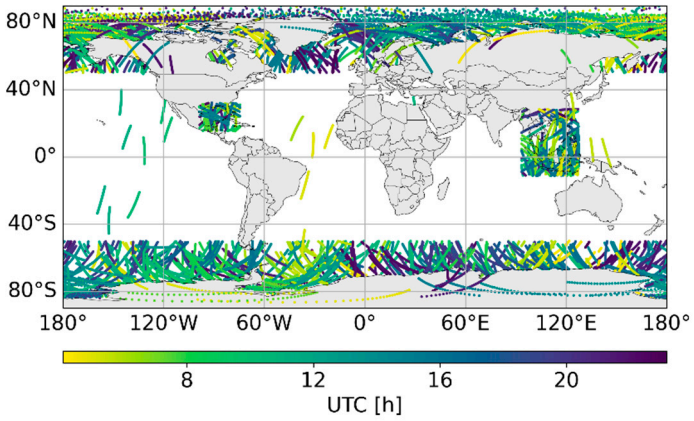

Figure 2. Specular point tracks provided by the Spire Lemur-2 CubeSats on 1 March 2021, color-coded according to coordinated universal time (UTC) in hours.

Each Lemur-2 satellite event lasts an average of 4 min, resulting in a total of about 80 h of recorded data. The recording durations vary, with a minimum of 1 min and a maximum of 6 min. Table 1 shows the number of events per region (north, tropics, and south) along with their corresponding durations in minutes.

Table 1. Total number of events per region and durations.

Region	Number of Events	Total Minutes
North	474	1704
Tropics	168	760
South	546	2335
Total	1188	4798

A total of 21 CubeSats from the Spire constellation are evaluated. The metadata include the space vehicle number (SVN) of the Lemur-2 satellite, as well as information about the GNSS satellite and constellation from which the CubeSat receives the reflected signals. For the simulation in this study, the GNSS constellation employed is GPS (global positioning system). Upon analyzing the Spire data, it is found that each Lemur-2 satellite receives the reflected signal from 4 to 19 GPS satellites during different time windows, depending on the positions of the transmitters and the receiver. The Spire SVN and GPS pseudo-random noise code (PRN) are presented in Table 2.

Table 2. Space Vehicle Numbers of Lemur-2 CubeSats and GPS Satellite PRNs on 01/03/2021.

	Spire SVN	GPS PRN
	79, 84, 99, 100, 101, 102, 103, 104, 106, 113, 115, 116, 117, 119, 120, 121, 122, 124, 125, 128, 129	1, 3, 5, 6, 7, 8, 9, 10, 12, 15, 17, 24, 25, 26, 27, 29, 30, 31, 32
Total	21	19

2.2. Specular Point Positions and Ray Points

The specular point positions and the ray tracing of the direct, incident, and reflected signals are calculated based on the methodology presented in [11,20]. A geometrical model is employed to characterize specular reflections and determine the specular point position, considering the Earth's surface curvature. For this model, the transmitter (T_x) and receiver (R_x) positions are needed in an Earth-centered Earth-fixed (ECEF) frame. The R_x position is extracted from the Spire data files. To obtain this position, the Lemur-2 satellites are equipped with a zenith dual-frequency (L1 and L2) antenna, which facilitates precise orbit

determination (POD). The T_x position is derived from the broadcasted GPS ephemeris. The Earth's curvature is modeled with an osculating spherical surface with respect to the WGS-84 ellipsoid at a reference specular point. An iterative solution is employed to find the best-fitting sphere that satisfies the condition of equal incident and reflected angles (specular reflection) [20]. The specular point positions are calculated at 10 s intervals on the receiver trajectory. A ray-tracing module is set to compute ray points every 10 km along the three ray paths: T_x to SP (incident), SP to R_x (reflected), and T_x to R_x (direct). The positions of the ray points (latitude, longitude, and ellipsoidal height) are subsequently utilized to obtain the electron density from the ionospheric electron density models. Figure 3 illustrates an example of the electron density retrieval from the NEDM2020 model depicting the change along the specular point tracks every 10 s (blue stars), and the ray points change every 10 km (red dots) along the incident (in), reflected (re), and direct (dr) ray paths.

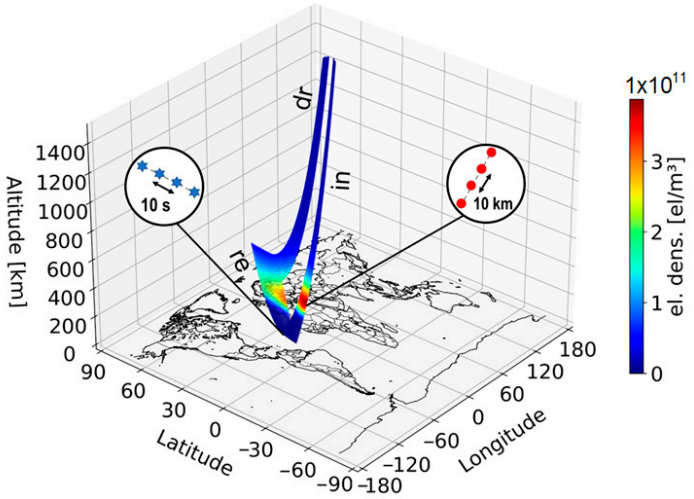

Figure 3. Representation of the specular point change along track (blue stars) for the SVN 79 and PRN 30 every 10 s (~45 km) and the ray points every 10 km along the direct, incident, and reflected ray paths (red dots).

Following the ray tracing, a total of 28,790 reflection events are obtained. The total number of reflection events by region is depicted in Figure 4a. Additionally, Figure 4b illustrates the distribution of reflection events concerning the elevation angle by region. Notably, the south pole region exhibits a higher number of events; however, all regions show similar behavior, with a higher concentration of events in the elevation range between 5° and 20°.

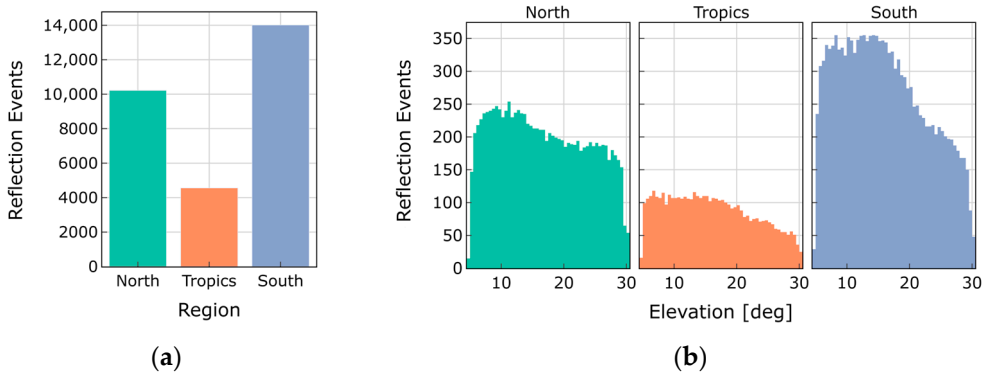

Figure 4. (**a**) Total number of reflection events on 1 March 2021 by region. (**b**) The number of reflection events across grazing angles, ranging from 5° to 30°.

3. Methodology

3.1. Electron Density Models

The electron density in this study is obtained from two three-dimensional and time-dependent electron density models: the Neustrelitz Electron Density Model (NEDM2020) [18] and the NeQuick 2 model [15]. For both models, the input values depending on solar activity are the solar radio flux index F10.7, month, geographic latitude and longitude, height, and universal time (UT). The output obtained is the electron concentration at the specified location and time.

The NeQuick 2 model was developed at the Aeronomy and Radiopropagation Laboratory of The Abdus Salam International Centre for Theoretical Physics (ICTP), Trieste, Italy, and at the Institute for Geophysics, Astrophysics, and Meteorology (IGAM) of the University of Graz, Austria. This model comprises vertical profiles consisting of multiple Epstein layers, and it derives essential electron peak density and height parameters through spatial and temporal interpolation from a comprehensive set of global maps. Consequently, NeQuick 2 incurs significant computational demands in terms of time and processing power [14].

On the other hand, the NEDM2020 model was developed at the German Aerospace Center in the Institute for Solar–Terrestrial Physics (DLR-SO), Neustrelitz, Germany. Including the NTCM model, this model relies on about 100 model coefficients and a set of empirically fixed parameters. Remarkably, the electron density values can be directly computed for any specified location and time without the requirement for the specialized temporal or spatial interpolation of parameters, making it faster than the NeQuick 2 model in terms of computational efficiency [21].

A model comparison of electron density profiles is presented in Figure 5 featuring one example at very low (first row) and mid-low (second row) elevation angle events. The first column displays the electron density per ray mapped along the specular point change using the NEDM2020 model. The subsequent columns (second, third, and fourth) illustrate the electron density profile comparison between the NEDM2020 and NeQuick 2 models for the incident, reflected, and direct rays, respectively.

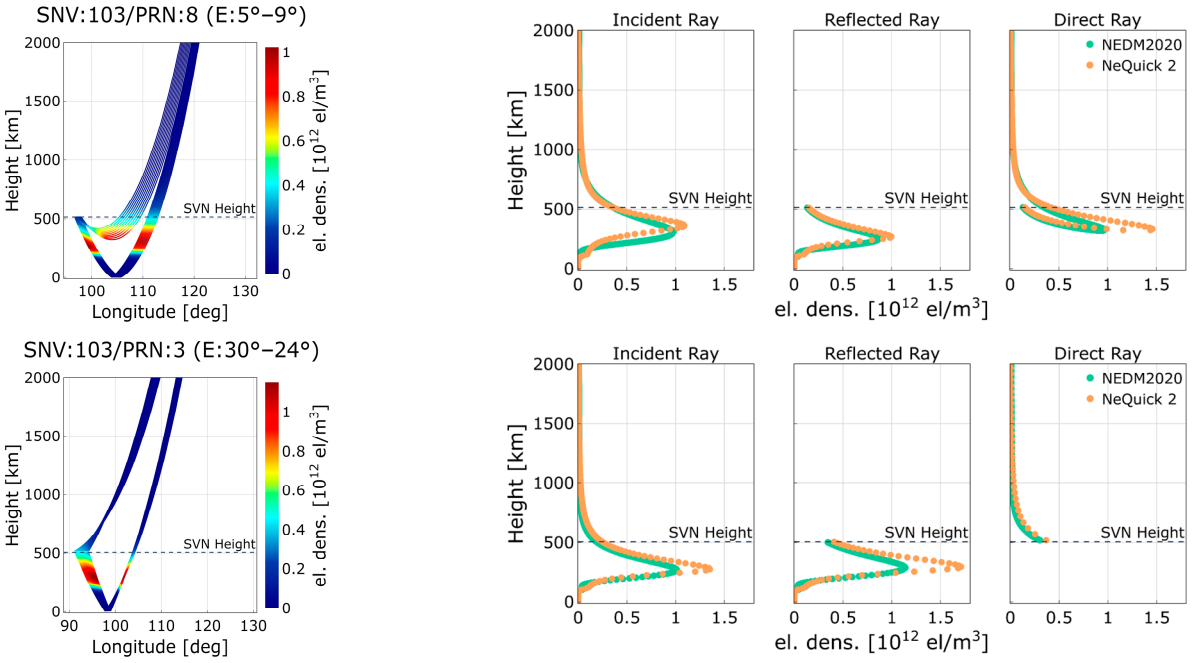

Figure 5. Electron density variations along the change and model profile comparison for the incident, reflected, and direct rays at very low and mid-low elevation angles (F10.7 = 75).

3.2. Ionospheric Group Delay Computation

The GNSS electromagnetic signal propagation speed in the ionosphere depends on electron density (N_e), which is influenced by daytime ionization and nighttime recombination processes. According to [13], when considering the signal code measurements, the difference between the measured range (using a signal of frequency f in Hz) and the Euclidean distance between the satellite and receiver is expressed as follows:

$$\Delta_{gr}^{iono} = +\frac{40.3}{f^2}\int N_e dl \tag{1}$$

Δ_{gr}^{iono} is the term used for the group ionospheric refraction, and the integral is known as the slant total electron content $(sTEC)$, representing the numerical integration of the electron density along the ray path. f corresponds to the GNSS signal frequency, and in this study, the GPS L1 frequency is 1575.42 MHz. The $sTEC$ is computed for each ray, including the incident $(sTEC_{in})$, reflected $(sTEC_{re})$, and direct $(sTEC_{dr})$ rays, respectively. The $sTEC$ is expressed in total electron content units (TECUs) where one TECU corresponds to 10^{16} electrons per square meter $\left(el/m^2\right)$. Finally, the group ionospheric delay in meters (for each ray) is obtained from:

$$I_{in,re,dr} = +\frac{40.3 * 10^{16}}{f^2} sTEC_{in,re,dr} \tag{2}$$

As presented in [22], the relative delay between the direct and reflected signals is denoted as $\Delta_p = p_r - p_d$, where p_r is the cumulative path of the incident and reflected rays, while p_d corresponds to the direct path. The relative delay can be influenced by various contributing factors, such as the standard sources of delay within the GNSS signals. Therefore, the extended version of Δ_p can be written as:

$$\Delta_p = \Delta_{p_{geo}} + \Delta_{p_{trop}} + \Delta_{p_{iono}} + \Delta_{p_{rgh}} + \Delta_{p_{instr}} + n \tag{3}$$

where $\Delta_{p_{geo}}$ represents the relative geometrical delay, and $\Delta_{p_{trop}}$ and $\Delta_{p_{iono}}$ correspond to the relative tropospheric and ionospheric delays, respectively. $\Delta_{p_{rgh}}$ is a bias induced by the surface roughness. The instrumental error is denoted by $\Delta_{p_{instr}}$, and n represents unmodeled errors.

GNSS-R Group Delay Altimetry and Ionospheric Delay Uncertainty

Based on the analysis conducted in [23], the ionospheric delay constitutes a significant component within the error budget associated with GNSS-R ocean surface altimetry retrievals. At elevation angles above 60°, the uncorrected ionospheric delay can reach ~15 m during daytime and ~7 at nighttime. The ionospheric group delay bias propagates to an altimetric bias based on the relation between the height offset Δ_h and the signal path Δ_p. Consequently, when considering only the ionospheric altimetric error, where E is the elevation angle, it can be expressed as:

$$\Delta h_{iono} = \frac{\Delta_{p_{iono}}}{2 * \sin E} \tag{4}$$

Assuming a relative uncertainty of 30% for the ionospheric delay bias, as established in [20], we introduce normally distributed random errors with a respective standard deviation $\left(\delta_{iono} = \mathrm{N}\left(0, 0.3^2\right)\right)$.

3.3. Doppler Shift Computation

The Doppler shift of a GNSS signal is predominantly influenced by the relative velocity between the transmitter satellite and the receiver, along with a common offset that is proportional to the error in the receiver clock's frequency. However, as demonstrated in [24,25], various ionospheric effects, such as changes in the redistribution and density

of electrons in the ionosphere, lead to frequency variations in the electromagnetic waves emitted by a stable transmitter. These variations are manifested as the Doppler shift and can be quantified as the time derivative of the phase path of the signal. When considering only the ionospheric delay term in the carrier phase observation model [26], the residual phase path expressed in units of cycles can be given by:

$$\phi = \frac{\Delta_{p_{iono}}}{\lambda} \tag{5}$$

where λ is the wavelength of the GPS L1 frequency (0.1905 m). As the Doppler shift (f_d) of a given signal corresponds to the rate of change of its carrier phase over time, it can be computed using the following equation:

$$f_d = \frac{d\phi}{dt} \tag{6}$$

3.4. Peak Electron Density Height

Diurnal variations significantly impact the ionosphere, where daytime and nighttime conditions manifest contrasting characteristics. The properties of the ionosphere, such as height, ionized particle concentration, and the presence of distinct layers, change dynamically over time. Regions characterized by high electron densities are designated as the D, E, and F layers. In diurnal cycles, the F layer undergoes separation into two distinct layers termed the F1 and F2 during daytime, while the D layer experiences complete dissipation throughout the nocturnal period [27]. This shifts the height at which the high electron concentration is found. In order to analyze changes in the ionospheric altitude, the height corresponding to the maximum peak of the electron density profile (Hm) is used as the reference point. Hm is obtained for both the incident and reflected rays using the NEDM2020 model.

The LEO GNSS-R space-borne configuration, which enables the simultaneous collection of data from multiple reflections, presents several advantages for ionospheric studies. Firstly, thanks to the fast trajectory change of the LEO satellite, the GNSS-R signal rapidly scans along the ionospheric layers, providing a snapshot view of ionospheric structures [8]. Secondly, the ability to obtain peak electron density points at different locations within a short time interval allows for the mapping of ionospheric structures at varying distances. Assuming the Earth's radius is 6371 km, with a maximum electron density ionospheric shell at a 300 km height, the distance between the incident and reflected Hm points varies depending on the elevation angle as observed in Figure 6.

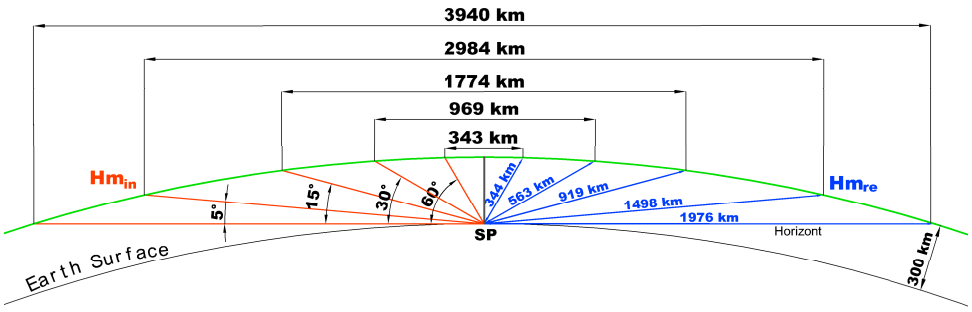

Figure 6. Distances between peak electron density height points depending on the elevation angle change at 300 km height.

4. Results

4.1. Slant Total Electron Content Analysis

The computed sTEC, obtained from the NEDM2020 and NeQuick 2 models, serves as the foundational parameter for the subsequent derivations of the relative ionospheric

group delay and Doppler shift. The assessment of the sTEC is presented across different grazing elevation ranges: 5°–10° (very low), 10°–20° (low), and 20°–30°(mid-low), along with the distinct regions of north, tropics, and south. The outcomes of the NEDM2020 and NeQuick 2 sTEC computations during LSA are depicted in Figures 7 and 8, respectively. While discrepancies of up to ~60 TECUs between the two models are noticeable in the tropics region at very low angles for the direct ray, both models consistently demonstrate similar behavior across all analyzed scenarios.

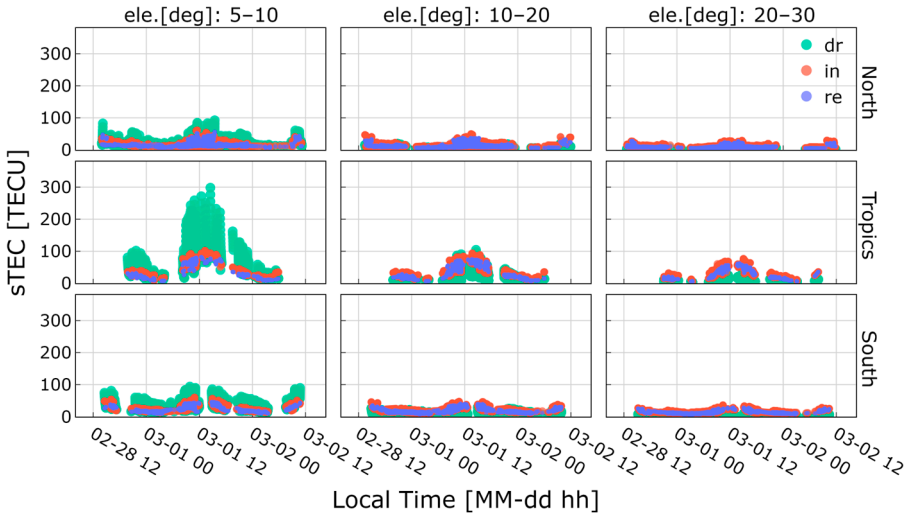

Figure 7. sTEC obtained from NEDM2022 model. Color-coded according to the direct (dr), incident (in), and reflected (re) rays.

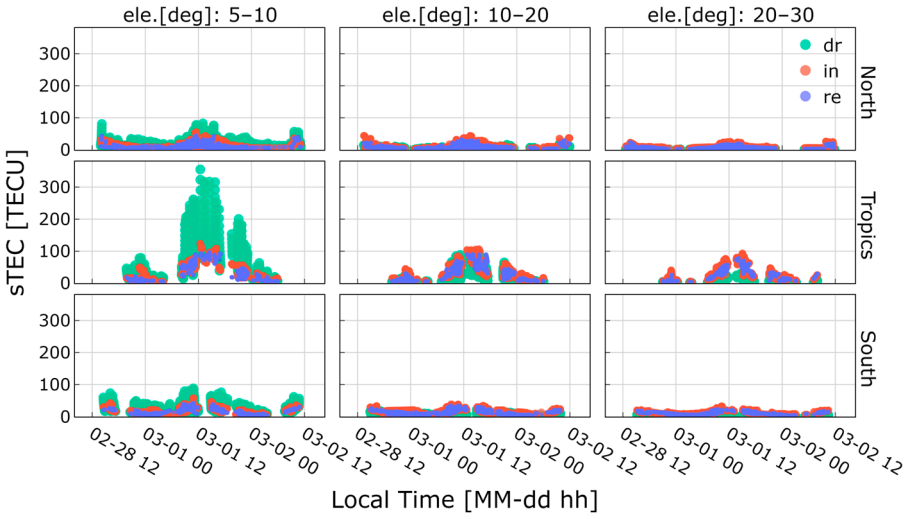

Figure 8. sTEC obtained from NeQuick 2 model. Color-coded according to the direct (dr), incident (in), and reflected (re) rays.

The highest sTEC is prominently observed at elevation angles ranging from 5° to 10° within the tropics region, and to a lesser extent in polar regions, but with lower magnitudes, specifically for the direct ray. This behavior occurs because, at such elevation angles, the direct ray traverses a longer path through the ionosphere than the incident and reflected rays. This effect diminishes as the elevation angle increases. At low elevations, the magnitudes of the sTEC are relatively similar for each ray, while at mid-low elevations, the contribution of the incident and reflected rays becomes more prominent in comparison to the direct ray.

Across all scenarios, local time, representing solar radiation, plays a pivotal role in sTEC retrievals. Figures 7 and 8 illustrate how the sTEC values exhibit a progressive increase as the noon-time period approaches, with the highest peaks occurring between 12:00 and 13:00 h. Following sunset, the electron density and consequently the sTEC values gradually decrease accordingly.

Table 3 provides a comparative analysis of both models, presenting the mean and standard deviation values for each ray in the distinct regions. To facilitate interpretation in terms of local time, the events have been categorized into two distinct periods: daytime (DT), spanning from 06:00 to 18:00, and nighttime (NT), encompassing the interval from 18:00 to 06:00. Notably, the range of sTEC magnitude for the direct ray is broader for the NeQuick model computations in the tropics region. However, the NEDM2020 computations consistently yield a higher mean sTEC in most cases except for the direct ray at very low elevations in the tropics during daytime. Particularly higher differences in mean values between the two models are evident in the south region (~6 TECUs), while comparatively smaller differences are observed in the tropics region (~2 TECUs).

Table 3. sTEC mean and standard deviation value comparison between NEDM2020 and NeQuick 2 models for F10.7 = 75.

		sTEC NEDM (TECU)									**sTEC NeQuick 2 (TECU)**								
		Ele.: 5°–10°			**Ele.: 10°–20°**			**Ele.: 20°–30°**			**Ele.: 5°–10°**			**Ele.: 10°–20°**			**Ele.: 20°–30°**		
		dr	**in**	**re**	**dr**	**in**	**re**	**dr**	**in**	**re**	**dr**	**in**	**re**	**dr**	**in**	**re**	**dr**	**in**	**re**
North																			
DT	mean	28	26	23	8	20	18	3	14	13	21	19	17	6	15	13	3	11	9
	std	13	8	11	3	8	7	1	6	5	12	8	9	3	7	6	1	5	4
NT	mean	21	16	13	7	13	11	3	9	8	14	8	7	4	7	5	2	6	4
	std	10	4	3	3	4	2	1	3	1	7	3	2	2	2	2	1	2	1
Tropics																			
DT	mean	121	72	63	33	62	52	16	48	39	126	63	60	31	57	49	14	43	37
	std	55	16	11	17	16	12	6	14	10	67	20	19	16	22	17	6	19	14
NT	mean	43	29	20	17	27	18	10	22	15	40	26	16	14	27	17	8	21	16
	std	25	9	7	7	7	6	3	6	4	35	16	12	10	16	11	6	12	10
South																			
DT	mean	43	34	32	13	28	25	6	22	18	31	26	25	10	22	20	5	17	14
	std	16	8	6	5	7	5	1	5	4	14	7	5	3	6	4	1	4	3
NT	mean	29	20	16	10	17	14	5	13	11	15	10	7	5	8	6	2	7	5
	std	10	4	3	4	3	2	1	2	2	8	4	3	2	3	2	1	2	2

4.2. Relative Ionospheric Group Delay Analysis

The relative ionospheric group delay $(\Delta_{p_{iono}})$ denotes the additional delay caused by the ionosphere along the aggregated path of the incident and reflected signals, in comparison to the direct signal. The mitigation of ionospheric delay holds significant importance in reflectometry LEO single-frequency missions, particularly within altimetry applications. The analysis of the relative ionospheric delay follows a similar approach to the sTEC analysis, encompassing the established regions, elevation angle ranges, local time variations, and the change in solar flux index. Figure 9 illustrates the potential ionospheric delays that arise from utilizing the sTEC derived from the NEDM2020 and NeQuick 2 models in conjunction with the GPS L1 frequency and F10.7 = 75.

Consistent with the sTEC analysis outcomes, it is observed that $\Delta_{p_{iono}}$ exhibits greater magnitudes within the tropics region, with the highest values occurring at very low elevation angles for both models. The occurrence of negative values in the relative ionospheric delay is attributed to the dominance of the direct signal contribution in the computation of $\Delta_{p_{iono}}$.

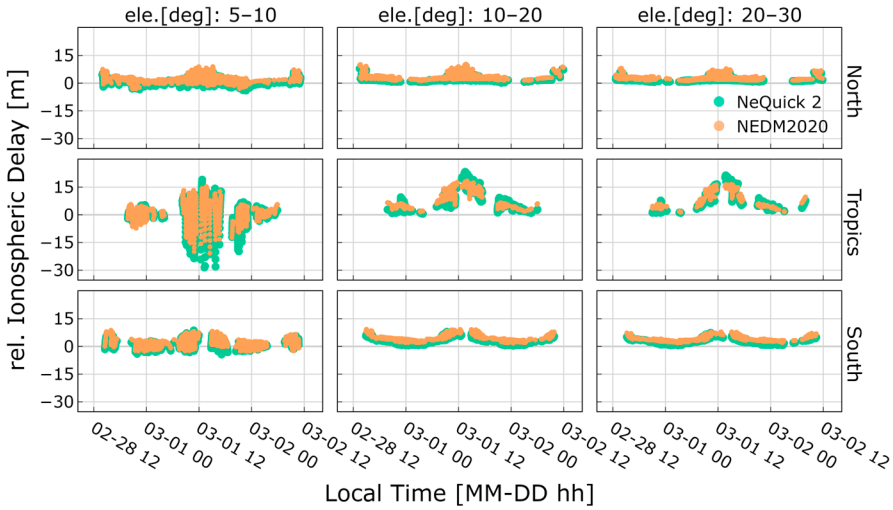

Figure 9. Relative ionospheric delay in the distinct regions and grazing angle elevation ranges along with local time variations.

While the outcomes from both models exhibit very similar behavior in terms of relative ionospheric delay, including their dependence on region, elevation angle, and local time, there are noticeable relative differences across the established groups. Taking as a reference the NEDM2020 model, the mean relative difference is computed as follows:

$$\%RD = \frac{mean\left(\left|\Delta_{p_{iono}}^{NeQuick\ 2} - \Delta_{p_{iono}}^{NEDM2020}\right|\right)}{mean\left(\left|\Delta_{p_{iono}}^{NEDM2020}\right|\right)} * 100 \quad (7)$$

Table 4 presents the mean relative differences between low- and high-solar-activity conditions. During LSA, the most significant relative differences occur at very low elevation angles in both the north and south regions during nighttime, showing a notable 64% variation between the two models. This difference decreases as the elevation angle increases. Conversely, during daytime, the differences in the polar regions remain relatively consistent across all scenarios, while variations are more pronounced in the tropics region. During HSA, during nighttime in the north region, the differences can reach up to 98% at very low elevation angles, while in the south region, the differences remain relatively similar when comparing low and high solar activity. In the tropics, an increase in the F10.7 index leads to a higher relative difference between the models during nighttime. However, during daytime, this difference decreases compared to the low-solar-activity condition (F10.7 = 75).

Table 4. Mean relative difference in the relative ionospheric delay between NEDM2020 and NeQuick 2 during high and low solar activity.

	LSA (F10.7 = 75)			**HSA (F10.7 = 180)**		
	Ele.: 5°–10°	**Ele.: 10°–20°**	**Ele.: 20°–30°**	**Ele.: 5°–10°**	**Ele.: 10°–20°**	**Ele.: 20°–30°**
North						
DT	30%	28%	26%	59%	17%	15%
NT	64%	49%	46%	98%	38%	28%
Tropics						
DT	48%	17%	17%	27%	16%	14%
NT	58%	35%	38%	88%	76%	48%
South						
DT	19%	21%	23%	41%	21%	24%
NT	64%	53%	51%	66%	56%	51%

The sTEC outcomes obtained from the NEDM2020 model, utilized as the reference model in this study, form the basis for the following analysis. Figure 10 illustrates the ionospheric delay distribution during low solar activity, categorized by elevation angles, regions, and local time distinguishing between daytime and nighttime. At low and mid-low elevation angles, the contribution of each ray to the delay remains relatively similar in magnitude, resulting in positive values for the relative ionospheric delay. Overall, during daytime events, the $\Delta_{p_{iono}}$ is on average 120% greater compared to nighttime events.

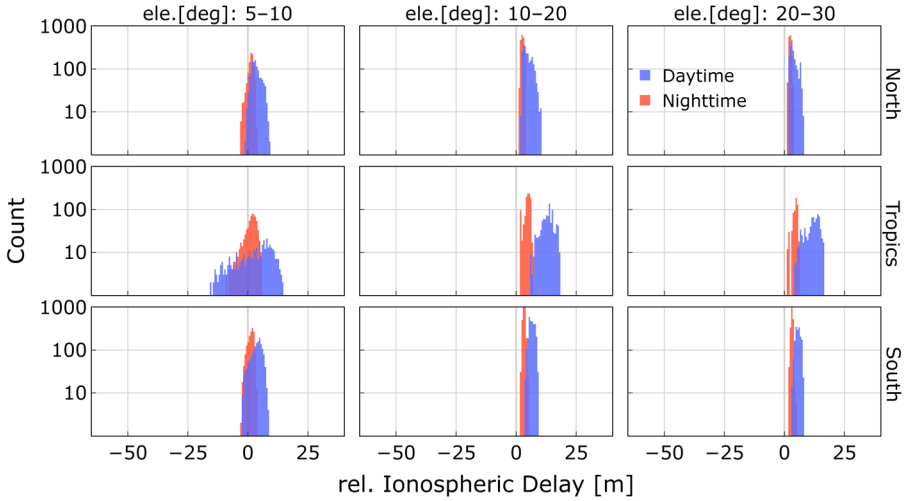

Figure 10. Distribution of relative ionospheric delay depending on elevation, daytime (DT), and nighttime (NT) using NEDM2020 sTEC retrievals with F10.7 = 75.

During HSA periods (F10.7 = 180), the relative ionospheric delay range can increase by up to 200% with respect to low-solar-activity periods, as seen in Figure 11. In low- and mid-low-elevation scenarios, the distribution of $\Delta_{p_{iono}}$ behaves similarly to LSA but with higher magnitude values. Notably, in the tropics region at very low elevations, the distribution is more widespread, with relative delays primarily consisting of negative values. This highlights the higher influence of the direct ray on $\Delta_{p_{iono}}$ compared to low-solar-activity periods.

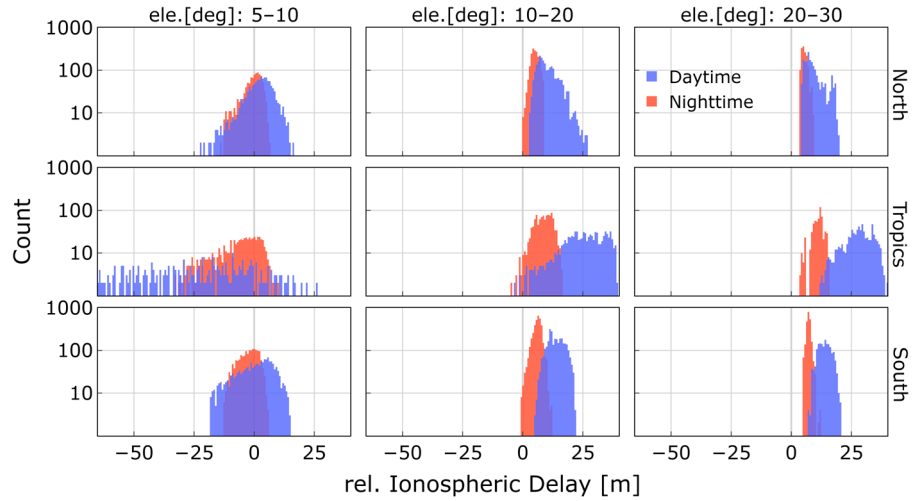

Figure 11. Distribution of relative ionospheric delay depending on elevation, daytime (DT), and nighttime (NT) using NEDM2020 sTEC retrievals with F10.7 = 180.

Group Delay Altimetry and Ionospheric Delay Uncertainty Analysis

As a single-frequency GNSS-R mission, PRETTY relies on ionospheric correction models to ensure precise sea surface height measurements, introducing a level of model uncertainty in the correction process. Figure 12 presents the altimetric uncertainty at grazing elevation angles. Figures 10 and 11 depict the distribution of the relative ionospheric delay, showing a noticeable diurnal cycle effect where daytime observations exhibit higher relative ionospheric delays compared to nighttime observations. This diurnal variation is also reflected in the sea surface height uncertainties. Furthermore, it is evident that ionospheric uncertainties have a significantly greater impact on sea height retrievals in the Tropics region, where the general level of ionization is higher. In this geographical area, we observe a higher altimetric uncertainty dispersion, particularly in the mid-low elevation angle regime (during daytime, 0.22 m mean and 4.08 m std), where the combined delay of the incident and reflected rays surpasses that of the direct ray. Consequently, this leads to higher relative delays and, by extension, a more pronounced impact on GNSS-R altimetric retrievals within this specific elevation range and region.

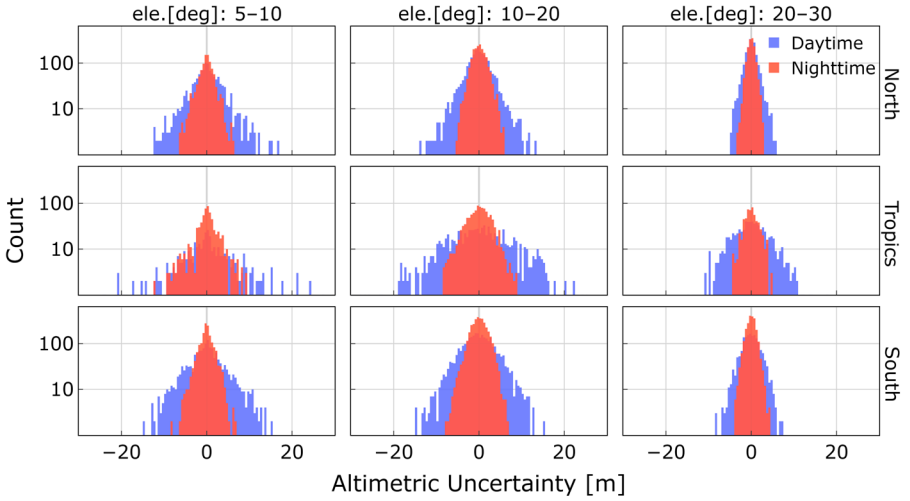

Figure 12. Altimetric uncertainty due to uncertainty in ionospheric delay model depending on elevation, daytime (DT), and nighttime (NT) using NEDM2020 during LSA.

4.3. Doppler Shift Analysis

The analysis extends to the Doppler shift observed at the GPS L1 frequency across varying ranges of elevation angles, while considering effects during both day and night periods. Figure 13 illustrates the distribution of the Doppler shift during low solar activity. The electron density variations in grazing angle reflectometry can induce a maximum Doppler shift of ± 2 Hz in the GPS L1 signal during daytime. The attenuation in the Doppler shift demonstrates a strong correlation with diurnal cycles, resulting in a reduction during nighttime periods. This phenomenon can be attributed to the decrease in the rate of electron density changes, which in turn leads to a corresponding decrease in the magnitude of the Doppler shift.

The Doppler shift histograms reveal a symmetrical distribution centered around approximately 0 Hz with a distinct separation in very-low-elevation cases. The distribution is also influenced by the transmitter motion relative to the specular point elevation angle. In Figure 14, it becomes evident that at very low elevation angles, a rising transmitter (ascendant elevation) induces a positive Doppler shift, while a setting transmitter (descendant elevation) results in a negative Doppler shift. However, at higher elevation angles (20° to 30°), the relationship may vary or even reverse.

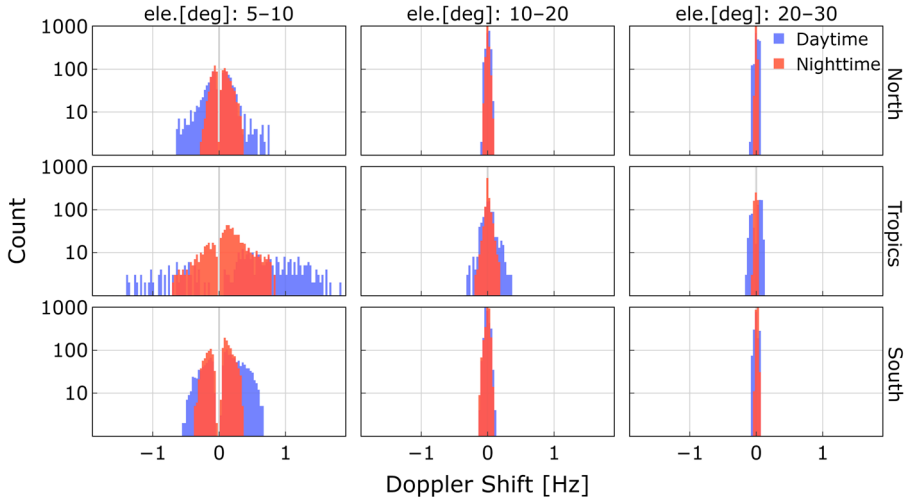

Figure 13. Distribution of Doppler shift depending on elevation, daytime (DT), and nighttime (NT) using NEDM2020 sTEC retrievals with F10.7 = 75.

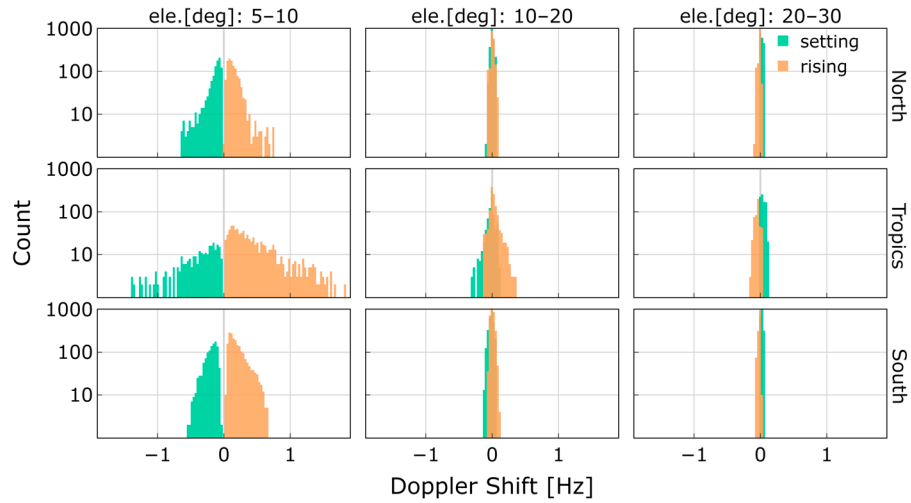

Figure 14. Distribution of Doppler shift depending on elevation and rising or setting event using NEDM2020 sTEC retrievals with F10.7 = 75.

The distribution of the Doppler shift for F10.7 = 180 exhibits an increase in dispersion, approximately doubling in all scenarios. In the elevation range of 5°–10° within the tropics region, the range of f_d is more extensive during daytime, reaching maximum values of up to ±4 Hz. The rising and setting event analyses present similar behavior, with negative magnitudes primarily observed during rising events and positive magnitudes during setting events.

4.4. Peak Electron Density Height Analysis

The NEDM2020 model is employed to determine the height at which the maximum electron density peak *Hm* is observed along the paths of both the incident and reflected rays. This altitude is significant as it represents the point of maximum ionization within the ionosphere that the signals traverse.

From a geometrical standpoint within the grazing GNSS-R configuration, variations in elevation angles directly correspond to changes in the segment of the signal ray that travels along the ionosphere. Furthermore, throughout the diurnal cycle, electron densities within the E and F layers exhibit greater magnitudes during daylight hours compared to nighttime, with the F layer generally obtaining higher electron concentrations. These fluctuations are examined to comprehend the intricate ionospheric interactions that the signals undergo

during their propagation. This phenomenon results in variations in the height of the maximum electron density peak, as depicted in Figure 15 for both day and nighttime.

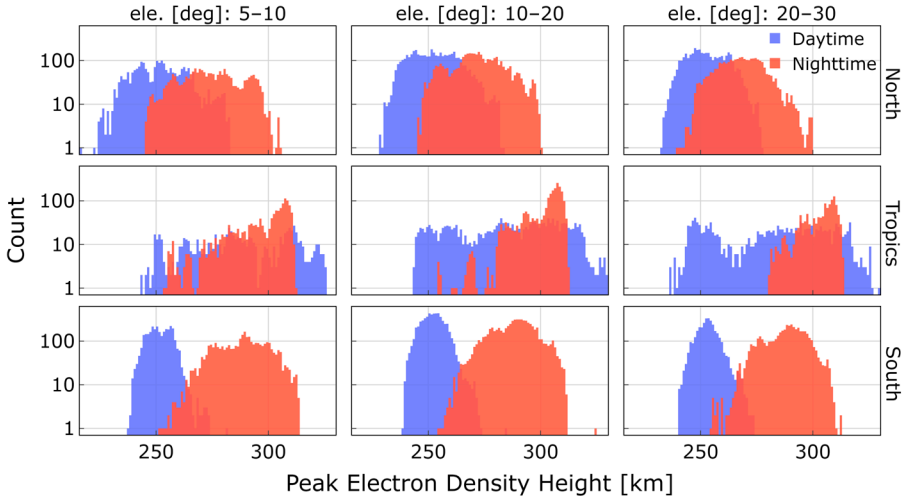

Figure 15. Peak electron density height variations depending on elevation ranges, regions, and day and nighttime using NEDM2020 sTEC retrievals with F10.7 = 75.

The overall average of the *Hm* during the LSA period is 270 km. Nevertheless, noticeable variations are evident with respect to daytime and nighttime. In general, during nighttime, the *Hm* is on average 10% higher than during daytime. The tropics region stands out as one of the most dynamically changing areas within the ionosphere. In this zone, the distribution of *Hm* during daytime exhibits a spread ranging from 236 to 326 km, lacking a distinct peak value. However, during nighttime, *Hm* reaches its maximum value at approximately 305 km. This highlights the substantial variations in electron density within this region, particularly during daytime. During HSA, the *Hm* exhibits a consistent increase of 21% across all scenarios.

5. Discussion

The analysis provides valuable insights into how ionospheric parameters such as slant total electron content, relative ionospheric delay, Doppler shift, and peak electron density height vary in response to different conditions. These findings are crucial for optimizing the accuracy of space-borne GNSS-R applications, particularly in altimetry, aiding in the development of robust models, and enhancing the interpretation of data acquired through grazing GNSS-R configurations.

Under low-solar-activity conditions (F10.7 = 75), the resulting sTEC values from NEDM2020 and NeQuick 2 reveal that both models exhibit similar behavior across different scenarios. However, it is important to note that while an extensive evaluation of the models is not carried out in this study, differences in the sTEC computations and the relative total delay are observed. Significant differences of ~60 TECUs and up to 64% in relative ionospheric delay are observed in polar regions at very low elevation angles during daytime when comparing NEDM2020 and NeQuick 2. Under high-solar-activity conditions (F10.7 = 180), the relative differences can reach values up to 98%.

Grazing elevation angles, local time, regions, and solar activity emerge as the crucial factors determining ionospheric effects in GNSS-R. The observed elevation angle significantly influences the path traversed by GNSS signals through the ionosphere, while electron density variations rising from ionospheric diurnal cycles and geographical location contribute to fluctuations in the sTEC computation. The sTEC values exhibit a noticeable increase as the elevation angle decreases (very low to mid-low angles) in all regions during both daytime and nighttime.

Daytime events consistently result in higher sTEC values, larger relative ionospheric delay values, and higher Doppler shift magnitudes compared to nighttime events across all regions and elevation angles. The tropics region consistently displays the highest sTEC values across all elevation angle ranges, indicating the presence of higher electron densities. To provide a comprehensive synthesis of the study's findings based on the electron density retrievals from the NEDM2020 model, Tables 5 and 6 provide a summary of the results by presenting the median and standard deviation for each parameter outlined in the Section 4 for F10.7 = 75 and F10.7 = 180, respectively. The parameters provided by the summary tables are the relative ionospheric delay $(\Delta_{p_{iono}})$ in meters, absolute value of Doppler shift $(|f_d|)$ in Hertz, and peak electron density height (Hm) in kilometers.

Table 5. Overview of ionospheric parameters from the NEDM2020 sTEC computations during low solar activity (F10.7 = 75).

		Very Low: 5°–10°			**Low: 10°–20°**			**Mid-Low: 20°–30°**		
		$\Delta_{p_{iono}}$ **(m)**	$\lvert f_d \rvert$ **(Hz)**	Hm **(km)**	$\Delta_{p_{iono}}$ **(m)**	$\lvert f_d \rvert$ **(Hz)**	Hm **(km)**	$\Delta_{p_{iono}}$ **(m)**	$\lvert f_d \rvert$ **(Hz)**	Hm **(km)**
North										
DT	median	3.10	0.133	251.7	4.35	0.022	252.3	3.33	0.026	252.2
	std	1.96	0.142	11.7	1.81	0.019	10.5	1.44	0.021	8.5
NT	median	1.38	0.097	274.0	2.61	0.009	271.9	2.27	0.011	268.3
	std	1.19	0.067	12.9	0.60	0.014	11.6	0.47	0.006	9.7
Tropics										
DT	median	3.96	0.729	287.9	13.50	0.048	287.4	12.12	0.067	285.3
	std	7.57	0.415	21.4	2.61	0.070	22.4	2.87	0.028	23.8
NT	median	1.63	0.219	302.6	4.95	0.016	305.4	4.74	0.014	305.4
	std	2.82	0.195	13.1	1.18	0.033	9.1	1.05	0.013	7.3
South										
DT	median	3.98	0.220	252.2	6.49	0.030	252.2	5.63	0.014	253.1
	std	2.26	0.138	5.2	1.15	0.021	5.2	1.02	0.022	4.9
NT	median	1.41	0.145	289.0	3.36	0.012	288.8	3.17	0.015	289.1
	std	1.27	0.073	11.2	0.48	0.021	9.8	0.40	0.007	9.2

In general, as the F10.7 index increases, notable observations emerge: (1) There is a compensation effect, attributed to the direct signal contribution, leading to a decrease in the median level of relative ionospheric delay as elevation decreases, particularly at very low elevations. (2) The absolute Doppler shift exhibits a substantial increase in median values, scaling up to one order of magnitude, as elevation angles decrease to their lowest. (3) Notably, in tropical regions characterized by higher density peak heights, there is a more pronounced compensation by direct signal contribution in $\Delta_{p_{iono}}$ at the lowest elevations, resulting in negative median delay values.

For a LEO GNSS-R mission employing the GPS L1 frequency, findings show that relative ionospheric delays can reach ~19 m during periods of LSA and ~70 m during HSA, equivalent to about 120 and 430 TECUs. The forthcoming ESA PRETTY mission will pioneer grazing altimetry at the L5 frequency, which, with its longer wavelength (~0.2548 m), is more sensitive to ionospheric group delays. Using 120 and 430 TECUs as benchmarks, relative ionospheric corrections of approximately 35 and 125 m can be expected for group delay altimetry during low and high solar activity.

Table 6. Overview of ionospheric parameters from the NEDM2020 sTEC computations during high solar activity (F10.7 = 180).

		Very Low: 5°–10°			**Low: 10°–20°**			**Mid-Low: 20°–30°**		
		$\Delta_{p_{iono}}$ **(m)**	$\lvert f_d \rvert$ **(Hz)**	Hm **(km)**	$\Delta_{p_{iono}}$ **(m)**	$\lvert f_d \rvert$ **(Hz)**	Hm **(km)**	$\Delta_{p_{iono}}$ **(m)**	$\lvert f_d \rvert$ **(Hz)**	Hm **(km)**
North										
DT	median	2.77	0.516	306.8	9.18	0.075	307.6	8.09	0.049	307.5
	std	6.00	0.496	13.9	4.24	0.085	12.7	3.79	0.043	10.4
NT	median	0.03	0.330	333.8	5.11	0.051	331.7	5.31	0.015	327.2
	std	3.90	0.148	15.9	1.64	0.066	14.4	1.16	0.011	12.0
Tropics										
DT	median	−21.45	2.329	349.5	25.56	0.246	348.4	28.45	0.139	345.2
	std	24.43	0.698	26.7	9.30	0.377	27.3	5.96	0.068	28.9
NT	median	−5.21	0.817	368.1	8.82	0.144	371.9	11.55	0.022	371.9
	std	9.88	0.352	15.7	3.74	0.173	10.9	2.40	0.024	8.8
South										
DT	median	1.46	0.812	307.2	13.57	0.084	306.9	13.97	0.037	307.9
	std	7.58	0.333	6.5	3.39	0.109	6.4	2.62	0.043	6.0
NT	median	−1.98	0.472	351.7	6.26	0.081	351.2	7.17	0.015	351.8
	std	3.99	0.146	14.1	1.84	0.092	12.3	0.92	0.015	11.4

6. Conclusions

In this paper, we have analyzed ionospheric effects in GNSS-R at grazing angles. This study encompasses the characterization of slant total electron content, relative ionospheric delay, the influence of ionospheric correction model uncertainties on GNSS-R group delay altimetry retrievals, the Doppler effect, and peak electron density height changes. Various factors have been considered such as satellite geometry, latitude-dependent regions, temporal variations, and solar activity.

When analyzing the results during LSA (low solar activity) and HSA (high solar activity), it becomes evident that as the elevation decreases into the grazing regime below 20°, the median relative ionospheric delay decreases due to the compensation from the direct signal contribution. However, it is important to note that the standard deviation of the delay, especially in terms of the Doppler shift, undergoes a substantial increase. This behavior poses a significant challenge for the model-based correction of ionospheric delay in GNSS reflectometry altimetry at grazing elevation angles.

While model uncertainties do affect group delay sea height estimates it is important to highlight that these effects are not uniform across all GNSS-R observations. Coherent phase observations, for instance, offer a remarkable level of precision, down to the centimeter scale. Along reflection tracks characterized by consistent ionospheric bias, relative altimetry at a centimeter precision level can be achieved. This means that even in the presence of ionospheric delay bias, LEO space-borne GNSS-R systems, as reported in [26], can still provide precise results in the altimetric inversion.

Total electron content, a crucial ionospheric parameter, exhibits complex variations spanning diurnal, monthly, seasonal, and 11-year solar cycles. Extended temporal coverage is essential for deciphering these patterns, especially in dynamic regions allowing analysis of seasonal trends. This study highlights the importance of spatially extended data, particularly in tropical areas with substantial ionospheric variability. Such data is key to comprehending ionospheric parameter evolution across different time scales and regions, influenced by factors like solar activity and geomagnetic storms.

GNSS-R (global navigation satellite system reflectometry) stands as a valuable and complementary remote sensing tool in ionospheric studies, effectively addressing areas not covered by alternative methods. This capacity offers significant contributions to the modeling, prediction, and comprehension of ionospheric effects.

Author Contributions: Conceptualization: M.M., M.S. and G.S.; methodology: M.M., M.S. and G.S.; software: M.M. and M.S.; data resources: M.M. and M.S.; writing—original draft preparation: M.M.; writing—review and editing: M.S., G.S., M.H. and J.W.; visualization, M.M.; supervision, M.S., J.W. and M.H. All authors have read and agreed to the published version of the manuscript.

Funding: This research was funded by the German Aerospace Center, Institute for Solar-Terrestrial Physics (DLR-SO).

Data Availability Statement: Data are available under the authorization of Spire Global Inc.

Acknowledgments: The authors would like to thank Spire Global for providing real orbit from Lemur-2 constellation LEO satellites.

Conflicts of Interest: The authors declare no conflict of interest. The funders had no role in the design of the study; in the collection, analyses, or interpretation of data; in the writing of the manuscript, or in the decision to publish the results.

References

1. Hagfors, T. 2.1. The Ionosphere. In *Methods in Experimental Physics*; Meeks, M.L., Ed.; Astrophysics; Academic Press: Cambridge, MA, USA, 1976; Volume 12, pp. 119–135.
2. Dubey, S.; Wahi, R.; Gwal, A.K. Ionospheric Effects on GPS Positioning. *Adv. Space Res.* **2006**, *38*, 2478–2484. [CrossRef]
3. Wickert, J.; Michalak, G.; Schmidt, T.; Beyerle, G.; Cheng, C.Z.; Healy, S.B.; Heise, S.; Huang, C.Y.; Jakowski, N.; Kohler, W.; et al. GPS Radio Occultation: Results from CHAMP. GRACE and FORMOSAT-3/COSMIC. *Terr. Atmos. Ocean. Sci.* **2009**, *20*, 35–50. [CrossRef]
4. Xing, J.; Datta-Barua, S.; Garrison, J.; Ridley, A.; Pervan, B. Relative Ionospheric Ranging Delay in LEO GNSS Oceanic Reflections. *IEEE Geosci. Remote Sens. Lett.* **2015**, *12*, 1416–1420. [CrossRef]
5. Ruf, C.; Gleason, S.; Jelenak, Z.; Katzberg, S.; Ridley, A.; Rose, R.; Scherrer, J.; Zavorotny, V. The NASA EV-2 Cyclone Global Navigation Satellite System (CYGNSS) Mission. In Proceedings of the 2013 IEEE Aerospace Conference, Big Sky, MT, USA, 2–9 March 2013; pp. 1–7.
6. Camps, A.; Park, H.; Foti, G.; Gommenginger, C. Ionospheric Effects in GNSS-Reflectometry From Space. *IEEE J. Sel. Top. Appl. Earth Obs. Remote Sens.* **2016**, *9*, 5851–5861. [CrossRef]
7. Unwin, M.; Jales, P.; Tye, J.; Gommenginger, C.; Foti, G.; Rosello, J. Spaceborne GNSS-Reflectometry on TechDemoSat-1: Early Mission Operations and Exploitation. *IEEE J. Sel. Top. Appl. Earth Obs. Remote Sens.* **2016**, *9*, 4525–4539. [CrossRef]
8. Wang, Y.; Morton, Y.J. Ionospheric Total Electron Content and Disturbance Observations From Space-Borne Coherent GNSS-R Measurements. *IEEE Trans. Geosci. Remote Sens.* **2022**, *60*, 1–13. [CrossRef]
9. Liu, L.; Morton, Y.J.; Wang, Y.; Wu, K.-B. Arctic TEC Mapping Using Integrated LEO-Based GNSS-R and Ground-Based GNSS Observations: A Simulation Study. *IEEE Trans. Geosci. Remote Sens.* **2022**, *60*, 1–10. [CrossRef]
10. Roesler, C.; Wang, Y.; Morton, Y.J.; Nerem, R.S. Coherent GPS Reflections Over Ocean Surface. In Proceedings of the IGARSS 2020–2020 IEEE International Geoscience and Remote Sensing Symposium, Waikoloa, HI, USA, 26 September–2 October 2020; pp. 6218–6221.
11. Moreno, M.; Semmling, M.; Stienne, G.; Dalil, W.; Hoque, M.; Wickert, J.; Reboul, S. Airborne Coherent GNSS Reflectometry and Zenith Total Delay Estimation over Coastal Waters. *Remote Sens.* **2022**, *14*, 4628. [CrossRef]
12. Issa, H.; Stienne, G.; Reboul, S.; Raad, M.; Faour, G. Airborne GNSS Reflectometry for Water Body Detection. *Remote Sens.* **2021**, *14*, 163. [CrossRef]
13. Subirana, J.S.; Zornoza, J.M.J.; Hernández-Pajares, M. *GNSS Data Processing*; Contactivity bv; ESA Communications: Leiden, The Netherlands, 2013; Volume I, Fundamentals and Algorithms; ISBN 978-92-9221-886-7.
14. Hoque, M.M.; Jakowski, N.; Osechas, O.; Berdermann, J. Fast and Improved Ionospheric Correction for Galileo Mass Market Receivers. In Proceedings of the 32nd International Technical Meeting of the Satellite Division of the Institute of Navigation (ION GNSS+ 2019), Miami, FL, USA, 11 October 2019; pp. 3377–3389.
15. Nava, B.; Coïsson, P.; Radicella, S.M. A New Version of the NeQuick Ionosphere Electron Density Model. *J. Atmos. Sol. Terr. Phys.* **2008**, *70*, 1856–1862. [CrossRef]
16. Ionospheric Correction Algorithms | European GNSS Service Centre. Available online: https://www.gsc-europa.eu/support-to-developers/ionospheric-correction-algorithms (accessed on 27 July 2023).
17. Dielacher, A.; Fragner, H.; Koudelka, O. PRETTY—Passive GNSS-Reflectometry for CubeSats. *Elektrotech. Inftech.* **2022**, *139*, 25–32. [CrossRef]
18. Hoque, M.M.; Jakowski, N.; Prol, F.S. A New Climatological Electron Density Model for Supporting Space Weather Services. *J. Space Weather Space Clim.* **2022**, *12*, 1. [CrossRef]
19. Nguyen, V.; Jales, P.; Garbacz, H. Spire Earth Observations for NASA's CSDA Program—Lunch & Learn. 2022. Available online: https://www.earthdata.nasa.gov/s3fs-public/2022-10/2022%2010%2006%20Spire%20Earth%20Observations%20for%20NASA%27s%20CSDA%20Program%20-%20Lunch%20%26%20Learn_0.pdf (accessed on 20 July 2023).

20. Semmling, A.M.; Leister, V.; Saynisch, J.; Zus, F.; Heise, S.; Wickert, J. A Phase-Altimetric Simulator: Studying the Sensitivity of Earth-Reflected GNSS Signals to Ocean Topography. *IEEE Trans. Geosci. Remote Sens.* **2016**, *54*, 6791–6802. [CrossRef]
21. Hoque, M.M.; Jakowski, N.; Cahuasquí, J.A. Fast Ionospheric Correction Algorithm for Galileo Single Frequency Users. In Proceedings of the 2020 European Navigation Conference (ENC), Dresden, Germany, 23–24 November 2020; pp. 1–10.
22. Cardellach, E.; Ao, C.O.; de la Torre Juárez, M.; Hajj, G.A. Carrier Phase Delay Altimetry with GPS-Reflection/Occultation Interferometry from Low Earth Orbiters. *Geophys. Res. Lett.* **2004**, *31*. [CrossRef]
23. Mashburn, J.; Axelrad, P.; Lowe, S.T.; Larson, K.M. Global Ocean Altimetry With GNSS Reflections From TechDemoSat-1. *IEEE Trans. Geosci. Remote Sens.* **2018**, *56*, 4088–4097. [CrossRef]
24. Davies, K.; Watts, J.M.; Zacharisen, D.H. A Study of F 2-Layer Effects as Observed with a Doppler Technique. *J. Geophys. Res.* **1962**, *67*, 601–609. [CrossRef]
25. Jacobs, J.A.; Watanabe, T. Doppler Frequency Changes in Radio Waves Propagating Through a Moving Ionosphere. *Radio Sci.* **1966**, *1*, 257–264. [CrossRef]
26. Cardellach, E.; Li, W.; Rius, A.; Semmling, M.; Wickert, J.; Zus, F.; Ruf, C.S.; Buontempo, C. First Precise Spaceborne Sea Surface Altimetry With GNSS Reflected Signals. *IEEE J. Sel. Top. Appl. Earth Obs. Remote Sens.* **2020**, *13*, 102–112. [CrossRef]
27. Teunissen, P.J.G.; Kleusberg, A. GPS Observation Equations and Positioning Concepts. In *GPS for Geodesy*; Kleusberg, A., Teunissen, P.J.G., Eds.; Lecture Notes in Earth Sciences; Springer: Berlin/Heidelberg, Germany, 1996; pp. 175–217. ISBN 978-3-540-49447-8.

Journal of Geodesy (2025) 99:89
https://doi.org/10.1007/s00190-025-02010-z

ORIGINAL ARTICLE

Grazing-angle ionospheric delays observed during the GNSS-R PRETTY mission

Mario Moreno[1,4] · Maximilian Semmling[1] · Florian Zus[2] · Georges Stienne[3] · Andreas Dielacher[5,6] · Mainul Hoque[1] · Jens Wickert[2,4] · Hossein Nahavandchi[7]

Received: 21 November 2024 / Accepted: 30 September 2025

Abstract

Spaceborne GNSS reflectometry (GNSS-R) has emerged as a valuable technique for surface and atmospheric remote sensing, particularly under grazing-angle geometries where atmospheric effects are amplified. Single-frequency missions such as ESA passive REflecTomeTry and dosimetrY (PRETTY) rely on model-based corrections to account for ionospheric and tropospheric delays. In this study, we exploit PRETTY's capabilities to perform observations down to 1 degree (at the specular point) to investigate ionospheric effects at very low angles. We analyze six GNSS-R events recorded over the North Polar region in July 2024, focusing on the estimation of the relative ionospheric delay using code delay observations. Comparisons with model-based ionospheric delays from NEDM2020, NeQuick, and IRI show close agreement, with NEDM2020 consistently exhibiting the lowest residual differences, ranging from 1.28 to 4.39 m across all events. This supports the ability of GNSS-R code delay observables to capture the first-order ionospheric delay with reasonable fidelity. Uncertainty analysis reveals that the observed delay fitting process dominates the overall error budget, with additional contributions from tropospheric correction and surface height uncertainty. Furthermore, inversion of the fitted delays using the Chapman layer model yields plausible F-layer parameters, with peak heights ranging from 307 to 367 km and a mean delay RMSE of approximately 1.2 m (~ 4 TECU). Comparisons with ionosonde and EISCAT measurements show differences within ± 15 km. These results demonstrate the potential of single-frequency GNSS-R missions for retrieving ionospheric structure, particularly in remote regions where conventional techniques are limited or unavailable.

Keywords PRETTY · GNSS reflectometry · Ionospheric delay · Grazing angles · Code delay · NEDM2020 model

1 Introduction

The increasing use of CubeSats in a wide range of applications, including Earth observation and atmospheric science, reflects the growing versatility, reduced cost, and adaptability of these small satellite platforms. CubeSats are now contributing to advanced remote sensing techniques, including Global Navigation Satellite Systems Reflectometry (GNSS-R), which has demonstrated significant potential for monitoring Earth's surface and atmospheric properties. GNSS-R leverages signals from GNSS, reflected off Earth's surface, to derive information on surface characteristics and atmospheric conditions. Beyond its well-established use in sea surface altimetry (Cardellach et al. 2020) and sea ice monitoring (Alonso-Arroyo et al., 2016; Cartwright et al. 2019), GNSS-R is also emerging as a valuable technique for ionospheric and tropospheric studies, particularly in spaceborne Low Earth Orbit (LEO) platforms, enabling applications such

✉ Mario Moreno
mario.moreno@dlr.de

1 Deutsches Zentrum Für Luft- und Raumfahrt, Institut für Solar-Terrestrische Physik (DLR-SO), Neustrelitz, Germany

2 Deutsches GeoForschungsZentrum (GFZ), Potsdam, Germany

3 Laboratoire d'Informatique, Signal et Image de la Côte d'Opale (LISIC), Université Littoral Côte d'Opale (ULCO), Calais, France

4 Technische Universität Berlin (TUB), Berlin, Germany

5 Beyond Gravity Austria GmbH (BGA), Vienna, Austria

6 Technische Universität Graz (TUG), Graz, Austria

7 Norwegian University of Science and Technology (NTNU), Trondheim, Norway

Published online: 25 October 2025

as total electron content (TEC) estimation (Ren et al. 2022) or water vapor retrievals (Wang 2023b).

A critical atmospheric effect that needs to be accounted for spaceborne GNSS-R missions is ionospheric delay. As the GNSS signals traverse through the ionosphere, the TEC induces delays that affect the direct (GNSS-to-LEO), incident (GNSS-to-specular point), and reflected (specular point-to-LEO) paths. This effect is especially pronounced at lower elevation angles, which are typical of spaceborne GNSS-R observations under grazing geometries.

The importance of accounting for ionospheric delays in spaceborne GNSS-R has been highlighted in earlier works. Prior to the Cyclone Global Navigation Satellite System—-CYGNSS mission (Ruf et al. 2013a, b) launched in 2016, Xing et al. (2015) conducted simulations using the International Reference Ionosphere (IRI) Model (Bilitza et al. 2022) to quantify ionospheric delay effects on the Delay Doppler Map (DDM) observables. Their results indicated that the ionospheric delay is inversely proportional to satellite elevation and can reach up to 30 m for elevations as low as 30°. Based on the GNSS-R geometry considered in that study, the relative ionospheric delay was found to be primarily influenced by the contributions of the incident and reflected signal paths.

In another study Camps et al. (2016), used data from the single-frequency TechDemoSat-1 (TDS–1) mission (Unwin et al. 2016) and showed that at 55° elevation, ionospheric delays can range between 1 and 3 TECU (0.16–0.5 m in L1), with signal-to-noise ratio (SNR) fluctuations driven by ionospheric scintillation, especially within $\pm$ 20° latitude of the geomagnetic equator. However, neither of these studies addressed ionospheric effects at grazing geometries where atmospheric effects become even more pronounced and complex.

Recent developments in GNSS-R spaceborne missions have advanced the ionospheric corrections and retrievals, particularly through the use of dual-frequency observations Wang and Morton, (2022). used dual-frequency coherent GNSS-R observations from Spire CubeSats to retrieve relative TEC over sea ice and calm oceans at grazing angles, demonstrating high precision for ionospheric disturbance monitoring. However, these techniques rely on carrier phase observables and are limited in rough ocean regions where coherent reflections are not sustained.

To address these limitations Wang (2023a), introduced a novel approach to estimate ionospheric delay using single-frequency GNSS-R pseudorange measurements, especially leveraging the wideband GPS L5 and Galileo E5 signals. This method aims to extract ionospheric TEC from the residual of modeled pseudorange, correcting for geometric range, clock biases, surface height, and tropospheric delays. Wang presented that with proper corrections, pseudorange-based TEC retrieval can achieve sub-meter precision (2–3.4 TECU) for GPS L5 under moderate sea surface conditions. However, the study used simulations and L1/L2 data due to the lack of actual L5/E5 data at the time.

The ESA PRETTY (Passive Reflectometry and Dosimetry) CubeSat mission (Dielacher et al. 2022), launched in October 2023, represents a novel approach to GNSS-R by utilizing the L5/E5 signal bands for altimetric applications at grazing angles. Developed by Beyond Gravity Austria GmbH, Graz University of Technology, and Seibersdorf Laboratories, PRETTY aims to measure sea surface height and related geophysical parameters such as significant wave height, sea ice type, and concentration, primarily in polar regions, using single-frequency observations. Due to its reliance on a single frequency, PRETTY applies model-based corrections to compensate for atmospheric delays.

PRETTY's onboard software supports observations at very low-elevation angles—down to 0.01°—allowing precise analysis of atmospheric effects on reflected signals. The satellite can operate in both clean replica GNSS-R (cGNSS-R) and interferometric GNSS-R (iGNSS-R) modes. The cGNSS-R mode uses a locally generated reference signal for correlation, while the iGNSS-R relies on the direct signal received by the satellite as the reference for interferometric processing (Cardellach et al. 2018) .

PRETTY mission also provides both code delay and phase observables, offering valuable opportunities for atmospheric and geophysical studies. However, at the time of this study, the phase data and the iGNSS-R observations are still undergoing validation and verification by the mission team and are not yet available for scientific analysis.

In this study, we focus on the estimation of ionospheric delay using PRETTY code delay observations. Previous GNSS-R missions have focused either on correlation maps over delay doppler maps in near-nadir geometry with incidence at the reflection point below 60° (e.g., TDS-1, CYGNSS) or on a single coherent correlator sampling in grazing geometries with respective incidence angle above 60°, as in the spire constellation. The PRETTY mission provides correlation maps highly resolved in delay, even under grazing geometries. It allows us to study atmospheric effects using code delay observations in the grazing-angle regimes where atmospheric effects are especially variable.

We analyze six events collected over the Northern Polar region during July 2024 and estimate the 'relative' ionospheric delay—here defined as the difference in ionospheric delay between the reflected and direct signal paths in the GNSS-R geometry. Based on these estimations from PRETTY, we assess the feasibility of retrieving the vertical ionospheric structure by fitting a Chapman layer model to the observed delay profiles, aiming to derive key F-layer parameters such as the peak electron density, peak height, and scale height.

This paper is structured as follows: Sect. 2 details the methodology, describing the data used and the approach to compute relative ionospheric and tropospheric delays. Section 3 presents the results, including the delay maps, the correction and estimation of relative ionospheric delay, and Chapman layer parameter inversion. Finally, Sect. 4 concludes with key takeaways and outlines directions for future work, including opportunities enabled by using PRETTY data.

2 Data and methodology

2.1 GNSS-R PRETTY data

The ESA PRETTY CubeSat is a GNSS Reflectometry mission launched in October 2023 into a sun-synchronous polar LEO orbit at 560 km in height and an inclination of 97.66°. The mission's primary objective is to measure the sea surface height and other sea ice properties, particularly at grazing angles (Dielacher et al. 2022). PRETTY is a pioneering mission in the field of GNSS reflectometry, utilizing E5/L5 signal bands from the European Galileo and U.S. GPS satellites. Its system is highly adaptable and capable of conducting observations across a wide range of elevation angles, from 30° down to as low as 0.01°, offering flexibility for diverse data acquisition scenarios. As of September 2024, the PRETTY mission has conducted multiple measurements across various locations, with a primary focus on the North Polar region. These observations have been carried out using signals from both the GPS and Galileo constellations, covering a wide range of grazing-angle elevations. The distribution of reflection point tracks recorded by PRETTY is shown in Fig. 1.

A total of six events were selected for this study. These observations represent the cases with the highest signal-to-noise ratio (SNR) levels, computed as the peak signal power relative to the noise level in decibels (dB), and featuring elevation grazing angles down to 1° or lower. The selected events also cover different levels of solar activity, as indicated by the variability in the solar flux index F10.7.

Table 1 summarizes the key information for each selected event, including the date, GNSS constellation and PRN, observation start time in UTC, elevation range, duration of the analyzed event, SNR range, and the corresponding F10.7 index value (in solar flux units, sfu), obtained from the National Research Council and Natural Resources Canada.

In Fig. 2, the left panel displays the locations of the selected events, color-coded by the date of recording, with markers indicating the GNSS constellation, stars for Galileo, and circles for GPS. The right panel illustrates the corresponding SNR levels for each event.

2.2 Delay maps and code delay

The raw data from the PRETTY receiver is recorded as complex waveforms sampled at 1 ms intervals. From this raw data, the next-level data product, known as the Delay Map (DM) observable, is derived. The DM is a time-delay representation of the reflected GNSS signals, offering insight into how these signals arrive at different delays relative to the direct signals, after bouncing off the reflecting surface. In the DM, the y-axis shows the signal delay, representing the excess path length of the reflected signal relative to the direct signal, while the signal intensity is color-coded. The DM has been employed in GNSS-R for applications such as ice sheet altimetry, as demonstrated in Rius et al. (2017) using TDS–1 data.

The PRETTY DM is generated during postprocessing in two steps. First, the signal is coherently integrated every 20 ms. This is followed by an incoherent integration every second, allowing for longer integration periods since it does not depend on maintaining phase information. The location of the peak intensity on the y-axis for each power waveform in the DM represents the relative observed code delay. The PRETTY DMs are configured into 200 taps along the delay axis, with each tap corresponding to a resolution of 7.8071 m. This offers a finer delay range resolution compared to the 37.5 m resolution of the TDS-1 mission (Foti et al. 2015) and the 25 m resolution of the CYGNSS mission (Ruf et al. 2013a, b).

The ability to observe GNSS-R signals down to 1° of elevation is a key advantage of the PRETTY mission. At such grazing angles, the reflected signal paths traverse longer atmospheric segments, significantly amplifying atmospheric delay signatures, particularly those related to ionospheric and tropospheric effects. This geometry enables greater sensitivity to the vertical structure of the atmosphere, especially the ionosphere. Moreover, surface roughness effects become less dominant at very low elevations, favoring conditions for coherent reflections, especially over calm ocean or ice surfaces. These coherent returns enhance the detectability of systematic delay trends.

As illustrated in the Delay Maps in Fig. 3, when the elevation falls below approximately 4°, the relative code delay exhibits a marked drift (i.e., a nonlinear increase), continuing until it reaches the lowest elevation of ~ 1°. This delay curvature is indicative of the influence of atmospheric refraction and dispersion at low-elevation angles. These features would remain undetectable at higher elevation regimes (e.g., > 5°).

As shown in Table 1, all observations correspond to setting events (i.e., decreasing elevation angles). The events on 06 July and 16 July extend down to 1° in elevation (at the specular point location), whereas the events from 25 July onward reach as low as 0.01°. However, in the Delay Maps from these latter events, it becomes evident that below 1° of

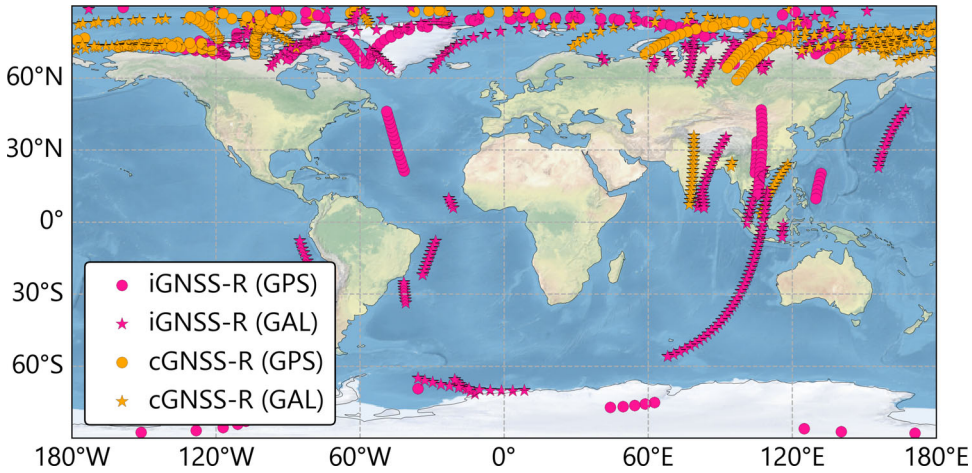

Fig. 1 Location of reflection point tracks recorded by PRETTY as of September 2024 using cGNSS-R (orange) or iGNSS-R (magenta) and Galileo (stars) or GPS (dots) system

Table 1 Overview of the selected events, summarizing key observational parameters

Date	GNSS-PRN	UTC	Ele. [deg]	Duration [mm:ss]	SNR [dB]	F10.7 [sfu]
2024/07/06	GAL–7	01:35:48	7–1	03:09	5.10–9.44	169.9
2024/07/16	GAL–7	00:55:51	10–1	04:12	5.25–9.11	242.4
2024/07/25	GPS–4	05:05:53	9–0.01	03:58	6.31–12.09	172.0
2024/07/27	GPS–8	04:55:51	11–0.01	06:34	5.96–10.26	186.7
2024/07/28	GPS–8	04:50:52	13–0.01	07:21	5.61–11.59	216.6
2024/07/29	GPS–8	04:45:50	15–0.01	08:10	5.88–12.11	224.2

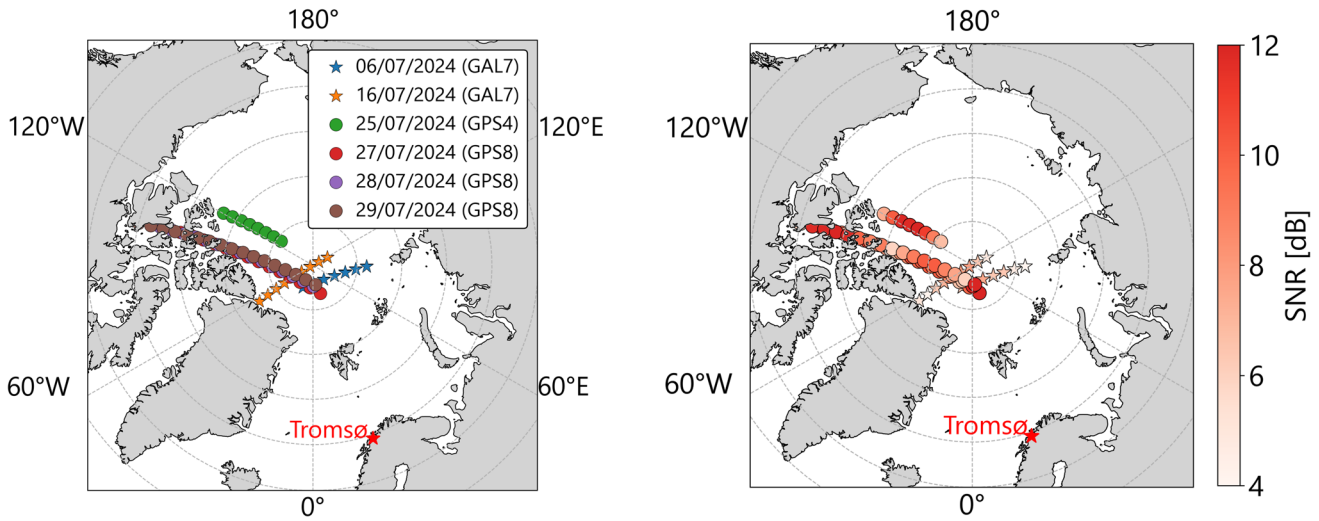

Fig. 2 Left: Specular points tracks, color-coded by date (stars: Galileo events, and circles: GPS events). Right: SNR levels of the selected events. The Tromsø ionosonde (EISCAT station) is located near the observed events

elevation, the relative code delay becomes noisier, and the direct signal delay starts to appear with increased intensity, making it more challenging to identify the relative code delay peak. As a result, all event samples have been truncated at the 1° elevation limit to ensure reliable analysis.

2.2.1 Code delay fitting

After the Delay Map is computed, the peak value of each power waveform is selected, and the corresponding code delay over time is extracted. In this step, it is necessary to remove outliers to ensure the consistency of the retrieved code delays. These outliers, such as signal power dissipation

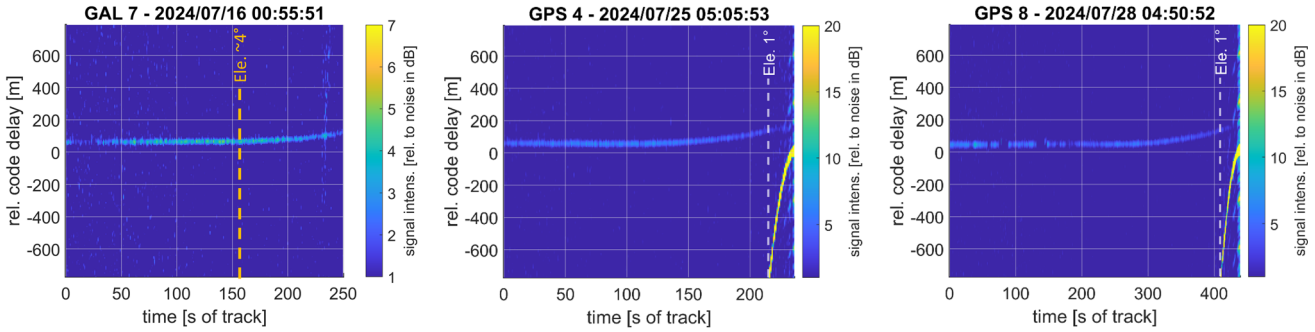

Fig. 3 PRETTY Delay Maps from 16, 25, and 28 July. The x-axis represents the seconds of the track, while the y-axis indicates the relative code delay converted to meters

in the DM, typically correspond to locations where the specular point crosses over land or rougher surfaces. For instance, in the DM from 28 July (Fig. 3, right), a power drop (or gap) is observed before the 100 s mark of the track, coinciding with the specular point crossing over Ellef Ringnes Island in Canada.

As presented in Fig. 4, the observed code delays exhibit a discrete stepped behavior, resulting from the delay resolution of the DMs. This quantization effect arises from the discrete tap configuration of the correlator, where each step corresponds to one delay bin (7.8071 m). To capture the underlying trend in the code delay, a fitting process is applied to the observations over the entire duration of each event. The model that best captures this trend is an exponential function of the form $y = a \cdot e^{bx} + c$, where y represents the code delay, and x is the independent variable, which in this case is time.

After the fitting process, the coefficient of determination R^2 is found to be close to 1, indicating a strong fit between the model and the observed code delay data. The uncertainty envelope associated with the fitting is derived using the 5th and 95th percentiles of the residuals, corresponding to the range within which 90% of the observations are expected to fall. The typical uncertainty range associated with the fitting is approximately $\pm$ 2.6 m.

Figure 4 presents the observed code delays along with the fitted curves and associated uncertainty bounds for the events on 16, 25, and 28 July.

2.3 Atmospheric delays

In GNSS-R, the relative path delay Δ_p, also referred to as the interferometric path delay, represents the difference between the reflected path delay, p_r (which includes both the incident and reflected rays), and the direct path delay, p_d (Cardellach et al. 2004). Considering the common sources of delay that affect GNSS signals, the relative delay can be expressed as follows:

$$\Delta_\mathrm{p} = \Delta_{\mathrm{p_{geo}}} + \Delta_{\mathrm{p_{trop}}} + \Delta_{\mathrm{p_{iono}}} + \Delta_{\mathrm{p_{rgh}}} + \Delta_{\mathrm{p_{instr}}} + n \quad (1)$$

where $\Delta_{\mathrm{p_{geo}}}$ represent the geometrical delay, $\Delta_{\mathrm{p_{trop}}}$ accounts for the relative path delay caused by tropospheric refraction, and $\Delta_{\mathrm{p_{iono}}}$ corresponds to the relative ionospheric path delay. Additionally, there is an induced bias due to surface roughness, denoted as $\Delta_{\mathrm{p_{rgh}}}$, while instrumental and unmodeled errors are represented by $\Delta_{\mathrm{p_{instr}}}$ and n, respectively.

Due to the geometry of spaceborne GNSS-R at grazing angles, the signals traverse a longer path through the atmosphere, resulting in a larger atmospheric impact. In this study, we focus on correcting and analyzing the two major atmospheric contributions: the relative tropospheric delay $\Delta_{\mathrm{p_{trop}}}$ and the relative ionospheric (group) delay $\Delta_{\mathrm{p_{iono}}}$. Since PRETTY is a single-frequency (E5/L5) mission, it relies on atmospheric models to account for the delays introduced along the direct, incident, and reflected signal paths. Corrections for geometric and instrumental delays are handled by the mission's onboard processing. The following section describes the methodologies used to compute the model-based tropospheric delay applied for correction, as well as the ionospheric delays used for comparison with the estimates derived from the observations.

2.3.1 Model-based relative ionospheric delay

The ionosphere, a layer of the upper atmosphere composed of charged particles, induces delays in GNSS signals that depend on the TEC (Morton et al. 2020). The slant TEC (sTEC) refers to the total number of electrons per square meter (electron density) along the signal path between a GNSS satellite and a receiver, and it is commonly measured in total electron content uits (TECU), where one TECU is equivalent to 10^{16} electrons per square meter.

In this study, the model-based sTEC along each ray path is computed using three different models: the Neustrelitz electron density model—NEDM2020 (Hoque et al. 2022), the NeQuick model (Nava et al. 2008), and the International Reference Ionosphere Model (IRI) (Bilitza et al. 2022). These sTEC values are used to compute the modeled relative ionospheric delay. The resulting modeled delays are then

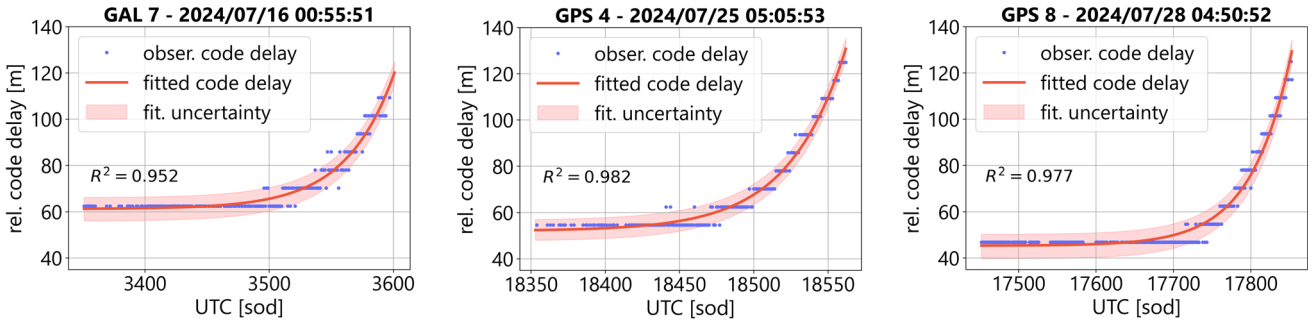

Fig. 4 Code delay observations with the exponential model fit, the coefficient of determination R^2, and its corresponding model uncertainty bounds

compared with the corresponding delay estimated from the PRETTY code delay observations.

The computation methodology follows the approach described by Moreno et al. (2023). The positions of the transmitter, receiver, and specular reflection point are obtained from PRETTY mission metadata, with the specular point already corrected for surface elevation using a digital elevation model integrated into the onboard system. Based on these positions, ray points are defined every 10 km along the ray paths of the direct (di), incident (in), and reflected (re) signals.

The electron density for each ray point is obtained from the respective three models. Both NEDM2020 and NeQuick provide electron density values directly for any 3D coordinate using inputs latitude, longitude, altitude, date, local time, and solar flux index. For the IRI model, electron density profiles are extracted from IRI-2016 and assembled into a 3D electron density field with a horizontal resolution of $2° \times 2°$. By integrating the electron density along each ray, the sTEC for the direct, incident, and reflected signals is obtained. The relative sTEC, $\Delta sTEC$, is then computed as $sTEC_{\text{in}} + sTEC_{\text{re}} - sTEC_{\text{di}}$. Finally, the model-based relative ionospheric delay (in meters) can be determined as follows:

$$\Delta_{piono} = +\frac{40.3 * 10^{16}}{f^2} \Delta sTEC \tag{2}$$

where f represents the GNSS carrier frequency in Hertz. For the PRETTY mission, this applies to the GPS L5 and Galileo E5 frequency bands, which operate at 1176.45 MHz.

2.3.2 Model-based relative tropospheric delay

The lowest layer of the Earth's atmosphere is the troposphere. The troposphere induces delays in GNSS signals that depend on variations in temperature, pressure, water vapor, and the relative positions of the transmitter and receiver (Hofmann-Wellenhof et al. 2012). To account for this effect, we retrieve model-based tropospheric corrections using ray-tracing techniques supported by numerical weather model data.

Specifically, we use the ERA5 reanalysis data (Hersbach et al. 2020) from the European Centre of Medium-Range Weather Forecasts (ECMWF), which provides atmospheric fields on 37 pressure levels at a horizontal resolution of $0.25° \times 0.25°$.

The computations are based on the point-to-point algorithm developed by Zus et al. (2012), which determines the signal path between transmitter and receiver and integrates the refractive index along that path to compute the optical length.

The process begins by computing the geometric path length P. Following the methodology described by Semmling et al. (2016), this path is first computed under the assumption of no atmospheric effects, using the known positions of the GNSS transmitter and the PRETTY receiver, thereby deriving an initial reflection point. The reflection point is then iteratively adjusted until the incident and reflected rays satisfy the law of reflection (i.e., the incidence angle equals the reflection angle). With the troposphere included, the new path length is computed and denoted as P_t. Finally, the ionospheric delay is added using the same reflection geometry, yielding the total atmospheric path length P_i. The total path length P_i can be expressed as:

$$P_{\text{i}} = P + (P_{\text{t}} - P) + (P_{\text{i}} - P_{\text{t}}) \tag{3}$$

In this approach, $\Delta P_{\text{t}} = (P_{\text{t}} - P)$ represents the model-based relative tropospheric delay, and $\Delta P_{\text{i}} = (P_{\text{i}} - P_{\text{t}})$ represents the relative ionospheric delay.

3 Results

3.1 Model-based atmospheric delays analysis

The model-based relative tropospheric and ionospheric delays are computed for each ray individually for all six selected events. Figure 5 illustrates three examples, showing the ionospheric delay (dashed lines) retrieved from the NEDM2020 model, and the modeled tropospheric delay

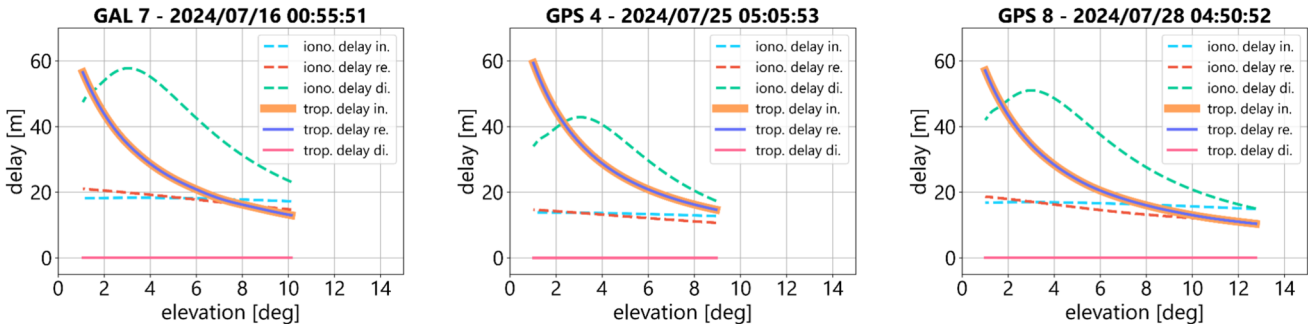

Fig. 5 Ionospheric (NEDM2020) and tropospheric delays for each ray –incident (in), reflected (re), and direct (di)– during the events on 16 July (GAL 7), 25 July (GPS 4), and 27 July (GPS 8)

(solid lines) for the events on 16, 25, and 28 July, color-coded to indicate the respective rays: incident, reflected, and direct. The event on 16 July corresponds to the day with the highest solar activity among the analyzed events (see Table 1).

Regarding the tropospheric delay in the three examples in Fig. 5, the contributions from the incident and reflected signals are similar, in agreement with the tropospheric correction approach presented by Fabra et al. (2011). Both exhibit an exponential increase as the elevation angle decreases, reaching values close to 60 m at an elevation of 1°. In contrast, the direct signal does not contribute within this elevation range. The ionospheric delay, however, shows more dynamic behavior across the three rays, with variations influenced by the solar activity level on each respective day. Ionospheric delay values are notably higher on days with increased solar flux. Moreover, the direct ray exhibits a pronounced increase in ionospheric delay across all days, peaking at around 3° of elevation in all cases, after which the delay contribution from the direct signal delay begins to decrease.

The model-based relative ionospheric and tropospheric delays are calculated as described in Sect. 2.3. When applying the modeled total atmospheric delay correction, i.e., the sum of the tropospheric and ionospheric delays, an offset remains between the observations and the model. This offset is primarily due to the configuration of the onboard code generator in the field-programmable gate array (FPGA) on the PRETTY satellite during clean replica observations. In this mode, processing begins by determining the direct signal delay to configure the code generator and compensate for any instrumental delays. Initially, the software estimates the delay error of the direct signal in an open-loop process by correlating it with a code delayed by an initial value, accounting for the discrepancy between the peak and estimated taps.

This initial compensation includes the geometric, ionospheric, and tropospheric delays at the first epoch of the observation. A correction using the first epoch of the total modeled atmospheric delay for the direct signal is applied to align the observed code delay with the modeled. Since the tropospheric delay is absent from the direct signal, the correction relies solely on the ionospheric delay. Applying this correction improves the alignment between the observations and the model, as shown in Fig. 6. The figure shows the modeled atmospheric delays alongside the observed code delay and the fitting curve. The orange curve represents the relative tropospheric delay, the blue curve is the relative ionospheric delay from NEDM2020, and the green curve is the total atmospheric delay. A clear trend agreement between the observed and modeled delays is evident, with both showing an exponential increase, particularly below 5° of elevation, indicating that the models reasonably capture the atmospheric delay dynamics.

3.2 Relative ionospheric delay estimation

To estimate the relative ionospheric delay, the modeled tropospheric delay is subtracted from the fitted code delay observations, as the geometric and instrumental delays are already corrected during onboard processing. This step isolates the ionospheric contribution by effectively removing the tropospheric influence. Focusing solely on the ionosphere enables a detailed examination of its impact on signal propagation and allows for direct comparison between the estimated and model-based relative ionospheric delays, helping to identify potential anomalies or discrepancies.

Figure 7 shows the relative ionospheric delay computed using the three different models: NEDM2020, NeQuick, and IRI. It also includes the estimated relative ionospheric delay (red curve), with associated uncertainty derived from model fitting errors and a tropospheric correction uncertainty of less than 1% (Zus et al. 2012). This uncertainty estimate for the tropospheric correction is based on statistical comparisons between weather model–based and GNSS-derived tropospheric delays. Therefore, it is a conservative estimate as it also includes the uncertainty of the GNSS estimates.

Overall, the relative ionospheric delay estimations align well with the selected models, with the NEDM2020 model

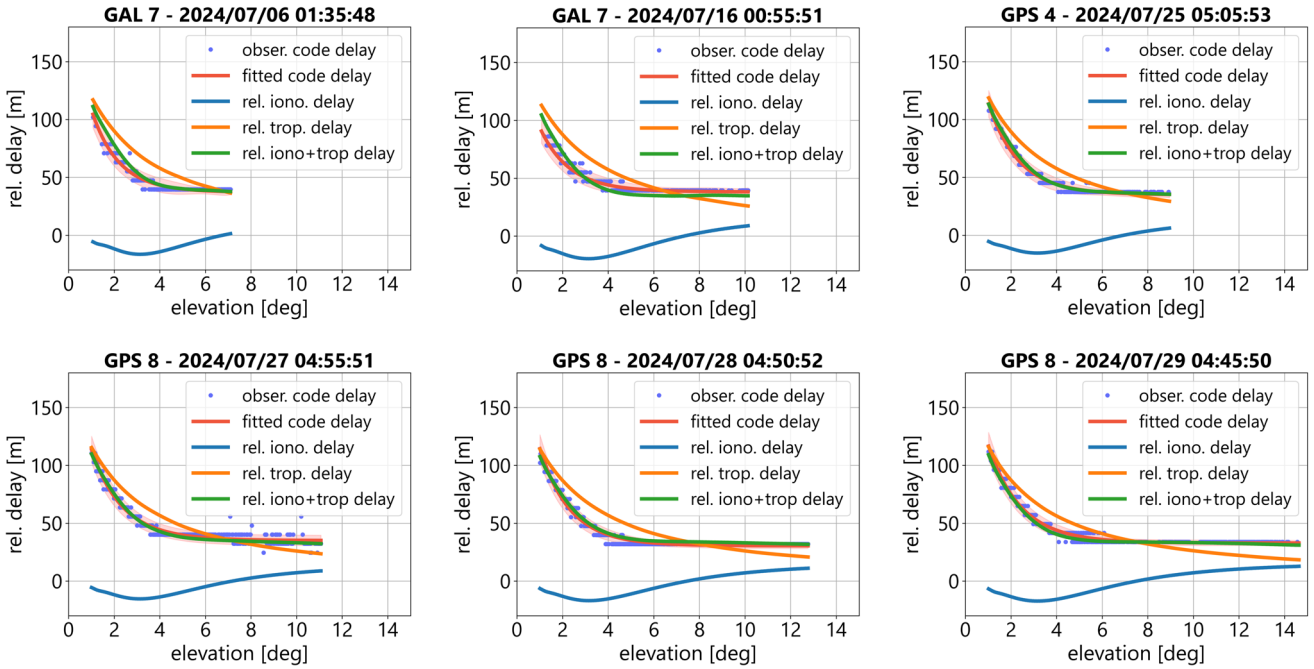

Fig. 6 Observed code delay with its fitting curve after applying the correction based on the first epoch total modeled atmospheric delay, along with the modeled relative ionospheric and tropospheric delays and their sum, representing the total modeled delay

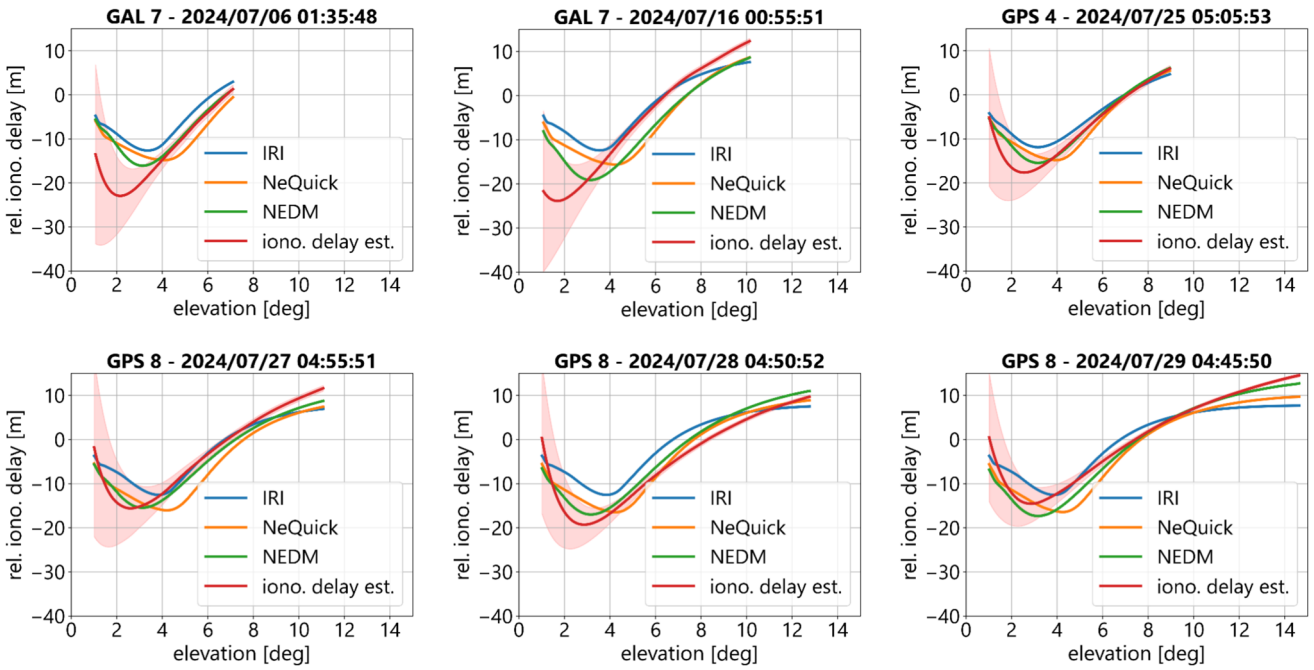

Fig. 7 Relative ionospheric delay computed using the IRI, NeQuick, and NEDM2020, along with the estimated relative ionospheric delay and its associated uncertainties from model fitting and tropospheric correction

Table 2 Residual standard deviations (in meters) between the GNSS-R estimated relative ionospheric delays and the corresponding values from each ionospheric model

Date	GNSS-PRN	UTC	NEDM2020	NeQuick	IRI
2024/07/06	GAL–7	01:35:48	3.75	5.49	3.82
2024/07/16	GAL–7	00:55:51	4.39	6.20	5.46
2024/07/25	GPS–4	05:05:53	1.79	2.82	4.86
2024/07/27	GPS–8	04:55:51	1.55	2.88	3.11
2024/07/28	GPS–8	04:50:52	1.39	2.42	3.27
2024/07/29	GPS–8	04:45:50	1.28	1.99	2.90

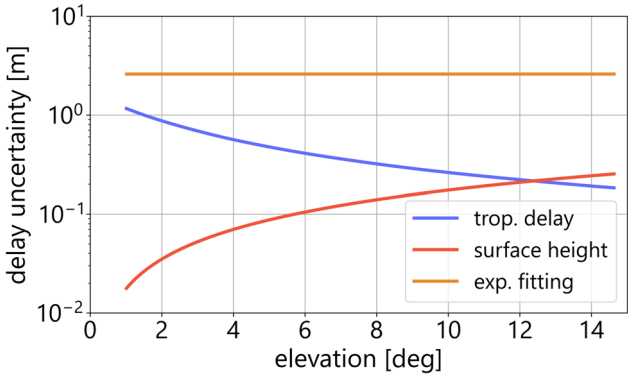

Fig. 8 Uncertainty contributions to the estimated relative ionospheric delay as a function of elevation angle

consistently exhibiting the lowest residual standard deviations across all events, as shown in Table 2. This close alignment suggests that NEDM2020 more accurately captures the slant delay variations observed under the specific conditions of each event. The reduced spread of residuals further supports that the estimation effectively retrieves the first-order ionospheric delay, which is directly proportional to the total electron content.

Notably, the largest deviations across all three models occur on 16 July, coinciding with the highest solar activity levels. This underscores the limitations of empirical models in capturing ionospheric variability under disturbed space weather conditions.

Figure 8 presents the uncertainties associated with the relative ionospheric delay estimations arising from the exponential fitting process, the model-based tropospheric delay correction, and including the reflecting surface height. Each contribution is evaluated as a function of elevation angle.

The uncertainty from the exponential fitting is approximately $\pm$ 2.6 m, as derived from the residual statistics during the curve fitting process. This value reflects the influence of PRETTY's delay map resolution and the discrete nature of peak tracking, which limits the precision in capturing continuous delay variations.

The uncertainty in the tropospheric delay correction is primarily based on ray-tracing simulations using ERA5 profiles and is estimated to contribute a standard deviation of approximately 0.5 m at 1° elevation, decreasing to below 0.2 m above 10°, corresponding to relative errors of 1% or less (Zus et al. 2012).

The uncertainty related to the surface level comes from residual biases or unmodeled errors in the onboard correction using the digital elevation model. A conservative 0.5 m surface height uncertainty translates to an increasing delay error with elevation, contributing more significantly at higher elevation angles due to the steeper signal geometry.

As shown in Fig. 8, the overall uncertainty budget is dominated by the fitting process. While PRETTY offers a higher delay resolution compared to previous missions, the quantization of the Delay Map still imposes limitations on tracking precision.

3.3 Estimation of chapman parameters from GNSS-R relative ionospheric delay

As the estimations of the relative ionospheric delay have demonstrated the capability to capture the first-order ionospheric effects with good agreement, a further step involves the inversion of Chapman layer parameters from the reflectometry-based ionospheric delay estimates. The goal is to retrieve information about the vertical structure of the ionosphere.

The Chapman layer function (Chapman 1931) models the electron density N_e as a function of altitude h providing a representation of the ionospheric F-layer. This model helps to understand how ionospheric conditions influence GNSS signal propagation at different altitudes.

The electron density profile as a function of height h is described by the following expression:

$$N_{\mathrm{e}}(h) = N_0 \cdot \exp\left(\frac{1}{2} * \left(1 - \left(\frac{h - h_m}{H}\right) - \exp\left(-\frac{h - h_{\mathrm{m}}}{H}\right)\right)\right) \quad (4)$$

where N_0 represents the peak electron density of the F-layer, h_{m} is the height of the F-Layer peak, and H represents the scale height.

The objective of the inversion is to determine the set of Chapman parameters h_{m}, N_0 and H that best reproduce the observed GNSS-R relative ionospheric delays. For each set of parameters, the electron density is computed along the ray point heights derived from the direct, incident, and reflected paths. These values are then integrated to calculate the Chapman-based sTEC per ray, from which the modeled relative ionospheric delay is obtained.

To fit the model to the observations, a cost function is defined as the root mean square error (RMSE) that minimizes the difference between the GNSS-R-derived ionospheric delay estimates and the Chapman-modeled delays:

$$\mathrm{RMSE} = \sqrt{\frac{1}{N}\sum_{i}\left(\Delta_{\mathrm{p}_{iono}(\mathrm{obs}),\,i} - \Delta_{\mathrm{p}_{iono}(\mathrm{chp}),\,i}(h_{\mathrm{m}},\,N_0,\,H)\right)^2} \tag{5}$$

Here, $\Delta_{\mathrm{piono(obs)}}$ represents the GNSS-R-based relative ionospheric delay estimates, and $\Delta_{\mathrm{piono(chp)}}$ is the corresponding delay computed using the Chapman model for a given parameter set.

The inversion is carried out using a constrained optimization procedure, with the following parameter bounds: $h_{\mathrm{m}} \in [150, 450]$ km, $N_0 \in [1\mathrm{e}11, 1.5\mathrm{e}12]$ el/m^3, and $H \in [30, 150]$ km, based on Cushley et al. (2017).

The comparison between the GNSS-R-derived relative ionospheric delay estimates and the Chapman model fits is presented in Fig. 9. The blue curve shows the GNSS-R-based ionospheric delay estimation, while the red-dashed curve represents the Chapman delay computed using the fitted parameters.

The results show a strong agreement between the GNSS-R observations, and the Chapman model estimates across all events. The Chapman fits successfully capture the overall shape and magnitude of the relative ionospheric delay, including the location of the local minima typically observed between 2° and 4° of elevation. In most cases, the fitting reproduces both the curvature and the steep increase in delay at lower elevations, which is primarily driven by the longer ionospheric path lengths and increased sensitivity to the F-layer structure.

Some slight discrepancies are observed near the lowest elevations, where the GNSS-R estimations show more rapid changes than the Chapman model. This could be attributed to local ionospheric irregularities, the influence of the E-layer (the lower the elevation, the tangent point can fall below the F-layer), and limitations in resolving fine vertical structure using a simplified Chapman formulation.

Overall, the inversion demonstrates that GNSS-R code delay observations at grazing angles are capable of retrieving ionospheric vertical profile characteristics consistent with the classical Chapman layer model.

The fitted Chapman layer parameters for each event are summarized in Table 3. The fitting results demonstrate stable retrievals across the six events, with h_m ranging from approximately 307 to 361 km and.

H varying between 100 and 126 km. These values are in agreement with typical F-layer parameters reported in high-latitude regions under conditions of high solar activity (Bilitza et al. 2011).

The RMSE values of the fits remain below 1.7 m for all cases, indicating good consistency between the GNSS-R-derived ionospheric delay and the Chapman model reconstructions. The highest RMSE (1.66 m) corresponds to the 16 July event, which also had the highest solar flux level (F10.7 = 242), potentially reflecting enhanced ionospheric variability that is not fully captured by the smooth analytical Chapman model.

The retrieved F-layer peak heights (h_m) from GNSS-R observations are compared with ionosonde and EISCAT measurements reported in the global Ionospheric radio observatory (GIRO) database (Reinisch and Galkin 2011). The GIRO database provides access to ionograms from ionosonde and incoherent scatter radar stations, which probe the ionosphere to derive electron density profiles and associated parameters, including the F-layer peak height. For comparison, three stations located near the analyzed GNSS-R events were selected: two stations in Tromsø, northern Scandinavia—TROMSØ (URSI code TR169), EISCAT TROMSØ (TR170), and THULE (THJ76) in Greenland. Table 4 presents a comparison between the GNSS-R-derived h_m estimates (in kilometers) and those reported by the GIRO database.

The results show that the GNSS-R retrieved F-layer peak heights are generally in good agreement with those reported by nearby ionosonde and EISCAT stations. For most events, the differences between the estimates and the reference values remain within $\pm$ 15 km, which is consistent with expected spatial and temporal variations in the ionosphere. Notably, the event on July 28 exhibits the highest retrieved peak value (361.29 km), closely matched by EISCAT TROMSØ (TR170) at 350.60 km, suggesting enhanced ionospheric activity under elevated solar flux conditions. The largest discrepancies, such as the difference between the GNSS-R estimate and THJ76 on July 28, may be attributed to dynamic ionospheric conditions that introduce localized variability, spatial separation between the GNSS-R events and the ground-based stations, as well as limitations in model resolution or temporal collocation.

While the F-layer peak height h_m retrieved from the Chapman inversion provides valuable insight into the vertical ionospheric structure, further analysis is necessary to assess the horizontal consistency of this estimation across the GNSS-R geometry. In particular, the horizontal separation between the peak electron density points of the incident

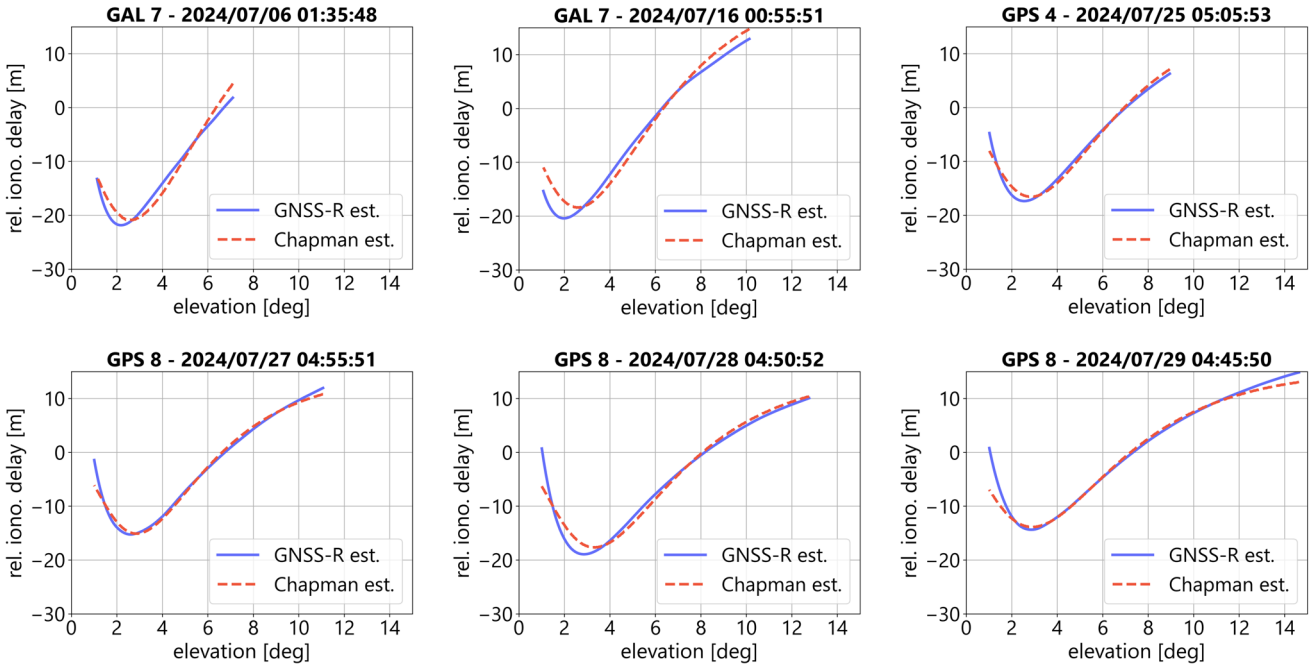

Fig. 9 Comparison between GNSS-R-derived relative ionospheric delay estimates from PRETTY observations (blue) and Chapman model estimations (red dashed) for six events in July 2024

Table 3 Retrieved Chapman layer parameters for each analyzed event, including the h_m, N_0, H, and the RMSE between the GNSS-R estimated and Chapman-modeled relative ionospheric delays

Date	GNSS-PRN	UTC	h_m [km]	N_0 [el/m^3]	H [km]	RMSE [m]
2024/07/06	GAL–7	01:35:48	315.71	5.35e11	123.48	1.47
2024/07/16	GAL–7	00:55:51	307.35	6.34e11	120.81	1.66
2024/07/25	GPS–4	05:05:53	323.26	4.33e11	115.22	0.83
2024/07/27	GPS–8	04:55:51	310.34	3.64e11	100.81	0.74
2024/07/28	GPS–8	04:50:52	361.29	4.09e11	111.61	1.31
2024/07/29	GPS–8	04:45:50	337.49	3.80e11	126.18	1.25

Table 4 F-layer peak height h_m (in km) retrieved from GNSS-R in comparison with stations from the GIRO database

Date	GNSS-PRN	UTC	GNSS-R	TR170	TR169	THJ76
2024/07/06	GAL–7	01:35:48	315.71	313.30	309.90	307.60
2024/07/16	GAL–7	00:55:51	307.35	ND	315.30	299.30
2024/07/25	GPS–4	05:05:53	323.26	318.50	307.50	294.10
2024/07/27	GPS–8	04:55:51	310.34	307.20	294.00	300.20
2024/07/28	GPS–8	04:50:52	361.29	350.60	327.50	306.30
2024/07/29	GPS–8	04:45:50	337.49	339.60	297.40	327.30

and reflected rays can span from approximately 2000 km at 14° elevation to over 3800 km at 1° elevation. This is relevant because such large distances imply that the two ray paths sample different regions of the ionosphere, where horizontal gradients and localized structures may influence the reliability of the inversion.

Figure 10 illustrates the relationship between the horizontal distance separating the h_m locations of the incident and reflected rays and the vertical difference in their respective peak heights. The data are color-coded by elevation angle and correspond to all six analyzed events. The h_m values are extracted from the NEDM2020 model as the altitude at which the maximum electron density occurs along each ray. From those peak points, the vertical height difference and geographic distance are computed.

Although the horizontal distances are considerable, the vertical differences in h_m remain within a relatively narrow

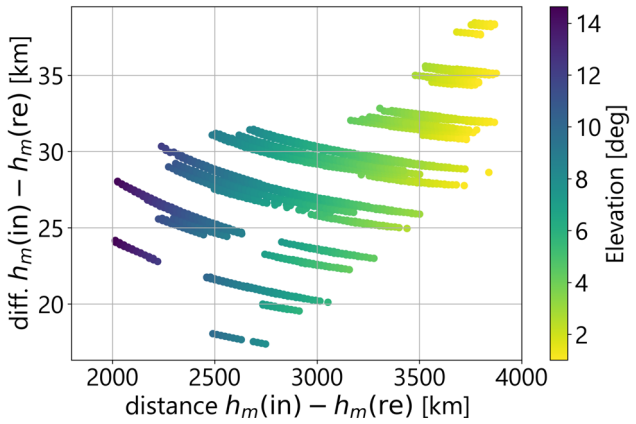

Fig. 10 Horizontal distance between the F-layer peak locations along the incident and reflected ray paths versus the corresponding vertical difference in peak height h_m

range of 18 to 37 km. This suggests that, despite the large separation between ionospheric penetration points, the retrieved h_m values are relatively stable, with limited vertical variability, partly because the climatological models used resolve rather smooth features. Nevertheless, the Chapman-based estimation of F-layer peak height can be reasonably interpreted as representative of the ionospheric structure along the GNSS-R track under the analyzed conditions, as further supported by the agreement with nearby ionosonde and EISCAT data.

3.4 Relative ionospheric delay cancelation point and the f-layer structure

In addition to the Chapman-based inversions, we identify a cancelation point in the relative ionospheric delay, defined as the elevation angle where the contributions from the direct and combined incident-reflected signal paths cancel out, resulting in a net delay of zero. This point is evident in Fig. 7 across all of the events, where the delay curve intersects the zero line. To explore the physical basis of this phenomenon, Chapman layer simulations are performed, varying the N_0 with values of 0.5e12 m^{-3}, 1.0e12 m^{-3}, and 1.5e12 m^{-3}, while assigning h_m values of 250 km, 300 km, and 350 km. The results of the different scenarios are presented in Fig. 11. The color-coded lines represent variations in the F-layer peak height, while the dashed line styles represent variations in peak electron density.

As shown in Fig. 11, there is a clear relationship between the elevation angle of the cancelation point and the F-layer peak height. For example, a cancelation point at approximately 6.83° elevation (July 06) corresponds to an h_m of 317 km, while a shift to 8.29° (July 28) aligns with an h_m of 367 km. Table 5 present the retrieved h_m using the cancelation point method. While some discrepancies remain, the results show good agreement with the h_m values obtained from Chapman-based fitting. These findings suggest that this cancelation point could serve as a proxy for estimating the F-layer peak height. Future work will further investigate its applicability, considering factors such as horizontal ionospheric gradients and the sensitivity to GNSS-R geometry.

4 Conclusions

This study demonstrates that, after accurately correcting for the tropospheric delay, it is possible to successfully estimate the first-order relative ionospheric delay using code delay observations at grazing angles from the ESA PRETTY mission. These findings highlight the potential of single-frequency GNSS-R missions like PRETTY to capture ionospheric delay effects accurately, even at very low-elevation angles, using model-based atmospheric corrections.

Thanks to PRETTY's extended observation capabilities down to 1° of elevation, we determined that the relative ionospheric delay reaches its maximum negative value at around 3°, averaging − 20 m across the six events analyzed in the North Pole region, with variations influenced by solar activity. This elevation coincides with the peak delay contribution from the direct signal, which accounts for approximately 60% of the total ionospheric delay at 3°, with the remaining 40% from the combined incident and reflected paths. At higher elevations (e.g., 10°), this proportion shifts, with the direct ray contributing only about 40%. This highlights that ionospheric effects, particularly from the direct signal path, must not be neglected in GNSS-R applications operating at low elevations, consistent with the conclusions of Camps et al. (2016).

The uncertainty analysis shows that the dominant source of error in the relative ionospheric delay estimation comes from the delay fitting process. While PRETTY offers improved delay resolution (~ 7.8 m) compared to previous missions, the discrete sampling of the Delay Map and the peak detection method lead to uncertainties of ± 2.6 m. Nevertheless, the exponential model used in the fitting process provides a high degree of confidence, with R^2 values near 1 for all events.

The uncertainty from the relative tropospheric delay correction is smaller, ranging from ~ 0.2 m at 15° to ~ 1 m at 1°, and the uncertainty due to surface level bias or unmodeled errors remains below ~ 0.25 m. These sources must be considered when interpreting delay estimates for the purpose of retrieving ionospheric parameters.

The application of a Chapman-based inversion to GNSS-R code delay observations shows promising potential for retrieving the vertical structure of the ionosphere. F-layer peak heights h_m estimated from the fitted Chapman model ranged from 307 to 367 km, in agreement with expected

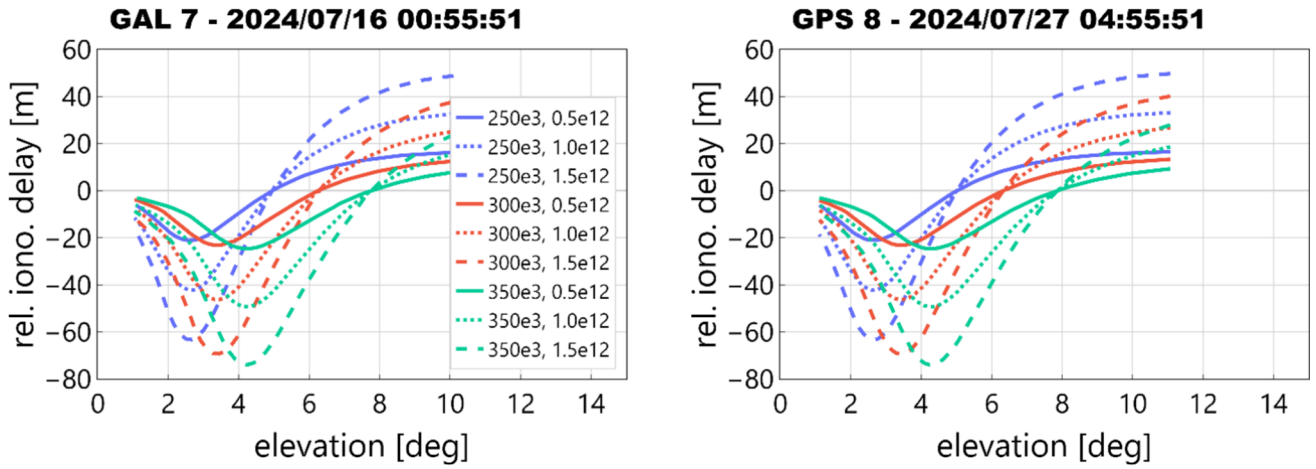

Fig. 11 Chapman layer simulation for the events of 16 and 27 July. Color-coded lines present variations in peak height (h_m), while dashed style indicates variations in peak electron density (N_0). The legend order is h_m, N_0

Table 5 Estimated F-layer peak heights derived from the elevation angle of the relative ionospheric delay cancelation point

Date	GNSS-PRN	UTC	Elevation. [deg]	h_m[km]
2024/07/06	GAL–7	01:35:48	6.83	317
2024/07/16	GAL–7	00:55:51	6.41	303
2024/07/25	GPS–4	05:05:53	7.20	330
2024/07/27	GPS–8	04:55:51	6.85	318
2024/07/28	GPS–8	04:50:52	8.29	367
2024/07/29	GPS–8	04:45:50	7.44	338

values for high-latitude regions under high solar activity conditions (F10.7 = 150–250). The inversion process yielded a mean RMSE of 1.2 m (approximately 4 TECU) across all analyzed events, indicating strong consistency between GNSS-R-derived ionospheric delay and the modeled Chapman reconstruction.

This concept of inverting Chapman parameters is similar to that applied in GNSS radio occultation (GNSS-RO) studies, such as (Elvidge et al. 2024), where a flexible Chapman function (Vary-Chap) was implemented within a one-dimensional variational framework to reconstruct electron density profiles from bending angle measurements.

While the observables and geometries differ, GNSS-R, relying on reflected code delays and GNSS-RO using limb-sounding bending angles, both techniques aim to retrieve key parameters of the ionospheric F-layer, namely, peak electron density (N_0), peak height (h_m), and scale height (H), through Chapman model fitting. These findings reinforce the notion that GNSS-R reflectometry is a valuable and complementary technique for ionospheric characterization, particularly in regions and conditions, such as polar or oceanic areas, where traditional ground-based methods are unavailable or limb-sounding techniques are limited.

Comparison with independent measurements from nearby ionosonde and EISCAT stations shows generally good agreement. For most events, the differences between the GNSS-R-derived h_m values and those reported by the ground-based stations remain within $\pm$ 15 km, which is within the expected range of spatial and temporal ionospheric variability. Smaller differences were observed with respect to the EISCAT TROMSØ (TR170) station, while larger discrepancies were noted when compared with THULE (THJ76), likely due to dynamic ionospheric conditions, increased spatial separation, or the lack of precise temporal collocation.

Accurate characterization and correction of ionospheric delays are essential for achieving high-precision positioning, satellite altimetry (including reflectometry), and atmospheric sounding. The results indicate that GNSS-R can retrieve first-order ionospheric delays at grazing angles and provide valuable input for multi-technique ionospheric studies, enhancing the understanding of the spatiotemporal behavior of the F-layer peak and electron density profiles. This work contributes to space geodesy by introducing an alternative technique for retrieving ionospheric parameters under challenging low-elevation geometries, potentially extending global ionospheric mapping capabilities beyond those offered by ground-based networks and radio occultation.

Future work could delve deeper into the relationship between the relative ionospheric delay cancelation point and the F-layer peak height, as well as assess the sensitivity of these estimations to GNSS-R geometry and horizontal ionospheric gradients. In addition, residual discrepancies between the estimated and modeled delays may also reveal second-order ionospheric effects, including geomagnetic effects. Once PRETTY's phase observables complete their ongoing verification and validation and become available to the scientific community, their combination with code observables could enable absolute TEC retrievals, further enhancing ionospheric characterization through GNSS-R reflectometry at grazing angles.

Acknowledgements The authors would like to thank Beyond Gravity Austria GmbH (BGA) for providing PRETTY data.

Author contribution Conceptualization, M.M., M.S., G.S., and F.Z.; methodology, M.M., M.S., and F.Z.; software, M.M., M.S., A.D., and F.Z.; data resources, M.M., M.S., F.Z., and A.D.; writing—original draft preparation, M.M.; writing—review and editing, M.M., M.S., F.Z., G.S., A.D., M.H., J.W., and H.N.; visualization, M.M.; supervision, M.S., J.W., and M.H.

Funding Open Access funding enabled and organized by Projekt DEAL.

Data availability Data are available upon reasonable request from the corresponding author and under the authorization of BGA.

Declarations

Conflict of interest The authors declare no conflict of interest.

References

AlonsoArroyo A, Zavorotny VU, Camps A (2016) Sea ice detection using GNSS-R data from UK TDS-1. IEEE Int Geosci Remote Sens Symp (IGARSS) 2016:2001–2004. https://doi.org/10.1109/IGARSS.2016.7729516

Bilitza D, McKinnell L-A, Reinisch B, Fuller-Rowell T (2011) The international reference ionosphere today and in the future. J Geodesy 85(12):909–920. https://doi.org/10.1007/s00190-010-0427-x

Bilitza D, Pezzopane M, Truhlik V, Altadill D, Reinisch BW, Pignalberi A (2022) The international reference ionosphere model: a review and description of an ionospheric benchmark. Rev Geophys. https://doi.org/10.1029/2022RG000792

Camps A, Park H, Foti G, Gommenginger C (2016) ionospheric effects in GNSS-Reflectometry from space. IEEE J Sel Top Appl Earth Obs Remote Sens. https://doi.org/10.1109/JSTARS.2016.2612542

Cardellach E, Ao CO, de la Torre Juárez M, Hajj GA (2004) Carrier phase delay altimetry with GPS-reflection/occultation interferometry from low Earth orbiters. Geophys Res Lett. https://doi.org/10.1029/2004GL019775

Cardellach E, Wickert J, Baggen R, Benito J, Camps A, Catarino N, Chapron B, Dielacher A, Fabra F, Flato G, Fragner H, Gabarró C, Gommenginger C, Haas C, Healy S, Hernandez-Pajares M, Høeg P, JäGgi A, Kainulainen J, Zuffada C (2018) GNSS transpolar earth reflectometry exploriNg system (G-TERN): mission concept. IEEE Access 6:13980–14018. https://doi.org/10.1109/ACCESS.2018.2814072

Cardellach E, Li W, Rius A, Semmling M, Wickert J, Zus F, Ruf CS, Buontempo C (2020) First precise spaceborne sea surface altimetry with gnss reflected signals. IEEE J Sel Topics Appl Earth Obs Remote Sens 13:102–112. https://doi.org/10.1109/JSTARS.2019.2952694

Cartwright J, Banks CJ, Srokosz M (2019) Sea Ice detection using GNSS-R data from TechDemoSat-1. J Geophys Res: Oceans 124(8):5801–5810. https://doi.org/10.1029/2019JC015327

Chapman S (1931) The absorption and dissociative or ionizing effect of monochromatic radiation in an atmosphere on a rotating earth part II Grazing incidence. Proc Phys Soc 43(5):483. https://doi.org/10.1088/0959-5309/43/5/302

Cushley AC, Kabin K, Noël J-M (2017) Faraday rotation of automatic dependent surveillance-broadcast (ADS-B) signals as a method of ionospheric characterization. Radio Sci 52(10):1293–1300. https://doi.org/10.1002/2017RS006319

Dielacher A, Fragner H, Koudelka O (2022) PRETTY: passive GNSS-reflectometry for CubeSats. E & i Elektrotech Informationstech 139(1):25–32. https://doi.org/10.1007/s00502-022-00993-7

Elvidge S, Healy SB, Culverwell ID (2024) One-dimensional variational ionospheric retrieval using radio occultation bending angles: 2. validation. Sp Weather. https://doi.org/10.1029/2023SW003571

Fabra F, Cardellach E, Rius A, Ribo S, Oliveras S, Nogues-Correig O, Belmonte Rivas M, Semmling M, D'Addio S (2011) Phase altimetry with dual polarization GNSS-R over sea ice. IEEE Trans Geosci Remote Sens 50(6):2112–2121. https://doi.org/10.1109/TGRS.2011.2172797

Foti G, Gommenginger C, Jales P, Unwin M, Shaw A, Robertson C, Roselló J (2015) Spaceborne GNSS reflectometry for ocean winds: first results from the UK TechDemoSat-1 mission. Geophys Res Lett 42(13):5435–5441. https://doi.org/10.1002/2015GL064204

Hersbach H, Bell B, Berrisford P, Hirahara S, Horányi A, Muñoz-Sabater J, Nicolas J, Peubey C, Radu R, Schepers D, Simmons A, Soci C, Abdalla S, Abellan X, Balsamo G, Bechtold P, Biavati G, Bidlot J, Bonavita M, Thépaut J (2020) The ERA5 global reanalysis. Q J R Meteorol Soc 146(730):1999–2049. https://doi.org/10.1002/qj.3803

Hofmann-Wellenhof B, Lichtenegger H, Collins J (2012) Global positioning system: theory and practice. Springer Science & Business Media, Germany

Hoque MM, Jakowski N, Prol FS (2022) A new climatological electron density model for supporting space weather services. J Sp Weather Sp Clim 12:1. https://doi.org/10.1051/swsc/2021044

Moreno M, Semmling M, Stienne G, Hoque M, Wickert J (2023) Characterizing ionospheric effects on gnss reflectometry at grazing angles from space. Remote Sens. https://doi.org/10.3390/rs15205049

Morton YJ, Yang Z, Breitsch B, Bourne H, Rino C (2020) Ionospheric Effects, Monitoring, and Mitigation Techniques. In Position, Navigation, and Timing Technologies in the 21st Century (pp. 879–937). John Wiley & Sons, Ltd. https://doi.org/10.1002/9781119458449.ch31

Nava B, Coïsson P, Radicella SM (2008) A new version of the NeQuick ionosphere electron density model. J Atmos Solar Terr Phys 70(15):1856–1862. https://doi.org/10.1016/j.jastp.2008.01.015

Reinisch BW, Galkin IA (2011) Global ionospheric radio observatory (GIRO). Earth, Planets Space,. https://doi.org/10.5047/eps.2011.03.001

Ren X, Liu H, Zhang J, Mei D, Zhang X (2022) An improved method for ionospheric TEC estimation using the spaceborne GNSS-R observations. IEEE Trans Geosci Remote Sens 60:1–12. https://doi.org/10.1109/TGRS.2022.3192983

Rius A, Cardellach E, Fabra F, Li W, Ribó S, Hernández-Pajares M (2017) Feasibility of GNSS-R ice sheet altimetry in greenland using TDS-1. Remote Sens. https://doi.org/10.3390/rs9070742

Ruf C, Gleason S, Jelenak Z, Katzberg S, Ridley A, Rose R, Scherrer J, Zavorotny V (2013a) The NASA EV-2 cyclone global navigation satellite system (CYGNSS) mission. IEEE Aerosp Conf 2013:1–7. https://doi.org/10.1109/AERO.2013.6497202

Ruf C, Unwin M, Dickinson J, Rose R, Rose D, Vincent M, Lyons A (2013b) CYGNSS: enabling the future of hurricane prediction [Remote Sensing Satellites]. IEEE Geosci Remote Sens Mag 1(2):52–67. https://doi.org/10.1109/MGRS.2013.2260911

Semmling AM, Leister V, Saynisch J, Zus F, Heise S, Wickert J (2016) A phase-altimetric simulator: studying the sensitivity of earth-reflected gnss signals to ocean topography. IEEE Trans Geosci Remote Sens 54(11):6791–6802. https://doi.org/10.1109/TGRS.2016.2591065

Unwin M, Jales P, Tye J, Gommenginger C, Foti G, Rosello J (2016) Spaceborne GNSS-reflectometry on techDemoSat-1: early mission operations and exploitation. IEEE J Sel Top Appl Earth Obs Remote Sens 9(10):4525–4539. https://doi.org/10.1109/JSTARS.2016.2603846

Wang Y, Morton YJ (2022) Ionospheric total electron content and disturbance observations from space-borne coherent GNSS-R measurements. IEEE Trans on Geosci Remote Sens 60:1–13. https://doi.org/10.1109/TGRS.2021.3093328

Wang Y (2023a) Ionosphere TEC Observation Over Ocean Using Single-Frequency Wideband GNSS Signal Reflectometry. Proceedings of the 36th International Technical Meeting of the Satellite Division of The Institute of Navigation (ION GNSS+ 2023). 3941–3946. https://doi.org/10.33012/2023.19415

Wang Y (2023b) Troposphere sensing using grazing-angle GNSS-R measurement from LEO satellites. Geophys Res Lett. https://doi.org/10.1029/2023GL106249

Xing J, Datta-Barua S, Garrison J, Ridley A, Pervan B (2015) Relative ionospheric ranging delay in LEO GNSS oceanic reflections. IEEE Geosci Remote Sens Lett 12(7):1416–1420. https://doi.org/10.1109/LGRS.2015.2404912

Zus F, Bender M, Deng Z, Dick G, Heise S, Shang-Guan M, Wickert J (2012) A methodology to compute GPS slant total delays in a numerical weather model. Radio Sci. https://doi.org/10.1029/2011RS004853